Abstract

Over the past decade, in Hall-A of the Thomas Jefferson National Accelerator Facility (TJNAF), both the HAPPEX and PREx collaborations have carried out various high-precision polarized elastic electron scattering experiments to explore the nuclear structure, the nucleon form factor and the weak charge of proton and electron. They have done so through the technique of the parity-violating asymmetry measurement with limited theoretical uncertainties. My dissertation focuses on the study of nuclear structure, namely the thickness of the neutron skin, using elastic electron scattering experiments.

The direct measurement of the thickness of the neutron skin in heavy nuclei, where neutron are two-fold more than protons, constrains the slope of changes in binding energies of every single heavy nucleus with respect to the full nucleus density, including proton and neutron densities. In addition, a more precise description of the neutron density profile for each heavy nucleus can help us gain better understanding of nuclear binding energies and has astrophysical implications for neutron stars. As far as we know, the proton and charge RMS (root-mean-square) radii in heavy nuclei such as Lead ($^{208}_{82}$Pb) have been measured with an accuracy of 0.02 fm and 0.002 fm, respectively. However, there is no clear picture of the neutron density profile through a high precision neutron RMS radii measurement free from the strong interaction until now.

Through a series simulations, both theorists and experimentalists have studied the sensitivity of the parity-violating asymmetry to the extraction of the neutron radii in heavy nuclei. Under some specific conditions, for instance, a fixed scattering angle of 5 degrees and a fixed Q^2 of 0.0088 GeV^2, a 3% statistic uncertainty of parity-violating asymmetries corresponds to a merely 1% error of the neutron radii in Lead ($^{208}_{82}$Pb). That is, the uncertainties of neutron radii in Lead ($^{208}_{82}$Pb) is three-fold smaller than the error of the parity-violating asymmetry. Since Mar. 2010, we performed the first electroweak

experiment to probe the neutron radii in Lead ($^{208}_{82}$Pb). The normalized parity-violating asymmetries, after addressing false asymmetries, background asymmetries, to the 90% partially polarized electron beam and the momentum-transfer (Q^2) is $0.656 \pm 0.06(\mathrm{stat}) \pm 0.014(\mathrm{sys})$ ppm (part-per-million), which corresponds to the thickness of the neutron skin of $0.33^{+0.16}_{-0.18}$ fm. One of the most significant systematic uncertainties results from the discrepancies in beam parameters such as position, angle and energy on the target, leading to the difference in the differential cross-section between two helicity states. The helicity-correlated (window-to-window or pulse-to-pulse) beam asymmetries thus arise. My primary contribution to this experiment is to establish an analysis strategy used to control the size of the helicity-correlated beam asymmetries during the data-taking period. This analysis is especially addressed in Chapter 6.

In sum, the neutron radii of $0.33^{+0.16}_{-0.18}$ fm in Lead ($^{208}_{82}$Pb) supports the existence of the neutron skin in the neutron-rich matter. A second future run will yield a much higher precision neutron radii measurement. Moreover, the strong correlation between the neutron skin in Lead ($^{208}_{82}$Pb) and the neutron start radius indicates an approach from nuclear physics to understand the astrophysical equation of state (EOS) for a neutron star.

First Leptonic Probe of Neutron Radii in Lead ($^{208}_{82}$Pb) at Low-Q^2

by

Chun-Min Jen

B.S. Degree in Physics at *Soochow University*, Taipei, Taiwan, 1997-2001

M.S. Degree in Physics at *National Taiwan University (NTU)*, Taipei, Taiwan, 2002-2005

DISSERTATION

Submitted in partial fulfillment of the requirements

for the degree of Doctor of Philosophy in Physics

in the Graduate School of Syracuse University

May 2013

Prof. Paul A. Souder (Principal Investigator)

©Copyright 2013 Chun-Min Jen

All Rights Reserved

Dedicated to My Loving and
Supportive Parents and Family

Acknowledgement

First and foremost, I'd like to sincerely express my deep appreciation to my thesis adviser, Prof. **Paul Souder**, for not only accepting me as his graduate student in April, 2009 but selflessly offering me countless research opportunities to work on. Prof. **Paul Souder** rarely tells me what I need to do and how I conduct my research project directly. In addition, he all the time allows me to make countlessly careless mistakes but never blames me. Prof. **Paul Souder** is not an adviser who shows a clear, plain and banal path to have me smoothly walk on it step-by-step toward the completion of my PhD degree without any surprise, unless I want to be treated as an idiot or a slave. In contrast, Prof. **Paul Souder** is a very reliable supporter who provides tremendous resources to assist me developing myself to be an independent researcher. For example, Prof. **Paul Souder** allows me to establish a new methodology (approach) exclusively for my main thesis analysis on my own without regarding what other colleagues think or caring whether my innovative trial might end up with the failure or not. Instead, he chose to spend his precious time discussing plentiful of ideas with me, and meanwhile, distributing more much higher level of background knowledge without hiding anything from me. Most importantly, Prof. **Paul Souder** makes use of his profoundly critical thinking style to challenge every of my research works through innumerable trials. Prof. **Paul Souder** never tells me the answer of questions he asks, but he does have me explore my own limits, uncover my potential, and in the meantime, never forgets to encourage me not to give in to his severe reasoning ability. I really enjoy every moment of our frequent discussions. Successfully surpassing the high standard which Prof. **Paul Souder** sets for my dissertation analysis always attracts me to concentrate on my thesis work with more time and energies. I do believe Prof. **Paul Souder** is absolutely a so-called resourceful adviser and also able to be regarded as an extremely experienced educationist. In short, the more freedom and

patience Prof. **Paul Souder** supplies, the more I am willing to make progress. Despite no regulation, I at all times feel obliged to regularly brief Prof. **Paul Souder** what I am doing currently and what I am going to do in the near future.

In June, 2011, I suddenly realize I can switch my research interest from nuclear physics to neutrino physics. A friend of mine, now a postdoctoral research associate at Brookhaven National Laboratory, despised this possibility, for I barely give a presentation to show my research work to others in some well-known conferences. Hence, it's very difficult to let other people know me and further understand my contribution to my thesis experiment. Eight months later, after giving a very formal *seminar* talk in Indiana University at Bloomington, I just learn that the quantity of talks is actually not the criterion to show the reliability of what I have done in the past few years. In the contrary, the quality and credibility of my fully completed research jobs during my PhD years are evident to play important roles to manifest how reliable I am. I am very thankful for being immersed in such an excellent research environment provided by Jefferson Lab. Aside from the excitement of overcoming all challenges brought in by the unique of my thesis experiment (regarded as one of ten most challenging experiments performed at Jefferson Lab during a time period of twenty-five years), the local collaboration is more like a pretty special and intimate collaboration (aka: parity family) to me. I feel deeply honored to be regarded as a member of the parity family and feel an immense gratitude to belonging to the parity family. Undoubtedly, it's a pleasure to work with other family members, especially as I have been admitted to providing myself a great asset to this family. I have no doubt to continue paying more and more for the debt I owe to this family, for the ticket price for the entrance of this family is invaluable to me.

During the past year, I feel so blessed that I got few opportunities to give seminar talks. I learn a lot about how to appropriately interact with the research profession. Besides, through giving a talk, I also realize the importance of possessing effective communication skills. For instance, the feedback I heard from the audience on the *seminar* talk in State University of New York at Stony Brook taught me how to organize my presentation in order to clearly convey sophisticated concepts to a group of people who are not specifically familiar with the research topic which I am primarily interested in. To attract the audience's interests and to have them try asking the speaker more and more questions are fairly critical for fulfilling a successful oral presentation. Thanks to Prof. **Paul Souder**, I owe the success in my career development to his non-stop encouragement and everlasting confidence in me.

I have no word to express my intense gratitude to my parents and family for their considerate understanding and decent efforts to arrange the days of my staying with them in every of my trip home. My younger brother, *Chun-Yu Jen*, got married in last December (on Dec. 29th, 2012), but it's a pity that I cannot attend his marriage ceremony in person. I owe *Chun-Yu* so much to all of his forever care to our parents. My other two younger brothers, sons of one of my father's younger brothers, Chun-Hao (Howard) Jen and Chun-Kai (Kyle) Jen, got admitted to department of medicine at well-known medical schools in Taiwan in Fall 2009 and Fall 2012, respectively. I expect there will be three Dr. Jen in our generation in a couple of years, and I am not only the eldest child in this generation but the first one who earns the degree of doctoral of philosophy.

Contents

Abstract 1

Acknowledgement vi

1 Introduction 1

- 1.1 Theory of Elastic Scattering . . . 4
- 1.2 Binding Energy Models . . . 12
- 1.3 Parity-violating . . . 19
  - 1.3.1 Analysis I: Fit to Mean Field Models . . . 21
  - 1.3.2 Analysis II: Helm Model Weak Form Factor . . . 24
- 1.4 Application: Impact on our Knowledge of the Neutron Star . . . 27

2 Experimental Design 30

- 2.1 Experimental Goal . . . 30
- 2.2 Technical Issues . . . 30
  - 2.2.1 Electron Beam Source and Charge Asymmetry . . . 31
  - 2.2.2 Beam Modulation System and Helicity-Correlated Beam Parameters . 31
  - 2.2.3 Beam Polarimeter and Beam Polarization . . . 32
  - 2.2.4 Data Acquisition System and Parity-Violating Asymmetry . . . 32
  - 2.2.5 Target . . . 33
  - 2.2.6 HRS and Septum Magnets . . . 33
  - 2.2.7 Collimator . . . 34
  - 2.2.8 Focal Plane Detectors . . . 34
- 2.3 Optimization . . . 35
  - 2.3.1 Statistical Uncertainty . . . 37
  - 2.3.2 Systematic Uncertainty . . . 41

2.3.3 Background 43
2.3.4 Blind Analysis 45

3 Experimental Instrument **46**
3.1 PREx Overview 46
3.2 Polarized Electron Source 47
3.2.1 GaAs Photocathodes 48
3.2.2 Pockels Cells 48
3.3 Slow Helicity Reversal 49
3.3.1 Inserted Half-Wave Plate 50
3.3.2 Double Wien 50
3.4 Beam Polarimeter 50
3.4.1 Møller Polarimeter 51
3.4.2 Compton Polarimeter 52
3.5 Beam Monitors and Beam Modulation System 54
3.5.1 Beam Modulation System 55
3.5.2 Beam Position Monitors 57
3.5.3 Beam Current Monitors 58
3.5.4 Low-Current Cavity Monitors 59
3.6 DAQ 60
3.6.1 Integrating (Parity) DAQ 60
3.6.2 Counting DAQ 61
3.7 Target and Raster 62
3.8 HRS 64
3.9 Detectors 65

4 Beam Polarization Measurement **66**
4.1 Formalism 66

4.2 Experimental Measurement of Electron Polarization via Compton Polarimeter 69
4.2.1 Differential Polarization Measurement 69
4.2.2 Integrated Polarization Measurement 70
4.2.3 Energy Weighted Polarization Measurement 70
4.3 Photon Detector and Flash ADCs for Compton Photon Analysis 71
4.3.1 Accumulator Mode 73
4.3.2 Trigger Mode 74
4.4 Compton Photon Analysis 75
4.4.1 Formalism of Compton Scattering Asymmetry Calculation 76
4.4.2 Optimization of Selection Criteria 84
4.4.3 Background Fluctuation 92
4.4.4 Comparison of Asymmetry Measurements Derived from Different Methods 95
4.5 GEANT4 Simulation for Compton Polarimeter 96
4.6 Electron Polarization Result for PRExI via Compton Polarimeter 98

5 Helicity-Correlated Beam Asymmetry (HCBA) 108
5.1 Formalism 108
5.2 PITA Effects 112
5.3 Phase Gradients 112
5.4 Controlling Helicity-Correlated Position Differences 113
5.4.1 Sources of Helicity-Correlated Position Differences 116
5.4.2 Sources of Helicity-Correlated Spot Size and Shape Difference 116
5.5 Final Optimization 117
5.5.1 Offset Term 117
5.5.2 2θ Term 118
5.6 Wien Optimization 119

6 Developed Strategies to Control Helicity-Correlated Beam Asymmetry 122

6.1 Motivation 122

6.2 Introduction to 2x2 dithering analysis 132

6.3 Fractional error of dithering slope 133

6.4 Fractional errors of α, β, Λ, $\mathcal{K}$ and 2x2 dithering coefficients 140

6.5 Introduction to 3x3 dithering analysis 147

6.6 Correlation removal 157

7 Review of $\mathcal{A}_T$ (or $\mathcal{A}_n$) Analysis for PREx 161

A Derivation of Dithering Coefficients 186

B Derivation of Dithering Coefficients w/ PREx geometry 187

List of Tables

1.1 Given MFT models, proton RMS radii ($< R_p^2 >^{1/2}$) and neutron RMS radii ($< R_n^2 >^{1/2}$) in $^{208}_{82}$Pb with a beam energy of 1.05 GeV and a laboratory scattering angle of five degrees. 3

1.2 Least square fits of parameters to non-relativistic and relativistic mean field model weak charge densities. Parameters, R_0 and a_n, stand for the Wood Saxon weak charge density function as described in Equation 1.30. 24

1.3 Least square fits of parameters to theoretical mean field model weak charge densities. Parameters, R_h and σ (see Equation 1.34), are for Helm model weak charge density. 26

2.1 Model root mean square proton R_p and neutron R_n radii for $^{208}_{82}$Pb. 35

2.2 Experimental parameters including beam current (I), beam polarization (P), detector solid angle ($\Delta\Omega$), number of atoms (N), energy resolution (ΔE) and radiation loss factor (ζ). 39

2.3 Statistical error estimates for measuring R_n in 30 days. Results are first presented for $^{208}_{82}$Pb, ^{48}Ca and ^{40}Ca at a laboratory scattering angle of 5°. ^{48}Ca results are also presented for a scattering angle of 4°. The neutron and proton densities are calculated in the Skyrme HF theory with the SLY4 interaction. 39

3.1 Important BM (aka: dithering) parameters in the **PREx** beam modulation system 55

3.2 The mapping of EPICS variables associated with the steering air-core coils and the energy vernier in **PREx** BM hardware. 56

3.3 BM symbols in the datastream for dithering analysis. 56

4.1 Relation between $\delta_{\text{sig.}}$ and $\mathcal{R}$. 90

4.2 Relation between $\delta_{\text{sig.}}$ and $\mathcal{A}_{bkg}$. 91

4.3 Accum0 signal sizes by laser states for PREx. 103

4.4 A table of Compton systematic uncertainties using the All accumulator during 2010 PREx. 103

6.1 parameter categories. 151

6.2 ρ_{pq}, $\mathbf{S}_{pp}$, $\mathbf{S}_{qq}$ and $\mathbf{S}_{pq}$ in low and high α, respectively. 157

7.1 dithered transverse asymmetries, $\mathcal{A}^{Pb}_{cor.}$ and $\mathcal{A}^{C}_{cor.}$, for Lead ($^{208}_{82}$Pb) and Carbon (^{12}C), physics transverse asymmetries, $\mathcal{A}^{Pb}_{phys}$ and $\mathcal{A}^{C}_{phys}$ ($\mathcal{A}_{Bi}$), the dilution factor and the electron beam polarization. 164

7.2 The order of magnitude for statistical errors of $\mathcal{A}^{Pb}_{phys}$ ($\sigma\mathcal{A}^{Pb}_{phys}$). 165

7.3 $\sigma\mathcal{A}^{C}_{phys}$. 165

7.4 The systematic of $\mathcal{A}^{phys.}_{T}$. (unit: ppm) 170

7.5 The systematic for both Lead and Carbon asymmetry corrections, $\Delta\mathcal{A}^{flase}_{Lead}$ and $\Delta\mathcal{A}^{flase}_{Carbon}$. The dilution factor is 0.0854, and the electron beam's polarization is 0.892. (unit: ppb) 176

7.6 The summary systematic of $\mathcal{A}^{phys.}_{T}$ for Lead and Carbon. (unit: ppm) 177

List of Figures

1.1 The charge density of ${}^{208}_{82}$Pb (red solid line), accurately measured in the elastic electron scattering experiment. 3

1.2 Elastic electron scattering at low incident energies. P_1 is the incident momenta; P_3 is the scattering momenta. 5

1.3 The direction of helicity, defined as the projection of the electron spin onto the momentum axis, is either parallel or anti-parallel to the beam momentum. 9

1.4 Electron energies of the incident beam are high enough to see the internal charge distribution of atomic nuclei. 10

1.5 (Left) The differential scattering cross-section of ${}^{208}_{82}$Pb versus Q^2 (momentum transfer, $Q = 2|\vec{p}|\sin\frac{\theta}{2}$, at the center-of-mass energy of 502 MeV. (Right) the charge density function, the inverse Fourier transform of the form factor. . . 12

1.6 Average binding energy per nucleon (MeV) vs. atomic number (number of nucleons in one atom). 13

1.7 Binding energy spectra to describe the EOS of the nuclear system with 18 Skyrme type of MFT models. Dots are Friedman-Pandharipande (FP) [4] variational calculations; crosses are SkX [5]. 15

1.8 Lead neutron skin vs. the derivative of EOS of the neutron system for 18 Skyrme sets. 16

1.9 (Left) Δr_{np} versus a_4; (middle) Δr_{np} versus p_0; (right) Δr_{np} versus ΔK_0 for a variety of mean-field models. The remarkably small spread of p_0 shows no significant separation of different theory models. 17

1.10 Calculated form factor, $F_n(Q^2)$, versus $< R_n^2 >^{1/2}$ of ${}^{208}_{82}$Pb (fm). At some fixed low-Q^2 value, $F_n(Q^2)$ is found to be strongly correlated to the size of neutron RMS radii, $< R_n^2 >^{1/2}$ in a heavy nucleus. 18

1.11 Tree-level Feynman diagrams: (a) single photon exchange, and (b) Z^0 exchange for the electron scattering from the nucleus. 19

1.12 $\mathcal{A}_{PV}^{DWBA}$ for the polarized elastic electron scattering from the Lead ($^{208}_{82}$Pb) versus the scattering angle, θ. The dotted curve is a plane-wave approximation for $\mathcal{N}_N = \mathcal{N}_Z$ nuclei. The long-dashed curve is a plane-wave approximation for $\mathcal{N}_N \neq \mathcal{N}_Z$ nuclei. The full distorted wave results is solid curve at 850 MeV. 22

1.13 $\mathcal{A}_{PV}^{DWBA}$ versus scattering angle, θ, for the polarized elastic electron scattering from $^{208}_{82}$Pb at the beam energy of 1.05 GeV. 23

1.14 $\mathcal{A}_{pv}^{DWBA}$ versus $< R_n^2 >^{1/2}$ for both non-relativistic and relativistic mean field interaction models. The experimental asymmetry measurement, $\mathcal{A}_{pv}^{Pb}$, corresponding to the extracted $< R_n^2 >^{1/2}$, is also depicted on this graph and labelled as PREx-I (2010 PREx). The expected asymmetry result for the proposed running experiment, PREx-II (2014 PREx), overlaps on the same central value as PREx-I's with a precision statistical improvement of three-fold. 25

1.15 (Color on line) Helm model weak charge density-ρ_W(r) of $^{208}_{82}$Pb that is consistent with the 2010 PREx result (solid black line). The brown error band shows the incoherent sum of experimental and model errors. The red dashed curve is the experimental (electromagnetic) charge density ρ_{ch} and the blue dotted curve shows a sample mean field result based on FSUGold interaction [23]. . 27

2.1 Parity-violating asymmetry ($\mathcal{A}_{pv}^{DWBA}$) versus laboratory angle for elastic scattering electrons from the Lead target at 1.05 GeV. Different curves correspond to different mean field models used to do the least square fits of neutron density function's parameters. 36

2.2 Sensitivity of the parity-violating asymmetry ($\mathcal{A}_{pv}^{DWBA}$) for $^{208}_{82}$Pb to the change in the neutron radius. The solid (dash) line corresponds to the beam energy of 1.05 (1.80) GeV. The non-relativistic mean field model, SLY4, was used here. 37

3.1 Schematic of CEBAF. 47

3.2 A schematic of the strained-layer (a) and superlattice (b) photocathode structure. 48

3.3 A schematic of the polarized electron source set-up in the injector part at JLab. The laser light was circularly polarized by PC. Through the photoemission from a GaAsP photocathode, the polarized electrons were released, because they were excited from the valence band to the conducting band via the absorption of the incident photon energies from the circularly polarized laser light. The polarity of the laser light determines the helicity state of the electron beam. 49

3.4 For PREx, only the second solenoid and the horizontal Wien filter were used. The set of solenoids and Wien filters along the beamline help reduce HC systematic uncertainties. In addition, the horizontal Wien can optimize the longitudinal beam polarization. 51

3.5 PREx Compton used a 532nm (2.33eV) laser, and Fabry-P$\acute{e}$rot cavity contained a circulating power of ~ 3.5kW. 53

3.6 A schematic of Hall-A beam monitors and beam modulation coils located along the beamline. 54

3.7 PREx low-current cavity monitors provide very accurate and reliable beam position and current measurements. Due to the extremely high scattering rate, 20 MHz/μA, during PREx, the conventional Hall-A detector package and parity DAQ cannot perform appropriately at the low beam current below 1μA without the adoption of the low-current cavity monitors. In addition, the stripline BPMs and those BCMs as mentioned above were also not reliable to provide the correct beam position and current measurements at the beam current below 1μA. 59

3.8 PREx production-mode targets. 62

3.9 HRS separated the elastically scattering electrons from inelastic events and meanwhile forced the elastic electron signals to be focused onto the focal plane of the detectors. 64

3.10 The angle of incident electrons on these detectors is at 45° to ensure the optimized collection of the quartz scintillator's *Čherenkov* radiation in the PMTs. The bottom detector had a $3.5 \times 14.0 \times 0.5$ cm^3 quartz, and the top detector had a $3.5 \times 14.0 \times 1.0$ cm^3 quartz. 65

4.1 Schematic of electron and photon polarization. 67

4.2 This graph shows you $\mathcal{A}_{th}$ is related to the scattered photon energy (unit: MeV). $\mathcal{A}_{th}$ is negative at low scattered photon energies, and positive at higher photon energy region. $\mathcal{A}_{th}$ crosses zero at the scattered photon energy around 20MeV. The maximum $\mathcal{A}_{th}$ near the Compton edge is close to 0.037. 71

4.3 Front (left) and side (right) view of the GSO detector housing including the tungsten converters and scintillators used to determine the position of the photon beam. 72

4.4 The timing structure for helicity windows. 73

4.5 The six accumulator modes are explicitly drawn. 74

4.6 The quality of Compton data for one standard run. (Top left) beam current monitor vs. time; (top middle) the high voltage monitor vs. time; (top right) the photon laser's cavity power vs. time; (bottom left) the photon laser's cavity polarization vs. time; (bottom middle) the trigger rate vs. time; (bottom right) MPS signal check. The data quality information is sent out in the form of scalers for each helicity window. As a result, the selection criteria on a basis of window-to-window, say, each MPS signal interval, can be easily applied to data-analysis. 76

4.7 A schematic of Compton data-taking during a series of cavity-locked and -unlocked periods. 78

4.8 The mean of asymmetry measurement is determined in each laser cycle after the subtraction of local background as calculated in Equation 4.19 was made. The polarization state of the photon laser in each cycle is either right- (red) or left-hand (blue). 79

4.9 Background-subtracted Compton asymmetry "Gaussian" histograms comprising pairs of asymmetry measurements from all of the helicity windows in one single two hour long Compton run. The y-axis represents the total number of helicity pairs. The red (blue/dark) histogram represents the pair-wise asymmetry measurement for the photon polarization of laser-right (left/off). 81

4.10 The local mean asymmetry (after the background subtraction) in each laser cycle is measured for either laser-right (red) or -left (blue) photon polarization state. This graph shows several local mean asymmetry measurements for a bunch of Compton runs with the same IHWP and Wein states. All of these Compton runs belong to ONE slug, where both IHWP and Wein states remain unchangeable until either IHWP or both IHWP and Wein flip their signs. . . 82

4.11 Histogram of the non-background subtracted numerator of the Compton asymmetry as shown in Equation 4.15. 83

4.12 Histogram of the non-background subtracted denominator of the Compton asymmetry as shown in Equation 4.15. 84

4.13 Integration of accumulator data in laser-on (red-dotted) and -off (black-dotted) periods vs. MPS helicity window for Compton run 23129. 86

4.14 Asymmetry vs. laser cycle for Compton run 23129. Red (blue): Laser-right (left) **before** fixing the MPS length; green (yellow): Laser-right (left) **after** fixing the MPS length. 87

4.15 Integration of accumulator data in laser-on (red-dotted) and -off (black-dotted) periods vs. MPS helicity window for Compton run 22975. 87

4.16 Asymmetry vs. laser cycle for Compton run 22975. Red (blue): Laser-right (left) **before** fixing the MPS length; green (yellow): Laser-right (left) **after** fixing the MPS length. 88

4.17 Mean laser-wise asymmetry vs. Compton run. Black dot w/ green (purple) error bar represents the normal runs before (after) fixing the MPS length. Red (magenta) dot w/ green (purple) error bar represents the problematic runs before (after) fixing the MPS length. 89

4.18 (Top panel) $\mathcal{R}$ vs. Compton run. (Bottom panel) $\mathcal{R}$ histogram. 90

4.19 (Top panel-left) $\mathcal{A}_{bkg}$ vs. Compton run. (Top panel-right) $\mathcal{A}_{bkg}$ histogram. (Bottom panel-left) pull of $\mathcal{A}_{bkg}$ vs. Compton run. (Bottom panel-right) pull of $\mathcal{A}_{bkg}$ histogram.. 92

4.20 This graph represents the average of adjacent background differences over all of the laser cycles for each Compton run. The unit of the x-axis is each individul Compton run. (Top pannel) The subtraction of "before" background from "after". (Second pannel) Zoom in the top pannel. (Third pannel) The subtraction of "after" background from "before". (Bottom pannel) Zoom in the third pannel. 93

4.21 The pull plots for the background study in Fig. 4.20. 94

4.22 The possible background pattern. 94

4.23 $< \sum_i \mathrm{diff}^i_{\mathrm{On}} >$ vs. laser cycle for Compton run 22956. Red dots are those low-statistics cycles which were cut from data. 96

4.24 Background-subtracted Compton asymmetry "non-Gaussian" histograms from the pair-wise method for Compton run 22597. 97

4.25 (Upper left) the pair-wise asymmetry in laser-right; (upper right) the pair-wise asymmetry in laser-left; (lower left) the pair-wise background asymmetry followed by the laser-on right period; (lower left) the pair-wise background asymmetry followed by the laser-on left period. 97

4.26 A typical waveform from the GSO calorimeter for incident photons from the Compton scattering. The x-axis is time (ns). The y-axis is summed FADC channels. The standard trigger mode reads Compton photon signals from the first three helicity windows, and then only reads out the random samples in the forth helicity window. This way can help save more disk space. 99

4.27 A waveform with higher deposited photon energies in the calorimeter. The sample can be used to study the background as well as the pile-up effect. . . 99

4.28 Logarithmic Compton photon energy spectrum integrated from the GSO photon detector during a typical run. The red curve shows the background spectrum during the laser-off periods. The blue curve gives the background-subtracted spectrum during the laser-on periods. The region indicated by arrows contains the background-only spectrum, and is used to normalize the rest of regions, where both signal and background spectra are overlapped to each other. 100

4.29 MC fit to the measured Compton photon energy spectrum, where the data were taken from FADC with the trigger mode. 100

4.30 The measured Compton asymmetry vs. ADC response channels, where the energies of scattered photons were deposited in the GSO. 101

4.31 $\mathcal{A}_{\text{th}}$ vs. collimator position 104

4.32 Measured asymmetry vs. PREx data set (in the unit of slug: data accumulation/per day). The error bar for each round point is statistical only for the laser-wise method. 105

4.33 Measured electron beam polarization vs. PREx data set. 105

4.34 Measured asymmetry vs. PREx Compton run. The error bar for each round point is statistical only for the laser-wise method. 106

4.35 Measured asymmetry vs. PREx Compton run. The error bar for each round point is statistical only for the laser-wise method. 106

4.36 $\sigma_{\mathcal{A}_{cor}}$ vs. σ_s (%). 107

4.37 Measured background asymmetry vs. PREx Compton run. The error bar for each round point is statistical only for the laser-wise method. 107

5.1 A schematic of the polarized electron source set-up in the injector part at JLab. The laser light was circularly polarized by PC. Through the photoemission from a GaAsP photocathode, the polarized electrons were released, because they were excited from the valence band to the conducting band via the absorption of the incident photon energies from the circularly polarized laser light. The polarity of the laser light determines the helicity state of the electron beam. The insertable mirror guides the beam onto either a quad-photodiode (QPD) or a linear array-photodiode (LAPD) detector during the laser table studies. On the other hand, the insertable mirror and the insertable polarizer are retraced during the electron beam studies and the production data-taking as well. In addition, the insertable half-wave plate is inserted and retraced alternatively during the laser table studies, the electron beam studies and the production data-taking period. 111

5.2 A typical PITA scan plot. HCBA ($\mathcal{A}_{\rm q}$) is plotted on the y-axis, and $V_{\rm PC}^{\rm R(L)}$ is on the x-axis. In a PITA scan, $V_{\rm PC}^{\rm R(L)}$ is adjusted anti-proportionally, and $\mathcal{A}_{\rm q}$ is measured at each of the specific $V_{\rm PC}^{\rm R(L)}$. 113

5.3 A spatially varying Δ-phase leads to the helicity-correlated phase shift across the beam spot. The amount of the residual linear polarization is larger on the left relative to the right. 114

5.4 The linear relation between Δ and the beam's spatial displacement (top panel). The change in the intensity of the laser light between two helicity states as expressed in Equation 5.2 versus the beam's displacement toward two opposite directions for each helicity state respectively. The solid line represents the left-handed intensity, and the dash line corresponds to the right-handed intensity (bottom pannel). 114

5.5 A schematic of flowchart for the suppression of $\mathcal{A}_\mathrm{q}$, Δ_X and Δ_Y as shown in Equation 5.4 and Equation 5.8. 121

6.1 The schematic geometry of the beam modulation system. 123

6.2 Strip line monitors near the target on the Hall-A beam line. The beam was deflected by steering coils. 124

6.3 (top panel) The response of the beam monitor (BPM4B) to the modulation by driving the VME-DAC to one selected coil (coil-5) in the direction of x with waveforms generated by the sine waveform generator. (bottom panel) One coil, e.g. coil-5, is driven by VME-DAC to perturbe the beam movement along x. Each colorful point indicates the phase point, and different colors are used to identify individual phases. (data: dithering cycle 65, parity run 4755, slug 40) 124

6.4 The corresponding dithering slope, $\frac{\partial \mathcal{M}_{4bx}}{\partial \mathcal{C}_5}$, to the beam modulation as depicted in Fig. 6.3 with an arbitrary unit. Each point refers to the average size of one phase point for BPM4B (y-axis) and coil such as coil-5 (x-axis), in a full dithering cycle. (data: dithering cycle 65, parity run 4755, slug 40) 125

6.5 (top panel) The response of one detector, sitting on the top side behind the left-arm high resolution spectrometer, to the modulation by driving the VME-DAC to one selected coil (coil-1) in the direction of x with waveforms generated by the sine waveform generator. (bottom panel) Similar plot to the bottom of Fig. 6.3 but with respect to a different coil, e.g. coil-1. (data: dithering cycle 65, parity run 4755, slug 40) 125

6.6 Similar to Fig. 6.4. The corresponding dithering slope, $\frac{\partial \sigma_4}{\partial \mathcal{C}_1}$, to the beam modulation as depicted in Fig. 6.5 with an arbitrary unit. Each point refers to the average size of one phase point for the detector, sitting on the top side behind the left-arm high-resolution spectrometer (y-axis), and the coil, e.g. coil-1 (x-axis), in a full dithering cycle. (data: dithering cycle 65, parity run 4755, slug 40) 126

6.7 This graph reflects the slow drift of the signal flux in one detector which responds to the modulation via coil-5 during the whole period of one dithering cycle due to the variation in temperature of the instrument. (data: dithering cycle 63, run 4755, slug 40) 126

6.8 This graph reflects the wiggling of the signal flux in one detector which responds to the modulation via coil-1 during the whole period of one dithering cycle. (data: dithering cycle 65, run 4755, slug 40) 127

6.9 The shift in the responding phases of both detector and beam position monitor against the driving phase of coil-3 is maximum and around 35°. 127

6.10 Histograms of different shifts in phase with respect to different coils. 128

6.11 History plots of root-mean-square errors for $\frac{\partial \mathcal{M}_{4bx}}{\partial \mathcal{C}_1}$ (top-left pannel), $\frac{\partial \mathcal{M}_{4bx}}{\partial \mathcal{C}_5}$ (top-right pannel), $\frac{\partial \sigma_4}{\partial \mathcal{C}_1}$ (bottom-left pannel) and $\frac{\partial \sigma_4}{\partial \mathcal{C}_5}$ (bottom-right pannel) vs. good dithering cycle. 135

6.12 Correlations of residuals between $\frac{\partial \mathcal{M}_{4bx}}{\partial \mathcal{C}_5}$ and $\frac{\partial \mathcal{M}_{4ax}}{\partial \mathcal{C}_5}$ (left pannel) and $\frac{\partial \mathcal{M}_{4bx}}{\partial \mathcal{C}_1}$ and $\frac{\partial \mathcal{M}_{4ax}}{\partial \mathcal{C}_1}$ (right pannel). 136

6.13 Correlations of residuals between $\frac{\partial\mathcal{M}_{4bx}}{\partial\mathcal{C}_5}$ and $\frac{\partial\sigma_4}{\partial\mathcal{C}_5}$ (top-left pannel) and $\frac{\partial\mathcal{M}_{4bx}}{\partial\mathcal{C}_1}$ and $\frac{\partial\sigma_4}{\partial\mathcal{C}_1}$ (bottom-left pannel). Histograms of residuals for $\frac{\partial\sigma_4}{\partial\mathcal{C}_5}$ (top-right pannel) and $\frac{\partial\sigma_4}{\partial\mathcal{C}_1}$ (top-left pannel). 136

6.14 Histograms of residuals for dithering slopes such as $\frac{\partial\mathcal{M}_{4bx}}{\partial\mathcal{C}_1}$ (top-left pannel), $\frac{\partial\mathcal{M}_{4ax}}{\partial\mathcal{C}_1}$ (top-right pannel), $\frac{\partial\mathcal{M}_{4bx}}{\partial\mathcal{C}_5}$ (bottom-left pannel) and $\frac{\partial\mathcal{M}_{4ax}}{\partial\mathcal{C}_5}$ (bottom-right pannel). 138

6.15 History plots of $\frac{\partial\mathcal{M}_{4bx}}{\partial\mathcal{C}_1}$ (black) and $\frac{\partial\mathcal{M}_{4bx}}{\partial\mathcal{C}_5}$ (blue) vs. good dithering cycle. . . 139

6.16 History plots of $\frac{\partial\sigma_4}{\partial\mathcal{C}_1}$ (black) and $\frac{\partial\sigma_4}{\partial\mathcal{C}_5}$ (blue) vs. good dithering cycle. 139

6.17 constant ratio, β over α, history plot. 143

6.18 α (red solid dot), β (blue solid dot), Λ (magenta solid dot) and $\mathcal{K}$ (green solid dot) history plots. 144

6.19 fractional errors of α (red), β (blue), Λ (magenta) and $\mathcal{K}$ (green) (in the cycle-average level), where $0.25 < \alpha < 0.4$. 145

6.20 fractional errors of α (red), β (blue), Λ (magenta) and $\mathcal{K}$ (green) (in the cycle-average level), where $\alpha > 0.4$ or $\alpha < 0.25$. 146

6.21 2x2 (top panel) $\frac{\partial\sigma_j^m}{\partial\mathcal{M}_{4ax}}$ and (bottom panel) $\frac{\partial\sigma_j^m}{\partial\mathcal{M}_{4bx}}$ dithering coefficient history plots (unit: $\frac{ppm}{\mu m}$). From left to right: right-arm detector at the bottom side; right-arm detector at the top side; left-arm detector at the bottom side; left-arm detector at the top side. 147

6.22 the fractional error comparison/correlation between $\sigma(\frac{\partial\sigma_j^m}{\partial\mathcal{M}_{4ax}})$ (x-axis) and $\sigma(\frac{\partial\sigma_j^m}{\partial\mathcal{M}_{4bx}})$ (y-axis) for the individual detectors. Upper left: the right-arm detector on the bottom side; upper right: the right-arm detector on the top side; lower left: the left-arm detector on the bottom side; lower right: the left-arm detector on the top side. 148

6.23 the fractional error comparison between $\sigma\beta$ (blue solid dot) and $\sigma(\frac{\partial\sigma_j^m}{\partial\mathcal{M}_{4ax}})$ (open square) for the individual detectors. Upper left: the right-arm detector on the bottom side; upper right: the right-arm detector on the top side; lower left: the left-arm detector on the bottom side; lower right: the left-arm detector on the top side. 149

6.24 the fractional error comparison between $\sigma\beta$ (blue solid dot) and $\sigma(\frac{\partial\sigma_j^m}{\partial\mathcal{M}_{4bx}})$ (open triangle) for the individual detectors. Upper left: the right-arm detector on the bottom side; upper right: the right-arm detector on the top side; lower left: the left-arm detector on the bottom side; lower right: the left-arm detector on the top side. 150

6.25 a simple depiction of position and angular fluctuations as measured in the collimator. 152

6.26 (red open square) $\frac{\partial\mathcal{M}_{12x}}{\partial\mathcal{N}_1}$ (correlation to the position fluctuations) and (blue open triangle) $\frac{\partial\mathcal{M}_{12x}}{\partial\mathcal{N}_2}$ (correlation to the angular fluctuations) history plot. . . 153

6.27 (left panel) 2x2 vs. (right panel) 3x3 $\frac{\partial\sigma_j^m}{\partial\mathcal{M}_{4ax}}$ (red open square) and $\frac{\partial\sigma_j^m}{\partial\mathcal{M}_{4bx}}$ (open blue triangle) dithering coefficient history plots (unit: $\frac{ppm}{\mu m}$). From top to bottom: right-arm detector at the bottom side; right-arm detector at the top side; left-arm detector at the bottom side; left-arm detector at the top side.154

6.28 3x3 $\frac{\partial\sigma_j^m}{\partial\mathcal{M}_{12x}}$ dithering coefficient history plot (unit: $\frac{ppm}{\mu m}$). Upper left: the right-arm detector on the bottom side; upper right: the right-arm detector on the top side; lower left: the left-arm detector on the bottom side; lower right: the left-arm detector on the top side. 155

6.29 (red open square) $\frac{\partial\mathcal{M}_{12x}}{\partial\mathcal{M}_{4ax}}$ and (blue open triangle) $\frac{\partial\mathcal{M}_{12x}}{\partial\mathcal{M}_{4bx}}$ history plot. 155

6.30 $\frac{\delta}{\alpha}$ history plot. 156

6.31 take run 4749: the correlation between $\Delta\mathcal{M}_{4ax}$ and $\Delta\mathcal{M}_{4bx}$ (left : $\rho_{pq} \neq 0$) within quartet windows; the correlation between $\Delta\mathcal{N}_1$ and $\Delta\mathcal{N}_2$ (right : $\rho_{12} = 0$) within quartet windows. 159

6.32 take runs 4674-4749: the correlation of residuals between $\Delta\mathcal{M}_{4ax}$ and $\Delta\mathcal{M}_{4bx}$ (left : $\rho_{pq} \neq 0$) within different runs; the correlation of residuals between $\Delta\mathcal{N}_1$ and $\Delta\mathcal{N}_2$ (right : $\rho_{12} = 0$) within different runs. 160

7.1 the physics asymmetry for Lead 166

7.2 the physics asymmetry for Carbon 167

7.3 the corrected asymmetry for Lead 168

7.4 the corrected asymmetry for Carbon 169

7.5 the charge asymmetry ($\mathcal{A}_Q^{raw}$) for Lead 172

7.6 the charge asymmetry ($\mathcal{A}_Q^{raw}$) for Carbon 173

7.7 the physics charge asymmetry ($\mathcal{A}_Q^{phys}$) for Lead with the correction of the Carbon contamination and the electron beam's polarization. 174

7.8 the physics charge asymmetry ($\mathcal{A}_Q^{phys}$) for Carbon with the correction of the Carbon contamination and the electron beam's polarization. 175

7.9 the weighted average of the asymmetry correction in the run-average level for Lead with separate insertable half-wave plat and wein angle (spin flipper) states.178

7.10 the weighted average of the asymmetry correction in the run-average level for Carbon with separate insertable half-wave plat and wein angle (spin flipper) states. 179

7.11 the standard set of beam position monitor difference structures ($\Delta\mathcal{M}_j^{j=4ax}$, $\Delta\mathcal{M}_j^{j=4bx}$, $\Delta\mathcal{M}_j^{j=4ay}$, Δ
for Lead in separate half-wave plat states and wein angle states. 180

7.12 the standard set of beam position monitor difference structures ($\Delta\mathcal{M}_j^{j=4ax}$, $\Delta\mathcal{M}_j^{j=4bx}$, $\Delta\mathcal{M}_j^{j=4ay}$, Δ
for Carbon in separate half-wave plat states and wein angle states. 181

7.13 the dithering coefficients (unit: ppm/μm) for the left-arm detector versus beam position (or energy) monitors ($\frac{\partial\mathcal{D}_k^{k=L}}{\partial\mathcal{M}_j}$) in Lead. 182

7.14 the dithering coefficients (unit: ppm/μm) for the right-arm detector versus beam position (or energy) monitors ($\frac{\partial\mathcal{D}_k^{k=R}}{\partial\mathcal{M}_j}$) in Lead. 183

7.15 the dithering coefficients (unit: ppm/μm) for the left-arm detector versus beam position/energy monitors ($\frac{\partial \mathcal{D}_k^{k=L}}{\partial \mathcal{M}_j}$) in Carbon. 184

7.16 the dithering coefficients (unit: ppm/μm) for the right-arm detector versus beam position/energy monitors ($\frac{\partial \mathcal{D}_k^{k=R}}{\partial \mathcal{M}_j}$) in Carbon. 185

B.1 the geometry of the beam modulation system. 188

Chapter 1

Introduction

Binding energies, along with a series of parameters, such as charge (proton) radii, regarded as the size of the atomic nucleus, electric charge, mass, and the nuclear system's energies of excited states, are used to characterize the basic properties of a single nucleus. Consider Helium ($^4_2$He), for example. The nuclear binding energy of Helium ($^4_2$He) is determined by the famous Einstein's mass-energy relation as follows:

$$BE \;=\; \Delta m C^2 = 2 \times (m_p C^2 + m_n C^2) - m_{He} C^2, \tag{1.1}$$

where BE stands for binding energies of the four-nucleon system and m_p, m_n and m_{He} are the rest masses for the proton, neutron and Helium, respectively. Generally speaking, binding energies of each single nucleus are the amount of energies required to separate an atom into its constituent nucleons, protons and neutrons. For heavy nuclei, where neutrons ($\mathcal{N}_N$) are more than protons ($\mathcal{N}_Z$), part of binding energies, which is zero in light nuclei ($\mathcal{N}_N = \mathcal{N}_Z$), is named the asymmetry energy, $E_1(\rho_n, \rho_p)$, to account for the energy cost as each nucleus departs from equal number of protons and neutrons. So, in heavy nuclei, binding energies are expressed in terms of two separate parts:

$$E(\rho_n, \rho_p) \;=\; E_0(\rho) + E_1(\rho_n, \rho_p), \tag{1.2}$$

where ρ is the nucleus density. Also, $E_0(\rho)$ is generalized to be the binding energy for the symmetric part of every single nuclei, while $E_1 \simeq S(\rho)(\frac{\rho_n - \rho_p}{\rho})^2$ contributes to the rest of binding energy for the asymmetric part. According to Equation 1.2, the entire binding energy, $E(\rho_n, \rho_p)$, is a function of both proton and neutron densities. For the neutron-rich heavy nuclei, $E_1(\rho_n, \rho_p)$, the asymmetry energy, can become the dominant contribution to the binding energy. In addition, the asymmetric contribution is predicted to be linearly correlated with the average nucleus density via various non-relativistic and relativistic mean-field models. That is, the change in the nucleus density results in the variation in binding energy of the entire nucleus, and vice versa. Unfortunately, over the past eighty years of nuclear physics development, the neutron density profile is still ambiguous to us, whereas the proton (charge) density profile has been quite accurately pinned down with a precision of 2% (0.04%) via a variety of non-parity violating elastic electron scattering experiments in the 70's. Hence, a high precision neutron radii measurement, giving rise to the more insightful density profile determination, is important to describe the full binding energy for neutron-rich matter.

As mentioned above, through elastic electron scattering experiments over a range of Q^2 [1, 2], the electromagnetic charge (or proton) density, ρ_{ch} (or ρ_p), as drawn in Fig. 1.1 has been measured with the precision of both charge and proton root-mean-square (RMS), $< R_{ch}^2 >^{1/2}$ and $< R_p^2 >^{1/2}$, up to 0.04% (± 0.002 fm) and 2% (± 0.02 fm), respectively. As a result, so far, both the charge and proton RMS radii have been regarded as a measure of one nucleus size. Given that the knowledge of binding energy as well as the well-known ρ_{ch}, a range of neutron RMS radii ($< R_n^2 >^{1/2}$) in Lead ($^{208}_{82}$Pb) as defined in Equation 1.3 can be theoretically predicted by non-relativistic and relativistic mean field (MF) interaction models which are listed in Table 1.1.

$$< R_n^2 >^{1/2} \quad = \quad \sqrt{\frac{\int \mathrm{d}^3r \, r^2 \rho_n(r)}{\int \mathrm{d}^3r \, \rho_n(r)}}. \tag{1.3}$$

Table 1.1: Given MFT models, proton RMS radii ($< R_p^2 >^{1/2}$) and neutron RMS radii ($< R_n^2 >^{1/2}$) in $^{208}_{82}$Pb with a beam energy of 1.05 GeV and a laboratory scattering angle of five degrees.

MF Interaction	$< R_p^2 >^{1/2}$ (fm)	$< R_n^2 >^{1/2}$ (fm)
Skyrme I [24] (non-rel.)	5.38	5.49
Skyrme III [25] (non-rel.)	5.52	5.65
Skyrme SLY4 [26] (non-rel.)	5.46	5.62
FSUGold [23] (rel.)	5.47	5.68
NL3 [27] (rel.)	5.46	5.74
NL3p06 [28] (rel.)	5.51	5.60
NL3m05 [28] (rel.)	5.50	5.85

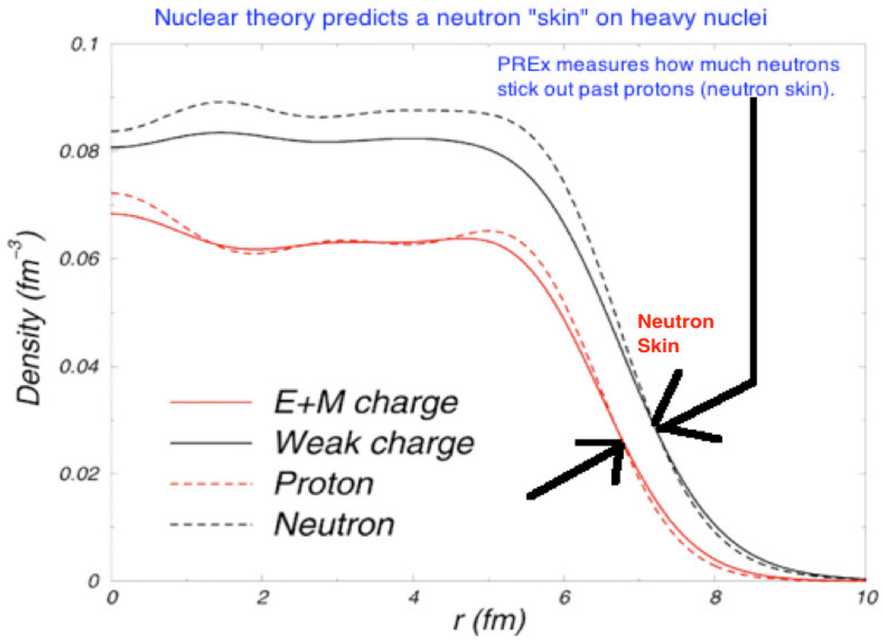

Figure 1.1: The charge density of $^{208}_{82}$Pb (red solid line), accurately measured in the elastic electron scattering experiment.

Heavy nuclei contain about 50% more neutrons than protons. After regarding the Coulomb repulsion between protons, the neutron radii are still expected to be larger than proton's for neutron-rich nuclei. Nuclei with the larger neutron excess, $\frac{\mathcal{N}_N - \mathcal{N}_Z}{A(\mathcal{N}_N + \mathcal{N}_Z)}$, appear to form a neutron-rich skin, Δr_{np}, defined as the difference in root-mean-square radii between protons and neutrons in Equation 1.4.

$$\Delta r_{np} \quad = \quad < R_n^2 >^{1/2} - < R_p^2 >^{1/2} . \tag{1.4}$$

Experimentally, we are able to find $< R_p^2 >^{1/2}$, RMS radii, from the electron scattering experiment. The size $< R_p^2 >^{1/2}$ of a saturating nucleus system is defined with a characteristic length scale, r_0, below:

$$< R_p^2 >^{1/2} \quad \sim \quad r_0 A^{1/3}, \tag{1.5}$$

where $r_0 \equiv 1.2$ fm, the slope given by plotting $< R_p^2 >^{1/2}$ against $A^{1/3}$, and the density of one single nucleus is assumed to be roughly constant.

1.1 Theory of Elastic Scattering

Since the proton is charged, the nuclear ρ_{ch} and ρ_p as drawn in Fig. 1.1 can be accurately measured via the scattering of electrons from the nucleus.

In the $e^- p \to e^- p$ scattering, the nature of the electromagnetic interaction between the virtual photon and protons in the atomic nucleus strongly depends on incident energies of the electron beam. For instance,

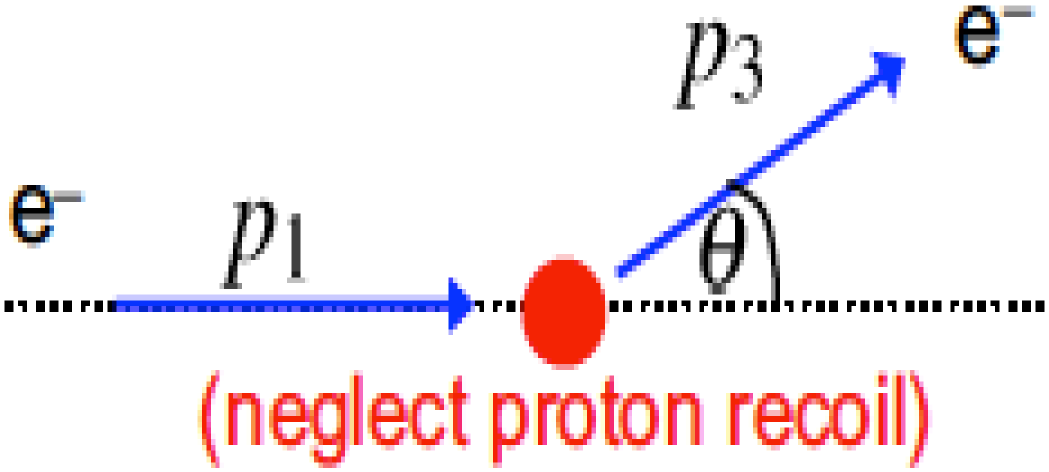

Figure 1.2: Elastic electron scattering at low incident energies. P_1 is the incident momenta; P_3 is the scattering momenta.

- at extremely low Q^2, where $\lambda_e \gg r_p$, the atomic nucleus seems like a point-like spin-less object;
- at low Q^2, where $\lambda_e > r_p$, the atomic nucleus is an extended object, comprising protons and neutrons;
- at high Q^2, where $\lambda_e < r_p$ (or $\ll r_p$), the atomic nucleus consists of constituent (valence) quarks and sea quarks.

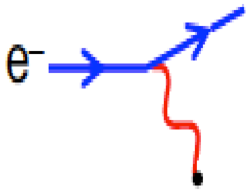

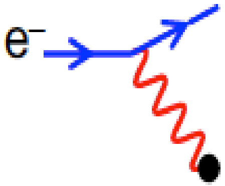

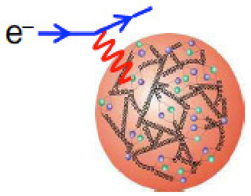

Note that r_p refers to the radius of every single proton.

Supposed that the target recoil momentum is negligible (elastic scattering), the initial and final state proton spinors (assuming no recoil) are:

$$u_{\uparrow}(0) = \sqrt{2\mathcal{M}_p}\begin{pmatrix} 1 \\ 0 \\ 0 \\ 0 \end{pmatrix}; u_{\downarrow}(0) = \sqrt{2\mathcal{M}_p}\begin{pmatrix} 0 \\ 1 \\ 0 \\ 0 \end{pmatrix}, \tag{1.6}$$

giving the proton currents:

$$\begin{aligned} j^p_{RR} &= \bar{u}_{\uparrow}(0)\gamma^{\mu}u_{\uparrow}(0) = 2\mathcal{M}_p[1,0,0,0]; \qquad (1.7) \\ j^p_{LL} &= \bar{u}_{\downarrow}(0)\gamma^{\mu}u_{\downarrow}(0) = 2\mathcal{M}_p[1,0,0,0]; \\ j^p_{RL} &= \bar{u}_{\uparrow}(0)\gamma^{\mu}u_{\downarrow}(0) = 0; \\ j^p_{LR} &= \bar{u}_{\downarrow}(0)\gamma^{\mu}u_{\uparrow}(0) = 0. \end{aligned}$$

On the other hand, presumably the incident electrons are non-relativistic, left-hand and right-hand electron spinors are:

$$u_{\uparrow} = \mathcal{N}\begin{pmatrix} c \\ e^{i\phi}s \\ \alpha c \\ \alpha e^{i\phi}s \end{pmatrix}; u_{\downarrow} = \mathcal{N}\begin{pmatrix} -s \\ e^{i\phi}c \\ \alpha s \\ -\alpha c \end{pmatrix}, \tag{1.8}$$

where $\mathcal{N} = \sqrt{E+m}$, $s = \sin(\theta/2)$, $c = \cos(\theta/2)$ and
$\alpha = \frac{|\vec{p}|}{E+m_e} = \begin{cases} \alpha \to 0 & \text{non-relativistic;} \\ \alpha \to 1 & \text{ultra-relativistic.} \end{cases}$ θ is the scattering angle with respect to the incident axis, and $\phi = 0°$ in this case. Therefore, the possible initial and final state electron

spinors are:

$$u_\uparrow(p_1) = \mathcal{N}_e \begin{pmatrix} 1 \\ 0 \\ \alpha \\ 0 \end{pmatrix}; u_\downarrow(p_{12}) = \mathcal{N}_e \begin{pmatrix} 0 \\ 1 \\ 0 \\ -\alpha \end{pmatrix}; u_\uparrow(p_3) = \mathcal{N}_e \begin{pmatrix} c \\ s \\ \alpha c \\ \alpha s \end{pmatrix}; u_\downarrow(p_3) = \mathcal{N}_e \begin{pmatrix} -s \\ c \\ \alpha s \\ -\alpha c \end{pmatrix} \tag{1.9}$$

So, we have the electron currents:

$$\begin{aligned} j^e_{RR} &= \bar{u}_\uparrow(p_3)\gamma^\mu u_\uparrow(p_1) = (E + m_e)[(\alpha^2 + 1)c, 2\alpha s, -2i\alpha s, 2\alpha c]; \qquad (1.10) \\ j^e_{LL} &= \bar{u}_\downarrow(p_3)\gamma^\mu u_\downarrow(p_1) = (E + m_e)[(\alpha^2 + 1)c, 2\alpha s, -2i\alpha s, 2\alpha c]; \\ j^e_{RL} &= \bar{u}_\uparrow(p_3)\gamma^\mu u_\downarrow(p_1) = (E + m_e)[(1 - \alpha^2)s, 0, 0, 0]; \\ j^e_{LR} &= \bar{u}_\downarrow(p_3)\gamma^\mu u_\uparrow(p_1) = (E + m_e)[(\alpha^2 - 1)s, 0, 0, 0]. \end{aligned}$$

Assuming that the incoming electrons are unpolarized, the scattering amplitudes for all four possible initial electron helicity states are evenly likely. The scattering amplitudes are expressed:

$$\begin{aligned} <|\mathcal{M}_{RR}|> &= \frac{e^2}{Q^2} j^p_{RR} j^e_{RR} = 2\mathcal{M}_p(E + m_e)[(\alpha^2 + 1)c, 2\alpha s, -2i\alpha s, 2\alpha c]; \qquad (1.11) \\ <|\mathcal{M}_{LL}|> &= \frac{e^2}{Q^2} j^p_{RR} j^e_{RR} = 2\mathcal{M}_p(E + m_e)[(\alpha^2 + 1)c, 2\alpha s, -2i\alpha s, 2\alpha c]; \\ <|\mathcal{M}_{RL}|> &= \frac{e^2}{Q^2} j^p_{RL} j^e_{RL} = 2\mathcal{M}_p(E + m_e)[(1 - \alpha^2)s, 0, 0, 0]; \\ <|\mathcal{M}_{LR}|> &= \frac{e^2}{Q^2} j^p_{LR} j^e_{LR} = 2\mathcal{M}_p(E + m_e)[(\alpha^2 - 1)s, 0, 0, 0]. \end{aligned}$$

All four matrix elements are non-zero in the non-relativistic limit, where $\alpha \to 0$. Therefore, the differential cross-section obtained by averaging over the initial spin states and summing over the final spin states:

$$\begin{aligned}\frac{\mathrm{d}\sigma}{\mathrm{d}\Omega} &= \frac{1}{4}\times\frac{1}{64\pi^2Q^2}\frac{|\vec{p}_f|}{|\vec{p}_i|} < |\mathcal{M}_{fi}|^2 > \qquad (1.12)\\ &= \frac{1}{4}\times\frac{1}{64\pi^2Q^2}(< |\mathcal{M}_{RR}|^2 > + < |\mathcal{M}_{RL}|^2 > + < |\mathcal{M}_{LR}|^2 > + < |\mathcal{M}_{LL}|^2 >)\\ &= \frac{1}{4}\times\frac{e^4}{64\pi^2Q^4}\times(16\mathcal{M}_p^2m_e^2)(4c^2+4s^2) = \frac{16\mathcal{M}_p^2m_e^2e^4}{Q^2},\end{aligned}$$

where $Q^2 = (\vec{p}_1 - \vec{p}_3)^2 = -4|\vec{p}|^2\sin^2(\theta/2)$ is the momentum transfer, and θ is the scattering angle with respect to the incident direction. The scattering amplitude is calculated by taking the sum of all possible scattering processes and then averaging the sum over the total number of combinations of initial helicity (spin) states, $\mathcal{N}_{com.}$:

$$\begin{aligned}< |\mathcal{M}_{fi}|^2 > &= \frac{1}{\mathcal{N}_{com.}}\sum_{\text{spins}}|\mathcal{M}_i|^2 \qquad (1.13)\\ &= \frac{1}{\mathcal{N}_{com.}}(|\mathcal{M}_{LL\to LL}|^2 + |\mathcal{M}_{LL\to LR}|^2 + |\mathcal{M}_{LL\to RR}|^2\\ &+ |\mathcal{M}_{LL\to RL}|^2 + ...)\end{aligned}$$

Hence, the differential cross-section is:

$$(\frac{\mathrm{d}\sigma}{\mathrm{d}\Omega}) = \frac{\alpha^2}{16E_k^2\sin^4(\theta/2)}, \qquad (1.14)$$

where $E_k^2 = \frac{|\vec{p}|^2}{2m_e}$ and $\alpha = \frac{e^2}{4\pi}$.

In the ultra-relativistic limit, where the target recoil momentum is too small to consider and $\alpha \to 1$, the electron currents become:

$$\begin{aligned}j^e_{RR} &= \bar{u}_\uparrow(p_3)\gamma^\mu u_\uparrow(p_1) = 2E[c, s, -is, c]; \qquad (1.15)\\ j^e_{LL} &= \bar{u}_\downarrow(p_3)\gamma^\mu u_\downarrow(p_1) = 2E[c, s, -is, c];\\ j^e_{RL} &= \bar{u}_\uparrow(p_3)\gamma^\mu u_\downarrow(p_1) = E[0, 0, 0, 0];\end{aligned}$$

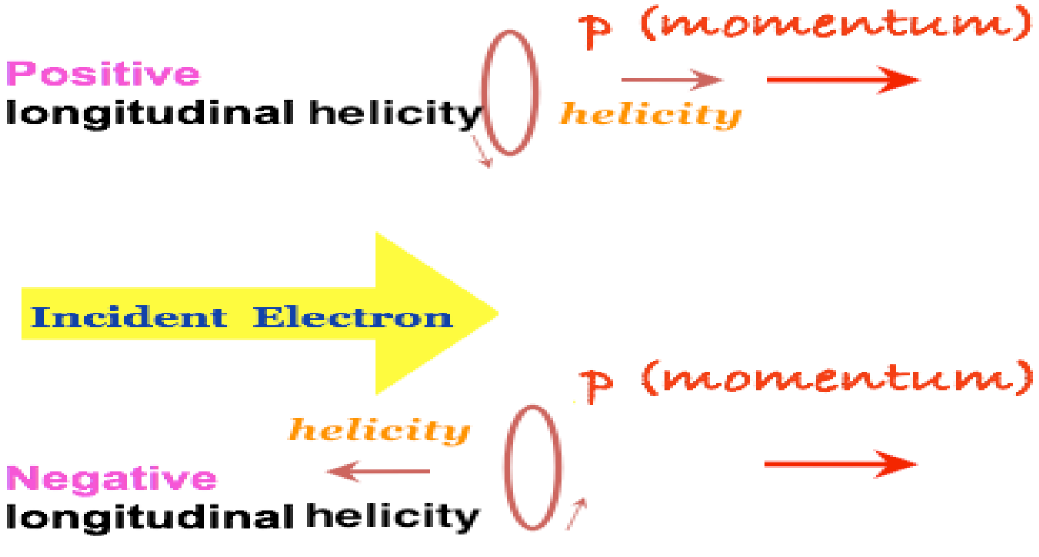
p (momentum)
Positive
longitudinal helicity
helicity
Incident Electron
p (momentum)
helicity
Negative
longitudinal helicity

Figure 1.3: The direction of helicity, defined as the projection of the electron spin onto the momentum axis, is either parallel or anti-parallel to the beam momentum.

$$j^e_{LR} \;=\; \bar{u}_\downarrow(p_3)\gamma^\mu u_\uparrow(p_1) = E[0,0,0,0].$$

In the polarized electron elastic scattering experiment running at Jefferson Lab., electron beam energies are at least above 1 GeV, and the electron helicity direction is either parallel or anti-parallel to the incident direction of the polarized electron beam's momentum. Hence, non-zero contributions of scattering amplitudes to the differential cross-section are j^e_{RR} and j^e_{LL}. The well-known differential cross-section formula for Mott scattering is:

$$(\frac{\mathrm{d}\sigma}{\mathrm{d}\Omega}) \;=\; \frac{\alpha^2}{4E^2\sin^4(\theta/2)}\cos^2\frac{\theta}{2}. \tag{1.16}$$

Nevertheless, electron energies for parity-violating experiments running at Jefferson Lab. are high enough to consider distributions of protons and neutrons, valence quarks and sea quarks. Consider the scattering of an electron in the electro-static field generated by

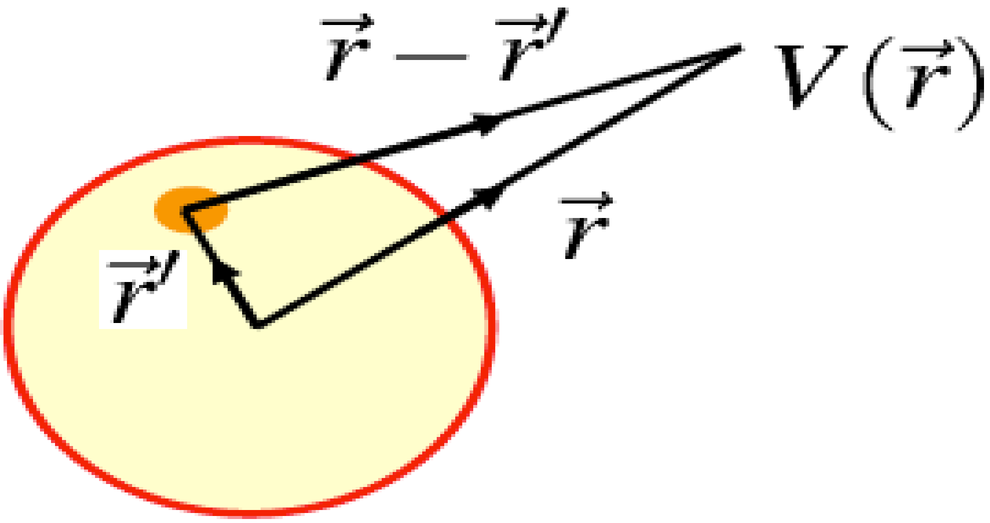

Figure 1.4: Electron energies of the incident beam are high enough to see the internal charge distribution of atomic nuclei.

extended proton distributions in the atomic nucleus:

$$V(\vec{r}) = \int \frac{Q_t \rho(\vec{r'})}{4\pi|\vec{r}-\vec{r'}|} \mathrm{d}^3\vec{r'}, \tag{1.17}$$

where the total charge, $\int \rho(\vec{r})\mathrm{d}^3\vec{r} = 1$ is normalized to the unity. The scattering matrix element is:

$$\mathcal{M}_{fi} = <\Psi_f|V(\vec{r})|\Psi_i> = \int e^{-i\vec{p_3}\cdot\vec{r}} V(\vec{r}) e^{i\vec{p_1}\cdot\vec{r}} \mathrm{d}^3\vec{r}, \tag{1.18}$$

where we assume both of the incident and scattering electron waves are the plane wave, according to the first-order approximation of the perturbation theory. After plugging the potential function from Equation 1.17 into Equation 1.18, we have:

$$\begin{aligned} \mathcal{M}_{fi} &= \int\int e^{i\vec{Q}\cdot\vec{r}} \frac{Q_t\rho(\vec{r'})}{4\pi|\vec{r}-\vec{r'}|} \mathrm{d}^3\vec{r'}\mathrm{d}^3\vec{r} \qquad (1.19) \\ &= \int\int e^{i\vec{Q}\cdot(\vec{r}-\vec{r'})} e^{i\vec{Q}\cdot\vec{r'}} \frac{Q_t\rho(\vec{r'})}{4\pi|\vec{r}-\vec{r'}|} \mathrm{d}^3\vec{r'}\mathrm{d}^3\vec{r} \\ &= \int e^{i\vec{Q}\cdot\vec{R}} \frac{Q_t}{4\pi|\vec{R}|} \mathrm{d}^3\vec{R} \int \rho(\vec{r'}) e^{i\vec{Q}\cdot\vec{r'}} \mathrm{d}^3\vec{r'} = (\mathcal{M}_{fi})_{\text{point}} F(\vec{Q}^2), \end{aligned}$$

where $F(\vec{Q^2})$, defined as the Fourier transform of the density function for different scattering phases, is the form factor. If for low Q^2, all scattering waves, compared to the size of the atomic nucleus (a point-like source), are long enough to be regarded as in phase. Then, $F(\vec{Q^2}) = 1$.

On the contrary, if for high Q^2, the incident electron waves, which are scattered from atomic nuclei with the finite size and structure, introduce different phase differences between scattering electron plane waves. Hence, the matrix element in Equation 1.19 is formed by taking the product of the matrix element in Equation 1.18 for the point-source electron scattering and the form factor, $F(\vec{Q^2}) = \int \rho(\vec{r'}) e^{i\vec{Q}\cdot\vec{r'}} \mathrm{d}^3\vec{r'}$. The corresponding differential cross-section for the finite-size scattering is:

$$\begin{aligned}
(\frac{\mathrm{d}\sigma}{\mathrm{d}\Omega})_{\mathrm{real}} &= (\frac{\mathrm{d}\sigma}{\mathrm{d}\Omega})_{\mathrm{Mott,point\ source}} |F(\vec{Q^2})| && (1.20)\\
&= \frac{\alpha^2}{4E^2\sin^4(\theta/2)} \cos^2\frac{\theta}{2} |F(\vec{Q^2})|. && (1.21)
\end{aligned}$$

In summary, from Equation 1.20, we learn that:

- the form factor, the Fourier transform of the charge density, can be determined by measuring the cross-section of the elastic electron scattering;
- the form factor depends on the momentum transfer. So, the data taken at a variety of Q^2 quantities can be combined by plotting $\frac{\mathrm{d}\sigma(\theta)}{\mathrm{d}\Omega}_{\mathrm{real}}$ w.r.t. Q^2;
- the charge density function is obtained by taking the inverse Fourier transform of the form factor. However, in order to invert properly, we need to know Q^2 up to the infinity. Obviously, it's impossible. At the smaller radius (with the higher Q^2-value), more experimental uncertainties cannot be avoided.

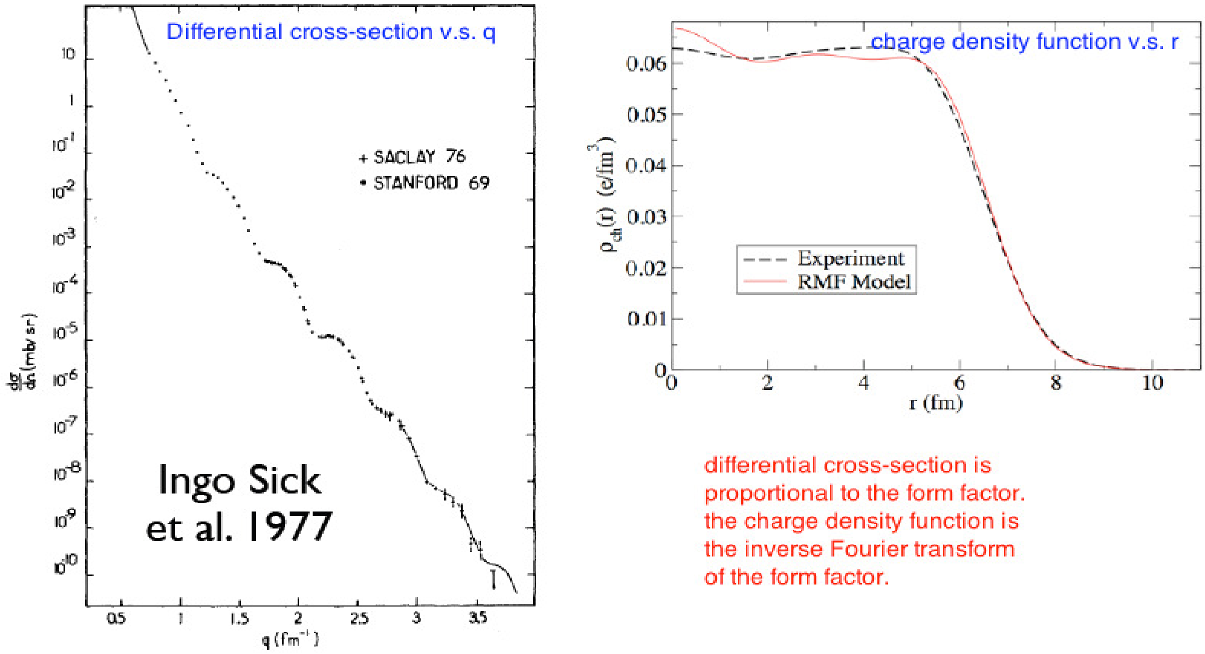

Differential cross-section v.s. q

Ingo Sick et al. 1977

charge density function v.s. r

differential cross-section is proportional to the form factor. the charge density function is the inverse Fourier transform of the form factor.

Figure 1.5: (Left) The differential scattering cross-section of $^{208}_{82}$Pb versus Q^2 (momentum transfer, $Q = 2|\vec{p}|\sin\frac{\theta}{2}$, at the center-of-mass energy of 502 MeV. (Right) the charge density function, the inverse Fourier transform of the form factor.

1.2 Binding Energy Models

The binding energy of the nucleus are the amount of energy cost to completely separate protons and neutrons, collectively called nucleons. Two largest forces in the nuclear atom are the nuclear force, the residual of the strong force to hold quarks together, is to pull protons and neutrons together, and the electric charges on protons to push them apart. The strong force is much stronger than the electric force at a short range of two and half times of the proton diameter. But at larger distances, the electric force dominates. As we add more nucleons in order to increase the atomic number, eventually each nucleon is generally a little more tightly bonded than the one added before. This continuously increases total binding energy up to reaching the element, iron (^{56}Fe). At this point, the nucleus has a radius more than two and half of each nucleons width, which we remember its the range in which the repulsive electromagnetic force began to dominate. Hence, as we gradually add

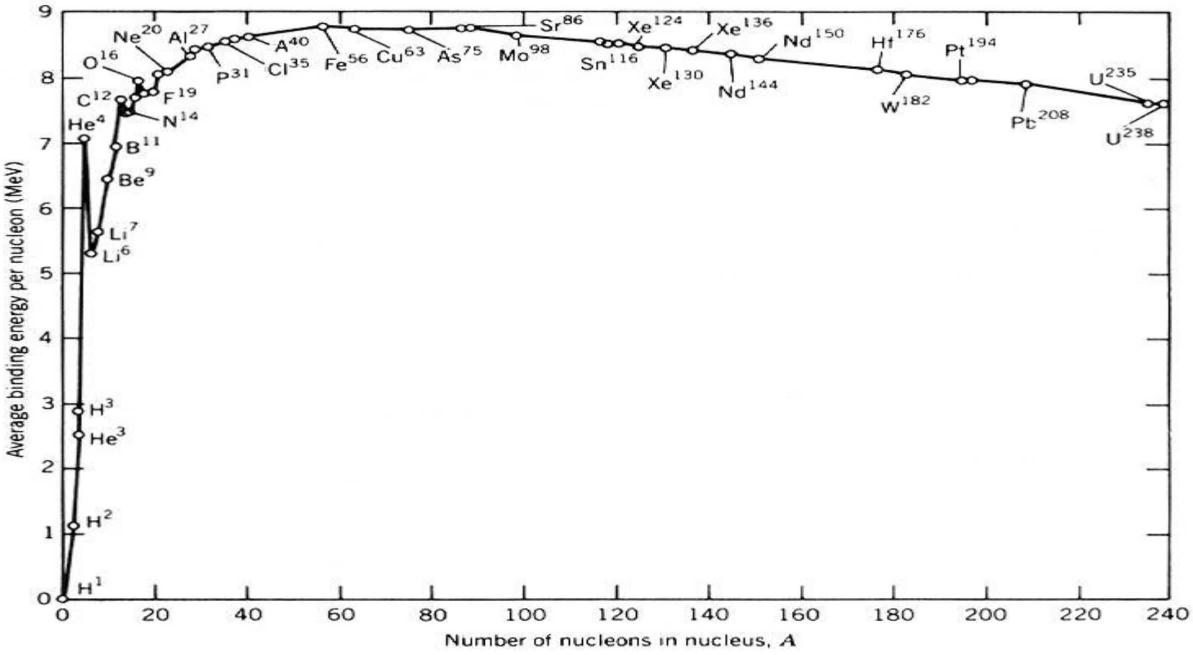

Figure 1.6: Average binding energy per nucleon (MeV) vs. atomic number (number of nucleons in one atom).

more nucleons passing this point, the electric force becomes stronger and starts winning. That is, one proton repulses the rest of protons, so that protons are pushed outward due to the Coulomb repulsive force, and the nucleon added later is thus less tightly bonded.

Each part of binding energy for every single nucleus, which is consist of constituent nucleons (a type of baryon), is from different sources of contributions as listed in Equation 1.22 as follows:

$$\begin{aligned} BE(\mathcal{N}_Z, A) &= \\ -a_V A + a_S A^{2/3} + a_C \frac{\mathcal{N}_Z(\mathcal{N}_Z - 1)}{A^{1/3}} &- a_A \frac{(\mathcal{N}_N - \mathcal{N}_Z)^2}{A} + \delta A; \\ \frac{BE(\mathcal{N}_Z, A)}{A} \text{ (for each nucleon in one single nucleus)} &= \\ -a_V + a_S \frac{1}{A^{1/3}} + a_C \frac{\mathcal{N}_Z(\mathcal{N}_Z - 1)}{A^{4/3}} &- a_A (\frac{\mathcal{N}_N - \mathcal{N}_Z}{A})^2 + \delta, \end{aligned} \tag{1.22}$$

where:

- a_V (volume): the interaction with nearest nucleon neighbors which are tightly bounded together as a result of the nuclear strong force;
- a_A (asymmetry): the balance between protons and neutrons. the change in baryon number between protons and neutrons results in the change in nuclear energies. (scaled by squaring the fractional difference, $(\frac{\mathcal{N}_N-\mathcal{N}_Z}{\mathcal{N}_N+\mathcal{N}_Z})^2$, in number between neutrons and protons);
- a_S (surface): the interaction with loosely-bounded nucleons spreading near the surface of the nucleus (scaled by the nuclear size, $\frac{1}{A^{1/3}} \sim \frac{1}{R}$);
- a_C (Coulomb): the interaction from the Coulomb repulsion between protons (scaled by the product of $\frac{(\mathcal{N}_Z-1)}{A^{1/3}}$ and $\frac{\mathcal{N}_Z}{A}$);
  - $\frac{(\mathcal{N}_Z-1)}{A^{1/3}}$: the potential energy due to the Coulomb repulsion between one proton and the rest of protons;
  - $\frac{\mathcal{N}_Z}{A}$: the proton fraction in every single nucleus.
- δ (paring): the proton-neutron transition energy in the β decay.

The asymmetry energy describe how a nuclear system increases its total binding energy, as one nucleus departs from equal number of protons and neutrons. In other words, asymmetry energy is the energy cost for the asymmetric matter ($\mathcal{N}_N \neq \mathcal{N}_Z$). Fig. 1.7 shows that 18 different binding energy models, developed based on mean-field theories, predict different contributions of asymmetry energy to the whole binding energy for each constituent nucleon. Clearly, binding energy for every single nucleon vary with respect to proton and neutron densities, and so do asymmetry energies.

The partial derivative of binding energy with respect to neutron densities is related to the pressure of the neutron-rich nuclear system. Fig. 1.8 shows that the partial derivative of binding energy at the near saturation density of 0.16 neutron/fm^3 is tightly correlated

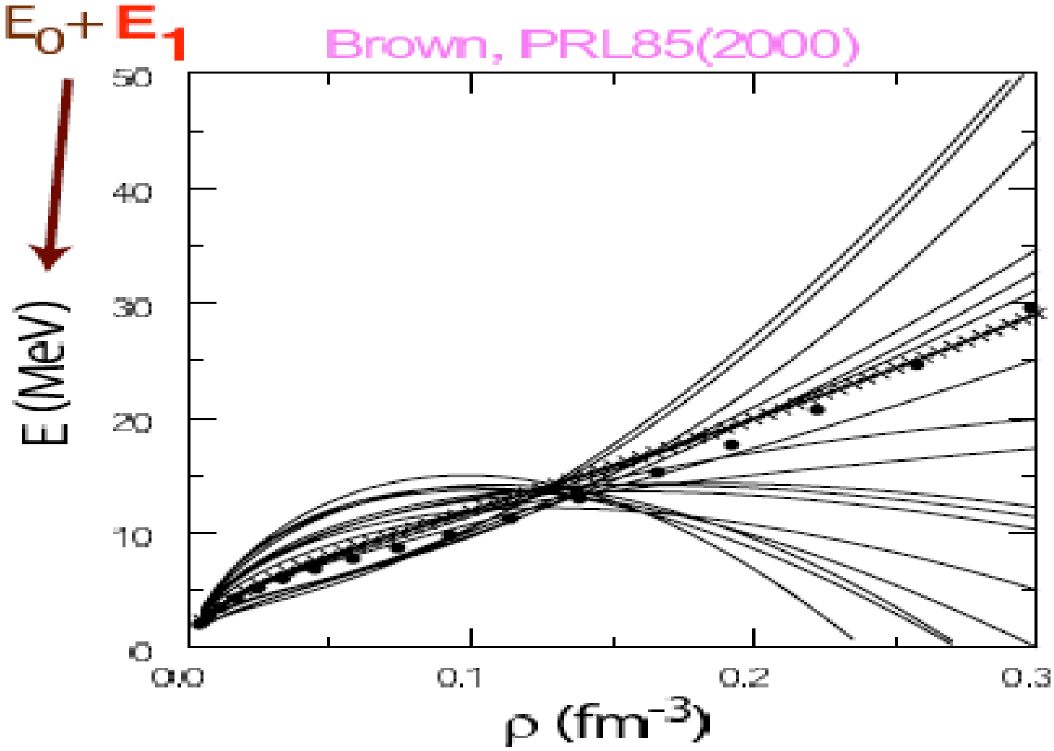

Figure 1.7: Binding energy spectra to describe the EOS of the nuclear system with 18 Skyrme type of MFT models. Dots are Friedman-Pandharipande (FP) [4] variational calculations; crosses are SkX [5].

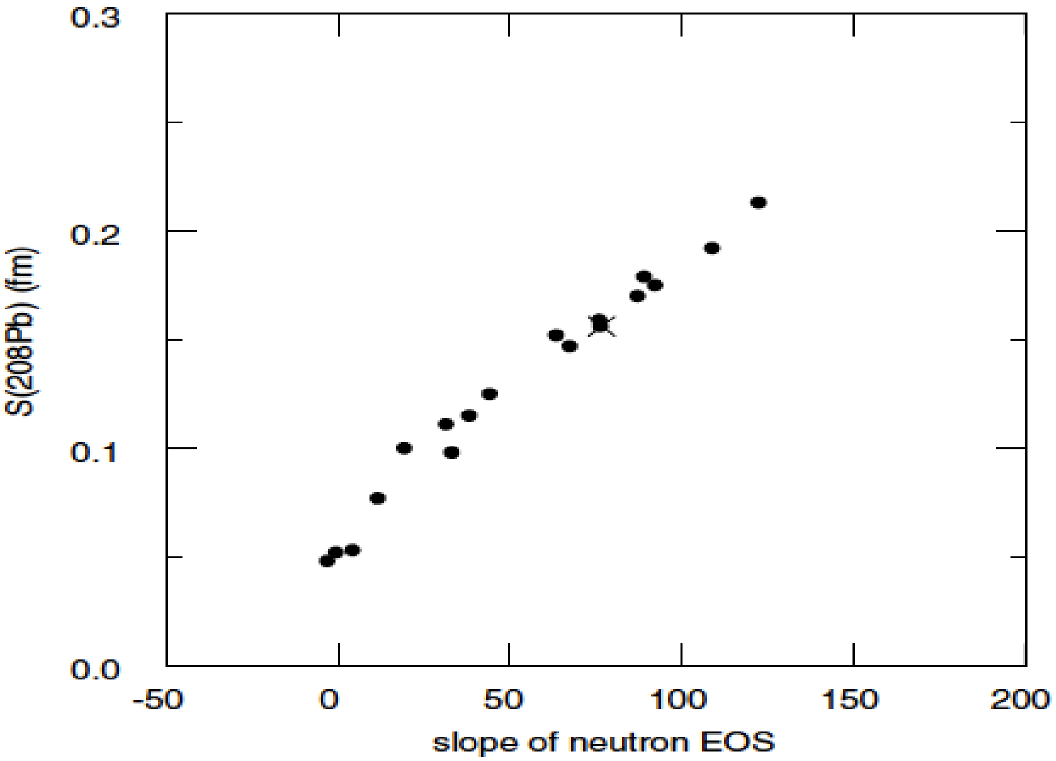

Figure 1.8: Lead neutron skin vs. the derivative of EOS of the neutron system for 18 Skyrme sets.

with the neutron skin, Δr_{np}, defined as:

$$\Delta r_{np} \;=\; < R_n^2 >^{1/2} - < R_p^2 >^{1/2} . \tag{1.23}$$

It implies that a precisely determined neutron density profile can further constrain the divergent energy-density correlation relations based on a wide range of various binding energy models. Through extrapolating this correlation relation from low to high neutron densities, binding energy of the neutron-rich matter can be further pin down. As a result, the partial derivative of binding energy with respect to neutron densities, indicating an important parameter, the pressure, used to describe EOS of neutron stars, is accordingly constrained within the limited region without being divergent. In conclusion, the high precision neutron density measurement plays an important role to describe EOS of neutron

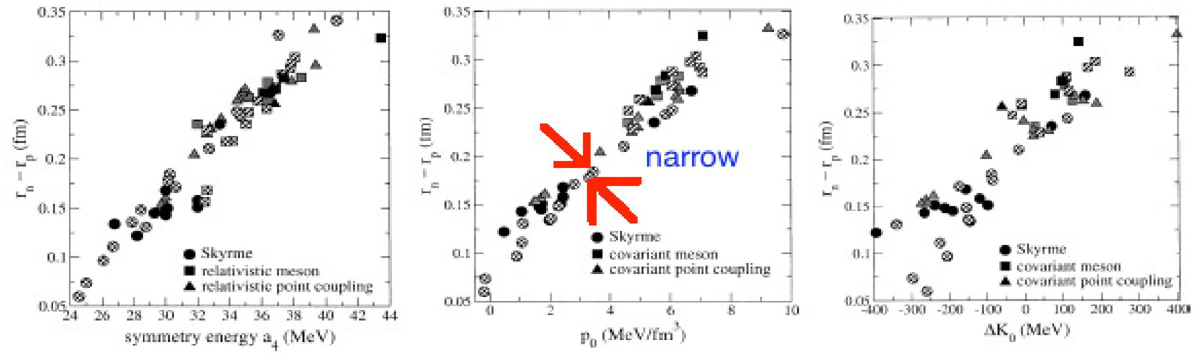

Figure 1.9: (Left) Δr_{np} versus a_4; (middle) Δr_{np} versus p_0; (right) Δr_{np} versus ΔK_0 for a variety of mean-field models. The remarkably small spread of p_0 shows no significant separation of different theory models.

stars and their formation processes and structures.

We can further express asymmetry energies, a_A as shown in Equation 1.22, in terms of a_4, p_0 and ΔK_0 as follows:

$$a_A \quad \approx \quad a_4 + A \times p_0(\rho_p + \rho_n - C) + B \times \Delta K_0(\rho_p + \rho_n - C)^2, \tag{1.24}$$

where A, B and C are constants. a_4 is a coupling constant, p_0 is the coefficient of the linear baryon density term, and ΔK_0 is the standard deviation of the incompressibility. The linear correlation between Δr_{np} and each component of a_A such as a_4, p_0 and ΔK_0 as shown in Fig. 1.9 (from left to right pannel) implies that Δr_{np} arises from the difference in density between protons and neutrons in an asymmetric ($\mathcal{N}_N \neq \mathcal{N}_Z$) nucleus. Most importantly, the linear relation between p_0 and Δr_{np} as drawn in Fig. 1.9 reflects the strong correlation between asymmetry energy and the whole nuclear densities, suggesting this correlation be irrelevant to the option of selected models (model independent). Consequently, the high precision $< R_n^2 >^{1/2}$ (also, Δr_{np}) measurement can narrow down the divergent energy-density correlation relation. According to Fig. 1.10, the neutron form factor, the inverse Fourier transform of ρ_n at one chosen Q^2, is highly correlated with $< R_n^2 >^{1/2}$ (also Δr_{np}) for different mean-field models. That means the neutron form factor

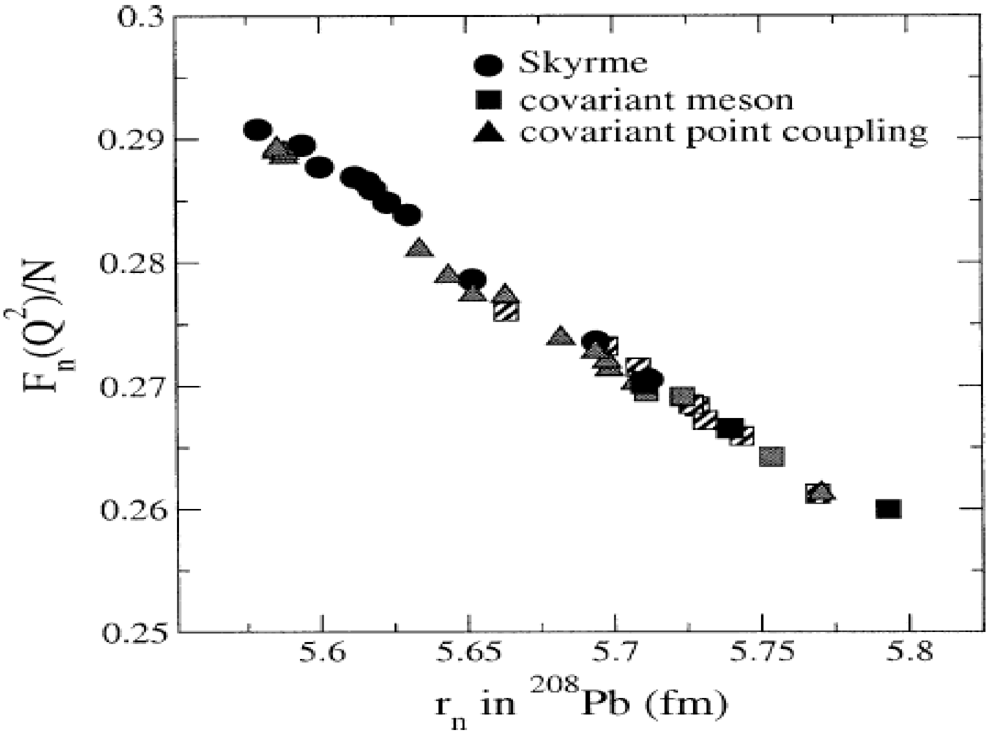

Figure 1.10: Calculated form factor, $F_n(Q^2)$, versus $< R_n^2 >^{1/2}$ of $^{208}_{82}$Pb (fm). At some fixed low-Q^2 value, $F_n(Q^2)$ is found to be strongly correlated to the size of neutron RMS radii, $< R_n^2 >^{1/2}$ in a heavy nucleus.

$(F_n(Q^2))$ is actually very sensitive to the extraction of neutron radii at some preferably selected Q^2, and this high sensitivity is actually model-independent.

In the non-parity violating electron scattering experiments running at low-Q^2, the proton form factor, proportional to the differential cross-section, as shown in Equation 1.25 gives the proton density function and proton RMS radii, $< R_p^2 >^{1/2}$.

$$\frac{\mathrm{d}\Omega}{\mathrm{d}\sigma} = \frac{\alpha^2 \cos^2 \frac{\theta}{2}}{4E^2 \sin^4 \frac{\theta}{2}} |F(Q^2)|^2. \tag{1.25}$$

As $Q^2 \to 0$,

$$F(Q^2) \approx F(0) + \frac{\mathrm{d}F}{\mathrm{d}Q^2}|_{Q^2=0} + ... = \int \rho(\vec{x})\mathrm{d}^3x - \frac{1}{6}Q^2 < r^2_{\text{charge}} > . \tag{1.26}$$

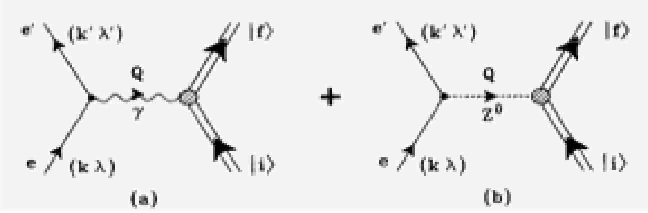

Figure 1.11: Tree-level Feynman diagrams: (a) single photon exchange, and (b) Z^0 exchange for the electron scattering from the nucleus.

The proton density as well as proton RMS radii can be accurately measured via electron scattering experiments, and the sensitivity of proton RMS radii measurements is up to 0.02 fm (2%). In contrast, the accuracy of neutron RMS radii measurements is not as high as 2% by using the hadronic scattering experiments because of considerable uncertainties in the strong interaction.

1.3 Parity-violating

Prior to PREx, the determination of neutron densities primarily resulted from hadronic type experiments such as elastic proton scattering [6, 7, 8], pion photon production [3] and anti-proton scattering [9, 10]. Nevertheless, due to the ambiguous interaction between the incident hadrons and nucleons embedded in the atomic nucleus, the uncertainties due to strong interactions cannot be avoided. As a consequence, the weak-interaction probe is free from most of strong interaction uncertainties.

In the elastic polarized electron scattering experiment running at low-Q^2 such as PREx, the interference between the larger axial coupling of Z^0 to the electron and the much stronger vector coupling of Z^0 to neutrons than protons as shown in Fig. 1.11 leads to the weak neutral current, from which the parity-violating asymmetry arises, in a heavier and spin-less neutron-rich nucleus such as Lead ($^{208}_{82}$Pb).

Consider the elastic electron scattering from a spin-less heavy nucleus in the ground state. Presumably the electron's wave function, Ψ, satisfies a Dirac Equation:

$$[\vec{\alpha}\cdot\vec{p}+\beta m_e \pm \hat{V}_{\pm}(r)]\Psi_{\pm} \;=\; E\Psi_{\pm}(r), \tag{1.27}$$

where E is the center of mass energy, the total potential energy, $\hat{V}_{\pm}(r) = V_C(r) \pm \gamma_5 A(r)$ [1], and the electron wave functions, $\Psi_{\pm} = \frac{1}{2}(1 \pm \gamma_5)\hat{\Psi}$ for positive (right-handed) and negative (left-handed) helicity electrons, respectively. Therefore, the positive helicity electrons scatter from a potential of (V+A), whereas the negative helicity electrons scatter from a potential of (V-A). One can simply calculates the fractional difference in the scattering amplitude between (V+A) and (V-A) to obtain $\mathcal{A}_{PV}^{BA}$ as follows:

$$\mathcal{A}_{PV}^{BA} \;=\; \frac{\frac{d\sigma_+^R}{d\Omega}-\frac{d\sigma_-^L}{d\Omega}}{\frac{d\sigma_+^R}{d\Omega}+\frac{d\sigma_-^L}{d\Omega}} = \frac{|\mathcal{M}_+^R|^2-|\mathcal{M}_-^L|^2}{|\mathcal{M}_+^R|^2+|\mathcal{M}_-^L|^2}, \tag{1.28}$$

where:

$$\begin{aligned}
\mathcal{M}_{+,-}^{R,L} &= \mathcal{M}_\gamma + \mathcal{M}_{Z,+,-}^{R,L},\\
\alpha &= \frac{e^2}{4\pi} \simeq \frac{1}{137},\\
\mathrm{G}_F &= \frac{\sqrt{2}}{8}\left(\frac{hc}{2\pi}\right)^3\left(\frac{g}{\mathcal{M}_Z}\right)^2, \quad \text{and}\\
|\mathcal{M}_{+,-}^{R,L}|^2 &= |\mathcal{M}_\gamma|^2 + \mathcal{M}_\gamma\mathcal{M}_{Z,+,-}^{R,L*} + \mathcal{M}_\gamma^*\mathcal{M}_{Z,+,-}^{R,L} + |\mathcal{M}_{Z,+,-}^{R,L}|^2,\\
|\mathcal{M}_+^R|^2-|\mathcal{M}_-^L|^2 &= \mathcal{M}_\gamma(\mathcal{M}_{Z,+}^{R*}-\mathcal{M}_{Z,-}^{L*}+\mathcal{M}_{Z,+}^{R}-\mathcal{M}_{Z,-}^{L})\\
&\approx 2\mathcal{M}_\gamma(\mathcal{M}_{Z,+}^{R}-\mathcal{M}_{Z,-}^{L}) \sim \frac{\alpha}{Q^2}\mathrm{G}_F,\\
|\mathcal{M}_+^R|^2+|\mathcal{M}_-^L|^2 &= 2|\mathcal{M}_\gamma|^2 \sim \left(\frac{\alpha}{Q^2}\right)^2. \quad \text{So, we have:}\\
\mathcal{A}_{PV}^{BA} &\simeq \frac{\mathcal{M}_{Z,+}^{R}-\mathcal{M}_{Z,-}^{L}}{\mathcal{M}_\gamma} \sim \frac{G_F Q^2}{\alpha} \sim \frac{Q^2}{\alpha\mathcal{M}_Z^2}, \quad \text{at low-}Q^2.
\end{aligned}$$

The parity-violating asymmetry ($\mathcal{A}_{PV}^{BA}$), according to the analytical expression of the plane-wave Born approximation (PWBA), is straightforwardly related to the neutron form factor, the Fourier transform of the neutron charge density function,

---

[1] $V_C(r) \approx 25$MeV, and $A(r) \approx 10$ eV

$F_n(Q^2) = \int \mathrm{d}^3 r \, \frac{\sin(Qr)}{Qr} \rho_n(r)$.

$$\begin{aligned} \mathcal{A}_{PV}^{PWBA} &= \frac{|\mathcal{M}_+^R|^2 - |\mathcal{M}_-^L|^2}{|\mathcal{M}_+^R|^2 + |\mathcal{M}_-^L|^2} \propto \frac{\frac{\mathrm{d}\sigma}{\mathrm{d}\Omega}\text{Weak}}{\frac{\mathrm{d}\sigma}{\mathrm{d}\Omega}\text{E+M}} \\ &\approx \frac{\mathrm{G}_F Q^2}{4\pi\alpha\sqrt{2}} \frac{F_n(Q^2)}{F_p(Q^2)} \quad (\text{or } \frac{F_n(Q^2)F_p(Q^2)}{F_p^2(Q^2)}). \end{aligned} \tag{1.29}$$

Z^0, carrying the weak force, primarily couples to neutrons, because the weak neutral current from the coupling of Z^0 to neutrons, β^n, is much stronger than to protons, β^p[2]. Hence, neutrons contain a much higher portion of weak charges than protons [11].

Full Coulomb distortions at electron energies from 502 MeV to 3000 MeV are included in the numerical asymmetry calculation using the distorted wave Born approximation (DWBA), and the calculated $\mathcal{A}_{PV}^{DWBA}$ as drawn in Fig. 1.12 was reduced by 30% dramatically. Surprisingly, as the beam energy increases, the Coulomb distortion effect does not decrease very much. In other words, the calculated $\mathcal{A}_{PV}^{DWBA}$ is not varying so much with the increasing beam energy, and meanwhile, just slightly shifts to higher Q^2. Fig. 1.13 shows that the calculated $\mathcal{A}_{PV}^{DWBA}$ can be very sensitive to the extraction of $< R_n^2 >^{1/2}$ up to the precision of 1% under the specifically selected conditions: the scattering angle of five degrees and a beam energy of 1.05 GeV.

1.3.1 Analysis I: Fit to Mean Field Models

Given that binding energy (BE(ρ_p,ρ_n)) as well as ρ_p have been well-understood in the 70's, through a series of non-relativistic and relativistic mean-field models as listed in Table 1.2, the shape of the weak density function can be parametrized using two important parameters: R_0 and a_n, of the Wood Saxon function (or called two-parameter Fermi function (2pF)) as defined in Equation 1.30 to describe the central radius and surface

---

[2] $\beta^n = -1, and \quad \beta^p = 1 - 4\sin^2\theta_W = 0.08$

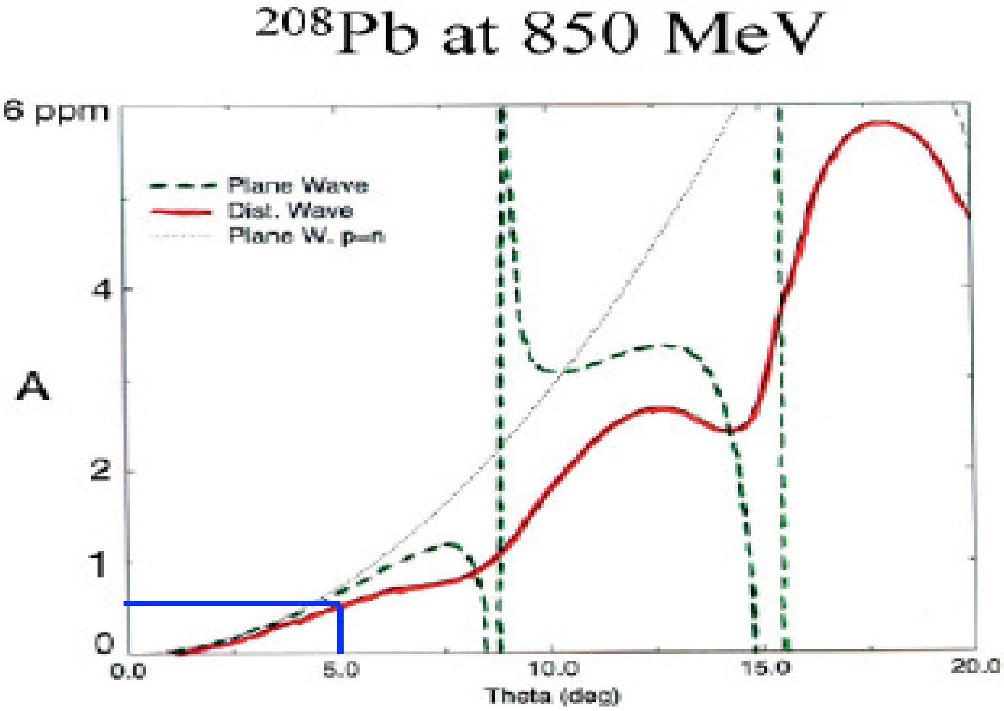

Figure 1.12: $\mathcal{A}_{PV}^{DWBA}$ for the polarized elastic electron scattering from the Lead ($^{208}_{82}$Pb) versus the scattering angle, θ. The dotted curve is a plane-wave approximation for $\mathcal{N}_N = \mathcal{N}_Z$ nuclei. The long-dashed curve is a plane-wave approximation for $\mathcal{N}_N \neq \mathcal{N}_Z$ nuclei. The full distorted wave results is solid curve at 850 MeV.

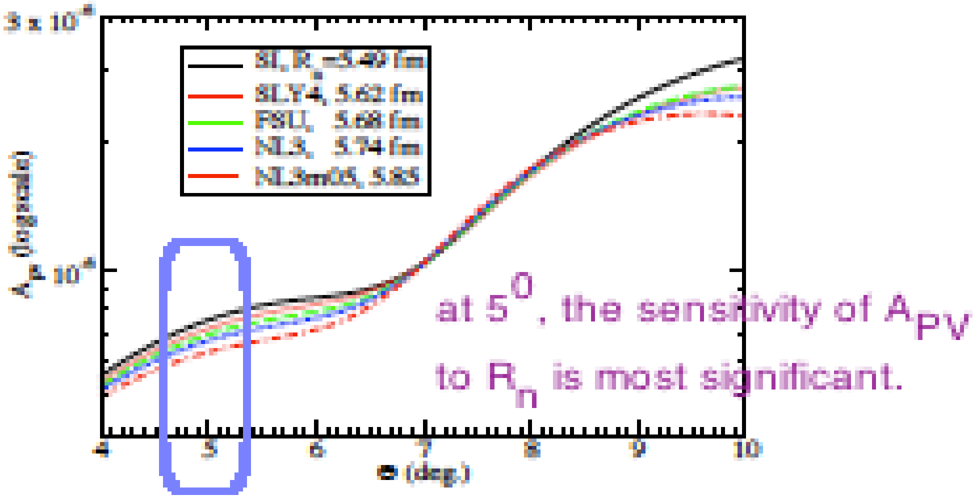

at 5^0, the sensitivity of A_{PV} to R_n is most significant.

Figure 1.13: $\mathcal{A}_{PV}^{DWBA}$ versus scattering angle, θ, for the polarized elastic electron scattering from ${}^{208}_{82}$Pb at the beam energy of 1.05 GeV.

thickness of the atomic nucleus, respectively.

$$\rho_W(r) \;=\; \frac{\rho_0}{1 + exp[(r - R_0)/a_n]}. \tag{1.30}$$

Through the Fourier transform of the weak charge density function in Equation 1.30, where R_0 and a_n are determined by seven non-relativistic and relativistic mean-field theory models, we then have the weak form factor, $F_W(\vec{Q}^2)$, as follows:

$$F_W(\bar{Q^2}) \;=\; \frac{\int \mathrm{d}^3 r \frac{\sin Qr}{Qr} \rho_W(r)}{Q_W} = 0.204 \pm 0.028(\mathrm{exp}) \pm 0.001(\mathrm{mod}). \tag{1.31}$$

The weak form factor is directly related to the theoretically calculated parity-violating asymmetry, $\mathcal{A}_{pv}^{DWBA}$, based on the distorted wave Born approximation (DWBA). After taking the first-order of the partial derivative of the weak form factor with respect to the momentum transfer, Q^2, the weak charge RMS radii ($< R^2_{\text{weak}} >^{1/2}$) is thus obtained. Consequently, we have the linear relationship between $\mathcal{A}_{pv}^{DWBA}$ and $< R_n^2 >^{1/2}$ as shown in

Table 1.2: Least square fits of parameters to non-relativistic and relativistic mean field model weak charge densities. Parameters, R_0 and a_n, stand for the Wood Saxon weak charge density function as described in Equation 1.30.

Wood Saxon

Mean field interaction model	R_0 (fm)	a_n (fm)
Skyrme I [24] (non-rel.)	6.655	0.564
Skyrme III [25] (non-rel.)	6.820	0.613
Skyrme SLY4 [26] (non-rel.)	6.700	0.668
FSUGold [23] (rel.)	6.800	0.618
NL3 [27] (rel.)	6.896	0.623
NL3p06 [28] (rel.)	6.730	0.606
NL3m05 [28] (rel.)	7.082	0.605
Average		0.61 ± 0.05

Fig. 1.14.

$$\mathcal{A}_{pv}^{Pb} = 0.656 \pm 0.060(\text{stat}) \pm 0.014(\text{syst}) \quad \text{ppm}. \tag{1.32}$$

The experimental asymmetry measurement in Equation 1.32 corresponds to the weak-charge size, $< R_W^2 >^{1/2}$, which is approximated to the neutron RMS radii, $< R_n^2 >^{1/2}$, as shown in Fig. 1.14. Alternatively, the neutron skin, Δr_{np} can be extracted:

$$\Delta r_{np} = 0.33^{+0.16}_{-0.18} \quad \text{fm}. \tag{1.33}$$

1.3.2 Analysis II: Helm Model Weak Form Factor

The Helm model weak charge density [31] was proven a very useful tool to analyze the unpolarized electron scattering form factors [32, 33]. In addition, the application of the Helm model to studying neutron-rich nuclei can be found in ref. [34]. Through the Helm

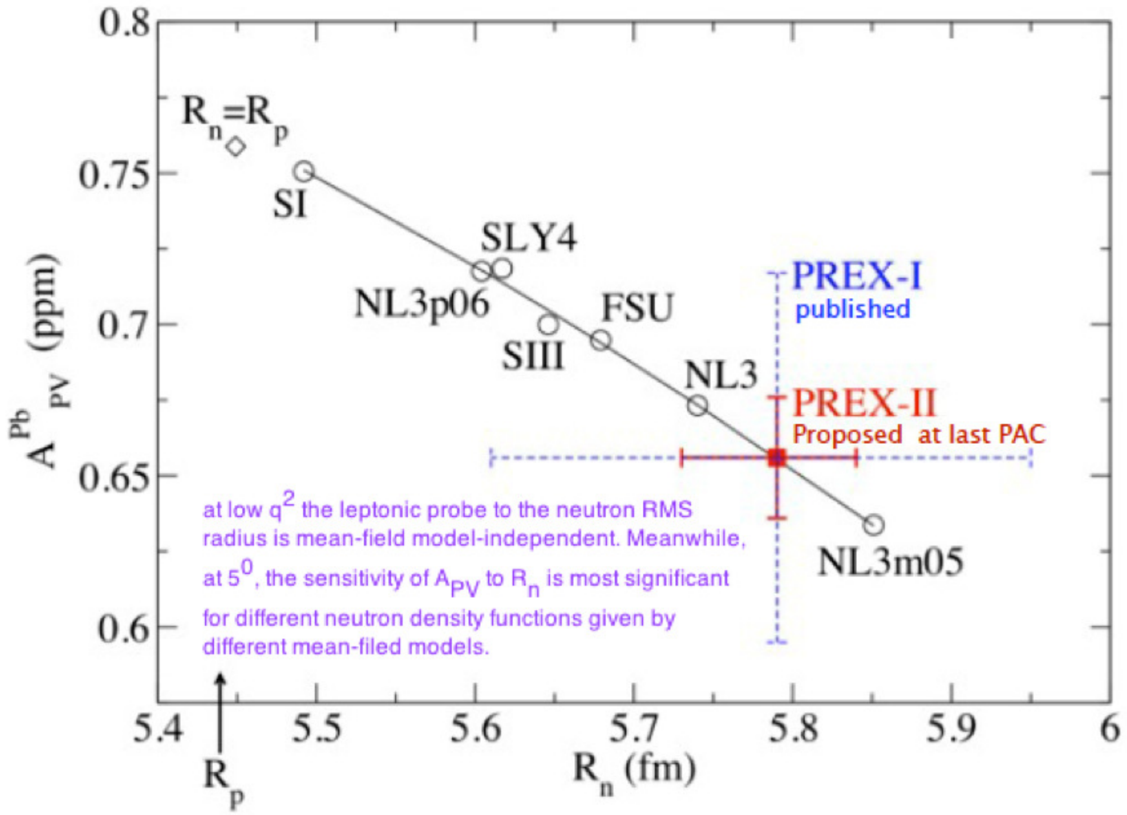

Figure 1.14: $\mathcal{A}_{pv}^{DWBA}$ versus $< R_n^2 >^{1/2}$ for both non-relativistic and relativistic mean field interaction models. The experimental asymmetry measurement, $\mathcal{A}_{pv}^{Pb}$, corresponding to the extracted $< R_n^2 >^{1/2}$, is also depicted on this graph and labelled as PREx-I (2010 PREx). The expected asymmetry result for the proposed running experiment, PREx-II (2014 PREx), overlaps on the same central value as PREx-I's with a precision statistical improvement of three-fold.

model, the weak form factor is expressed below:

$$F_W(Q) = \frac{3}{QR_h} j_1(QR_h) e^{-\sigma^2 Q^2/2}, \tag{1.34}$$

where σ is the width of a gaussian function of the final weak density after folding the weak charge density, that is firstly assumed to be uniform out to the diffraction radius, R_h. σ includes contributions from the surface thickness of the point nucleon densities and the single nucleon form factor, $j_1(x) = \frac{\sin x}{x^2} - \frac{\cos x}{x}$.

We compare Equation 1.34 to Equation 1.31, and thus σ (the surface thickness) and R_h as listed in Table 1.3 are extracted. Therefore, the square of weak charge radii is:

$$R_W^2 = \frac{3}{5}(R_h^2 + 5\sigma^2) = 5.83 \pm 0.18(\text{exp}) \pm 0.03(\text{mod}) \quad (\text{fm}). \tag{1.35}$$

Fig. 1.15 shows you the weak charge density function derived from Helm model according to the measured $^{208}_{82}$Pb experiment (PREx) [29].

Table 1.3: Least square fits of parameters to theoretical mean field model weak charge densities. Parameters, R_h and σ (see Equation 1.34), are for Helm model weak charge density.

Helm

Mean field interaction model	R_h (fm)	σ (fm)
Skyrme I [24] (non-rel.)	6.792	0.943
Skyrme III [25] (non-rel.)	6.976	1.024
Skyrme SLY4 [26] (non-rel.)	6.888	1.115
FSUGold [23] (rel.)	6.961	1.028
NL3 [27] (rel.)	7.057	1.039
NL3p06 [28] (rel.)	6.886	1.010
NL3m05 [28] (rel.)	7.231	1.012
Average		1.02 ± 0.09

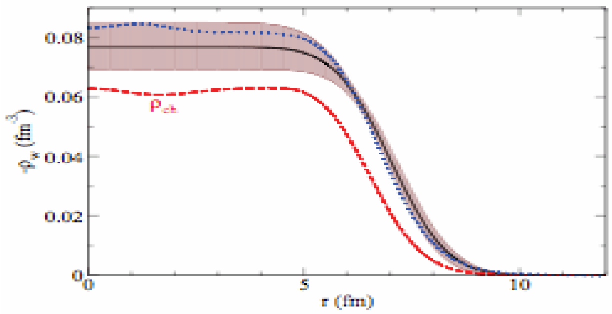

Figure 1.15: (Color on line) Helm model weak charge density-ρ_W(r) of $^{208}_{82}$Pb that is consistent with the 2010 PREx result (solid black line). The brown error band shows the incoherent sum of experimental and model errors. The red dashed curve is the experimental (electromagnetic) charge density ρ_{ch} and the blue dotted curve shows a sample mean field result based on FSUGold interaction [23].

1.4 Application: Impact on our Knowledge of the Neutron Star

A high-precision $< R_n^2 >^{1/2}$ measurement is useful to understand the neutron star structure. We have learned the strong correlation between the neutron skin thickness (Δr_{np}) in $^{208}_{82}$Pb and baryon density-dependent asymmetry energies, a_A, at the saturated nuclear density. Nuclear asymmetry energies, which are under control for the finite nuclei in the ground state near the saturation [37] nuclear density level, play important roles to describe the EOS of the neutron-rich matter. a_A are relevant to the pressure of EOS, because the larger pressure, indicating stiffer asymmetry energies, than the Coulomb repulsion pushes more neutrons than protons outward against the surface tension, giving rise to the neutron skin thickness (Δr_{np}) in the neutron-rich matter. Meanwhile, the precise $< R_n^2 >^{1/2}$ measurement can help calibrate the astronomical observation of the neutron star radius [38, 39], r_{NS}.

In addition to the strong correlation between Δr_{np} in $^{208}_{82}$Pb and the pressure of the neutron star near the saturation density [37, 14], several additional neutron star characteristics which are also correlated with Δr_{np} in $^{208}_{82}$Pb have been inferred [40]. These characteristics include:

(a) the crust-to-core transition density [39],

As discussed in the previous section, the larger $< R_n^2 >^{1/2}$ corresponds to stiffer symmetry energies. Hence, the solid phase favors a faster transition to the uniform liquid phase. Therefore, $< R_n^2 >^{1/2}$ are correlated with the density ρ_t, the transition of which is from the low density solid crust to the liquid core [39], in a neutron star.

(b) neutron star radii [38, 41], and

Generally speaking, the larger $< R_n^2 >^{1/2}$ of the neutron-rich matter result in stiffer symmetry energies at normal nuclear densities, and the larger pressure in the neutron star's EOS at ultra-high nuclear densities. Hence, the size of the neutron star, r_{NS}, becomes larger. [38]. Remarkably, the difference in size between the neutron-rich nuclei and the neutron star is 18 orders of magnitude [3]. Despite the huge discrepancy in size between the neutron-rich matter and the neutron star, the high precision $< R_n^2 >^{1/2}$ measurement make impacts on gaining better understanding EOS at the average, below or more times of nuclear densities. That is, both $< R_n^2 >^{1/2}$ and r_{NS} measurements can help determine EOS respectively at different nuclear density levels. In contrast, while stiffer symmetry energies, accompanying with larger $< R_n^2 >^{1/2}$ at the normal nuclear density, becomes gradually soft, the size of the neutron star gets smaller at a several times higher than the normal nuclear density. The softening process of EOS will result in the phase transition from nuclei to quark matter in the neutron star.

Neutron-rich matter	nuclei	neutron star
size	10 fm	10 km
normal nuclear density	at/below	more times higher
symmetry energy	stiffer w/ larger $< R_n^2 >^{1/2}$	softer w/ smaller r_{NS}

---

[3] $< R_n^2 >^{1/2} \approx$ 5.5 fm, and $r_{NS} \approx$ 10 km.

(c) the threshold density at the onset of the direct URCA process [42].

Asymmetry energies, a_A, help determine the composition of a neutron star. The larger a_A are, the more the fraction of protons is. While the proton percentage (fraction) is greater than 12%, neutrons near the Fermi surface would follow β-decay to produce one proton plus an anti-electron neutrino, and the inverse β-decay will generate an electron neutrino. A pair of electron neutrino and anti-electron neutrino will take away part of the neutron star's energy. Hence, the neutron star starts cooling down. This is called the direct URCA process. The direct URCA cooling depends on processes:

$$\begin{aligned} n &\to p + e^- + \bar{\nu}, \\ e^- + p &\to n + \nu. \end{aligned} \tag{1.36}$$

At the threshold nuclear density, the larger $< R_n^2 >^{1/2}$ at the normal nuclear density correspond to stiffer asymmetry energies, so $\frac{\mathrm{d}a_A}{\mathrm{d}\rho}$ becomes larger, too. a_A are more likely to get higher with more percentages of protons at the denser nuclear density. As a consequence, the direct URCA process is more likely to take place, and more energies of the neutron star are dissipated by pairs of neutrinos. Therefore, the temperature of the neutron star drops.

Chapter 2

Experimental Design

2.1 Experimental Goal

The aim of the high precision RMS neutron radii (R_n) in ${}^{208}_{82}$Pb measurement is with the sensitivity to 1% ($\pm$0.05 fm), and the corresponding statistical error of the experimentally measured parity-violating asymmetry is around 3% (15 ppb). The unexpected technical problems, however, took place during 2010 PREx data-taking period. Consequently, a great loss of time to collect valuable data led to a nearly three times higher statistical uncertainty of $\mathcal{A}_{pv}^{PWBA}$. On the other hand, 2010 PREx achieved a proposed 1% (5 ppb) goal of the systematic uncertainty. In order to meet the requirement of the highly precise measurement, a great deal of efforts to upgrade all aspects of the experimental apparatus was needed, so that we could guarantee that every piece of hardware instrument was well-controlled to run smoothly.

2.2 Technical Issues

2010 PREx required the longitudinal asymmetry of 0.5 ppm with the statistical uncertainty of 3% and the systematic uncertainty of $(1-2)$%, so that it was regarded as one of ten most challenging experiments running in JLab since 1984. The technical issues primarily focus on a list of categories as followed: 1) Helicity-Correlated Systematic Errors; 2) Q^2 Measurements; 3) High Power Target Design; 4) Septum Magnet, and 5) High Precision Polarimetry. In sum, both of the absolute error ($\sim$ 15 ppb) and relative error

(3%) were very difficult to accomplish. The former was induced by the proficient control of false asymmetry related to the helicity-correlated beam parameters, like, intensity, position, angle and energy. The later was due to the beam polarimetry and Q^2 measurement.

2.2.1 Electron Beam Source and Charge Asymmetry

The polarized electrons were generated by the photoemission from a GaAsP photocathode. The incident laser light with the specifically circular polarization was produced by the Pockels Cell (PC). The helicity signals from the helicity generator (HG) determine the polarity of the high voltage of PC, and hence the helicity state of the electron beam. An insertable half-wave plate (IHWP) was put and reversed along the path of the laser light once every single day. An additional half-wave plate, called rotatable half-wave plate (RHWP), together with IHWP are used to suppress the systematic uncertainty for the imperfect laser configuration. The charge asymmetry, also called the helicity-correlated (HC) beam intensity asymmetry, is defined as the fractional difference of integrated beam intensities between two opposite-sign helicity states. The charge asymmetry was induced by the imperfection of the electron beam source configuration.

2.2.2 Beam Modulation System and Helicity-Correlated Beam Parameters

The beam modulation system comprises the beam current monitors (BCMs) and the beam position monitors (BPMs). BCMs and BPMs are located along the beam line and belong to part of the accelerator . They are used not only to accurately measure the difference in HC beam parameters between two helicity states but to detect the instability of beam parameters. HC beam parameters include beam current, beam energy, beam position and beam angle. The instability of the beam gave arise to the false asymmetry, which ought to be subtracted from the measured parity-violating asymmetry.

2.2.3 Beam Polarimeter and Beam Polarization

Presumably the electron beam is 100% polarized, the experimental measurement of the parity-violating asymmetry is the same as the theoretical prediction. In practice, the actual beam is not fully polarized, so that we need to measure the longitudinal beam polarization for PREx using both Møller and Compton polarimeters in Hall-A. The physics asymmetry is obtained by scaling the experimentally measured asymmetry with the partially polarized electron beam.

2.2.4 Data Acquisition System and Parity-Violating Asymmetry

Two separate data acquisition systems (DAQs) were running during 2010 PREx. One is the integrating DAQ, also called parity DAQ; the other is the counting DAQ. The former is used to collect the parity-violating asymmetry data, while the later is exclusively for the low-current measurements to determine the asymmetry resulted from backgrounds, Q^2 and the high-resolution spectrometer (HRS) optics. The integration of the signal flux accumulated in each detector over one helicity window was not influenced by different scattering rates. More importantly, we took the advantage of the minimal deadtime for parity DAQ with the integration mode, because the electronic pick-up of the helicity correlated signals due to the deadtime is most likely to cause the serious helicity-correlated correction to the measured parity-violating asymmetry for the high scattering rate. In addition, since everything, including different sources of backgrounds, was integrated, we needed to remove the background contaminations from data in order to prevent them from biasing the interpretation of the final physics result. On the other hand, the disadvantage of the integrating DAQ is its sensitivity to the non-linearity of the detector photo-multiplier tube (PMT) and analog-to-digital (ADC) pedestal drifts.

2.2.5 Target

Since 2010 PREx aimed to measure RMS neutron radii in Lead ($^{208}_{82}$Pb), the lead target was selected for this elastic electron scattering experiment. The Lead target comprised of a 0.5 mm pure $^{208}_{82}$Pb foil which was sandwiched between two 0.15 mm diamond sheets, because $^{208}_{82}$Pb has a relatively low melting point of 600 K, and a poor thermal conductivity of merely 35 W/m/K. The diamond, however, has a much better thermal conductivity ($>$ 900 W/m/K) to hasten the transition of the heat, induced by the higher beam current, away from the $^{208}_{82}$Pb foil. As a result, the sandwich type of the target design is for the sake of preventing the target from being melt. During PREx, the temperature of the Lead target kept at 96 K for 50μA beam current. The target's edges were cooled with the cryogenic ^{4}He at 20 K.

2.2.6 HRS and Septum Magnets

HRS is composed of a set of superconducting magnets in sequence: two quadrupoles, a vertically bending dipole (45°), and a third quadrupole (QQDQ). The first two quadra-poles focused the beam onto the dipole, whereas a third quadrupole focused the beam onto the plane, where the detectors are located. The dipole possesses the high-momentum resolution (10^{-4}) in the scattering plane over the range of momentum from 0.8 to 6.0 GeV due to the 12 m dispersion; on the other hand, the quadrupoles are in charge of the focusing. The elastically scattering electrons from the target were transported onto the detectors through HRS, but the inelastically scattering ones were clearly separated at the detector's focal plane. The PREx kinematics required a extremely forward scattering angle (5°), but the minimal scattering angle for HRS is 12.5°; therefore, an additionally superconducting Septum magnet upstream of the HRS was needed in order to bend the 5° scattered electrons into the opening aperture of the HRS.

2.2.7 Collimator

Since the theoretical transverse asymmetry was predicted to be the same large as the longitudinal parity-violating asymmetry and regarded as one systematic uncertainty, it ought to be measured through the experimental apparatus. The collimator located between the target and the first quadrupole of HRS was designed to not only facilitate the transverse asymmetry measurement but suppress the unwanted backgrounds resulted from the inelastic scattering electrons by blocking them from entering HRS. The collimator had a semi-circular opening and a notch at the edge of the inner side of the semi-circle. The notch included Beryllium (Be), and the elastic scattering electrons, passing through Be, lost their energies. Consequently, after arriving the entrance of HRS, the elastic scattering electrons followed a slightly different trajectory through the semi-circular opening from that through the Be-contained notch. Eventually, elastic scattering electrons from two trajectories with a small separation arrived at different locations onto the detector's focal plane, and were in turn distinguished from each other.

2.2.8 Focal Plane Detectors

PREx acquired not only the longitudinal asymmetry data but the transverse ones. Hence, there are three individual detectors for each arm. Two of them are the main detectors used to collect longitudinal asymmetry data; the rest of them is specific for the transverse asymmetry study. Each detector is composed of quartz scintillators in order to absorb the Čerenkov radiation accumulated by PMTs. The radiation-hard materials were specially selected for these detectors to withstand the radiation damage caused by the high scattering rate at very forward angles. The non-linearity test systems were attached to all of the detectors for the further non-linearity study.

2.3 Optimization

In order to diminish the target's recoiling after colliding with incident electrons, the heavy target, composed of large atomic mass number nuclei, was hence chosen. Therefore, the momentum transfer, Q^2, could be suppressed to be minimal. More importantly, at low-Q^2, the average proton and neutron form factors, $F_p(\bar{Q}^2)$ and $F_n(\bar{Q}^2)$, can be approximately expressed in terms of Q^2 over a range of Q^2 using both non-relativistic and relativistic mean field theory models. Besides, only at $Q^2 = 0$, the weak charge radius is able to be precisely determined by taking the derivative of the weak form factor with respect to Q^2. According to Equation 1.28, $\mathcal{A}_{pv}^{PWBA}$ is roughly proportional to the magnitude of Q^2 and meanwhile anti- proportional to $\mathcal{M}_Z$. Therefore, the experimentally measured parity-violating asymmetry was in the magnitude of order of part per million (ppm) at $\bar{Q}^2 = 0.0088 \pm 0.0001$ GeV^2 for 2010 PREx.

Table 2.1: Model root mean square proton R_p and neutron R_n radii for $^{208}_{82}$Pb.

Interaction	R_p (fm)	R_n (fm)
Skyrme I [24]	5.38	5.49
Skyrme III [25]	5.52	5.65
Skyrme SLY4 [26]	5.46	5.62
FSUGold [23]	5.47	5.68
NL3 [27]	5.46	5.74
NL3p06 [28]	5.51	5.60
NL3m05 [28]	5.50	5.85

PREx is an extremely challenging experiment because of its small asymmetry of order 1ppm. Consequently, PREx also needs to acquire the relatively smaller statistical and systematic uncertainties. If the experimentally measured parity-violating asymmetry

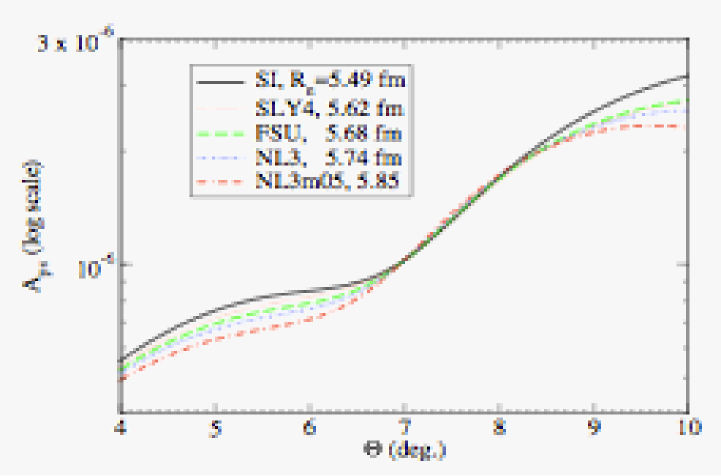

Figure 2.1: Parity-violating asymmetry ($\mathcal{A}_{pv}^{DWBA}$) versus laboratory angle for elastic scattering electrons from the Lead target at 1.05 GeV. Different curves correspond to different mean field models used to do the least square fits of neutron density function's parameters.

increases with the higher Q^2, the cross-section will in turn decrease. As a result, a careful study of a choice of PREx kinematics to optimize the sensitivity of $\mathcal{A}_{pv}^{PWBA}$ to the neutron RMS radius is strongly needed.

For the beam energy of 1.05 GeV, Fig. 2.1 shows that $\mathcal{A}_{pv}^{PWBA}$ is most sensitive to different predictions of R_n derived from different non-relativistic and relativistic mean field models at the scattering angle of $\sim 5°$. We then define the sensitivity parameter as an optimal factor below:

$$\epsilon_{R_n} = \frac{\mathrm{d}\, lnR_p}{\mathrm{d}\, lnR_n} = \frac{R_n}{\mathcal{A}_{pv}}\frac{\mathrm{d}\mathcal{A}_{pv}}{\mathrm{d}R_n}. \tag{2.1}$$

Fig. 2.2 shows ϵ_{R_n} peaks at 3 for the beam energy of 1.05 GeV and the scattering angle of $\sim 5°$. This is why a 3% statistical error of $\mathcal{A}_{pv}^{PWBA}$ corresponds to the sensitivity of RMS neutron radii R_n up to 1%.

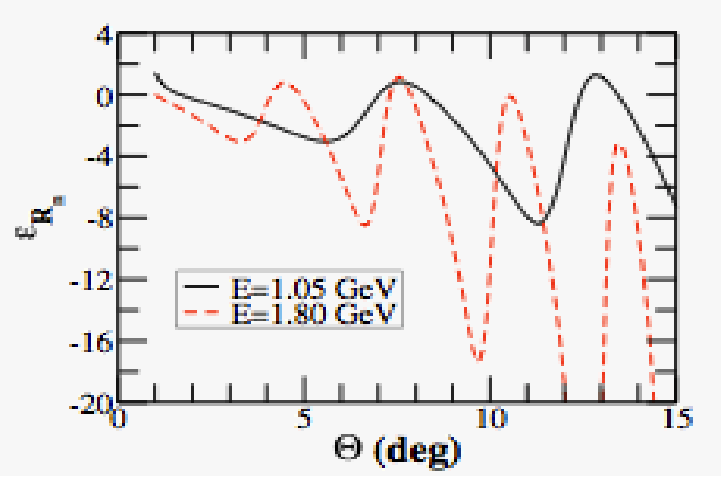

Figure 2.2: Sensitivity of the parity-violating asymmetry ($\mathcal{A}_{pv}^{DWBA}$) for $^{208}_{82}$Pb to the change in the neutron radius. The solid (dash) line corresponds to the beam energy of 1.05 (1.80) GeV. The non-relativistic mean field model, SLY4, was used here.

2.3.1 Statistical Uncertainty

Several factors which make an impact on the level of the statistical error are listed as follows:

(1) the pure counting statistics;

  (a) the beam intensity (I);

  (b) the duration of data accumulation (T);

  (c) the target's density (ρ_{tar});

  (d) the differential cross-section ($\frac{\mathrm{d}\sigma}{\mathrm{d}\Omega}$);

  (e) the radiation loss factor (ζ);

  (f) the detector's solid angle ($\Delta\Omega$);

  (g) the detector's energy resolution (ΔE).

  ⋆ the uncertainty of the beam polarization.

(2) the instrument noise in the beam modulation system (aka beam jitter);

(3) the ADC bit-resolution of the detector (aka electronics noise);

(4) the fluctuation of the detector's pedestal;

(5) the fluctuation of the target's density and the target's non-uniformity.

2.3.1.1 Counting Statistics

The total number of detected electrons, $\mathcal{N}_{total}$, the counting statistics, $\delta\mathcal{N}_{total}$, the experimentally measured parity-violating asymmetry, $\mathcal{A}_{pv}^{PWBA}$, and its statistical error of, $\delta\mathcal{A}_{pv}^{PWBA}$, are defined as listed below:

$$\begin{aligned}
\mathcal{N}_{total} &= IT\rho_{tar}\frac{\mathrm{d}\sigma}{\mathrm{d}\Omega}\Delta\Omega\zeta N, \\
\delta\mathcal{N}_{total} &\equiv \frac{\Delta\mathcal{N}_{total}}{\mathcal{N}_{total}}, \\
\mathcal{A}_{pv}^{PWBA} &= \mathcal{A}_{pv} \times P, \\
\delta\mathcal{A}_{pv}^{PWBA} &\propto \frac{1}{\sqrt{\mathcal{N}_{total}}}.
\end{aligned} \tag{2.2}$$

Hence, the statistical error of neutron RMS radii, $\delta R_n = \frac{\Delta R_n}{R_n}$, can be determined in terms of $\mathcal{N}_{total}$, $\mathcal{A}_{pv}$, P and the sensitivity parameter, ϵ_{R_n}. Likewise, according to Equation 2.1, we have:

$$\frac{\Delta R_n}{R_n} = \frac{1}{\epsilon_{R_n}}\frac{\mathrm{d}\mathcal{A}_{pv}^{PWBA}}{\mathcal{A}_{pv}^{PWBA}} \sim \frac{1}{\epsilon_{R_n}}\frac{1}{P\mathcal{A}_{pv}\sqrt{\mathcal{N}_{total}}} = (\epsilon_{R_n}^2 P^2 \mathcal{A}_{pv}^2 \mathcal{N}_{total})^{-1/2}. \tag{2.3}$$

Now, based on Equation 2.3, we can predict the sensitivity of neutron RMS radii to different conditions. As discussed, the optimized scattering angle is 5° with the beam energy of 1.05 GeV. Presumably, the running time is half of month, we can estimate

Table 2.2: Experimental parameters including beam current (I), beam polarization (P), detector solid angle ($\Delta\Omega$), number of atoms (N), energy resolution (ΔE) and radiation loss factor (ζ).

Parameter	Value
I	100μA
P	0.8
$\Delta\Omega$	0.0037 Sr
N	2
ΔE	4MeV
ζ	0.34

$\frac{\Delta R_n}{R_n} \sim 1\%$. This prediction might be too optimistic without considering other factors listed below which are more likely to reduce the sensitivity of R_n to $\mathcal{A}_{pv}^{PWBA}$:

(1) the uncertainty of the beam polarization (ΔP);

(2) the window of the scattering angle span;

(3) the size of the beam current.

Table 2.3: Statistical error estimates for measuring R_n in 30 days. Results are first presented for $^{208}_{82}$Pb, ^{48}Ca and ^{40}Ca at a laboratory scattering angle of 5°. ^{48}Ca results are also presented for a scattering angle of 4°. The neutron and proton densities are calculated in the Skyrme HF theory with the SLY4 interaction.

Nucleus	E (GeV)	$\mathcal{A}_{pv}(5°)$ (ppm)	$\frac{d\sigma}{d\Omega}(5°)$ (mb sr^{-1})	Rate (5°) (MHz/arm)	ϵ_{R_n}	$\Delta R_n/R_n$ (%)
$^{208}_{82}$Pb	1.05	0.7188	1339	1736	-2.762	0.6637
^{48}Ca	1.80	2.358	8.630	164.3	-4.266	0.4258
^{40}Ca	1.90	2.301	5.832	111.0	-3.920	0.5777
	E	$\mathcal{A}_{pv}(4°)$	$\frac{d\sigma}{d\Omega}(4°)$	Rate (4°)		$\Delta R_n/R_n$
hline ^{48}Ca	2.20	2.290	16.56	315.2	-3.961	0.3409

2.3.1.2 Other Sources of the Statistical Uncertainty

In addition to the counting statistics, other sources of errors also contributed to broadening the RMS width of the assumulated raw asymmetry distribution in each detector. The experimental goal is to reduce the noise levels from all of these souces and to make them much smaller than the counting statistics.

2.3.1.2.1 Fluctuations of the Target's Density

Through increasing the beam intensity (current) and the target's length, the scattering rate was enhanced. Therefore, the higher the electron scattering rate, the more the amount of beam energies was deposited in the target. The heat dissipated inside the target caused the target's density to be non-uniform. The non-uniformity led to the broader RMS width of measured raw asymmetry histogram, $\mathcal{A}^{PWBA}_{pv,meas}$, and hence limiting the accuracy of $\mathcal{A}^{PWBA}_{pv,meas}$.

2.3.1.2.2 Fluctuations of the Detector's pedestal

Presumably the total amount of integrated signal flux includes the actually deposited electrons at each detector, other detector-related sources and helicity-correlated beam sources:

$$\sigma_{\text{raw}} = \sigma_{\text{sig}} + \sigma_{\text{other}} + \sigma_{\text{HC}}. \tag{2.4}$$

According to the definition of $\mathcal{A}^{PWBA}_{pv,meas}$, we have:

$$\begin{aligned} \mathcal{A}^{\text{PWBA}}_{\text{pv,meas}} &= \frac{(\sigma^L_{\text{sig}} + \sigma^L_{\text{other}} + \sigma^L_{\text{HC}}) - (\sigma^R_{\text{sig}} + \sigma^R_{\text{other}} - \sigma^R_{\text{HC}})}{(\sigma^L_{\text{sig}} + \sigma^L_{\text{other}} + \sigma^L_{\text{HC}}) + (\sigma^R_{\text{sig}} + \sigma^R_{\text{other}} - \sigma^R_{\text{HC}})} \\ &\cong \mathcal{A}^{PWBA}_{\text{pv,true}}\left(1 - \frac{\sigma^L_{\text{other}} + \sigma^R_{\text{other}}}{\sigma^L_{\text{sig}} + \sigma^R_{\text{sig}}}\right) + \frac{\sigma^L_{\text{HC}} + \sigma^R_{\text{HC}}}{\sigma^L_{\text{sig}} + \sigma^R_{\text{sig}}}, \end{aligned} \tag{2.5}$$

where σ_{other} was resulted from: (1) the non-linearity of the ADCs and PMTs; (2) pedestal drifts of the ADCs. σ_{HC} was as a result of the helicity-correlated beam properties.

Obviously, $\sigma^L_{\text{other}} + \sigma^R_{\text{other}}$ in Equation 2.5 ought to be suppressed, so that the experimentally measured asymmetry wouldn't be biased.

$$\begin{aligned}
\delta\mathcal{A}^{PWBA}_{\text{pv,meas}} &= \delta\left(\frac{(\sigma^L_{\text{sig}} + \sigma^L_{\text{other}} + \sigma^L_{\text{HC}}) - (\sigma^R_{\text{sig}} + \sigma^R_{\text{other}} - \sigma^R_{\text{HC}})}{(\sigma^L_{\text{sig}} + \sigma^L_{\text{other}} + \sigma^L_{\text{HC}}) + (\sigma^R_{\text{sig}} + \sigma^R_{\text{other}} - \sigma^R_{\text{HC}})}\right) \\
&\cong \delta\mathcal{A}^{PWBA}_{\text{pv,true}}\left(1 - \frac{\sigma^L_{\text{other}} + \sigma^R_{\text{other}}}{\sigma^L_{\text{sig}} + \sigma^R_{\text{sig}}}\right) \qquad (2.6) \\
&- \mathcal{A}^{PWBA}_{\text{pv,true}}\delta\left(\frac{\sigma^L_{\text{other}} + \sigma^R_{\text{other}}}{\sigma^L_{\text{sig}} + \sigma^R_{\text{sig}}}\right) + \delta\left(\frac{\sigma^L_{\text{HC}} + \sigma^R_{\text{HC}}}{\sigma^L_{\text{sig}} + \sigma^R_{\text{sig}}}\right).
\end{aligned}$$

Based on Equation 2.6, we can clearly manifest different sources of the statistical uncertainty on $\mathcal{A}^{PWBA}_{\text{pv,true}}$:

- $\delta\mathcal{A}^{PWBA}_{\text{pv,true}}$: pure counting statistics;
- $\delta(\frac{\sigma^L_{\text{other}}+\sigma^R_{\text{other}}}{\sigma^L_{\text{sig}}+\sigma^R_{\text{sig}}})$: relevant to the fluctuations of the target's density, the non-uniformity of the target, the non-linearity of PMTs/ADCs and the pedestal drifts of ADCs;
- $\delta(\frac{\sigma^L_{\text{HC}}+\sigma^R_{\text{HC}}}{\sigma^L_{\text{sig}}+\sigma^R_{\text{sig}}})$: independent of $\mathcal{A}^{PWBA}_{\text{pv,true}}$ but make impact on $\mathcal{A}^{PWBA}_{\text{pv,meas}}$. Hence, it's the significant source of the systematic uncertainty (discussed in the next section).

2.3.2 Systematic Uncertainty

Achieving an accuracy of a asymmetry measurement up to the sub-ppm even at a tinier level, sub-ppb, is possible, because many of the absolute systematic uncertainties were cancelled in the numerator of the fractional difference calculation of differentital cross-sections. In Equation 2.5, $(\frac{\sigma^L_{\text{other}}+\sigma^R_{\text{other}}}{\sigma^L_{\text{sig}}+\sigma^R_{\text{sig}}})$ not only brodens the RMS width of $\mathcal{A}^{PWBA}_{\text{pv,true}}$ but change the magnitude of $\mathcal{A}^{PWBA}_{\text{pv,true}}$. Therefore, it is regarded as one of the systematic uncertainty sources.

Another factor which changed the size of $\mathcal{A}^{PWBA}_{\mathrm{pv,meas}}$ rather than $\mathcal{A}^{PWBA}_{\mathrm{pv,true}}$ is $\delta(\frac{\sigma^{L}_{\mathrm{HC}}+\sigma^{R}_{\mathrm{HC}}}{\sigma^{L}_{\mathrm{sig}}+\sigma^{R}_{\mathrm{sig}}})$. It was arisen from fluctuations of the helicity-correlated beam properties such as the intensity, energy, position and angle and thus caused instability in the detector flux, σ_{raw}. Hence, it was also treated as an important systematic uncertainty.

In order to investigate the source giving rise to $(\frac{\sigma^{L}_{\mathrm{HC}}+\sigma^{R}_{\mathrm{HC}}}{\sigma^{L}_{\mathrm{sig}}+\sigma^{R}_{\mathrm{sig}}})$, we applied two analysis techniques to study: (1) linear regression; (2) beam modulation. The beam modulation analysis is a reliable analysis tool to make the measured asymmetry correction for these helicity-correlated beam asymmetries (false asymmetries) and meanwhile to help estimate the associated systematic uncertainty with such corrections. Next, we will describe how to handle these beam-related corrections.

Supposed that the differential cross-section, $\frac{d\sigma}{d\theta}$, includes electron flux, other detector-related fake signals and helicity-correlated beam false sources, we can calculate the zero-th order of the asymmetry correction after normalizing the differential cross-section to the beam current.

$$\begin{aligned}
\mathcal{A}^{\mathrm{k,0th,PWBA}}_{\mathrm{pv,cor}} &= \frac{\frac{(\frac{d\sigma}{d\theta})^{k,R}}{I^R}-\frac{(\frac{d\sigma}{d\theta})^{k,L}}{I^L}}{\frac{(\frac{d\sigma}{d\theta})^{k,R}}{I^R}+\frac{(\frac{d\sigma}{d\theta})^{k,L}}{I^L}} = \frac{\frac{(\frac{d\sigma}{d\theta})^{k,L}+\delta(\frac{d\sigma}{d\theta})}{I^L+\delta I}-\frac{(\frac{d\sigma}{d\theta})^{k,L}}{I^L}}{\frac{(\frac{d\sigma}{d\theta})^{k,L}+\delta(\frac{d\sigma}{d\theta})}{I^L+\delta I}+\frac{(\frac{d\sigma}{d\theta})^{k,L}}{I^L}} \\
&= \frac{(\frac{d\sigma}{d\theta})^{k,L}\frac{1+\frac{\delta(\frac{d\sigma}{d\theta})}{\frac{d\sigma}{d\theta}}}{1+\frac{\delta I}{I^L}}-(\frac{d\sigma}{d\theta})^{k,L}}{(\frac{d\sigma}{d\theta})^{k,L}\frac{1+\frac{\delta(\frac{d\sigma}{d\theta})}{\frac{d\sigma}{d\theta}}}{1+\frac{\delta I}{I^L}}+(\frac{d\sigma}{d\theta})^{k,L}} = \frac{\frac{1+\frac{\delta(\frac{d\sigma}{d\theta})}{(\frac{d\sigma}{d\theta})^{k,L}}}{1+\frac{\delta I}{I^L}}-1}{\frac{1+\frac{\delta(\frac{d\sigma}{d\theta})}{(\frac{d\sigma}{d\theta})^{k,L}}}{1+\frac{\delta I}{I^L}}+1} \\
&\approx \frac{(1+\frac{\delta(\frac{d\sigma}{d\theta})}{(\frac{d\sigma}{d\theta})^{k,L}})(1-\frac{\delta I}{I^L})-1}{(1+\frac{\delta(\frac{d\sigma}{d\theta})}{(\frac{d\sigma}{d\theta})^{k,L}})(1-\frac{\delta I}{I^L})+1} \approx \frac{\frac{\delta(\frac{d\sigma}{d\theta})}{(\frac{d\sigma}{d\theta})^{k,L}}-\frac{\delta I}{I^L}}{2} \\
&= \mathcal{A}^{\mathrm{k,PWBA}}_{\mathrm{pv,meas}}-\mathcal{A}^{\mathrm{k,PWBA}}_{\mathrm{pv,I}} \\
&\cong \mathcal{A}^{\mathrm{k,PWBA}}_{\mathrm{pv,true}}(1-\frac{\sigma^{L,k}_{\mathrm{other}}+\sigma^{R,k}_{\mathrm{other}}}{\sigma^{L,k}_{\mathrm{sig}}+\sigma^{R,k}_{\mathrm{sig}}})+(\frac{\sigma^{L,k}_{\mathrm{HC}}+\sigma^{R,k}_{\mathrm{HC}}}{\sigma^{L,k}_{\mathrm{sig}}+\sigma^{R,k}_{\mathrm{sig}}}-\mathcal{A}^{\mathrm{k,PWBA}}_{\mathrm{pv,I}}),
\end{aligned} \tag{2.7}$$

where k indicates each individual detector. Clearly, the zero-th order of the asymmetry correction was from the beam current (charge). Here, $\mathcal{A}_{\text{pv,I}}^{\text{k,PWBA}}$ is also called the charge asymmetry.

The first order of the asymmetry correction was from the beam energy, position and angle and expressed in terms of beam properties as below:

$$\begin{aligned}\frac{\sigma_{\text{HC}}^{L,k}+\sigma_{\text{HC}}^{R,k}}{\sigma_{\text{sig}}^{L,k}+\sigma_{\text{sig}}^{R,k}}-\mathcal{A}_{\text{pv,I}}^{\text{k,PWBA}} &\cong \frac{\sum_j \frac{\partial\mathcal{D}_j^k}{\partial\mathcal{M}_j}\Delta\mathcal{M}^j+\frac{\partial\mathcal{D}^k}{\partial E}\Delta E}{\sigma_{\text{sig}}^{L,k}+\sigma_{\text{sig}}^{R,k}} \\ &+ \text{ the 2nd-order correction term,} \\ \mathcal{A}_{\text{pv,cor}}^{\text{k,1st,PWBA}} &\cong \mathcal{A}_{\text{pv,true}}^{\text{k,PWBA}}\left(1-\frac{\sigma_{\text{other}}^{L,k}+\sigma_{\text{other}}^{R,k}}{\sigma_{\text{sig}}^{L,k}+\sigma_{\text{sig}}^{R,k}}\right),\end{aligned} \tag{2.8}$$

where both $\frac{\partial\mathcal{D}_j^k}{\partial\mathcal{M}_j}$ and $\frac{\partial\mathcal{D}^k}{\partial E}$ are called beam correction coefficients (aka: dithering coefficients).

Equation 2.9 represented the correlations between each detector's signal flux and the beam parameters. In general, the magnitude of order of either $\frac{\partial\mathcal{D}_j^k}{\partial\mathcal{M}_j}$ or $\frac{\partial\mathcal{D}^k}{\partial E}$ is $10^1\ \frac{\text{ppm}}{\mu\text{m}}$ (or $\frac{\text{ppb}}{\text{nm}}$).

$$\begin{aligned}\Delta\mathcal{A}_{\text{pv,meas}}^{\text{k,PWBA}} &\cong \mathcal{A}_{\text{pv,I}}^{\text{k,PWBA}}+\frac{\sum_j \frac{\partial\mathcal{D}_j^k}{\partial\mathcal{M}_j}\Delta\mathcal{M}^j+\frac{\partial\mathcal{D}^k}{\partial E}\Delta E}{\sigma_{\text{sig}}^{L,k}+\sigma_{\text{sig}}^{R,k}} \\ &+ \text{ the 2nd-order correction term.}\end{aligned} \tag{2.9}$$

2.3.3 Background

We have discussed how to remove detector-related fake signals and the false asymmetry as a result of the helicity-correlated beam properties as well from elastic scattering electrons integrated in parity DAQ. Next, we need to consider the false asymmetry for background processes.

$$\sigma_{\mathrm{cor}} = \sigma_{\mathrm{sig}} + \sum_i \sigma^i_{\mathrm{bkg}} = (\sigma_{\mathrm{raw}} - \sigma_{\mathrm{other}} - \sigma_{\mathrm{HC}}) + \sum_i \sigma^i_{\mathrm{bkg}}, \tag{2.10}$$

where i represents different background sources.

$$\begin{aligned}
\mathcal{A}^{\mathrm{PWBA}}_{\mathrm{pv,cor}} &= \frac{\sigma^R_{\mathrm{cor}} - \sigma^L_{\mathrm{cor}}}{\sigma^R_{\mathrm{cor}} + \sigma^L_{\mathrm{cor}}} \qquad (2.11)\\
&= \frac{(\sigma^R_{\mathrm{sig}} - \sigma^L_{\mathrm{sig}}) + \sum_i(\sigma^{i,R}_{\mathrm{bkg}} - \sigma^{i,L}_{\mathrm{bkg}})}{(\sigma^R_{\mathrm{sig}} + \sigma^L_{\mathrm{sig}}) + \sum_i(\sigma^{i,R}_{\mathrm{bkg}} + \sigma^{i,L}_{\mathrm{bkg}})}\\
&= \frac{(\sigma^R_{\mathrm{sig}} - \sigma^L_{\mathrm{sig}})}{(\sigma^R_{\mathrm{sig}} + \sigma^L_{\mathrm{sig}}) + \sum_i(\sigma^{i,R}_{\mathrm{bkg}} + \sigma^{i,L}_{\mathrm{bkg}})} + \frac{\sum_i(\sigma^{i,R}_{\mathrm{bkg}} - \sigma^{i,L}_{\mathrm{bkg}})}{(\sigma^R_{\mathrm{sig}} + \sigma^L_{\mathrm{sig}}) + \sum_i(\sigma^{i,R}_{\mathrm{bkg}} + \sigma^{i,L}_{\mathrm{bkg}})}\\
&= \frac{(\sigma^R_{\mathrm{sig}} - \sigma^L_{\mathrm{sig}})}{(\sigma^R_{\mathrm{sig}} + \sigma^L_{\mathrm{sig}})} \frac{1}{1 + \frac{\sum_i(\sigma^{i,R}_{\mathrm{bkg}} + \sigma^{i,L}_{\mathrm{bkg}})}{(\sigma^R_{\mathrm{sig}} + \sigma^L_{\mathrm{sig}})}} + \sum_i \frac{(\sigma^{i,R}_{\mathrm{bkg}} - \sigma^{i,L}_{\mathrm{bkg}})}{(\sigma^{i,R}_{\mathrm{bkg}} + \sigma^{i,L}_{\mathrm{bkg}})} \frac{1}{1 + \frac{(\sigma^R_{\mathrm{sig}} + \sigma^L_{\mathrm{sig}})}{\sum_i(\sigma^{i,R}_{\mathrm{bkg}} + S^{i,L}_{\mathrm{bkg}})}}\\
&= \frac{(\sigma^R_{\mathrm{sig}} - \sigma^L_{\mathrm{sig}})}{(\sigma^R_{\mathrm{sig}} + \sigma^L_{\mathrm{sig}})} \left(1 - \frac{\sum_i(\sigma^{i,R}_{\mathrm{bkg}} + \sigma^{i,L}_{\mathrm{bkg}})}{(\sigma^R_{\mathrm{sig}} + \sigma^L_{\mathrm{sig}}) + \sum_i(\sigma^{i,R}_{\mathrm{bkg}} + \sigma^{i,L}_{\mathrm{bkg}})}\right)\\
&+ \sum_i \frac{(\sigma^{i,R}_{\mathrm{bkg}} - \sigma^{i,L}_{\mathrm{bkg}})}{(\sigma^{i,R}_{\mathrm{bkg}} + \sigma^{i,L}_{\mathrm{bkg}})} \frac{\sum_i(\sigma^{i,R}_{\mathrm{bkg}} + S^{i,L}_{\mathrm{bkg}})}{(\sigma^R_{\mathrm{sig}} + \sigma^L_{\mathrm{sig}}) + \sum_i(\sigma^{i,R}_{\mathrm{bkg}} + \sigma^{i,L}_{\mathrm{bkg}})}\\
&= \mathcal{A}^{\mathrm{PWBA}}_{\mathrm{pv,phys}}(1 - \sum_i f_i) + \sum_i \mathcal{A}_{i,\mathrm{bkg}} f_i,
\end{aligned}$$

where f_i, a so-called dilution factor, is the fraction of the flux for different background sources. $\mathcal{A}_{i,\mathrm{bkg}}$ is the asymmetry for the scattering electrons through separate background processes.

Equation 2.11 can be approximated to Equation 2.12. As f_i is much lesser than 1, the second-order f_i term is dropped out.

$$\begin{aligned}
\mathcal{A}^{\mathrm{PWBA}}_{\mathrm{pv,phys}} &= \frac{(\mathcal{A}^{\mathrm{1st,PWBA}}_{\mathrm{pv,cor}} - \sum_i f_i \mathcal{A}_{i,\mathrm{bkg}})}{(1 - \sum_i f_i)} \qquad (2.12)\\
&\approx (\mathcal{A}^{\mathrm{1st,PWBA}}_{\mathrm{pv,cor}} - \sum_i f_i \mathcal{A}_{i,\mathrm{bkg}})(1 + \sum_i f_i)
\end{aligned}$$

$$\sim \quad (1+\sum_i f_i)\mathcal{A}^{\text{1st,PWBA}}_{\text{pv,cor}} - \sum_i f_i \mathcal{A}_{i,\text{bkg}}.$$

As mentioned earlier, the electron beam was not 100% fully polarized. Hence, $\mathcal{A}^{\text{PWBA}}_{\text{pv,cor,phys}}$ is obtained by scaling $\mathcal{A}^{\text{PWBA}}_{\text{pv,cor}}$ with the electron beam polarization and the finite acceptance as below:

$$\begin{aligned} \mathcal{A}^{\text{PWBA}}_{\text{pv,cor,phys}} &= \frac{\frac{1}{P_b}\mathcal{A}^{\text{1st,PWBA}}_{\text{pv,cor}} - \sum_i f_i \mathcal{A}_{i,\text{bkg}}}{(1-\sum_i f_i)} \\ &\sim [\frac{1}{P_b}(1+\sum_i f_i)\mathcal{A}^{\text{1st,PWBA}}_{\text{pv,cor}} - \sum_i f_i \mathcal{A}_{i,\text{bkg}}], \end{aligned} \tag{2.13}$$

where P_b is the beam polarization. Furthermore, since PREx $\mathcal{A}_{pv}^{PWBA}$ was model-dependent over a range of momentum values and scattering angles, we needed to take the average of $\mathcal{A}_{pv}^{PWBA}$ for a more precise interpretation of the final physics result.

2.3.4 Blind Analysis

In order to avoid any artificial correction on the measured asymmetry from biasing the final interpretation of physics result, a blinding offset was added to the true asymmetry via parity-analyzer software (PAN). All of the integrated data were accumulated by parity DAQs without manipulating any blinding. However, the output asymmetry from PAN was reported as the blinded value. We unblinded our asymmetry measurement after all of the analysis procedures, including cuts and asymmetry corrections, were carefully done.

Chapter 3

Experimental Instrument

3.1 PREx Overview

The experimental instruments of the first generation of PREx was running in 2010 Spring in Hall-A, Thomas Jefferson National Accelerator Facility, abbreviated to Jefferson Lab (commonly called JLab). The accelerator comprises of superconducting radio-frequency (RF) accelerating cavities used to generate the continuous-wave electron beam. As a result, JLab is also called CEBAF, which means "Continuous-wave Electron Beam Accelerator Facility."

The electrons from the injector were accelerated through 5 passes of the machine to achieve a maximum beam energy up to 6 GeV. After a selected number of passes to establish different beam energies for three simultaneous runs in each experimental Hall, i.e. Hall-A, B and C, the beam was extracted for their uses. A schematic profile of JLab accelerator is shown in Figure 3.1.

A $(50-70)\mu$A continuous-wave electron beam, composed of longitudinally polarized electrons, was transported to Hall-A with the energy of 1.063 GeV. The incident electrons were scattering from a pure $^{208}_{82}$Pb target foil, whose thickness was 0.55 mm. Elastic scattering electrons were transported via a set of superconducting magnets in HRS onto the focal plane of the detectors. An additional magnet, downstream of the target but upstream of HRS, was performed in order to bend the electron beam at an extremely forward scattering, say, 5°. The HRS momentum was set to a magnitude of 1.063 GeV/c

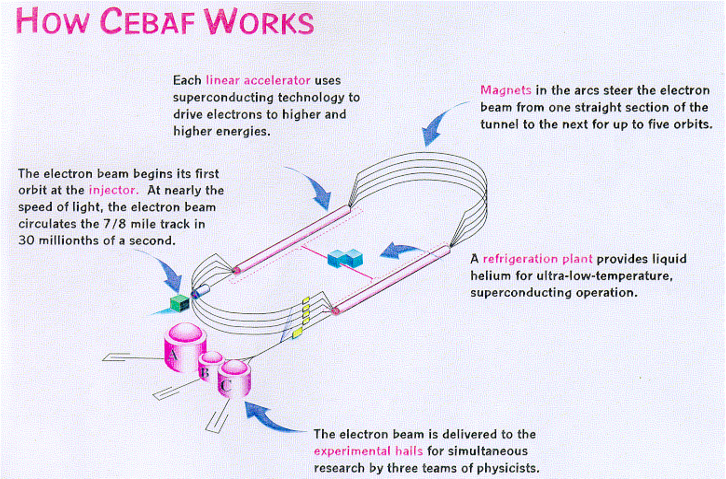
How CEBAF Works
Each linear accelerator uses superconducting technology to drive electrons to higher and higher energies.
Magnets in the arcs steer the electron beam from one straight section of the tunnel to the next for up to five orbits.
The electron beam begins its first orbit at the injector. At nearly the speed of light, the electron beam circulates the 7/8 mile track in 30 millionths of a second.
A refrigeration plant provides liquid helium for ultra-low-temperature, superconducting operation.
A
B
C
The electron beam is delivered to the experimental halls for simultaneous research by three teams of physicists.

Figure 3.1: Schematic of CEBAF.

with a high enough resolution, so that only elastically scattering electrons were focused onto the detectors. The solid angle of each HRS acceptance is around 3.7 mSr.

3.2 Polarized Electron Source

An electro-optic device, called Pockels Cell (PC), was performed to convert the linearly polarized laser light to either right or left-circularly polarized light. The polarity of the circularly polarized laser light was determined by the polarity of a high-voltage (HV) switch which was applied to PC. By illuminating GaAs (Gallium Arsenide) with the circularly polarized light, the electrons were released from the valence band to the conducting band. The polarity of the laser light determined the direction of the electron beam's longitudinal polarization. By reversing the polarity of the laser light with the change on the polarity of HV using the helicity generator (HG), the helicity state of the electron beam was reversed accordingly. For PREx, the helicity was rapidly reversed at either 120 Hz or 240 Hz due to a list of reasons as followed:

- the mitigation of 60 Hz power-line noise;
- the suppression of sensitivites to periodic background noises;

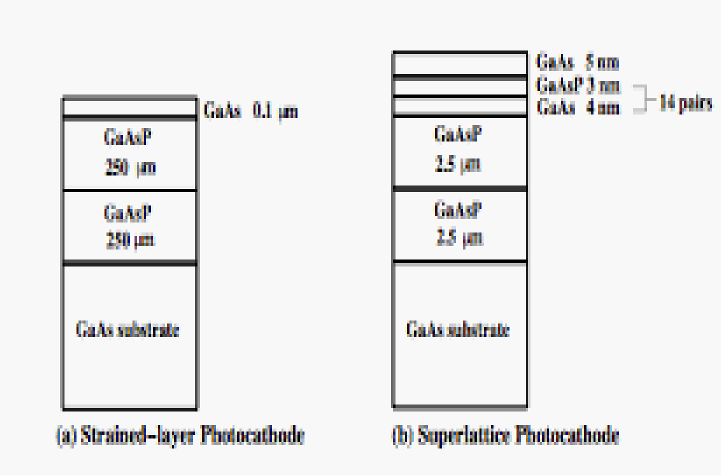
GaAs 0.1 μm
GaAsP
250 μm
GaAsP
250 μm
GaAs substrate
(a) Strained–layer Photocathode
GaAs 5 nm
GaAsP 3 nm
GaAs 4 nm
14 pairs
GaAsP
2.5 μm
GaAsP
2.5 μm
GaAs substrate
(b) Superlattice Photocathode

Figure 3.2: A schematic of the strained-layer (a) and superlattice (b) photocathode structure.

- the cancellation of history effects which existed in the non-random helicity sequences;
- the elimination of slow drifts due to the change on the temperature of experimental instruments.

3.2.1 GaAs Photocathodes

The cathode for 2010 PREx was called the superlattice cathode, composed of alternating layers of GaAs and GaAsP, as shown in Figure 3.2(b). The energy gap between the valence and conduction bands is 1.59eV for the superlattice cathode. The superlattice cathode can provide the quantum efficiency as high as 1% [1].

3.2.2 Pockels Cells

As discussed earlier, PC provides the fast-reversal of the electron beam's helicity state by altering the polarity of HV applied to PC using HG. PC's birefringence is linearly proportional to the magnitude of HV's electric field. PC [2] is used as a quarter-wave

---

[1] The quantum efficiency is defined as the ratio of emitted electrons from the cathode over the incident light's intensity.

[2] The PC is a KD*P, KD_2PO_4 crystal.

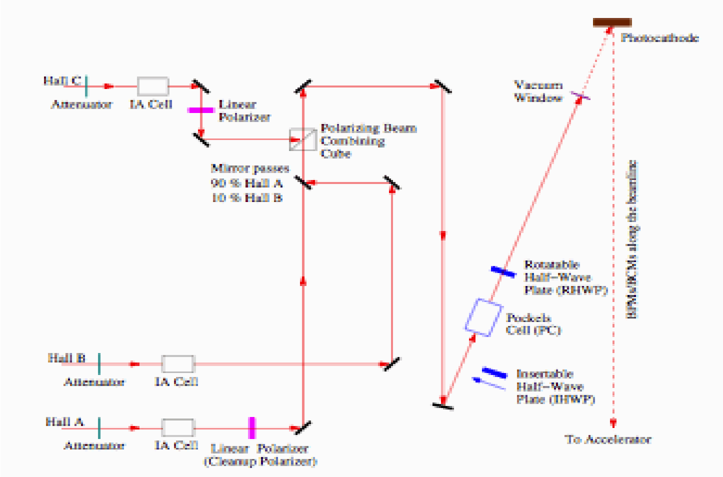
Photocathode
Hall C
Attenuator
IA Cell
Linear
Polarizer
Vacuum
Window
Polarizing Beam
Combining
Cube
Mirror passes
90 % Hall A
10 % Hall B
BPMs/BCMs along the beamline
Rotatable
Half−Wave
Plate (RHWP)
Pockels
Cell (PC)
Hall B
Attenuator
IA Cell
Insertable
Half−Wave
Plate (IHWP)
Hall A
Attenuator
IA Cell
Linear Polarizer
(Cleanup Polarizer)
To Accelerator

Figure 3.3: A schematic of the polarized electron source set-up in the injector part at JLab. The laser light was circularly polarized by PC. Through the photoemission from a GaAsP photocathode, the polarized electrons were released, because they were excited from the valence band to the conducting band via the absorption of the incident photon energies from the circularly polarized laser light. The polarity of the laser light determines the helicity state of the electron beam.

retarder in order to convert the linearly polarized laser light into the circularly polarized laser light. Despite this, the emitted laser light from PC is still not 100% perfectly circularly polarized. The residual linear polarization of the laser light can result in large charge asymmetries and helicity-correlated position differences. Hence, a rotatable half-wave plate is added downstream of PC for the sake of rotating the residual linear polarization diection of the laser light to minimize the effect on the helicity-correlated position differences.

3.3 Slow Helicity Reversal

In order to avoid the electronic helicity signals from being preferredly selected by the electronics, which is used for the fast helicity flip at either 120 Hz or 240 Hz in PREx, an instrument, called inserted half-wave plate (IHWP), was added upstream of PC to the beamline during the completion of one single day's data-taking and then removed for the next day's data collection. The former state of IHWP is called ”IN”; the later is ”OUT”. Two states were alternatively changing for every single day. That's how IHWP was performed to slowly and passively reverse the beam helicity.

3.3.1 Inserted Half-Wave Plate

IHWP rotates the linear polarization axis by 90°, so that the circular polarization direction of the laser light, determined by the polarity of PC's HV through the electronic helicity signals produced by HG, was altered to be the opposite sign to its original one. Since electronic helicity signals were blind to the alternation of two opposite helicity states operated by IHWP, the sign of the calculated asymmetry by parity DAQ would be automatically changed due to two additionally separate states of IHWP, IN and OUT. As a result, despite the presence of the preferred electronic helicity signals, the addition of IHWP into the beamline would help vary the sign of the calculated asymmetry. Eventually, the effect of the electronic pick-up of one helicity would be cancelled after the overall average of the asymmetries measured with two distinct IHWP states.

3.3.2 Double Wien

Double Wien filter, beside IHWP, was also performed for the slow helicity reversal during 2010 PREx, because the change on the direction of the magnetic field of the solenoids can reverse the electron beam's helicity state.

3.4 Beam Polarimeter

Both Møller and Compton polarimeters were running for 2010 PREx and provided two separately independent beam polarization measurements for the further comparison.

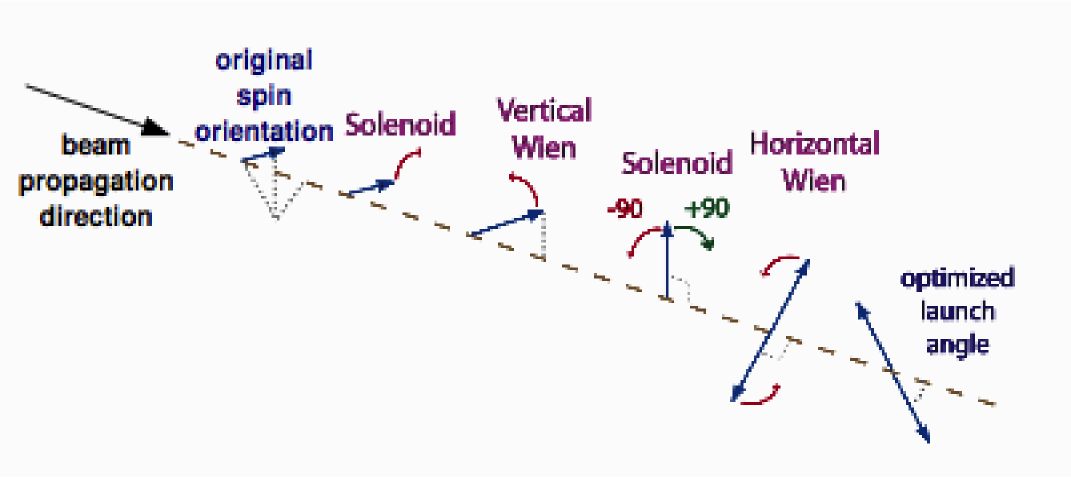

Figure 3.4: For PREx, only the second solenoid and the horizontal Wien filter were used. The set of solenoids and Wien filters along the beamline help reduce HC systematic uncertainties. In addition, the horizontal Wien can optimize the longitudinal beam polarization.

3.4.1 Møller Polarimeter

Møller polarimeter measures the asymmetry in the electron-electron scattering, where the cross section for the scattering process depends on the target polarization and the analyzing power of Møller scattering. The target foil is polarized along its plane and oriented at an angle of ±20° with respect to the plane parallel to the beam direction. Different options of the target angle can result in different Møller measurements of both longitudinal and transverse beam polarizations. The final Møller beam polarization measurement is obtained by taking the average of several Møller measurements based on different target foils in order to cancel the transverse polarization contributions and the helicity-correlated beam asymmetries. The Møller measurement is inherently invasive, for it acquires very low beam currents. Generally speaking, Møller polarmeter was performed once in a few weeks, while the nominal parity-data taking with the production mode was reuired to stop for a couple of hours. The final systematic uncertainty achieved by Møller polarimeter is 1.12% and is primarily dominated by the magnetized target foil polarization measurement.

PREx required the systematic uncertainty of each beam polarimeter be around 1%. Consequently, the focus to upgrade the Møller polarimeter for PREx is mainly on the suppression of the uncertainty caused by the target polarization measurement. First of all, the high-field magnet provided a magnetic field up to 3 T. At such the high magnetic field, almost most of the electrons in the ferromagnetic target foil were polarized, so the target was saturated. Hence, the target polarization can be measured precisely with the precision of 0.25%.

Secondly, the taget foil's thickness was reduced from (7-30) μm to (1-10) μm at the beam current up to 50 μA without being melt. Thirdly, Flash ADCs was also introduced and applied to Møller beam polarization measurements in order to deal with high scattering rates during PREx.

3.4.2 Compton Polarimeter

Since the Compton cross-section is small enough, the Compton scattered electrons interacting with photons in the middle of the magnetic chicane are able to be distinguished from the primary electron beam, delivered to the experimental target without being influenced [3]. Therefore, the Compton polarization measurement 3.2, unlike the Møller polarimeter, can be conducted simultaneously with the parity data-taking. A Fabry-P$\acute{e}$rot cavity is added in order to increase the photon density at the interaction point.

In PREx, the photon energy of the laser light is 2.33 eV with the corresponding wavelength which is 532 nm. At this photon energy, the Compton scattered electrons can be parted from the primary electron beam with a maximum separation distance up to 8.3 mm which is twice larger than that based on the normal laser setting [4]. The photon-electron beam crossing angle is 23.5 mrad. More importantly, the Compton

---

[3] The maximum separation of the Compton scattered electrons from the primary electron beam was 4.1mm at the standard Hall-A Compton Polarimeter.

[4] The conventional laser wavelength is 1064nm, corresponding to the photon energy of 1.16eV.

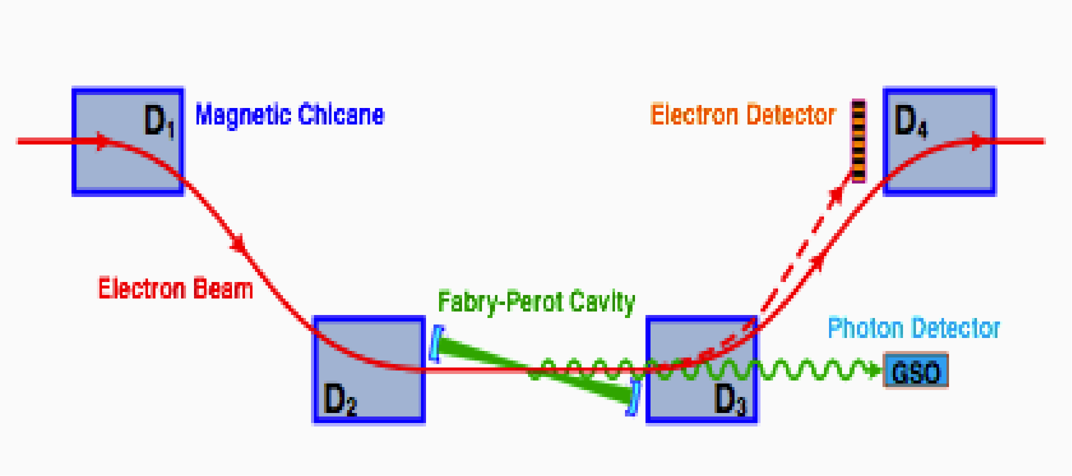

Figure 3.5: PREx Compton used a 532nm (2.33eV) laser, and Fabry-Pérot cavity contained a circulating power of ∼ 3.5kW.

asymmetry 3.1, measured from the Compton scattered electrons with a lower incident electron beam energy of 1.063 GeV from the higher photon energy of the laser light, achieved 1.7% or so, whereas it's only 0.88% at the normal laser light setting. The integration of back-scattered photons was performed by the custom Flash ADCs (FADC). The overall absolute systematic uncertainty achieved by the Compton polarimeter is 1.0%. The Compton beam polarization measurement 3.2 is determined by averaging the overall Compton asymmetries 3.1 conducted with two separate circular polarization states of the laser light, so that the helicity-correlated beam asymmetry effect can be highly suppressed. We will discuss the Compton photon analysis using FADC in great details in the next chapter.

$$\mathcal{A}\mathrm{exp} = \frac{\mathcal{N}_+ - \mathcal{N}_-}{\mathcal{N}_+ + \mathcal{N}_-}, \tag{3.1}$$

where $\mathcal{N}_+$ ($\mathcal{N}_-$) is for the Compton integration rate of the Compton scattered electrons with the right and left helicity states.

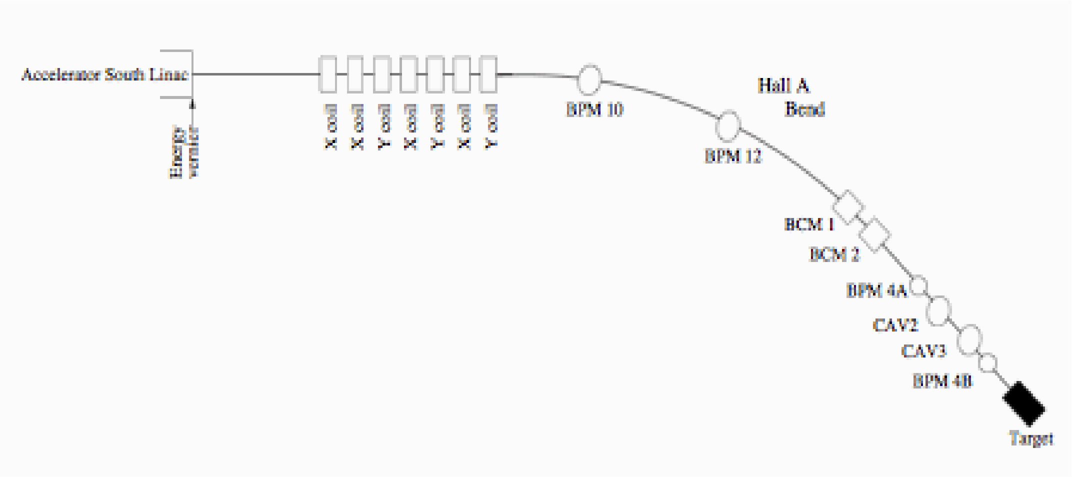
Accelerator South Linac
Energy vernier
X coil
X coil
Y coil
X coil
Y coil
X coil
Y coil
BPM 10
Hall A Bend
BPM 12
BCM 1
BCM 2
BPM 4A
CAV2
CAV3
BPM 4B
Target

Figure 3.6: A schematic of Hall-A beam monitors and beam modulation coils located along the beamline.

$$\mathcal{P}_{\mathrm{b}} = \frac{\mathcal{A}_{\mathrm{exp}}}{\mathcal{P}_{\gamma}\mathcal{A}_{\mathrm{th}}}, \tag{3.2}$$

where $\mathcal{P}_{\gamma}$ is the photon polarization $(97-99)\%$, and $\mathcal{A}_{th}$ is the Compton analyzing power (0.018).

3.5 Beam Monitors and Beam Modulation System

The beam monitors located throughout the accelerator and Hall-A beamline are very sensitive to the helicity-correlated fluctuation of beam properties which made a significant impact on the raw asymmetry measured in each detector. At the kinematics of PREx, the beam modulation (BM) system was upgraded to modulate two coils simultaneously, so that a set of BM parameters, beam positions (x and y), angles (θ_{X} and θ_{Y}) and energy (ΔE), can achieve the sufficient orthogonality. Without the sufficient orthogonality, the false asymmetry, arising from the helicity-correlated beam asymmetry, can not be expressed in terms of the beam parameters.

3.5.1 Beam Modulation System

The beam modulation system was designed to modulate a set of BM parameters as described above. Seven air-core coils upstream of the dispersive arc as shown in Figure 3.6 were used for both position and angle modulation. The dispersive arc is at the entrance of the hall, where the beam was bent. The energy modulation was performed by the vernier along the accelerator's south linac. Seven air-core coils and the vernier were manipulated by VME-4145 (digital-to-analogue (DAC) converter) controlled by parity DAQ. The sinusoidal waveforms were generated by VME-4145 DAC and used to modulate the beam through seven air-core coils and the energy vernier. The frequency of the sine wave form is 15 Hz. The phase of the sinusoidal waveform represents each integrating period recorded by parity DAQ.

Table 3.1: Important BM (aka: dithering) parameters in the **PREx** beam modulation system

BM (aka: dithering) parameters	value
frequency	15 Hz
$\mathcal{N}_{\text{period}}$/per coil	50/240 Hz ; 25/120 Hz
$\mathcal{N}_{\text{phase}}$/per period	$\frac{240}{15} = 16$ in 240 Hz; $\frac{160}{25} = 8$ in 120 Hz

Each modulation for either position and angle coils or the energy vernier took 4.23 seconds, and a whole period of one complete BM cycle, consisting of seven coils and one energy vernier modulated in sequence, lasted 85.68 seconds. The interval between two BM cycles is 9 minutes and 36 seconds. The position/angle air-core coils were modulated to make the beam excursive from the beam axis with a separation of (0.3-0.5) μm, and the energy vernier was modulated to disturbe the beam with a deviation of 0.75 mm.

Table 3.2: The mapping of EPICS variables associated with the steering air-core coils and the energy vernier in **PREx** BM hardware.

EPICS name	coil notation
MHF1C08H	coil-1 (bmwcoil1) for the direction of position/angle horizontal to scattering plane
MHF1C08V	coil-2 (bmwcoil2) for the direction of position/angle vertical to scattering plane
MHF1C10H	coil-3 (bmwcoil3) for the direction of position/angle horizontal to scattering plane
MHF1C10V	coil-4 (bmwcoil4) for the direction of position/angle vertical to scattering plane
MHF1C01H	coil-5 (bmwcoil5) for the direction of position/angle horizontal to scattering plane
MHF1C02H	coil-6 (bmwcoil6) for the direction of position/angle horizontal to scattering plane
MHF1C03V	coil-7 (bmwcoil7) for the direction of position/angle vertical to scattering plane
SL20	coil-8 (bmwcoil8) energy vernier

Table 3.3: BM symbols in the datastream for dithering analysis.

BM symbol	physics meaning
bmw_dither_frequency	= 15Hz
bmwcoil1	$bmwobj == 1$
bmwcoil2	$bmwobj == 2$
bmwcoil3	$bmwobj == 3$
bmwcoil4	$bmwobj == 4$
bmwcoil5	$bmwobj == 5$
bmwcoil6	$bmwobj == 6$
bmwcoil7	$bmwobj == 7$
bmwcoil8	$bmwobj == 8$
bmwcyc	supercycle notation
bmwfreq	= 15Hz
bmwobj	the running coil in sequence
bmwperiod	the number of periods running per coil
bmwphase	the number of phases running per period

3.5.2 Beam Position Monitors

For PREx, two of the most important BPMs located closest to the target were used to measure helicity-correlated position and angle differences of the beam. They are BPM4a and BPM4b, located 7.5 m and 2.2 m upstream of the target, respectively, in the free field region. Another important BPM, called BPM12, is located in the highest dispersive point along the arc in order to measure the energy difference. While the beam was bent along the arc, the position difference, Δx, parallel to the horizontal plane was measured, and the energy difference (ΔE) was in turn obtained.

PREx parity DAQ read out a great deal of information from numerous BPMs located inside the hall, the arc and the injector, and then fed it into the datastream. As mentioned above, BPM4a, BPM4b and BPM12 are three most important BPMs for PREx, and their information were recorded in the datastream for the further diagnostics during the online and offline data analysis.

BPMs are wire stripline monitors consisting of four antennas: X^+, X^-, Y^+ and Y^-, placed symmetrically at ±45° with respect to the horizontal/vertical plane around the beam pipe. The signal from each antenna is proportional to the beam intensity multiplied by the distance between the antenna and the beam. All four signals from each BPM were read out and integrated in parity DAQ. The measurement of a pair of beam positions is determined below:

$$\mathrm{x}' = \frac{\mathcal{X}^+ - \mathcal{X}^-}{\mathcal{X}^+ + \mathcal{X}^-} \times 18.76; \quad \mathrm{y}' = \frac{\mathcal{Y}^+ - \mathcal{Y}^-}{\mathcal{Y}^+ + \mathcal{Y}^-} \times 18.76, \tag{3.3}$$

where 18.76 is the distance from the center of the stripline axis to the base of the antennas in the unit of mm.

Both x and y beam positions were then determined by performing a rotation transformation on the coordinate system as shown in Equation 3.3. However, the placements of antennas inside those BPMs which are located in the 100 keV region of the injector are along the horizontal and vertical axes, respectively. Hence, no rotation transformation on x′ and y′ is needed.

$$\begin{pmatrix} \mathrm{x} \\ \mathrm{y} \end{pmatrix} = \begin{pmatrix} \sin 45^\circ & \cos 45^\circ \\ \cos 45^\circ & -\sin 45^\circ \end{pmatrix} \begin{pmatrix} \mathrm{x}' \\ \mathrm{y}' \end{pmatrix}.$$

3.5.3 Beam Current Monitors

Two current monitors, abbreviated BCM1 and BCM2, respectvely, are located 25 m upstream of the target. They are composed of radio-frequency (RF) resonant cavities with the high impedance, $Q \sim 3000$. These two RF cavities are cylindrical waveguides with the resonant frequency tuned to be the same as the frequency of the beam, 1497 Hz, so that the output voltage signal from RF waveguides is just proportional to the beam intensity. More importantly, the high precision measurement of the beam current is non-invasive without any need to interfer the production of data-taking. Due to the low noise and high resolution ADCs in these two beam current monitors, a precision of 3.8 ppm at 100 μA beam current over an integration length of 33.0 micro-seconds (2.06×10^{19}) was achieved.

The third BCM, called the Unser monitor (BCM3), is situated downstream of the target, and is used to provide an absolute reference for the beam current and to calibrate the cavity signals as well. However, since the output voltage signal drifted a lot every couple of minutes, it was not appropriate to regard as the primary beam current monitor. Like those BPMs outside of the hall along the beamline, other BCMs located in the region of the accelerator near the injector are primarily used for the source study of the electron beam.

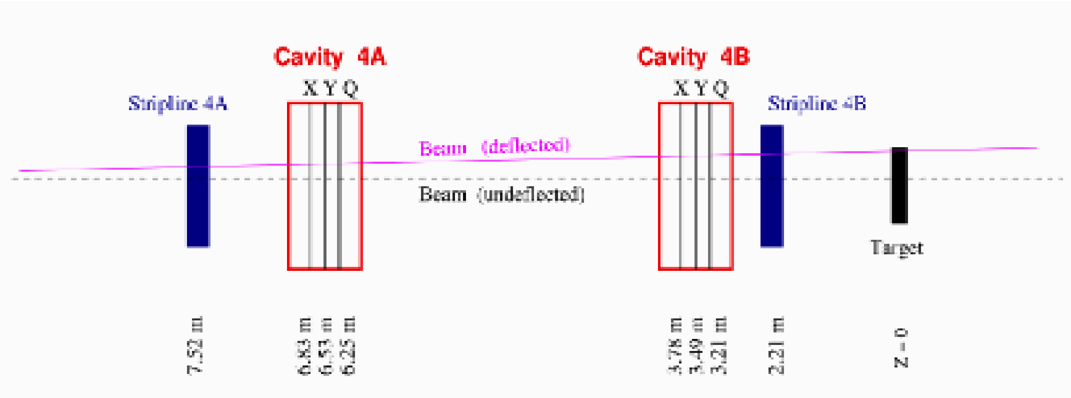

Figure 3.7: PREx low-current cavity monitors provide very accurate and reliable beam position and current measurements. Due to the extremely high scattering rate, 20 MHz/μA, during PREx, the conventional Hall-A detector package and parity DAQ cannot perform appropriately at the low beam current below 1μA without the adoption of the low-current cavity monitors. In addition, the stripline BPMs and those BCMs as mentioned above were also not reliable to provide the correct beam position and current measurements at the beam current below 1μA.

3.5.4 Low-Current Cavity Monitors

Three cavity triplets for high precision (1μm) and high bandwidth (100 kHz) position measurements were established at Hall-A. Each triplet of cavities contains two orthogonal TM110-mode cavities for both x and y measurements and one TM010-mode cavity to determine the beam current.

One cavity, called CAV2, is located ~1m downstream of BPM4A, and the other, CAV3, is located ~1m upstream of BPM4B. Both of them are drawn as shown in Fig. 3.7. PREx used low-current cavities for the four-momentum transfer squared (Q^2) measurements. In the past parity experiments running earlier than PREx, the standard Hall-A DAQ and detector packages were essential to determine Q^2. However, they became unreliable at the extremely high rate (20 MHz/μA) with a beam current of $> 1\mu$A scattering from the $^{208}_{82}$Pb target, because:

- the standard Hall-A DAQ had the typical deadtime of 20% at 2 KHz trigger rate, and the Vertical Drift Chambers (VDCs) of the standard Hall-A detector package was only working properly for the rate below 200 KHz;

- the stripline BPMs lost their reliability at the beam current of 1μA, and BCMs also cannot respond appropriately due to its non-linearity at the beam current of 5μA.

The low-current cavities were introduced, because they can provide the precise measurements of beam position and current with the beam current from 10 nA to 100μA.

3.6 DAQ

The DAQ typically consisted of Versa Module European (VME) crates. Each VME crate contained the digitization devices, including ADCs, time-to-digital converters (TDCs) and scalers, a single board computer, an ethernet network card and ethernet connection. A trigger supervisor (TS) supplied a single trigger to all of the crates, and synchronized the operation of these crates.

3.6.1 Integrating (Parity) DAQ

Parity DAQ is mainly used to accumulate the asymmetry data during the production mode of data-taking. It was triggered by the MPS pulse, and the MPS pulse was produced by HG. As a result, the accumulation rate is totally uncorrelated with the scattering rate. More importantly, parity DAQ didn't suffer from the deadtime too much at the extremely high scattering rate for PREx.

PREx parity DAQ comprises four VME crates: counting house (CH), left HRS (LHRS), right HRS (RHRS) and injector, named after their geographic locations. These crates were situated in different places throughout the accelerator along the beamline and inside of the hall, so that the noise and signal attenuations due to the long cable length would be minimized.

PREx parity DAQ used the 18-bit [5] custom ADCs, so the output signals were up to $2^{18} = 2.62 \times 10^5$ ADC channels. The 18-bit ADCs were designed to accommodate faster data acquisition rate and meanwhile to suppress the susceptibility to pedestal drifts and the non-linearity. All of the BPMs and detector packages were read out through ADCs during PREx.

On the other hand, PREx parity DAQ used the scaler to read out the information of the BM system. The frequency of any BM system is directly connected to the scaler. Through a voltage-to-frequency (V2F), the voltage signal was converted into the frequency one, and read out in the scaler. The timing board (HTB) in CH VME crates executed the timing scheme of parity DAQ.

3.6.2 Counting DAQ

Likewise, the counting DAQ consists of VME crates containing VME digitization devices, like ADCs, TDCs and scalers. However, the timing board was not applied to triggers in order to collect S0 scintillator coincidence signals, focal plane detector signals and a 1024 Hz pulser. In addition, a deadtime of 20% was measured at a trigger rate of 2 KHz. Hence, the counting DAQ was reliable exclusively for the sophisticated, low-current Q^2 measurement, for the deadtime is unavoidable at the higher current running production mode, where the scattering rate is also much higher.

---

[5] The number refers to the size of the ADC bit register.

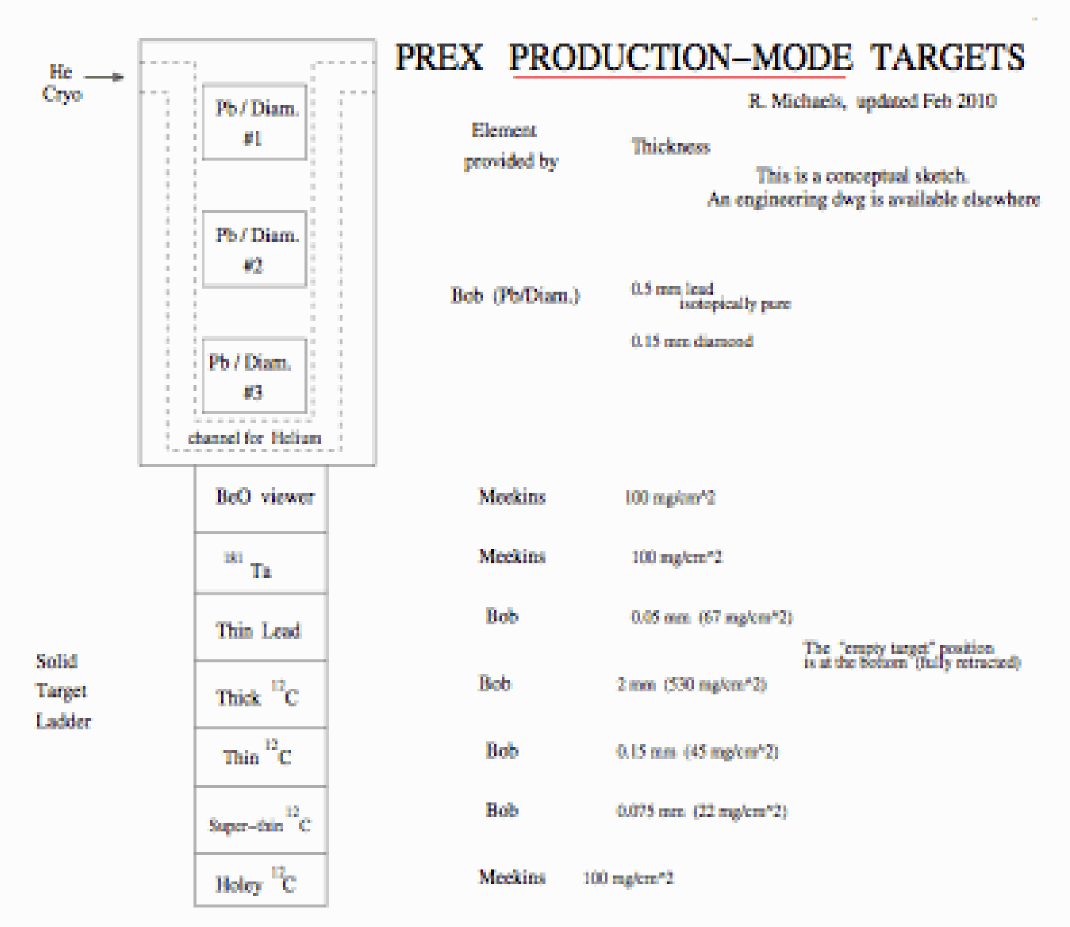
PREX PRODUCTION–MODE TARGETS
R. Michaels, updated Feb 2010
He Cryo
Pb / Diam. #1
Pb / Diam. #2
Pb / Diam. #3
channel for Helium
Element provided by
Thickness
This is a conceptual sketch.
An engineering dwg is available elsewhere
Bob (Pb/Diam.)
0.5 mm lead isotopically pure
0.15 mm diamond
Solid Target Ladder
BeO viewer
Meekins
100 mg/cm^2
^{181}Ta
Meekins
100 mg/cm^2
Thin Lead
Bob
0.05 mm (67 mg/cm^2)
The "empty target" position is at the bottom (fully retracted)
Thick ^{12}C
Bob
2 mm (530 mg/cm^2)
Thin ^{12}C
Bob
0.15 mm (45 mg/cm^2)
Super–thin ^{12}C
Bob
0.075 mm (22 mg/cm^2)
Holey ^{12}C
Meekins
100 mg/cm^2

Figure 3.8: PREx production-mode targets.

3.7 Target and Raster

Three lead-diamond targets were supplied for PREx to acquire the asymmetry data. Multiple $^{208}_{82}$Pb targets were built against the thermal failure of some of these targets. All of these targets were mounted on a copper frame. Besides the lead-diamond targets, a Beryllium Oxide (BeO), Tantalum (Ta), thick ^{12}Ca (2 mm thick), thin ^{12}Ca (0.15 mm thick), super-thin ^{12}Ca (0.075 mm thick) and a "holey" carbon target were also contained on the copper frame as drawn in Fig. 3.8.

The fluctuations of the target's density were not a serious problem for a long period of data-taking, because the noises caused by the instability of the target's density can be cancelled out due to the rapid flip of the helicity reversal. However, the boiling of the target resulted in the non-statistical broadening of the asymmetry width. During PREx, the non-uniformaity of the target's density as a result of the target's being melt caused the luminosity fluctuation. Hence, the asymmetry width increased by 40%.

The standard Hall-A rasterng system consists of two dipole magnets located 23 m upstream of the target. One is to move the beam vertically; the other is to drift the beam's movement horizontally. Two dipole magnets were driven by a 25 kHz triangular waveform at a phase difference of 120 Hz, so that the beam was uniformly distributed over a rectangular area on the target in order to prevent the target from being melt due to the locally substaintial heat with the high beam current. The size of the rectangular was adjusted by different inputs of modulation amplitudes of two dipole magnets.

However, the waveform's frequencies of the standard Hall-A rastering system were not able to be synched to the helicity signals triggered by the integrated parity DAQ. Hence, the standard Hall-A rastering system was reformed and customized in order to be operated in a different configuration for PREx. In PREx, Agilent frequency generators rather than the standard Hall-A rastering system were supplied to generate triangular raster waveform frequencies. We took the advantage of Agilent frequency generators for their arbitrarily different options of phase differences such as 120 Hz, 240 Hz, 480 Hz and 960 Hz over the run. In general, 240 Hz phase difference provided the effective suppression of the noise resulted from the target's non-uniformity. As the target was degraded gradually, the phase difference was increased to 480 Hz or 960 Hz in order to supply more suppression of the noise. The size of the raster was 4×4 mm^2 in 2010 PREx.

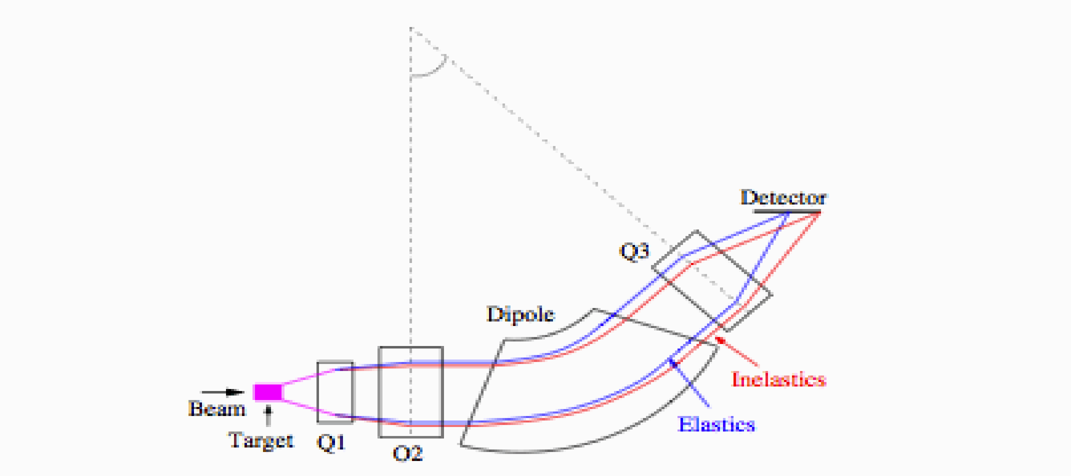

Figure 3.9: HRS separated the elastically scattering electrons from inelastic events and meanwhile forced the elastic electron signals to be focused onto the focal plane of the detectors.

3.8 HRS

HRS of each arm contains the Hall-A standard detector package used to measure the HRS optics, Q^2, scattering angles and backgrounds at the low beam current via the counting mode DAQ. The Hall-A standard detector package includes Vertical Drift Chambers (VDCs) and S0 scintillators. Each HRS has two VDCs, and each of the VDCs is used to detect the location of the incident electrons. The trajectories of electrons passing through these two VDCs onto the detectors are reconstructed altogether. On the other hand, through S0 scintillators, the elastically scattering electrons regarded as coincidence signals are able to be selected and distinguished from backgrounds. An insertabe sieve slit is located in a transfer box connecting the scattering chamber to the septum magnet and is rotated into places for the further optics studies.

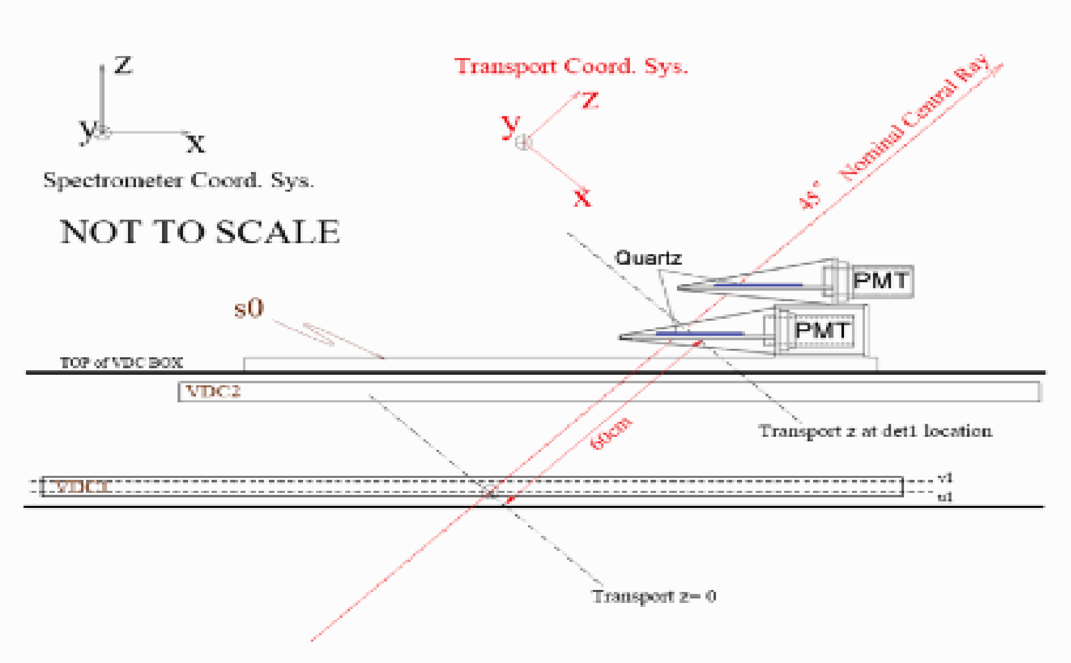
Z
y
X
Spectrometer Coord. Sys.
NOT TO SCALE
Transport Coord. Sys.
Z
y
X
45° Nominal Central Ray
Quartz
PMT
PMT
s0
TOP of VDC BOX
VDC2
Transport z at det1 location
60cm
VDC1
v1
u1
Transport z= 0

Figure 3.10: The angle of incident electrons on these detectors is at 45° to ensure the optimized collection of the quartz scintillator's *Čherenkov* radiation in the PMTs. The bottom detector had a $3.5 \times 14.0 \times 0.5$ cm^3 quartz, and the top detector had a $3.5 \times 14.0 \times 1.0$ cm^3 quartz.

3.9 Detectors

Each detector comprises 3.5×14.0 cm^2 quartz scintillators used to produce the Čherenkov radiation induced by the incident electrons onto the 2-inch quartz window of R7723 PMTs. The Čherenkov radiation was accumulated in the PMTs. The quartz scintillator's dimensions guarantee that only elastically scattering electron signals were propagating through the quartz detectors.

Chapter 4

Beam Polarization Measurement

Due to the stringent condition acquired by PREx, the data acquisition system of the Compon polarimeter was upgraded to be the integration mode in order to eliminate those systematic uncertainties inherited from the conventional counting mode DAQ. The longitudinal polarization of the electron beam is extracted from the Compton photon scattering asymmetry, the analyzing power and the laser's photon polarization. The analyzing power, i.e. the theoretical Compton scattering asymmetry, is a function of the scattered photon energy. Hence, the Compton photon scattering asymmetry is determined by the integration of the back-scattered photon energies deposited in the PMTs of the photon detector. This method is called the energy polarization weighted measurement.

4.1 Formalism

The Compton Polarimeter takes advantage of the electron beam's polarization relative to the polarization of the photons. In the Compton scattering cross-sections, the theoretical Compton photon asymmetry is defined as:

$$\mathcal{A}_{th} = \frac{\sigma^{\rightarrow}_{\Rightarrow} - \sigma^{\leftarrow}_{\Rightarrow}}{\sigma^{\rightarrow}_{\Rightarrow} + \sigma^{\leftarrow}_{\Rightarrow}}, \tag{4.1}$$

where the direction of both photon and electron polarizations is with respect to the electron beam axis, z axis.

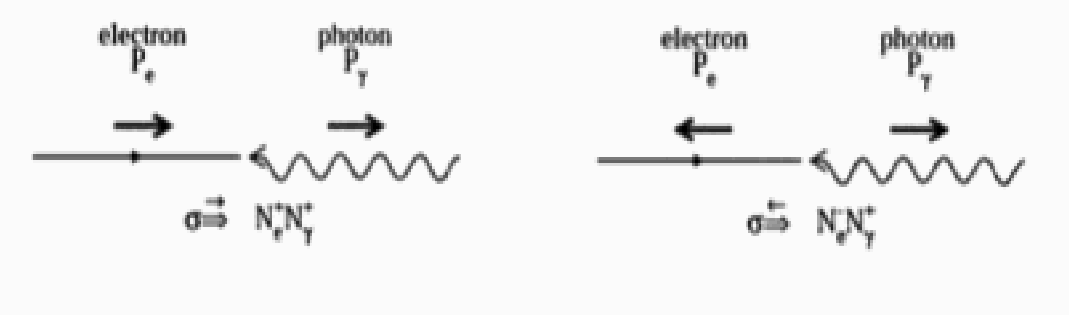
electron
P_e
photon
P_γ
$\sigma^{\overrightarrow{\Rightarrow}}$
$N_e^+ N_\gamma^+$
electron
P_e
photon
P_γ
$\sigma^{\overleftarrow{\Rightarrow}}$
$N_e^- N_\gamma^+$

Figure 4.1: Schematic of electron and photon polarization.

$\mathcal{A}_{th}$ can be determined by experimentally measuring the Compton photon scattering asymmetry as below:

$$\mathcal{A}_{\text{exp}} = \frac{N_\gamma^+ - N_\gamma^-}{N_\gamma^+ + N_\gamma^-}, \tag{4.2}$$

where N_γ^+ and N_γ^- are the integrated photon energies deposited in the PMTs of the photon detector for positive and negative helicity electrons, respectively. However, since the electron beam is not 100% perfectly polarized, $\mathcal{A}_{\text{exp}}$ is not quantitively the same as $\mathcal{A}_{th}$. As a result, the relation between $\mathcal{A}_{\text{exp}}$ and $\mathcal{A}_{th}$ can be expressed below:

$$\mathcal{A}_{\text{exp}} = \mathcal{P}_e \mathcal{P}_\gamma \mathcal{A}_{th}. \tag{4.3}$$

This is how the electron beam polarization, $\mathcal{P}_e$, is extracted using the Compton polarimeter. Here, $\mathcal{A}_{th}$ is calculated and derived by combining the calculated spin-dependent Compton cross-section with the experimental response function [44] using GEANT4 simulation [45].

Presumably the incident electrons and photons are head-to-heand colliding to each other, the scattered photon energies can be expressed as below:

$$k' = \frac{4kE^2}{4kE + m^2 + \theta_\gamma^2 E^2}, \tag{4.4}$$

where k and k' are the initial and scattered photon energies, respectively, and E is the incident electron energy. θ_γ is the photon's scattering angle. As $\theta_\gamma = 0$, k' is the maximum. On the other hand, while $\theta_\gamma = \pi$, k' is the minimum.

$$k' = \begin{cases} 4ak\frac{E^2}{m^2}, \quad \theta_\gamma = 0 & ; \\ k, \quad \theta_\gamma = \pi & . \end{cases} \tag{4.5}$$

Here, a in Equation 4.5 is $\frac{1}{1+\frac{4kE}{m^2}}$. The scattered electron energies for $\theta_\gamma = 0$ and $\theta_\gamma = \pi$ are:

$$E' = \begin{cases} E + k - 4ak\frac{E^2}{m^2}, \quad \theta_\gamma = 0 & ; \\ E, \quad \theta_\gamma = \pi & . \end{cases} \tag{4.6}$$

In order to separate scattered electrons, scattered photons and incident electrons for the further clear detection, the magnetic chicane was applied to deflecting the scattered and incident electrons. Hence, there is more room left for the laser configuration and the photon detector.

Next, we can derive the theoretical Compton photon asymmetry from integrating the differential unpolarized Compton scattering cross-section [46]:

$$\frac{\mathrm{d}\sigma}{\mathrm{d}\rho} = 2\pi r_0^2 a\left(\frac{\rho^2(1-a)^2}{1-\rho(1-a)} + 1 + \left(\frac{1-\rho(1+a)}{1-\rho(1-a)}\right)^2\right), \tag{4.7}$$

where $r_0 = \alpha_c \hbar c/mc^2 = 2.817 \times 10^{-13}$cm, and $\rho = \frac{k'}{k'_{max}}$. The total scattering cross-section is:

$$\sigma = \pi r_0^2 a \frac{-1 - 14a + 16a^2 - 2a^3 + a^4 + 2ln(a) - 12ln(a)a - 6ln(a)a^2}{(1-a)^3}. \tag{4.8}$$

Hence, the theoretical longitudinal differential asymmetry is given as:

$$\mathcal{A}_{th} = \frac{\sigma^{\rightarrow}_{\Rightarrow} - \sigma^{\leftarrow}_{\Rightarrow}}{\sigma^{\rightarrow}_{\Rightarrow} + \sigma^{\leftarrow}_{\Rightarrow}} = \frac{2\pi r_0^2 a}{\mathrm{d}\sigma/\mathrm{d}\rho}(1-\rho(1+a))[1-\frac{1}{(1-\rho(1-a))^2}]. \tag{4.9}$$

While $\theta_\gamma = 0$, the scattered photon energies have the maximum value, and the scattered electron energies, E', are minimized. Hence, $\rho = 1$, and $\mathcal{A}_{th}$ achieves to be maximized.

$$\mathcal{A}_{th}^{max} = \frac{(1-a)(1+a)}{1+a^2}. \tag{4.10}$$

According to Equation 4.9, we know $\mathcal{A}_{th} = 0$, as $\rho_0 = 1/(1+a)$.

4.2 Experimental Measurement of Electron Polarization via Compton Polarimeter

During 2010 PREx, the electron beam's polarization was reversed at a rate of 120 Hz or 240 Hz. In this section, we introduce three different methods used to extract the electron beam's polarization from the Compton photon scattering asymmetry.

4.2.1 Differential Polarization Measurement

The electron's polarization is determined by the weighted mean of the polarization distribution. Each polarization point in this distribution corresponds to one experimental Compton scattering photon asymmetry within a specific energy region of the scattered photons and electrons.

$$\mathcal{A}^i_{\mathrm{exp}} = \frac{N_\gamma^+ - N_\gamma^-}{N_\gamma^+ + N_\gamma^-} = \mathcal{P}_e\mathcal{P}_\gamma < \mathcal{A}_{th} > \approx \mathcal{P}_e\mathcal{P}_\gamma\mathcal{A}^i_{th}, \tag{4.11}$$

$$\begin{aligned}\mathcal{P}_e^i &\approx \frac{\mathcal{A}^i_{\exp}}{\mathcal{P}_\gamma \mathcal{A}^i_{th}},\\ \mathcal{P}_e &= \frac{\sum_i \frac{\mathcal{P}_e^i}{\mathrm{d}\mathcal{P}_e^{i2}}}{\sum_i \frac{1}{\mathrm{d}\mathcal{P}_e^{i2}}}.\end{aligned}$$

4.2.2 Integrated Polarization Measurement

This method is similar to the above. The difference, however, is to integrate all of the asymmetry measurements over a finite range of the scattered photon and electron energies [1] instead of calculating the electron's polarization for each asymmetry measurement, corresponding to different energies of the scattered photon and electron.

$$\begin{aligned}\mathcal{A}_{\exp} &= \mathcal{P}_e \mathcal{P}_\gamma \frac{\int_{\rho min}^1 \mathrm{d}\rho \epsilon(\rho) \frac{\mathrm{d}\sigma}{\mathrm{d}_\rho}(\rho) \mathcal{A}_{th}(\rho)}{\int_{\rho min}^1 \mathrm{d}\rho \epsilon(\rho) \frac{\mathrm{d}\sigma}{\mathrm{d}_\rho}(\rho)} = \mathcal{P}_e \mathcal{P}_\gamma < \mathcal{A}_{th} >, \qquad (4.12)\\ \mathcal{P}_e &= \frac{\mathcal{A}_{\exp}}{\mathcal{P}_\gamma < \mathcal{A}_{th} >},\end{aligned}$$

where $< \mathcal{A}_{th} >$ is obtained by normalizing to the total cross-section.

4.2.3 Energy Weighted Polarization Measurement

This method is almost the same as the method above. For a limit region of scattered photon energies deposited in the PMTs, we have:

$$\mathcal{A}_{\exp} = \mathcal{P}_e \mathcal{P}_\gamma \frac{\int_{\rho min}^1 \mathrm{d}\rho \epsilon(\rho) E(\rho) \frac{\mathrm{d}\sigma}{\mathrm{d}_\rho}(\rho) \mathcal{A}_{th}(\rho)}{\int_{\rho min}^1 \mathrm{d}\rho \epsilon(\rho) E(\rho) \frac{\mathrm{d}\sigma}{\mathrm{d}_\rho}(\rho)} = \mathcal{P}_e \mathcal{P}_\gamma \frac{< E\mathcal{A}_{th} >}{< E >}. \qquad (4.13)$$

---

[1] The energy threshold should be known.

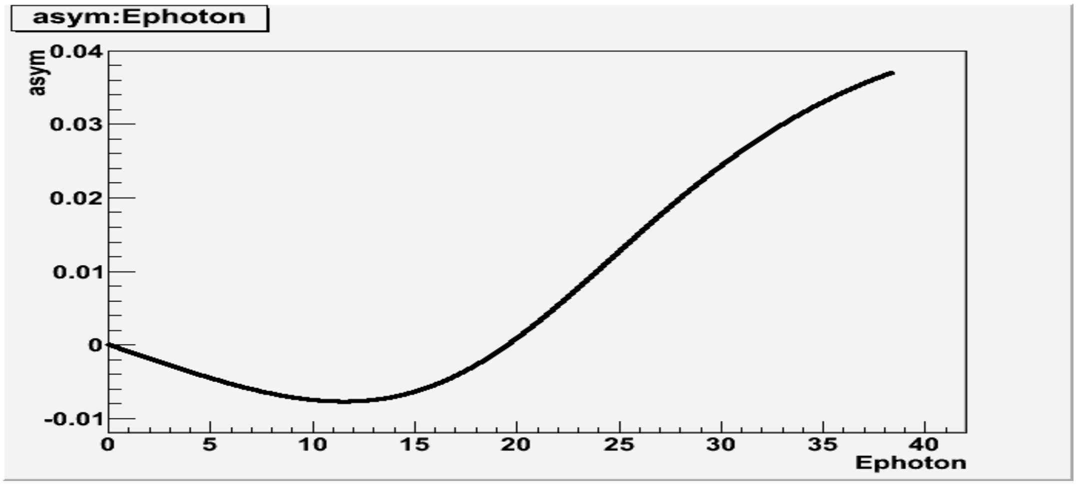

Figure 4.2: This graph shows you $\mathcal{A}_{th}$ is related to the scattered photon energy (unit: MeV). $\mathcal{A}_{th}$ is negative at low scattered photon energies, and positive at higher photon energy region. $\mathcal{A}_{th}$ crosses zero at the scattered photon energy around 20MeV. The maximum $\mathcal{A}_{th}$ near the Compton edge is close to 0.037.

Hence,

$$\mathcal{P}_e = \frac{E\mathcal{A}_{\text{exp}}}{\mathcal{P}_\gamma < E\mathcal{A}_{th} >}. \tag{4.14}$$

4.3 Photon Detector and Flash ADCs for Compton Photon Analysis

The photon detector is composed of one photon calorimeter, a cylindrical Ce-doped Gd_2SiO_5 crystal, and a single photomultiplier tube (PMT). The characteristic of GSO is that it can produce fast and bright signals, when the back-scattered photons were detected. The generated optical photons from GSO are around 450 per MeV with a stable signal width of $\sim$ 85 ns full width at half maximum.

The upgraded data scquisition system is based on a customized Flash ADCs (FADC)

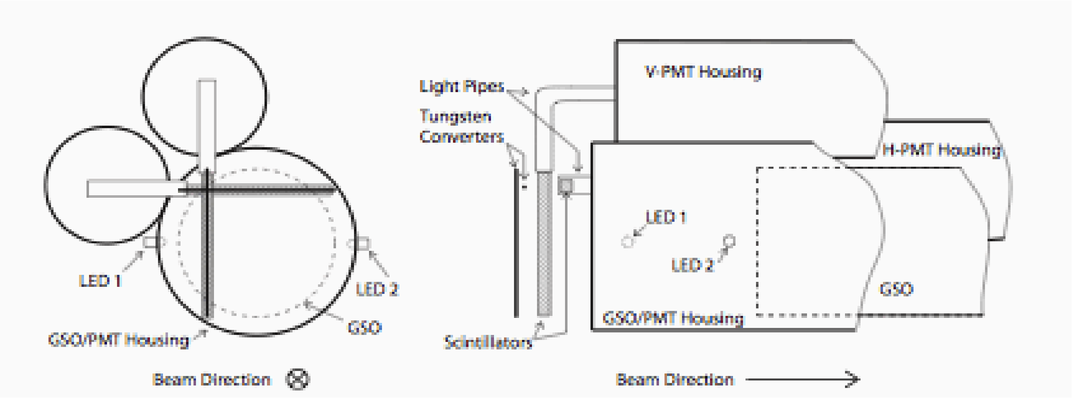

Figure 4.3: Front (left) and side (right) view of the GSO detector housing including the tungsten converters and scintillators used to determine the position of the photon beam.

with the accumulator mode. The FADC sums the sampled data into six 36-bit accumulators between an external T_{start} and T_{stop} timing signal in one helicity window. At the same time, FADC also stores all of the samples for each helicity window in the accumulation mode. On the other hand, for the sake of saving more disk space, only part of the fully sampled triggered pulses stored in the data is also stored for the further analysis by a handful of selected triggers during the trigger-mode running.

In addition, information used to diagnose the read-out data from the beam current and position monitors and the Compton cavity power are all sent out in the form of scalers for each helicity window. As a result, the selection criteria on a basis of window-to-window can be easily set and meanwhile directly applied to data during the analysis.

The timing signal is generated by the timing board and triggered by the accelerator helicity timing signals (MPS signals). The timing structure for the DAQ is shown in Fig. 4.4. The output of T_{start} follows after one MPS signal at least 15 μs later. The T_{stop} signal is sent after the T_{start}. An interval of time between T_{start} and T_{stop} signals is set to be less than the length of the accelerator's helicity window. The read-out of data starts after T_{stop}. During the period between T_{stop} and the next incoming T_{start}, both scalers and sampled data are read-out and stored by FADC with the accumulator mode. In parallel with the accumulator mode, part of the sampled data can be saved in the trigger

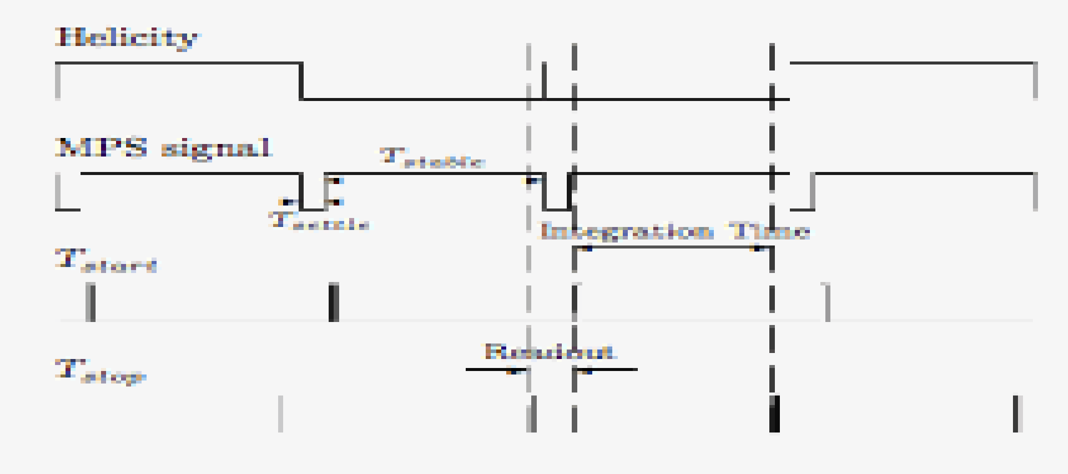

Figure 4.4: The timing structure for helicity windows.

mode of DAQ during the next helicity window followed after the completion of the read-out data, for the buffers are separate between two adjacent helicity windows.

4.3.1 Accumulator Mode

For the integration mode, there are six types of accumulators as listed below:

- All (Acc0): means to sum up all of the samples;
- Near (Acc1): integrates all pedestal samples, i.e. low-energy photons due to the synchrontron radiation, far behind the signal threshold;
- Window (Acc2): integrates all samples between the pedestal and signal threshold values;
- Far (Acc3): only sums up those samples, i.e. high-energy photons near the Compton edge from the bremsstrahlung radiation, far above the signal threshold;
- Stretched Window (Acc4=Acc1+Acc2-Acc3): only integrates those samples passing the signal threshold but exclude pedestals and those sample far above the signal threshold;

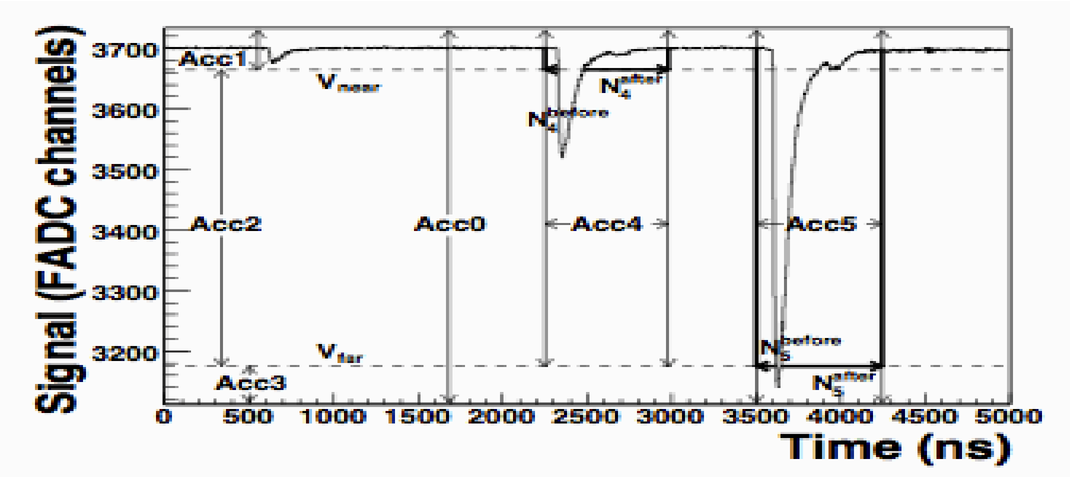

Figure 4.5: The six accumulator modes are explicitly drawn.

- Stretched Far (Acc5=Acc4+Acc3): is same as above but include those samples far beyond the signal threshold.

A variety of accumulator types can provide us more information to understand different background sources, so that a much cleaner analysis result can be achieved. PREx Compton photon analysis as described in the following section was accomplished with data collected by the integration mode FADC.

4.3.2 Trigger Mode

In order to study the background and pile-up effect, a sampled triggered mode is necessarily implemented to collect each individual pulse. For the triggered mode, the selected pulse's shape is continuously sampled by the FADC. The number of read-out samples must be limited during the short interval between T_{stop} and the next T_{start}, so that the read-out data won't be overwritten until the DAQ is finished storing them. In addition, the upper limit placed on the number of stored samples can help save more disk space.

Moreover, the GSO photon trigger is prescaled. A prescaled samples of the pulses firing the discriminator are sent to the latching scaler. The latching scaler counts and stores the clock ticks for the subsequent readout. During the read-out, a flexible (programmed by hand) sampling period, say, 500ns, is input from the FADC memory for each latched trigger time. Hence, the samples making up one pulse corresponding to one single trigger can then be summed numerically, and then only this sum is saved and written into the datastream.

4.4 Compton Photon Analysis

In this section, we will describe several ways used to calculate the Compton photon scattering asymmetry in details. In addition, a comparison of different methods is mandatory, because the discrepancy in the measured asymmetry can reflect a list of issues as followed:

- the electronic noises;
- the neutron background from the target;
- the bremsstrahlung radiation resulting in the big palse as a kind of fast background;
- the beam instability due to the temperature-related slow drifting;
- the laser instability.

As a result, in order to estimate the asymmetry and the associated statistical uncertainty appropriately, the laser-wise method prevails others. Before the asymmetry calculation, some basic data-quality selection criteria are listed below:

- The beam modulation system is off;
- No beam burp is found;

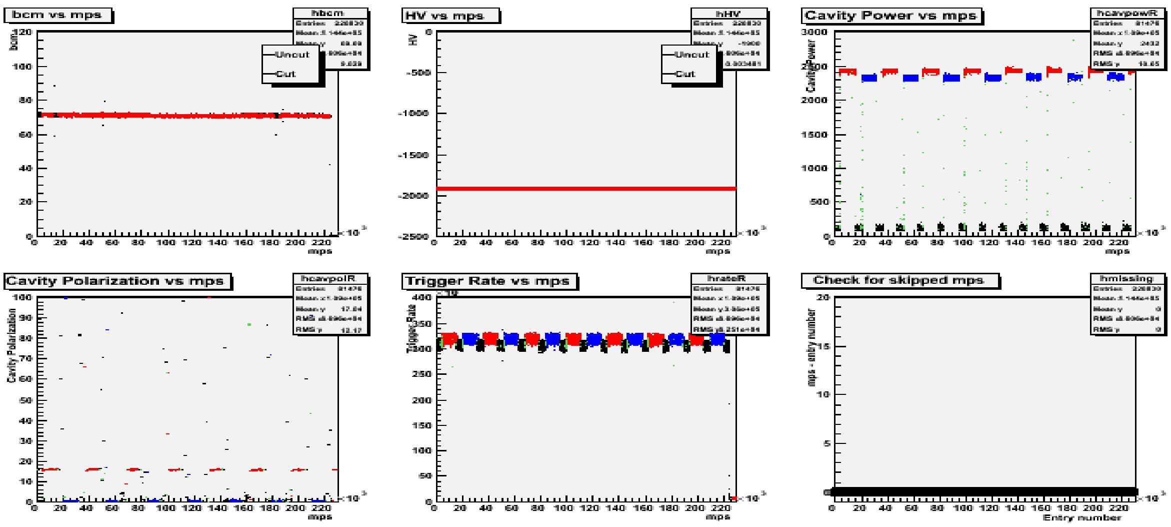

Figure 4.6: The quality of Compton data for one standard run. (Top left) beam current monitor vs. time; (top middle) the high voltage monitor vs. time; (top right) the photon laser's cavity power vs. time; (bottom left) the photon laser's cavity polarization vs. time; (bottom middle) the trigger rate vs. time; (bottom right) MPS signal check. The data quality information is sent out in the form of scalers for each helicity window. As a result, the selection criteria on a basis of window-to-window, say, each MPS signal interval, can be easily applied to data-analysis.

- No beam trip is seen during the run;
- No HV trip occures during the run;
- No rate fluctuation happens.

4.4.1 Formalism of Compton Scattering Asymmetry Calculation

In each laser cycle as shown in Fig. 4.4.1, there are a bunch of MPS pulsars. For each pair of MPS pulsars triggered by the opposite helicity electrons, the corrected asymmetry is:

$$\mathcal{A}_{cor} = \frac{\text{diff}_{\text{On}}}{\text{sum}_{\text{On}} - \text{bkg}_{\text{Off}}}, \tag{4.15}$$

for each pair(30Hz)/quartet(120Hz)/octet(240Hz) helicity pattern.

where $\mathrm{diff}_{\mathrm{On}}$ is the difference in the integration of photon signals between two helicity states, $\mathrm{sum}_{\mathrm{On}}$ is the total integration of signals with the subtraction of pedestal values, and $\mathrm{bkg}_{\mathrm{Off}}$ is the integration of background signals. The sub-scriptions of "On" and "Off" represent the cavity-locked and unlocked periods, respectively.

We have found the slight difference between $< \mathcal{A}_{cor} >$ and $\frac{1}{<\frac{1}{\mathcal{A}_{cor}}>}$. This discrepancy arises from the fluctuation of background. That is, the background is unstable with time. We assume that the noise level of background is ΔB ($\mathrm{B}_{\mathrm{meas.}}$-$\mathrm{B}_{\mathrm{true}}$). Then, we can express $\mathcal{A}_{cor}$ in terms of ΔB as below:

$$\mathcal{A}_{\mathrm{cor}} = \mathcal{A}_{\mathrm{raw}} \frac{T}{T - B_{\mathrm{true}}} \times (1 - \frac{\Delta B}{T - B_{\mathrm{true}}})^{-1}, \tag{4.16}$$

for each pair(30Hz)/quartet(120Hz)/octet(240Hz) helicity pattern.

For a bunch of pairs of Compton photon asymmetry measurements, the average of asymmetry can be taken in two ways. One is:

$$< \mathcal{A}_{\mathrm{cor}} > \;=\; < \mathcal{A}_{\mathrm{raw}} \frac{T}{T - B_{\mathrm{true}}} > \times < (1 - \frac{\Delta B}{T - B_{\mathrm{true}}})^{-1} >, \tag{4.17}$$

and the other is:

$$\frac{1}{< \frac{1}{\mathcal{A}_{\mathrm{cor}}} >} \;=\; \frac{1}{< \frac{1}{\mathcal{A}_{\mathrm{raw}} \frac{\mathrm{T}}{\mathrm{T\text{-}B}_{\mathrm{true}}}} >} \times \frac{1}{< \frac{1}{(1 - \frac{\Delta \mathrm{B}}{\mathrm{T\text{-}B}_{\mathrm{true}}})^{-1}} >}. \tag{4.18}$$

If ΔB is stable with time, $< \Delta B >$ will be the same as $\frac{1}{<\frac{1}{\Delta B}>}$. Therefore, by comparing $< \mathcal{A}_{\mathrm{cor}} >$ with $\frac{1}{<\frac{1}{\mathcal{A}_{\mathrm{cor}}}>}$, we can immediately realize how large the difference between $< \Delta B >$ and $\frac{1}{<\frac{1}{\Delta B}>}$. In other words, we also can judge whether or not the background fluctuation is significant based on the observation on this comparison. Next, three methods used to calculate the average of Compton photon asymmetry measurements will be introduced. The estimations of background size for separate methods are also different. We

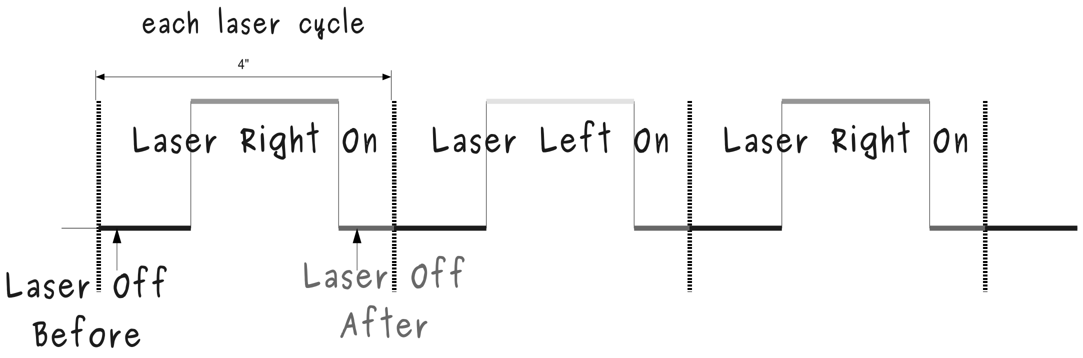

Figure 4.7: A schematic of Compton data-taking during a series of cavity-locked and -unlocked periods.

will discuss all of them and decide which method can yield the most accurate asymmetry average at a high precision level.

4.4.1.1 Lase-wise Methode

In the laser-wise method, one Compton photon scattering asymmetry in each laser cycle is obtained from averaging asymmetries over a selected number of good measurements during one cavity-locked period. The mean of local background from the cavity-unlocked period is determined based on three ways as listed in Equation 4.19.

$$\begin{aligned}
<\mathrm{B}^3_{\mathrm{off}}> &= \frac{\mathrm{N}^{\mathrm{before}}_{\mathrm{off}} \times \mathrm{BB}^{\mathrm{n}}_{\mathrm{off}} + \mathrm{N}^{\mathrm{after}}_{\mathrm{off}} \times \mathrm{BA}^{\mathrm{n}}_{\mathrm{off}}}{\mathrm{N}^{\mathrm{before}}_{\mathrm{off}} + \mathrm{N}^{\mathrm{after}}_{\mathrm{off}}}, \qquad (4.19)\\
<\mathrm{B}^1_{\mathrm{off}}> &= \frac{\mathrm{N}^{\mathrm{before}}_{\mathrm{off}} \times \mathrm{BB}^{\mathrm{n}}_{\mathrm{off}}}{\mathrm{N}^{\mathrm{before}}_{\mathrm{off}}},\\
<\mathrm{B}^2_{\mathrm{off}}> &= \frac{\mathrm{N}^{\mathrm{after}}_{\mathrm{off}} \times \mathrm{BA}^{\mathrm{n}}_{\mathrm{off}}}{\mathrm{N}^{\mathrm{after}}_{\mathrm{off}}},
\end{aligned}$$

where $\mathrm{N}^{\mathrm{before}}_{\mathrm{off}}$ is the total number of samples taken from the cavity-unlocked (laser-off) period just right before the incoming cavity-locked (laser-on) period, $\mathrm{N}^{\mathrm{after}}_{\mathrm{off}}$ is the total number of samples taken from the cavity-unlocked (laser-off) period following after the

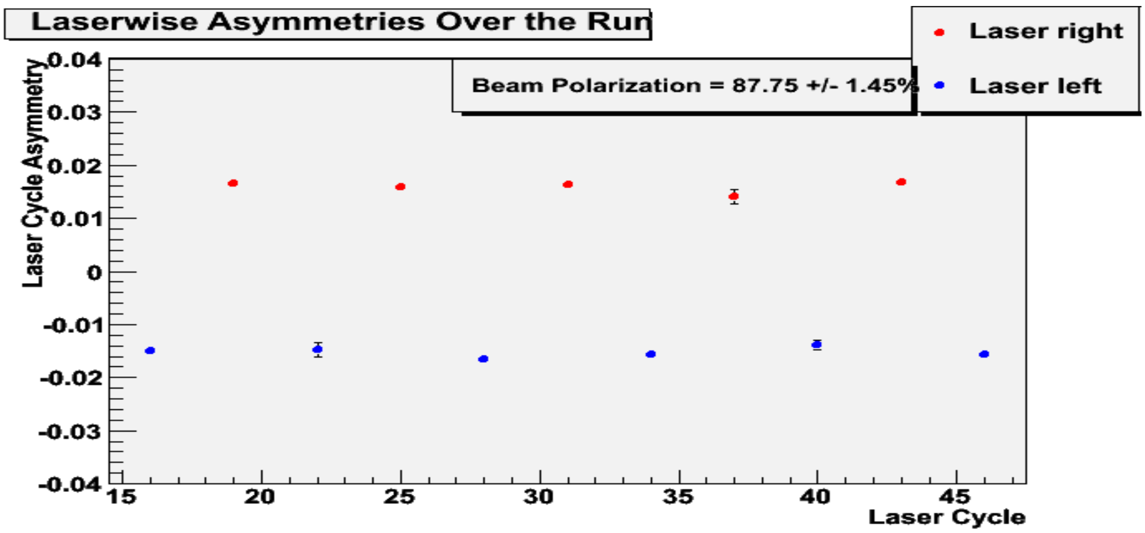

Figure 4.8: The mean of asymmetry measurement is determined in each laser cycle after the subtraction of local background as calculated in Equation 4.19 was made. The polarization state of the photon laser in each cycle is either right- (red) or left-hand (blue).

adjacent cavity-locked (laser-on) period, and $\text{BB}^{\text{n}}_{\text{off}}$ ($\text{BA}^{\text{n}}_{\text{off}}$) is the size of each background sample during the laser-off period just right before (after) the laser turning on. Each laser cycle contains two laser-unlocked periods which are adjacent to one laser-locked period at the same time. Generally speaking, bkg_{Off} as shown in Equation 4.15 is determined by $< \text{B}^3_{\text{off}} >$. Hence, the laser-wise asymmetry can be explicitly expressed in terms of $< \text{B}^3_{\text{off}} >$, diff_{On} and bkg_{Off} as below:

$$< \mathcal{A}_{\text{pair}} >_{\text{laser cycle}} = < \sum_i \frac{\text{diff}^i_{\text{On}}}{\text{sum}^i_{\text{On}} - < \text{B}^3_{\text{off}} >} >_{\text{laser cycle}} \tag{4.20}$$

i: for each pair(30Hz)/quartet(120Hz)/octet(240Hz) helicity pattern,

We have conducted an interesting study to investigate the pattern of the local background fluctuation. There are couples of useful ways to investigate what caused the background unstable:

(a) we compare the fractional error of $< \text{B}^1_{\text{off}} >$ (i.e. δ_{BB}) within different laser-off periods;

(b) we compare the fractional error of $< \mathrm{B}^2_{\mathrm{off}} >$ (i.e. δ_{BA}) within different laser-off periods;

(c) we subtract the total amount of $\mathrm{B}^1_{\mathrm{off}}$ from that of $\mathrm{B}^2_{\mathrm{off}}$ for each pair of laser-off periods, both of which are adjacent to "the same" laser-on period. then, we compare a handful of discrepancies in size between backgrounds in "before" and "after" within different laser-off periods;

(d) the first step is the same as (c);

  (1) we take the average of discrepancies over all of pairs of laser cycles for each Compton run;

  (2) the fractional error of the discrepancy in magnitude between $\mathrm{B}^1_{\mathrm{off}}$ and $\mathrm{B}^2_{\mathrm{off}}$ for each Compton run is obtained;

  (3) we compare (d)-(2) to (a), (b) and (c), respectively.

(e) the first step is the same as (c);

  (1) we take the average of discrepancies over all of pairs of laser cycles for each Compton run;

  (2) we divide the absolute error of this average discrepancy by the local mean signal taken from the laser-on period in each laser cycle; the run-average background difference relative to the local signal size in each laser cycle is thus obtained;

  (3) we average the relative ratios, run-avergae background over local mean signal, over all of the laser cycles in each Compton run.

Our investigations into different types of background behaviors corresponding to different time scales will be discussed in the next section.

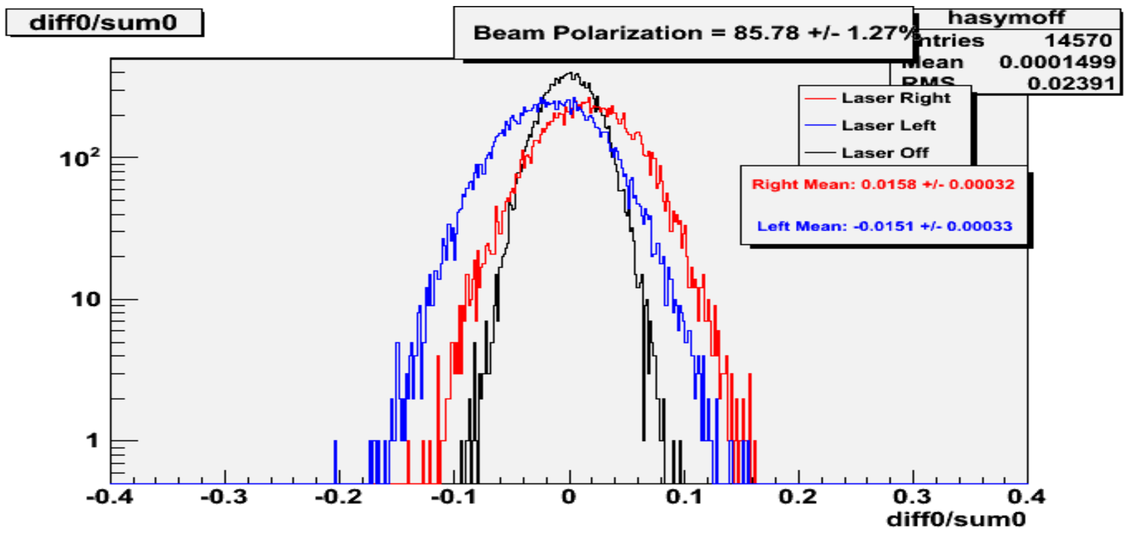

Figure 4.9: Background-subtracted Compton asymmetry "Gaussian" histograms comprising pairs of asymmetry measurements from all of the helicity windows in one single two hour long Compton run. The y-axis represents the total number of helicity pairs. The red (blue/dark) histogram represents the pair-wise asymmetry measurement for the photon polarization of laser-right (left/off).

4.4.1.2 Pair-wise Methode

The explicit form of the pair-wise asymmetry is:

$$< \mathcal{A}_{\text{pair}} >\text{run} = < \sum_i \frac{\text{diff}^i_{\text{On}}}{\text{sum}^i_{\text{On}} - < \sum_i \text{sum}^i_{\text{Off}} >\text{run}} >\text{run} \tag{4.21}$$

i: for each pair(30Hz)/quartet(120Hz)/octet(240Hz) helicity pattern,

The mean asymmetry for either laser-right or -left in Equation 4.21 is obtained based on the information of asymmetry histograms, such as weighted mean and RMS, as shown in Fig. 4.9 after the run-average background value taken from the laser-off period was subtracted from the total amount of accumulator signals integrated in the laser-on period.

We indeed find the discrepancy in the asymmetry magnitude between the laser- and pair-wise methods. We will show you the reasons and describe how to fix this difference in

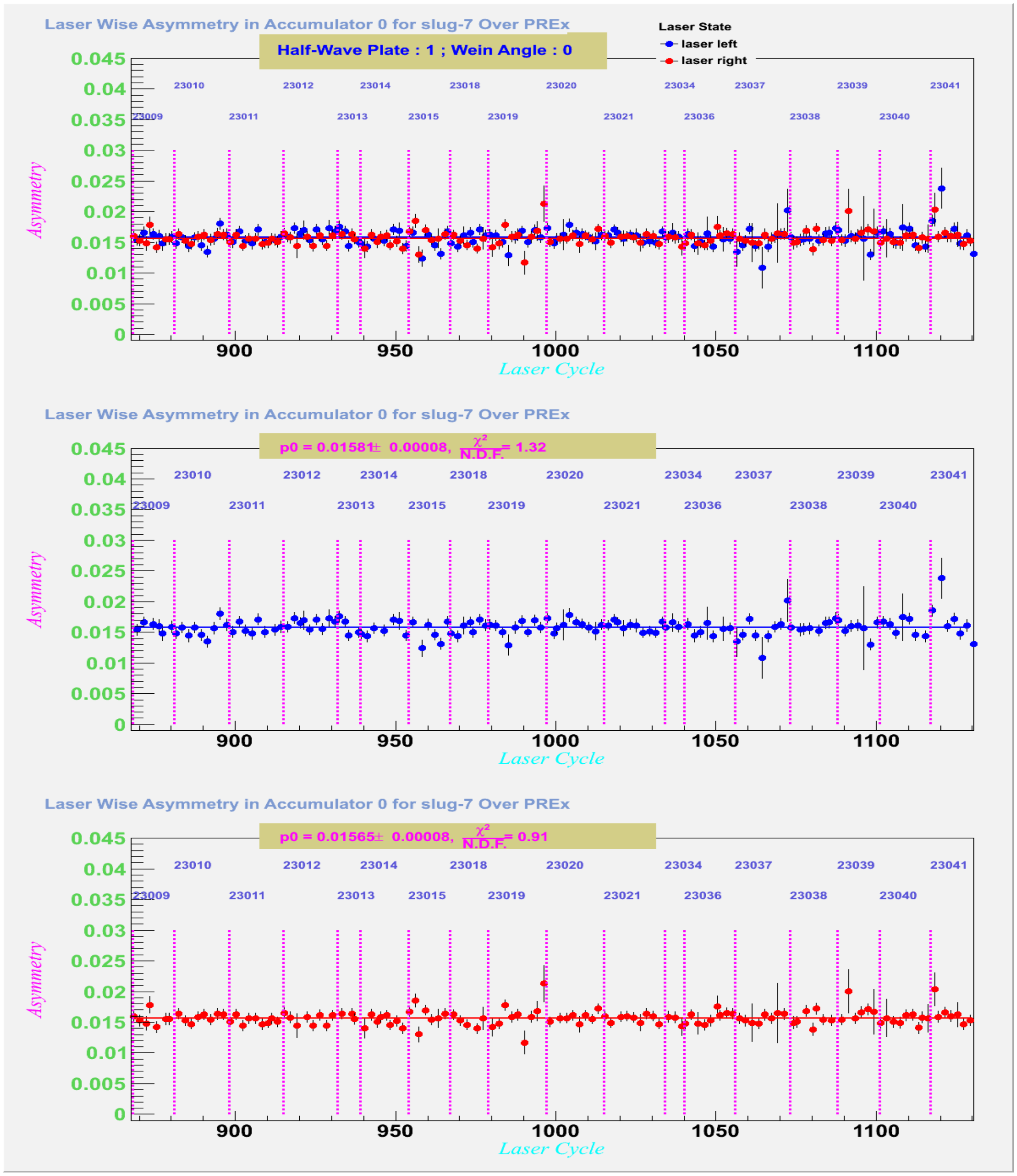

Figure 4.10: The local mean asymmetry (after the background subtraction) in each laser cycle is measured for either laser-right (red) or -left (blue) photon polarization state. This graph shows several local mean asymmetry measurements for a bunch of Compton runs with the same IHWP and Wein states. All of these Compton runs belong to ONE slug, where both IHWP and Wein states remain unchangeable until either IHWP or both IHWP and Wein flip their signs.

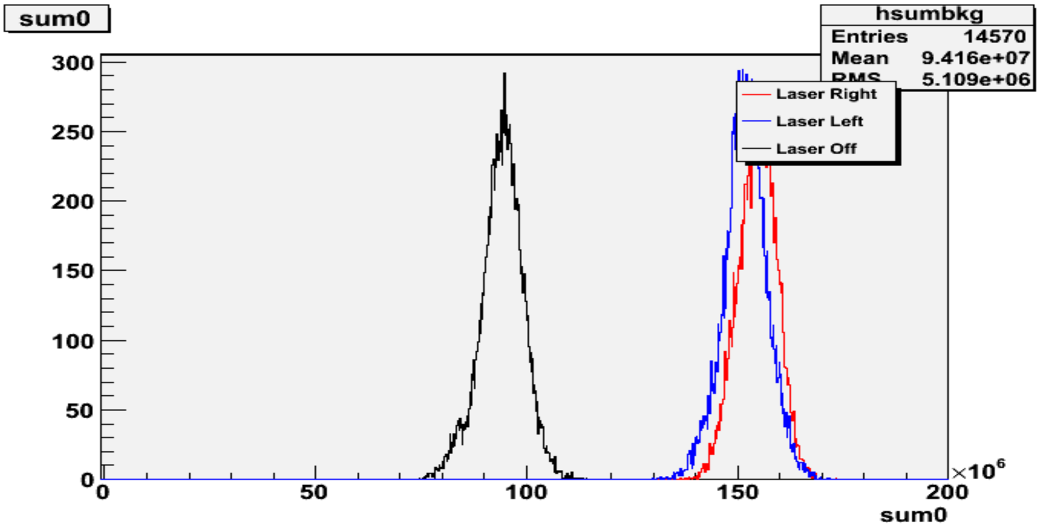

Figure 4.11: Histogram of the non-background subtracted numerator of the Compton asymmetry as shown in Equation 4.15.

order to make both results derived from two methods comparable to each other in the next section.

4.4.1.3 Run-wise Methode

The run-average asymmetry is obtained as below:

$$\mathcal{A}\text{run} = \frac{< \sum_i \text{diff}^i_{\text{On}} >\text{run}}{< \sum_i \text{sum}^i_{\text{On}} >\text{run} - < \sum_i \text{sum}^i_{\text{Off}} >\text{run}} \tag{4.22}$$

i: for each pair(30Hz)/quartet(120Hz)/octet(240Hz) helicity pattern,

, where the numerator and denominator terms as shown in Equation 4.15 are obtained by taking the means of histograms as drawn in Fig. 4.12 and Fig. 4.11, respectively, for both photon polarization states of laser-right (red) and -left (blue). The estimation of background size for the run-wise asymmetry calculation is the same as that for the pair-wise asymmetry calculation. A run-average background is obtained by averaging all of the background sizes over the entire background samples which were integrated during laser-off periods in each single run.

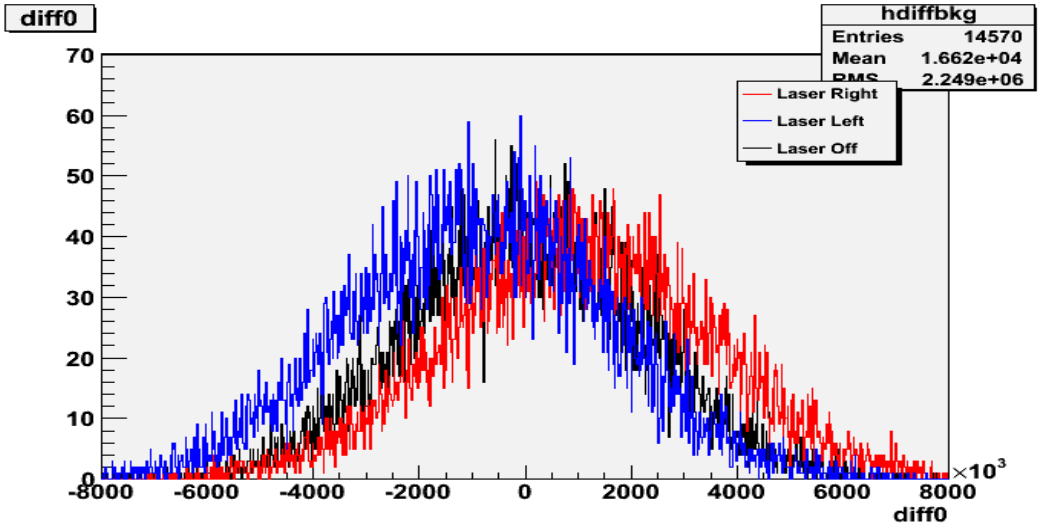

Figure 4.12: Histogram of the non-background subtracted denominator of the Compton asymmetry as shown in Equation 4.15.

4.4.2 Optimization of Selection Criteria

The cuts applied to the Compton data are as simple as possible. As mentioned earlier, the selection criteria are primarily pertinent to the data-quality, such as the stability of beam, cavity power and trigger rate, so they are the same for different asymmetry calculations. More importantly, in addtion to these data-quality cuts, the additional selection criteria used to remove the noisier runs are supposed to be unbiased for three separate asymmetry calculation methods, corresponding to different time scales and data statistics.

4.4.2.1 Cut Issues

Below include a iist of issues about how we decided the cuts and their criteria. We will discuss each of them in details.

4.4.2.1.1 Insufficient Statistics

We got rid of the low-statistics laser cycles, where the calculated laser-wise asymmetry entries is fewer than 10 for each laser-on period.

4.4.2.1.2 Lack of Laser State

In some of Compton runs, the presence of the photon laser state during the laser-on periods was found to be only either right-circular polarization or left as a result of the cut used to remove the low statistics laser cycles. Hence, the non-zero laser-wise asymmetry calculation is merely valid for one of the laser polarization states due to the lake of data with the other polarization state. Furthermore, we cannot compare the calculated laser-wise asymmetry result to those obtained by using the pair- and run-wise methods. In pair-wise method, we did not need to apply the low-statistics cut to those laser cycles with a small number of laser-wise asymmetry measurements fewer than 10.

4.4.2.1.3 Bad MPS

Since the PREx helicity frequency is higher than we had for HAPPEX-III and 6 GeV PVDIS by a factor of 4 and 8, respectively, the cut applied to the length of dead MPS for the accumulator raw data is supposed to be shorter. Otherwise, an inappropriate dead MPS length cut cannot remove the unstable data properly, so that the higher instability of the calculated asymmetry occured and thus led to the wrong asymmetry measurement.

Both Fig. 4.13 and Fig. 4.15 indicated that the inappropriate choice of the dead MPS length cannot effectively get rid of the noisier data. After re-adjusting the dead MPS length, this situation was improved in some runs but still remained unchangeable in the rest of problematic runs. For instance, in Fig. 4.14, the first cycle was cut after re-adjusting the dead MPS length, whereas the second cycle with noisier data still survived without

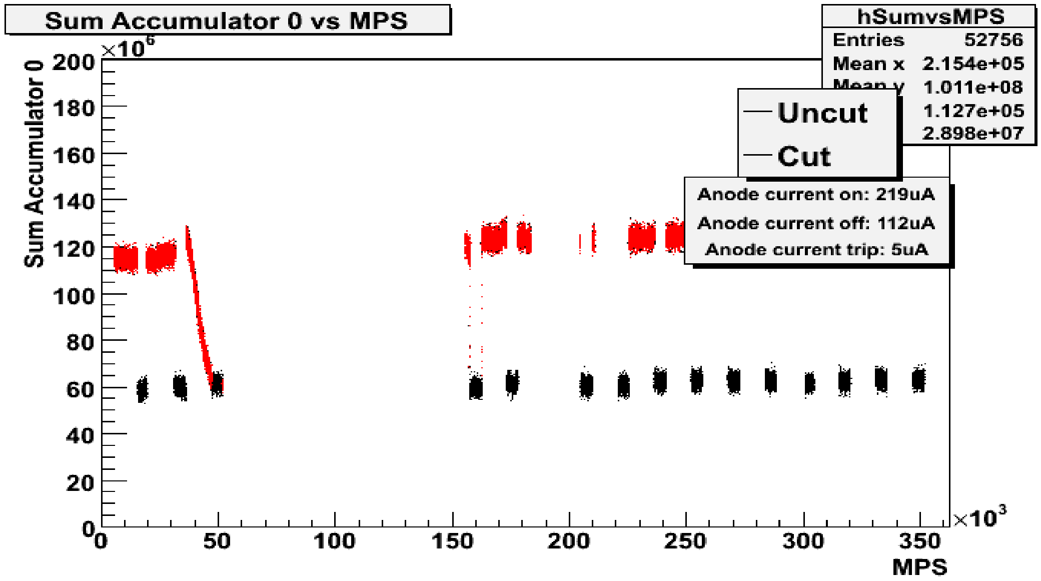

Figure 4.13: Integration of accumulator data in laser-on (red-dotted) and -off (black-dotted) periods vs. MPS helicity window for Compton run 23129.

being removed. On the other hand, another Fig. 4.16 showed that both the first and eighth cycles with more instable data than the rest of cycles were successfully disappeared at the same time due to the appropriate cut applied to them.

In sum, based on Fig. 4.17, we can compare the mean laser-wise asymmetry measurements obtained before re-adjusting the dead MPS length to those followed by fixing the dead MPS length. This graph also demonstrated how much the dead MPS length cut can change the asymmetry result as well as how effective this cut can fix the problem, and furthermore, improve the asymmetry, accordingly.

4.4.2.1.4 Fluctuations of Signal and Background

The signal fluctuation is defined as:

$$\delta_{\text{sig.}} = \frac{\sigma_{\text{T-B}}}{<\text{T}> - <\text{B}> \sqrt{N_{\text{T-B}}}} \tag{4.23}$$

for each Compton run in all of the laser-on periods.

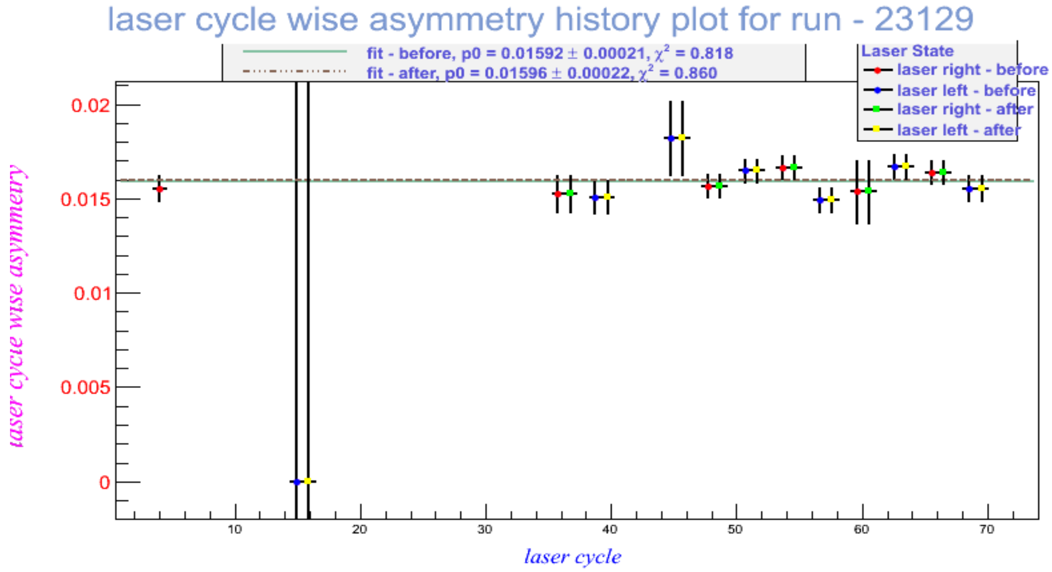

Figure 4.14: Asymmetry vs. laser cycle for Compton run 23129. Red (blue): Laser-right (left) **before** fixing the MPS length; green (yellow): Laser-right (left) **after** fixing the MPS length.

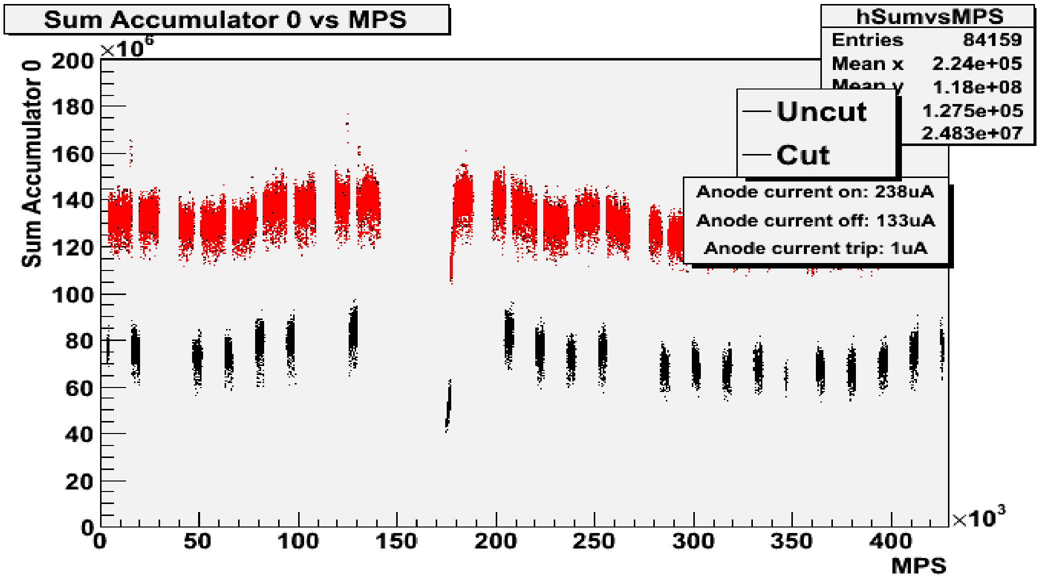

Figure 4.15: Integration of accumulator data in laser-on (red-dotted) and -off (black-dotted) periods vs. MPS helicity window for Compton run 22975.

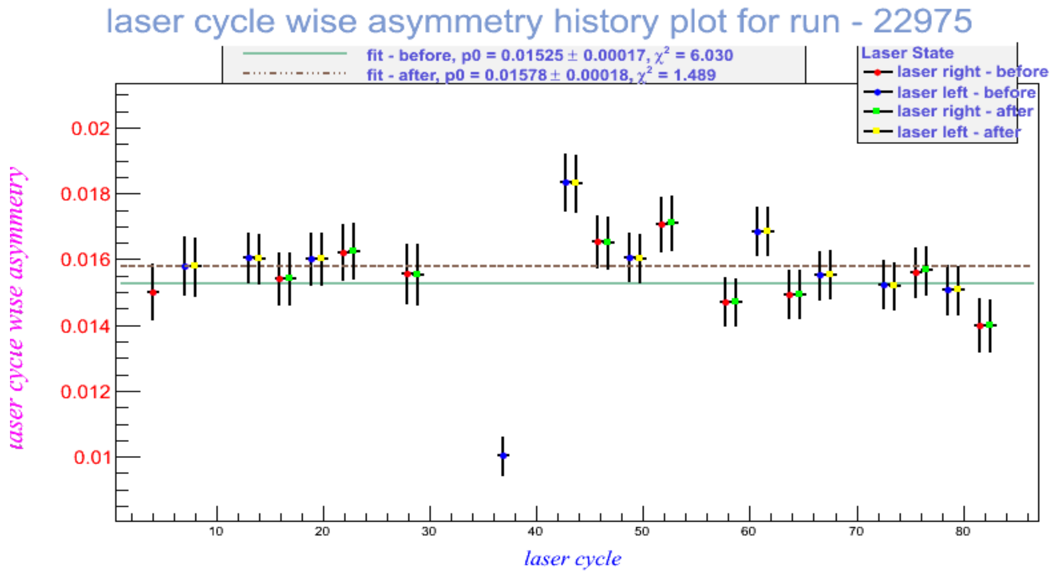

Figure 4.16: Asymmetry vs. laser cycle for Compton run 22975. Red (blue): Laser-right (left) **before** fixing the MPS length; green (yellow): Laser-right (left) **after** fixing the MPS length.

s We applied $\delta_{\text{sig.}} < 10\%$ cut to data. Besides, in order to further investigate the stability of the background offset in each laser cycle, we took the difference in the mean between both the local laser-off backgrounds which are adjacent to the same laser-on period in "before" and "after", respectively. Here, the cases of the missing "after" background found in few of laser cycles for each Compton run occurred rarely and randomly. In principle, it happened due to applying data-quality cuts, so part of laser cycles, containing unsatisfied data, was removed. Therefore, except for this exceptional case mentioned above, the background fluctuation relative to the signal level for each laser cycle can be expressed in terms of the definition below:

$$\mathcal{R} =< \frac{\sigma_{\text{BA--BB}}}{< \text{T} >_{local} - < \text{B} >_{local}} > \tag{4.24}$$

for each Compton run in all of the laser-off periods.

Through making different cut values on $\delta_{\text{sig.}}$, we would like to know the variation in the quantity of $\mathcal{R}$. Consequently, the $\mathcal{R}$ distribution with respect to $\delta_{\text{sig.}}$ can tell us whether or

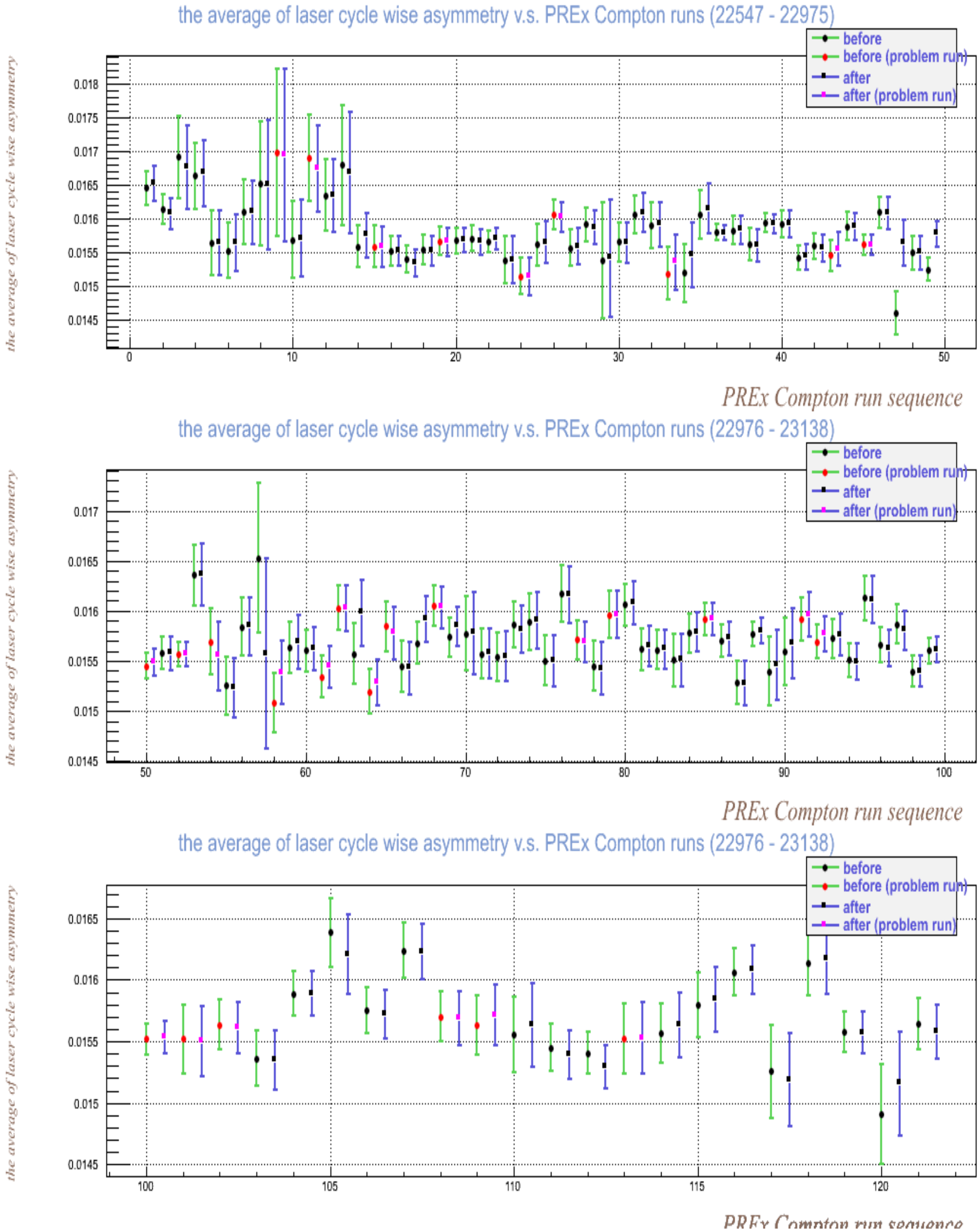

Figure 4.17: Mean laser-wise asymmetry vs. Compton run. Black dot w/ green (purple) error bar represents the normal runs before (after) fixing the MPS length. Red (magenta) dot w/ green (purple) error bar represents the problematic runs before (after) fixing the MPS length.

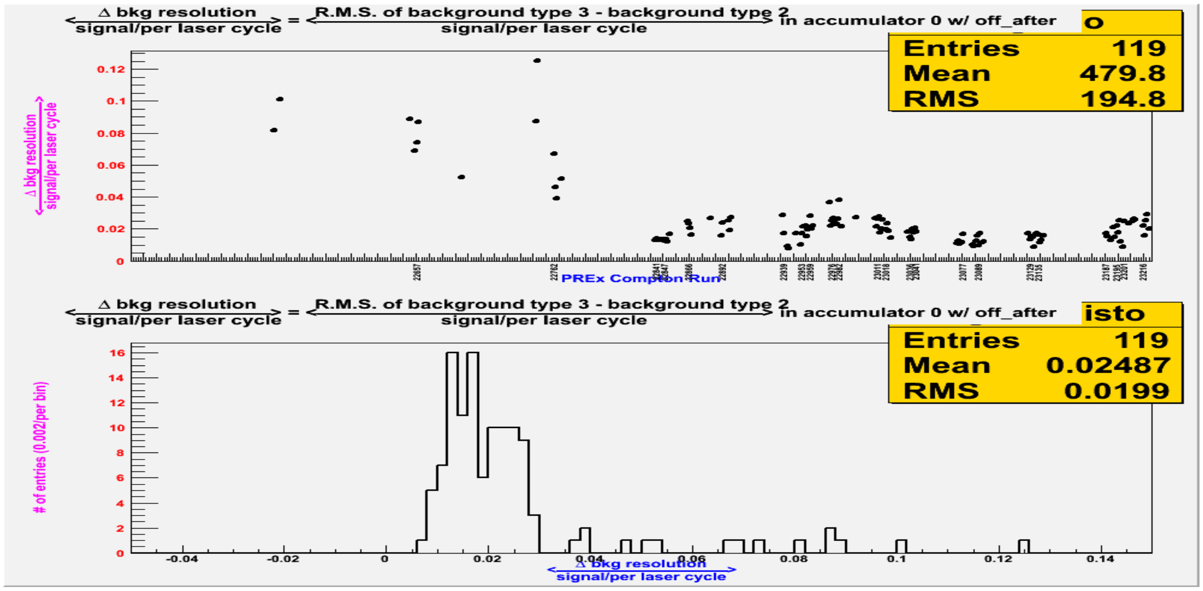

Figure 4.18: (Top panel) $\mathcal{R}$ vs. Compton run. (Bottom panel) $\mathcal{R}$ histogram.

not the noise sources cause not only the signal but the background more instable. Table 4.1 proves that the noise sources are uncorrelated with the photon laser's polarization states, and meanwhile, also blind (neutral) to both the laser-on and -off periods.

Table 4.1: Relation between $\delta_{\text{sig.}}$ and $\mathcal{R}$.

$\delta_{\text{sig.}}$	$\mathcal{R}$	$\sigma_{\mathcal{R}}$
$< 10\%$	0.02487	0.0199
$< 15\%$	0.02723	0.0241
$< 20\%$	0.03854	0.0542
$< 25\%$	0.04645	0.0664
$< 30\%$	0.04777	0.0669
$< 35\%$	0.0518	0.0716
0% (no cut)	0.1005	0.1513
$> 10\%$	0.2016	0.1887

4.4.2.1.5 Background Asymmetry

In contrast to the Compton photon scattering asymmetry, the background asymmetry is defined as:

$$\mathcal{A}_{bkg} = \frac{\text{diff}_{\text{Off}}}{\text{sum}_{\text{Off}}} \quad \text{for each helicity pair.} \tag{4.25}$$

Likewise, through making different cut values on $\delta_{\text{sig.}}$, the change in $\mathcal{A}_{bkg}$ with respect to different cuts of $\delta_{\text{sig.}}$ can tell us whether or not the background contributes to the measured Compton photon scattering asymmetry. According to Table 4.2, the background clearly did not yield any false asymmetry in the Compton signal asymmetry measurement. The "pull" is defined as:

Table 4.2: Relation between $\delta_{\text{sig.}}$ and $\mathcal{A}_{bkg}$.

$\delta_{\text{sig.}}$	$\mathcal{A}_{bkg}$	χ^2	pull of $\mathcal{A}_{bkg}$	pull of $\sigma_{\mathcal{A}_{bkg}}$	pull of χ^2
$< 10\%$	$-1.37 \times 10^{-5} \pm 1.76 \times 10^{-5}$	1.16	0.089 ± 0.107	1.008 ± 0.113	0.96
$< 15\%$	$-2.14 \times 10^{-5} \pm 1.57 \times 10^{-5}$	1.54	0.219 ± 0.091	1.047 ± 0.092	0.96
$< 20\%$	$-2.25 \times 10^{-5} \pm 1.53 \times 10^{-5}$	1.55	0.191 ± 0.095	1.134 ± 0.111	0.82
$< 25\%$	$-1.87 \times 10^{-5} \pm 1.51 \times 10^{-5}$	1.53	0.121 ± 0.092	1.113 ± 0.103	0.94
$< 30\%$	$-6.61 \times 10^{-6} \pm 1.48 \times 10^{-5}$	1.58	0.143 ± 0.097	1.183 ± 0.093	0.92
$< 35\%$	$-5.97 \times 10^{-6} \pm 1.48 \times 10^{-5}$	1.56	0.162 ± 0.096	1.167 ± 0.094	1.06
0% (no cut)	$-1.65 \times 10^{-5} \pm 1.40 \times 10^{-5}$	1.67	0.118 ± 0.093	1.175 ± 0.092	1.06
$> 10\%$	$6.73 \times 10^{-5} \pm 2.26 \times 10^{-5}$	2.20	0.375 ± 0.180	1.29 ± 0.30	1.28

$$\text{pull of}\,\mathcal{A}_{bkg} = \frac{x_i - \bar{x}}{\sigma_{x_i}} \quad \text{for each Compton run.} \tag{4.26}$$

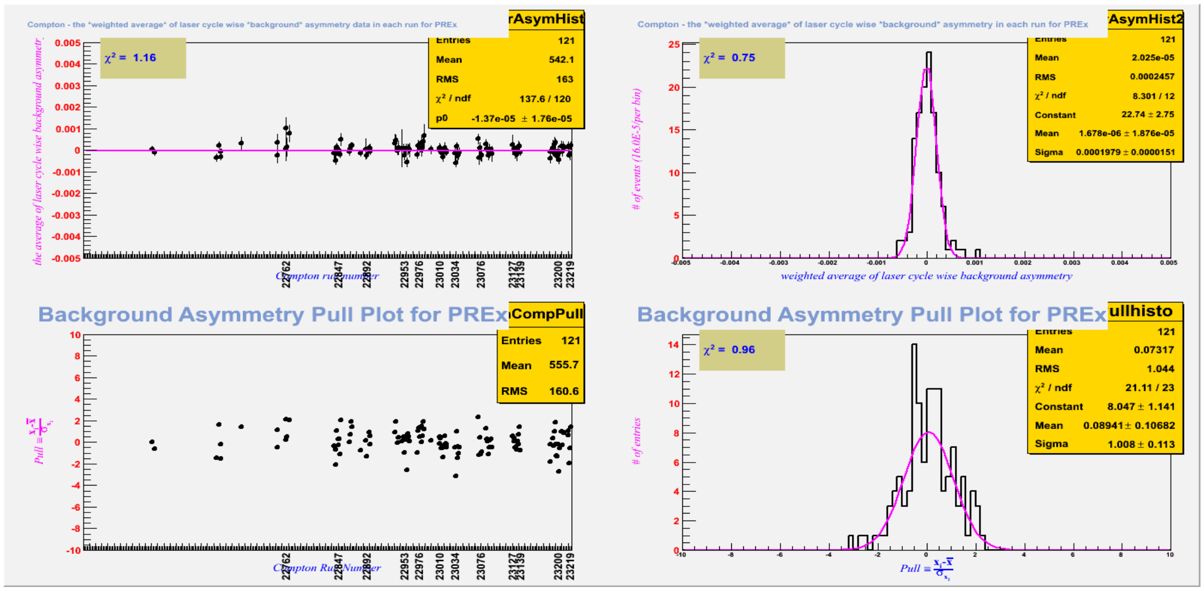

Figure 4.19: (Top panel-left) $\mathcal{A}_{bkg}$ vs. Compton run. (Top panel-right) $\mathcal{A}_{bkg}$ histogram. (Bottom panel-left) pull of $\mathcal{A}_{bkg}$ vs. Compton run. (Bottom panel-right) pull of $\mathcal{A}_{bkg}$ histogram.

4.4.3 Background Fluctuation

In order to understand the behavior of background, we study the fluctuation (variation) of background per laser cycle. That is, we chopped the whole background for each Compton run into several pieces and then looked at the variance between two adjacent backgrounds in each laser cycle. Then, we averaged all of the differences over the total number of laser cycles in each run. According to Fig. 4.20, it shows that the "after" background is higher than the "before" one in each pair of "before" and "after" backgrounds adjacent to the same laser-on period. Hence, we can depict the background patter in the way as shown in Fig. 4.22.

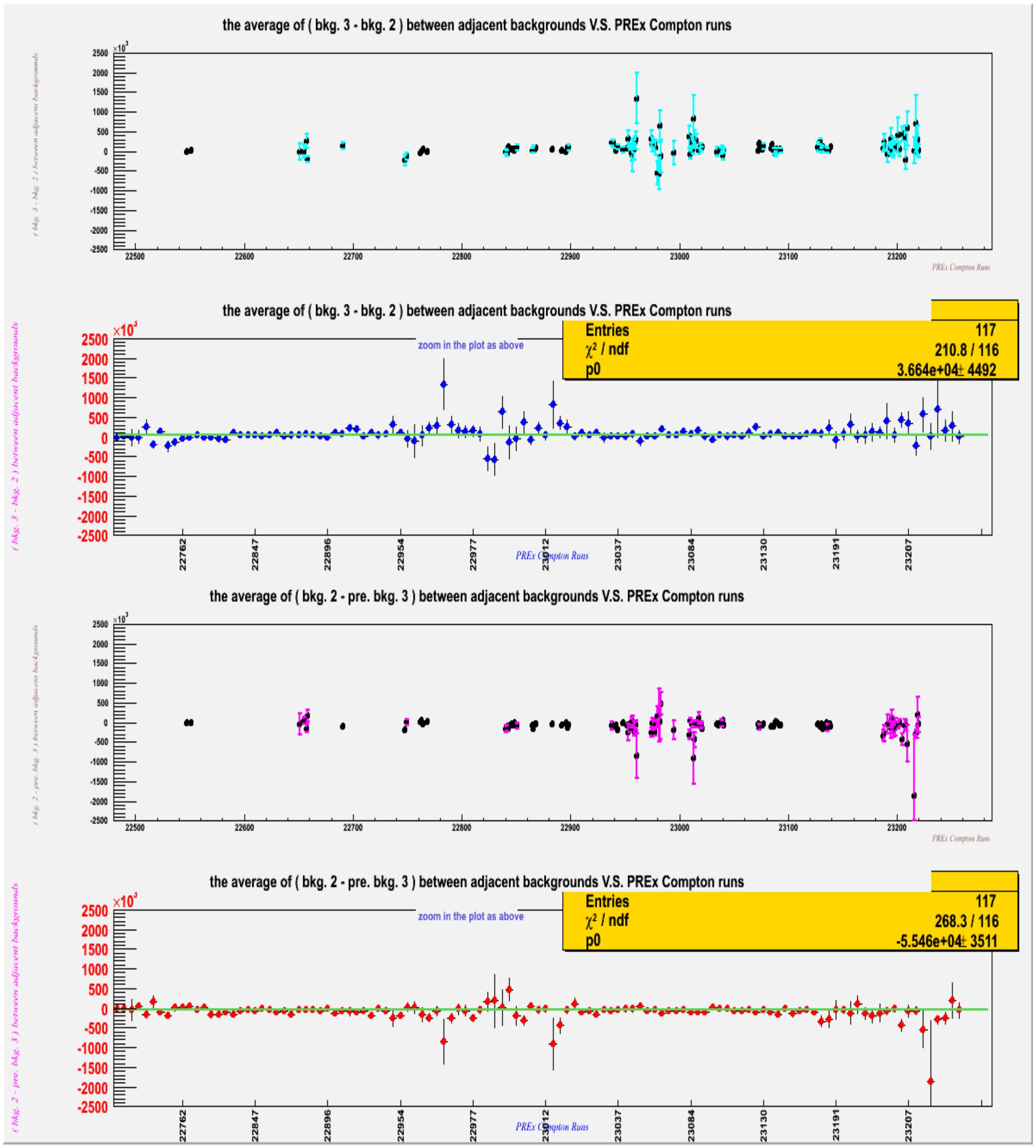

Figure 4.20: This graph represents the average of adjacent background differences over all of the laser cycles for each Compton run. The unit of the x-axis is each individul Compton run. (Top pannel) The subtraction of "before" background from "after". (Second pannel) Zoom in the top pannel. (Third pannel) The subtraction of "after" background from "before". (Bottom pannel) Zoom in the third pannel.

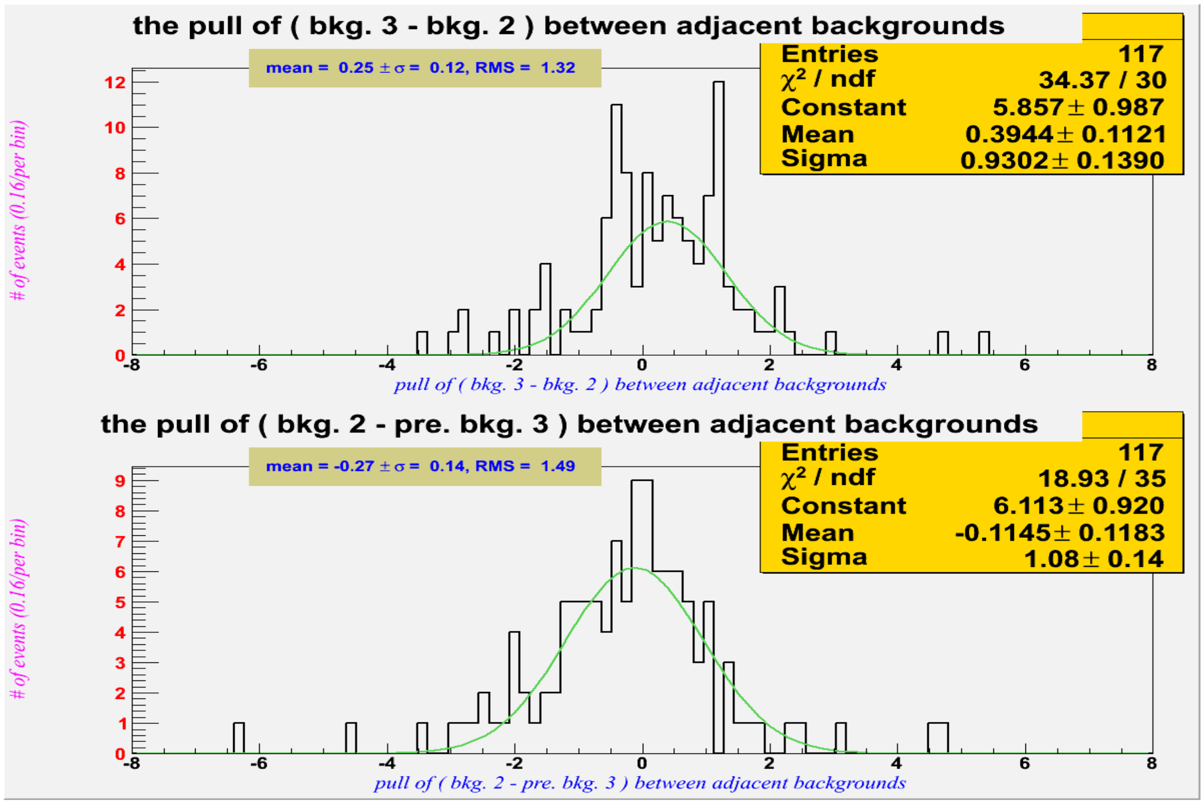

Figure 4.21: The pull plots for the background study in Fig. 4.20.

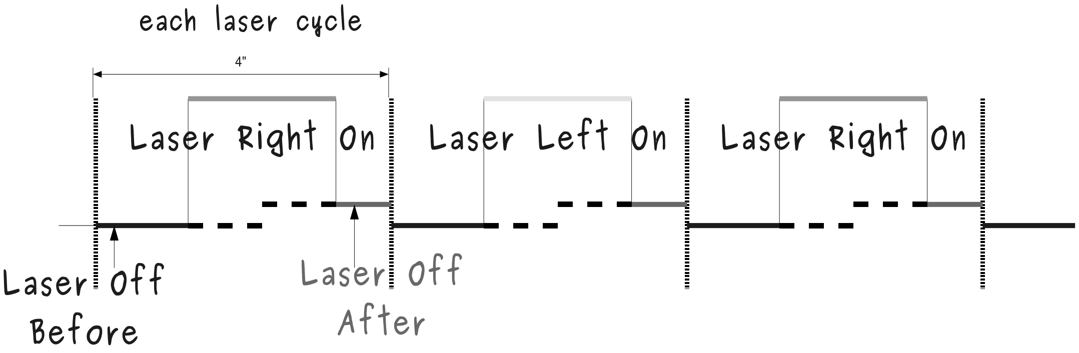

each laser cycle
4"
Laser Right On
Laser Left On
Laser Right On
Laser Off
Before
Laser Off
After

Figure 4.22: The possible background pattern.

4.4.4 Comparison of Asymmetry Measurements Derived from Different Methods

There are a list of reasons giving rise to the discrepancy in asymmetry between laser- and pair-wise methods. We will describe each of them in this section.

4.4.4.1 Lack of Laser State

While the data associated with one of the photon laser's polarization state were all removed due to the low statistics, we cannot calculate the Compton photon scattering asymmetry for this laser polarization using the laser-wise method. As a result, we are not able to compare the calculated laser-wise asymmetry result to the pair-wise's. In addition, if the low-statistics laser cycles are not neglected, the local mean laser-wise asymmetry will not be comparable to that derived from the pair-wise asymmetry for each laser cycle. Based on our careful study [49], while taking the local mean asymmetry for each laser cycle using the pair-wise method in Equation 4.27, we found the discrepancy in $< \mathcal{A}_{\text{pair}} >_{\text{laser cycle}}$ between the laser-wise and pair-wise methods is significant for each laser cycle with the low statistics. That's why the low-statistics laser cycles were needed to be removed, for both the pair-wise and laser-wise methods yield the inaccurate calculated asymmetry for the low-statistics data. Fig. 4.23 indicates the abnormal $< \sum_i \text{diff}^i_{\text{On}} >$ values in the numerator of Equation 4.20 for the low-statistics laser cycles.

$$< \mathcal{A}_{\text{pair}} >_{\text{laser cycle}} = < \sum_i \frac{\text{diff}^i_{\text{On}}}{\text{sum}^i_{\text{On}} - < \sum_i \text{sum}^i_{\text{Off}} >_{\text{run}}} >_{\text{laser cycle}} \tag{4.27}$$

i: for each pair(30Hz)/quartet(120Hz)/octet(240Hz) helicity pattern,

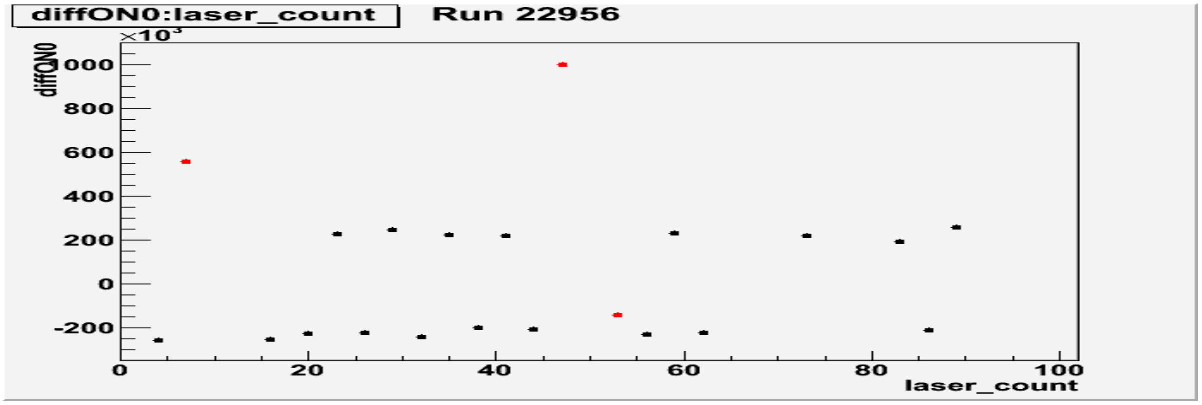

Figure 4.23: $< \sum_i \mathrm{diff}^i_{\mathrm{On}} >$ vs. laser cycle for Compton run 22956. Red dots are those low-statistics cycles which were cut from data.

4.4.4.2 High and Unstable Background over a run

In some runs, $< \sum_i \mathrm{sum}^i_{\mathrm{Off}} >$run> was found to be much higher than $\mathrm{sum}^i_{\mathrm{On}}$. As a consequence, for the pair-wise method, the background distribution becomes non-gaussian. Moreover, the corresponding signal distribution such as $\mathrm{diff}^i_{\mathrm{On}}$ in either laser-right or -left is also non-gaussian. Therefore, the pair-wise method cannot yield the correct mean asymmetry and the associated statistical uncertainty as well.

4.5 GEANT4 Simulation for Compton Polarimeter

In order to go closer to the real situation, pile-up events from real data are needed to be added into the simulated "pure" signals (photons are collected in the photon detector, and their energies are deposited in the PMTs). Therefore, we need to look at the pulse shape from the trigger data as shown in Fig. 4.26. The trigger window for Compton signals is within 30-40. The threshold, around 2384, is very low. Hence, even a small pulse can trigger a signal, but the pedestal value is 2390.75. It means only the pulse above the pedestal can be regarded as Compton signals. For each MPS, it includes 45 pulses. Only pulses which are above the pedestal (pedestal subtraction) are integrated in each MPS

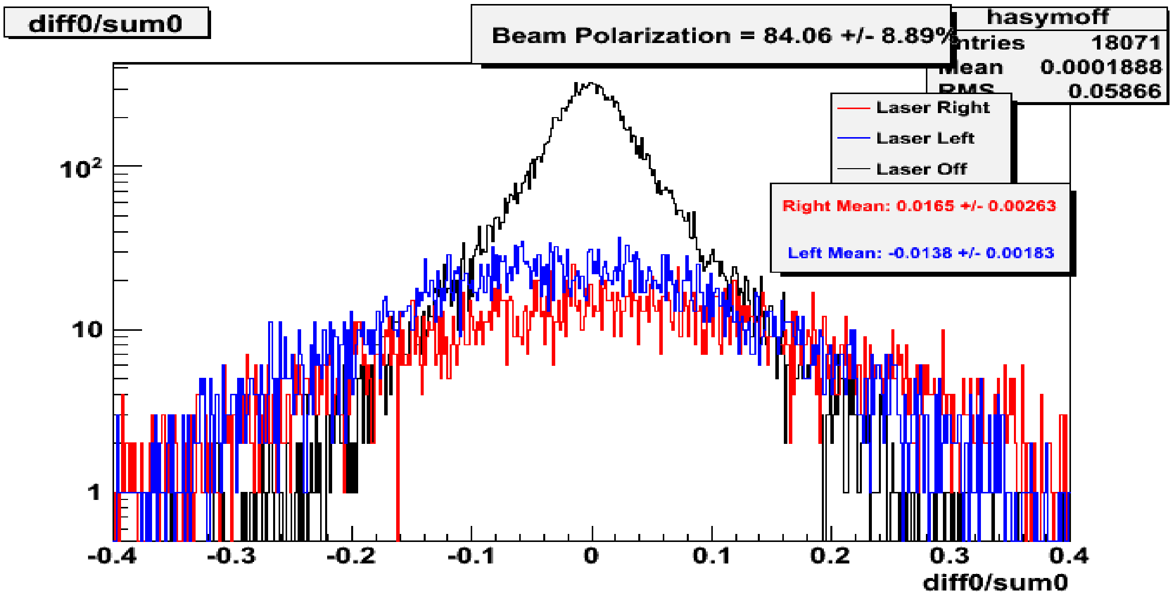

Figure 4.24: Background-subtracted Compton asymmetry ”non-Gaussian” histograms from the pair-wise method for Compton run 22597.

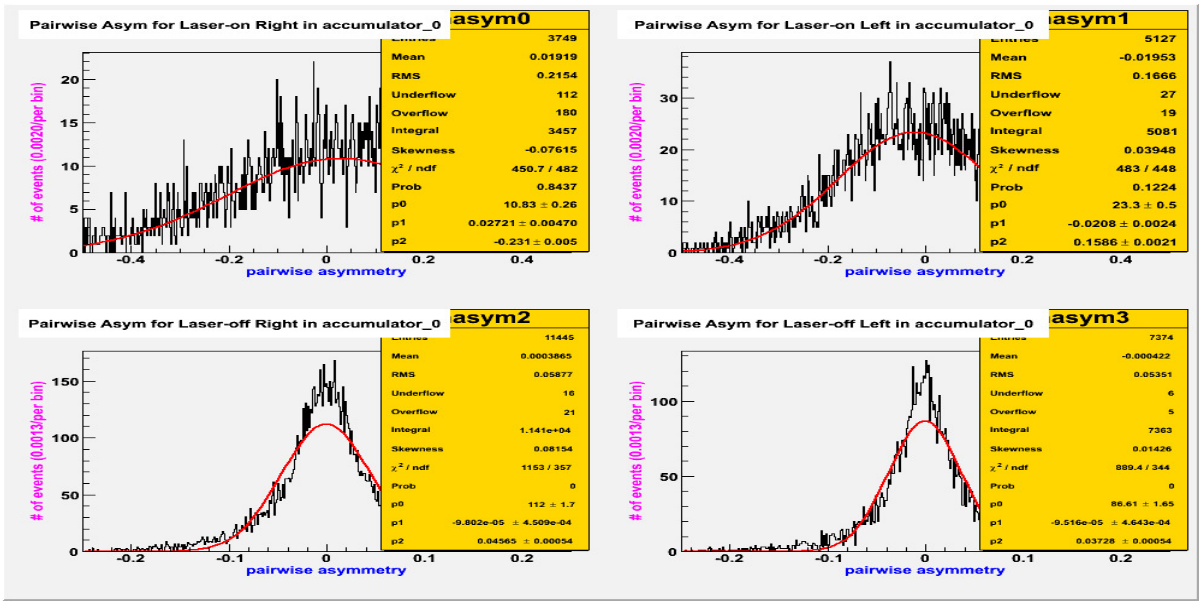

Figure 4.25: (Upper left) the pair-wise asymmetry in laser-right; (upper right) the pair-wise asymmetry in laser-left; (lower left) the pair-wise background asymmetry followed by the laser-on right period; (lower left) the pair-wise background asymmetry followed by the laser-on left period.

trigger window. Equivalently, the integration of all of the pulses is just the total amount of photon energies deposited in the PMT. That's how we obtain the Compton spectrum as shown in Fig. 4.28 and Fig. 4.29.

In addition, the background can be well-studied, based on the laser-off data. The pure background is above the Compton signal part as well as inside the pile-up events, say, from 46000 to 60000. The factor used to scale the laser-off spectrum inside the Compton signal region is thus obtained. Based on Equation 4.13, the PMT signals are weighted with the simulated theory asymmetry. In order to extract the photon polarization, first of all, we need to average the asymmetries which are weighted with the integration of ADC values bin-by-bin based on the energy spectrum of real data. Another scale factor is needed to obtain the truly measured asymmetry according to the fit of the energy sectrum in data to that generated by MC (GEANT4), while the "raw" asymmetry is extracted from deposited energies in real data after the pedestal subtraction for both laser-on and laser-off spectra. Thereafter, we integrate weighted asymmetries over all of the bins, and then divide it by the integration of ADC values, i.e. the total energy. We are thus able to see the raw asymmetry versus the total deposited energies in real data as shown in Fig. 4.30. Then, the photon polarization is as a result of the division of this asymmetry value to the cavity polarization.

4.6 Electron Polarization Result for PRExI via Compton Polarimeter

We have gone through the procedure used to extract the electron beam polarization in such a great deal of details. Now, we need to do a bit of error analysis. The associated statistical error with the measured Compton scattering photon asymmetry is assigned by dividing the RMS width of each sum, difference, and background distribution for either the

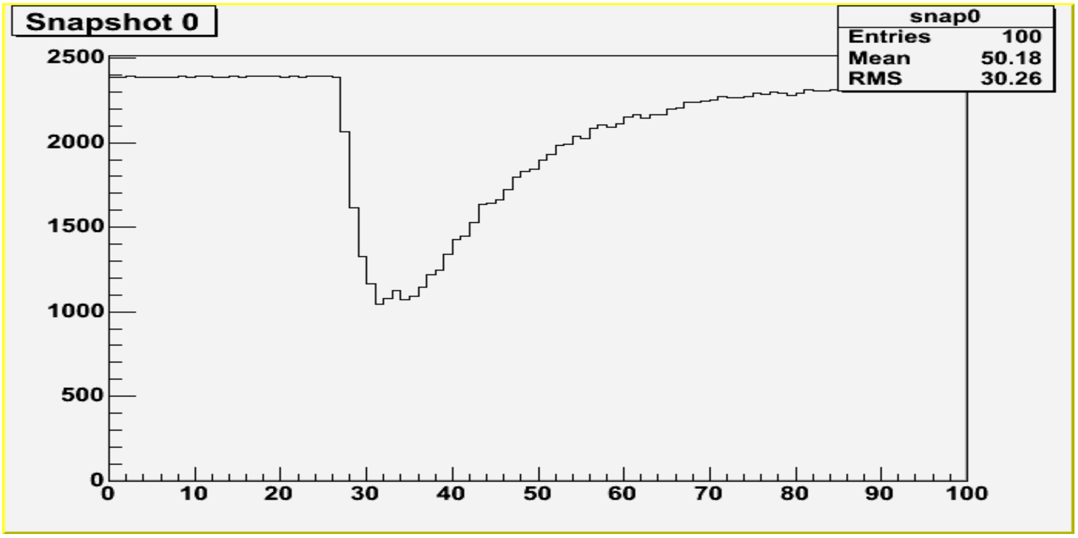

Figure 4.26: A typical waveform from the GSO calorimeter for incident photons from the Compton scattering. The x-axis is time (ns). The y-axis is summed FADC channels. The standard trigger mode reads Compton photon signals from the first three helicity windows, and then only reads out the random samples in the forth helicity window. This way can help save more disk space.

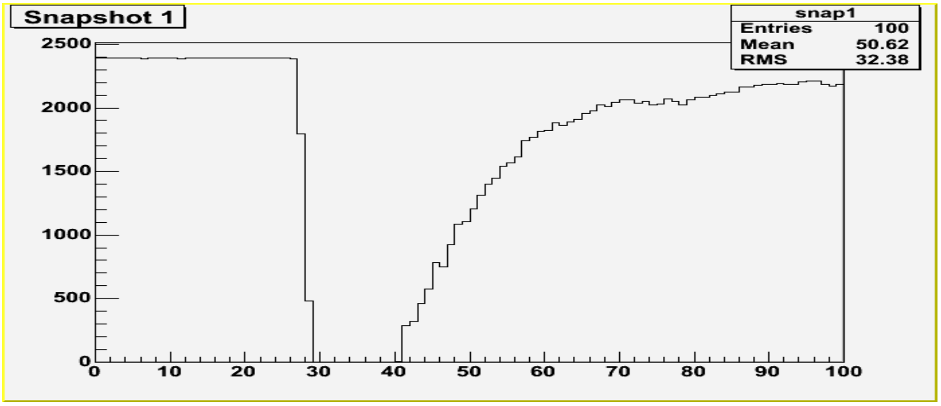

Figure 4.27: A waveform with higher deposited photon energies in the calorimeter. The sample can be used to study the background as well as the pile-up effect.

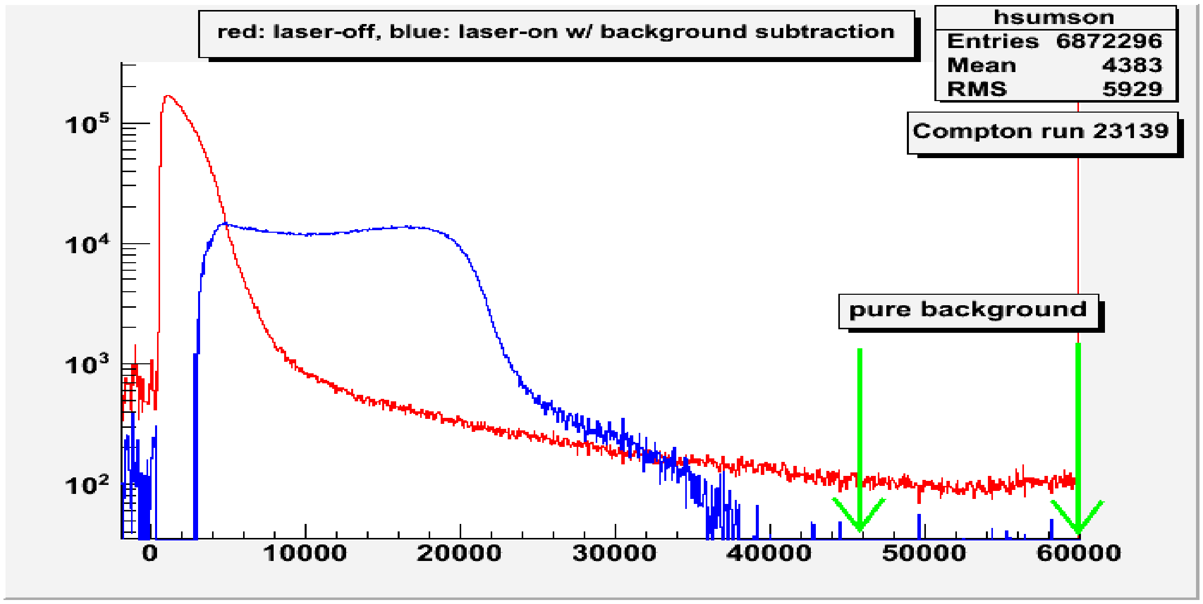

Figure 4.28: Logarithmic Compton photon energy spectrum integrated from the GSO photon detector during a typical run. The red curve shows the background spectrum during the laser-off periods. The blue curve gives the background-subtracted spectrum during the laser-on periods. The region indicated by arrows contains the background-only spectrum, and is used to normalize the rest of regions, where both signal and background spectra are overlapped to each other.

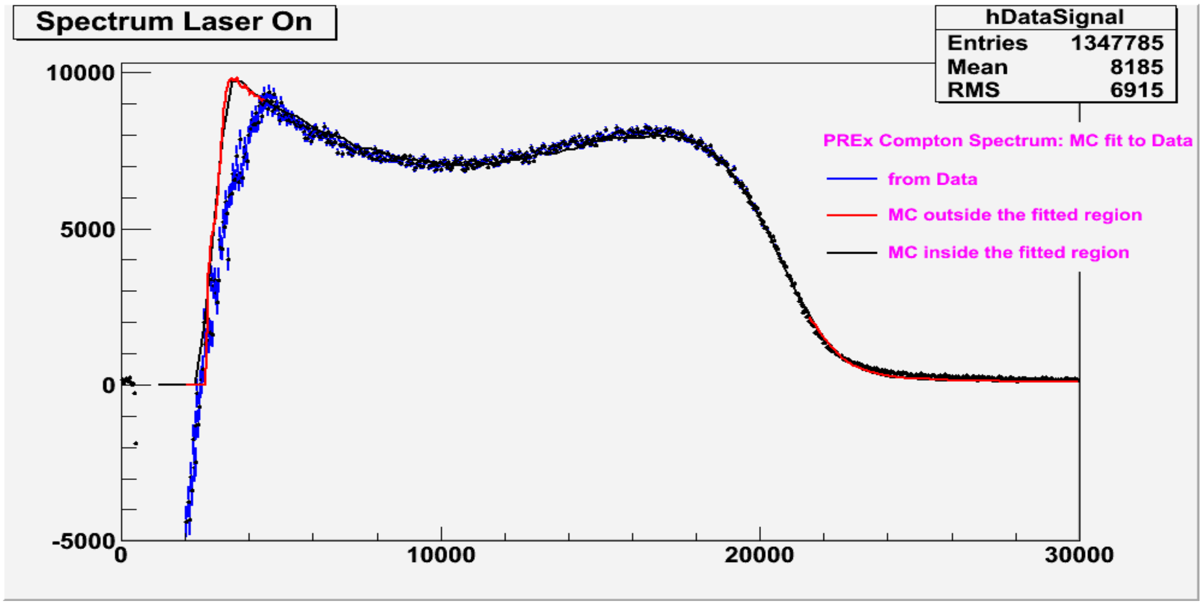

Figure 4.29: MC fit to the measured Compton photon energy spectrum, where the data were taken from FADC with the trigger mode.

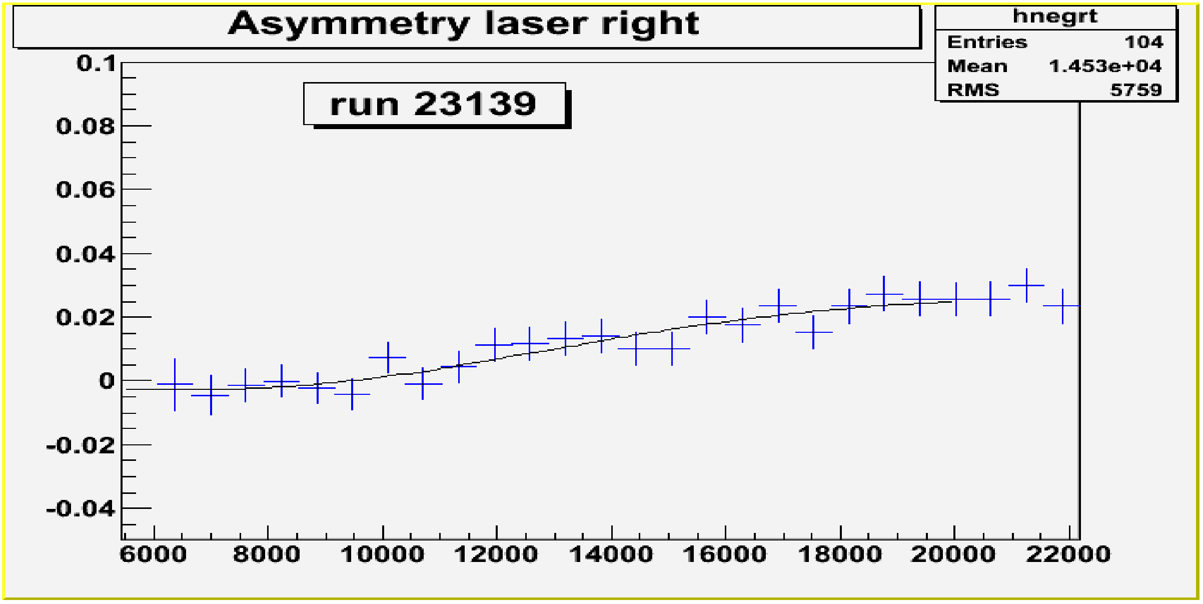

Figure 4.30: The measured Compton asymmetry vs. ADC response channels, where the energies of scattered photons were deposited in the GSO.

entire run or one complete lacer cycle by the square root of the number of data points, and it is labeled σ_s, σ_D and σ_B, respectively. Hence, the statistical uncertainty for each Compton photon scattering asymmetry can be determined as below:

$$\sigma_{\mathcal{A}_{cor}} = \frac{\sigma_D^2}{(\mathrm{sum_{On}} - \mathrm{bkg_{Off}})^2} + \frac{(\mathrm{diff_{On}})^2(\sigma_s + 2\sigma_B)^2}{(\mathrm{sum_{On}} - \mathrm{bkg_{Off}})^4}, \tag{4.28}$$

for each pair(30Hz)/quartet(120Hz)/octet(240Hz) helicity pattern.

where $\mathrm{diff_{On}}$, $\mathrm{sum_{On}}$ and $\mathrm{bkg_{Off}}$ are regarded as independent variables.

According to Fig. 4.36, it clearly shows that the statistical uncertainty is primarily dominated by the random noise in $\mathrm{diff_{On}}$. Likewise, we can estimate the background asymmetry based on Equation 4.25. According to Fig. 4.37, the background asymmetry is too small to detect. That means PREx Compton asymmetry measurement is very clean without being contained by any background source.

On the other hand, there is an observed 1% increase in the PMT gain between cavity-locked (laser-on) and cavity-unlocked (laser-off) states.

$$\begin{aligned} 1.01 &= \frac{G_{\text{on}}}{G_{\text{off}}} = \frac{G(1+\gamma(S+B))}{G(1+\gamma B)} \\ &\approx (1+\gamma S+\gamma B)(1-\gamma B) \sim 1+\gamma S+\gamma B-\gamma B = 1+\gamma S, \end{aligned} \tag{4.29}$$

where G is the gain at the nominal zero (dark) anode current, and S is the total amount of photon signal accumulations above the background level, labeled as B, in one laser-cycle. The ratio of gains for laser-on and -off as shown in Equation 4.30 is determined by flashing an LED regarded as Compton photon signals at a range of stable brightnesses. After taking the pile-up effect into consideration, any systematic difference in LED pulse size between laser-on (locking the photon Fabry-Pérot cavity) and -off (unlocking) states is as a result of the photon detector gain shift. Hence, the systematic uncertainty is overall due to the gain shift itself and the pedestal uncertainty.

We can further estimate this gain shift effect numerically during the analysis. While calculating the measured Compton photon asymmetry, we take the difference in the mean accumulator value, including both background and pedestal subtractions, per helicity window between two helicity states.

$$\begin{aligned} \text{diff}^{i}_{\text{On}} &= G_{\text{on}}(S+B+\frac{\delta S}{2}) - G_{\text{on}}(S+B-\frac{\delta S}{2}) \\ &= G[1+\gamma(S+B)](S+B+\frac{\delta S}{2}) \\ &- G[1+\gamma(S+B)](S+B-\frac{\delta S}{2}) \\ &= G\delta S[1+\gamma(B+S)], \\ \text{sum}^{i}_{\text{On}} &= G[1+\gamma(S+B)](S+B+\frac{\delta S}{2}) + G[1+\gamma(S+B)](S+B-\frac{\delta S}{2}), \\ \text{B}^{3}_{\text{off}} &= G(1+\gamma B)B + G(1+\gamma B)B \\ \text{sum}^{i}_{\text{On}} - \text{B}^{3}_{\text{off}} &= 2GS[1+\gamma(S+2B)]. \end{aligned} \tag{4.30}$$

As a result, the measured Compton photon asymmetry can be expressed in terms of the gain shift, δS, as below:

$$\begin{aligned}\mathcal{A}_{\text{cor}} &= \frac{\delta S}{2S}[1+\gamma(B+S)-\gamma(S+2B)] \\ &= \mathcal{A}_{\text{phys}}[1+\gamma(B+S)-\gamma(S+2B)] = \mathcal{A}_{\text{phys}}(1-\gamma B).\end{aligned} \tag{4.31}$$

The correction for PREx is:

$$\mathcal{A}_{\text{phys}} = \mathcal{A}_{\text{cor}}(1+\gamma S\frac{B}{S}) = \mathcal{A}_{\text{cor}}(1+0.01\frac{60}{96-60}) = 1.017\mathcal{A}_{\text{cor}}. \tag{4.32}$$

The systematic errors in the analyzing power is estimated by changing the beam line input into the GEANT4 MC, e.g. the photon beam position on the collimator, over the experimentally possible range of values, and the fractional change in $\mathcal{A}_{\text{th}}$ is quoted as the relative systematic uncertainty. However, Fig. 4.31 demonstrates the negligible effect on the change in $\mathcal{A}_{\text{th}}$ due to different collimator's positions along the beam line. Table 4.4 shows a list of factors which cause the fractional change in $\mathcal{A}_{\text{th}}$.

Table 4.3: Accum0 signal sizes by laser states for PREx.

laser state	PREx (120Hz, 5V ADC)	PREx (normalized)
off	30	60
on	48	96

Table 4.4: A table of Compton systematic uncertainties using the All accumulator during 2010 PREx.

Rel. Systematic Uncertainties	
Laser Polarization	0.7%
Analyzing Power:	
Non-linearity	0.3%
Collimator Position	0.02%
Total on Analyzing Power	0.3%
Total on Gain Shift	0.9%
Total	1.18%

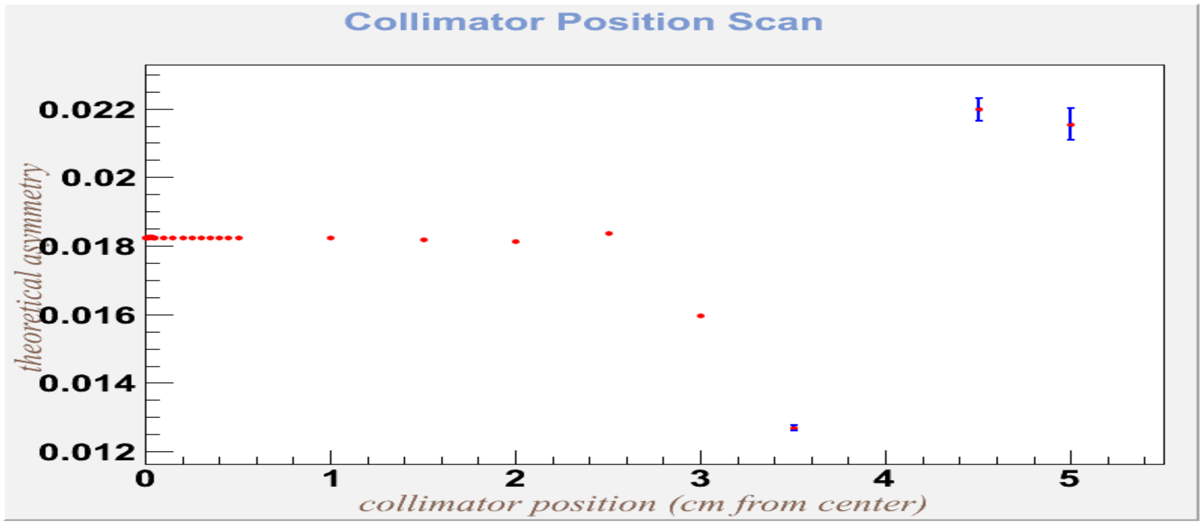

Figure 4.31: $\mathcal{A}_{\text{th}}$ vs. collimator position

Hence, due to the PMT gain correction on the polarization, this increases the polarization by $0.9 \pm 0.9\%$. The final result is $88.20 \pm 0.12(\text{stat}) \pm 1.041.04$.

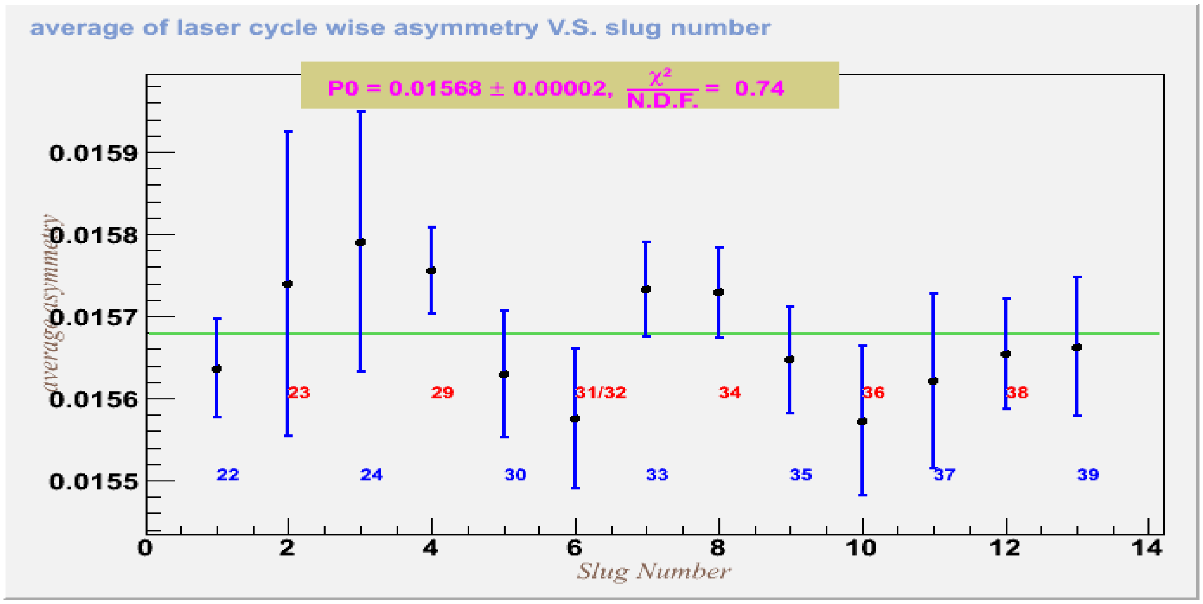

Figure 4.32: Measured asymmetry vs. PREx data set (in the unit of slug: data accumulation/per day). The error bar for each round point is statistical only for the laser-wise method.

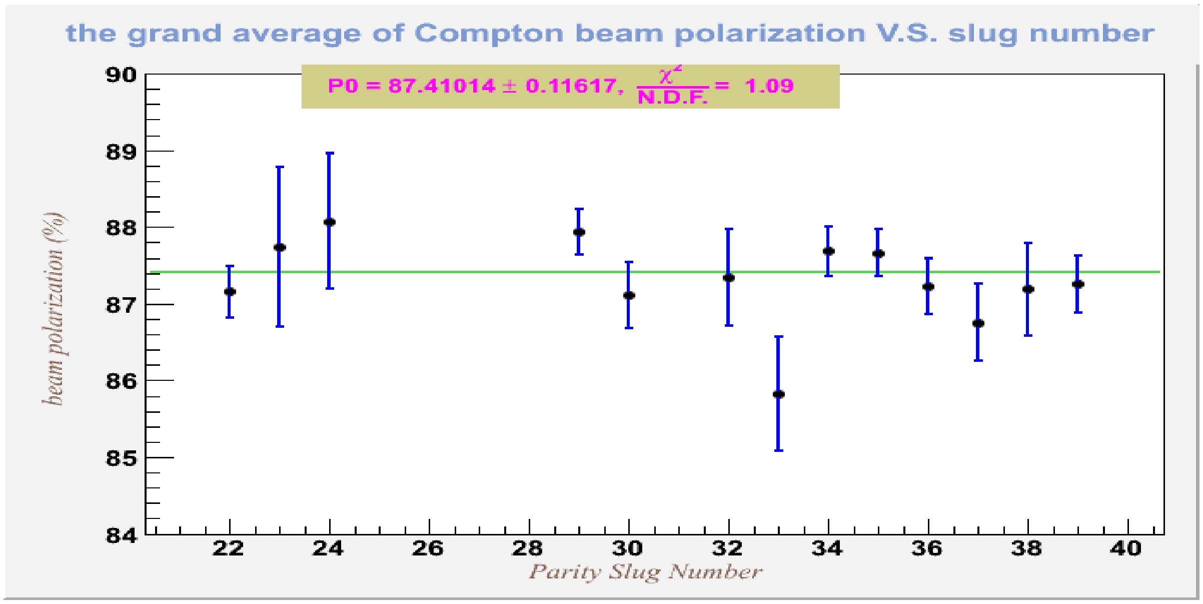

Figure 4.33: Measured electron beam polarization vs. PREx data set.

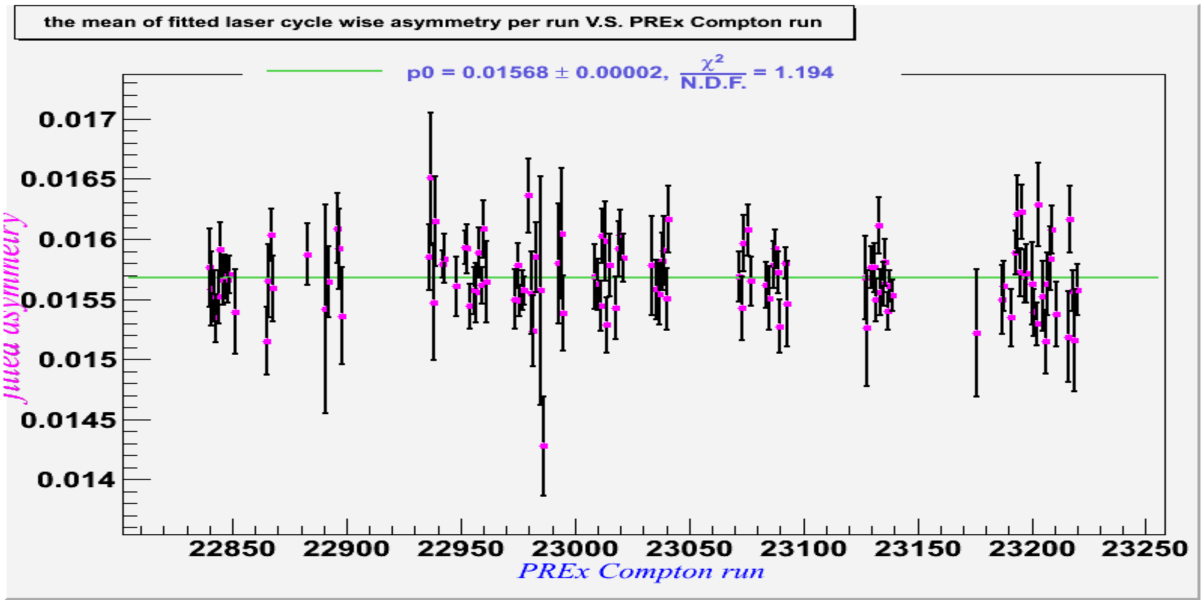

Figure 4.34: Measured asymmetry vs. PREx Compton run. The error bar for each round point is statistical only for the laser-wise method.

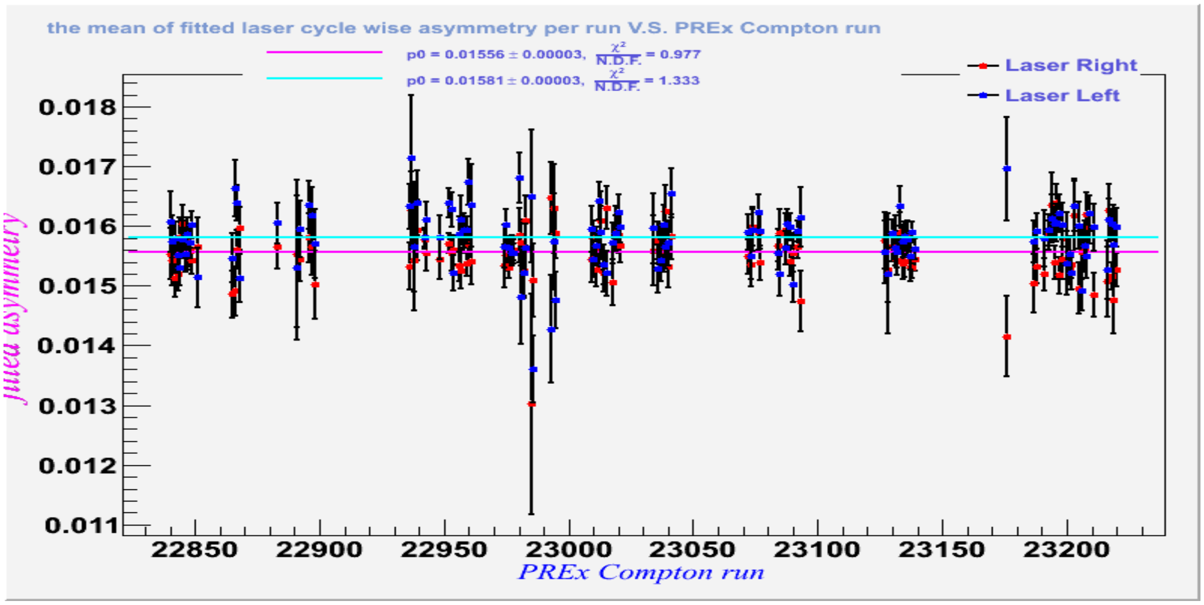

Figure 4.35: Measured asymmetry vs. PREx Compton run. The error bar for each round point is statistical only for the laser-wise method.

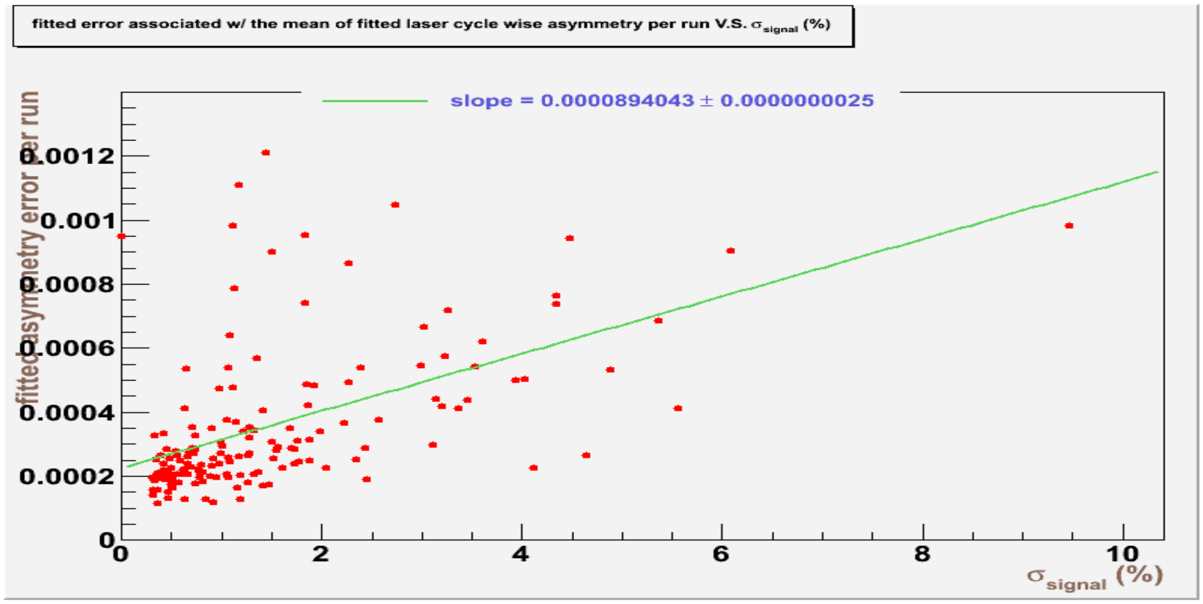

Figure 4.36: $\sigma_{\mathcal{A}_{cor}}$ vs. σ_s (%).

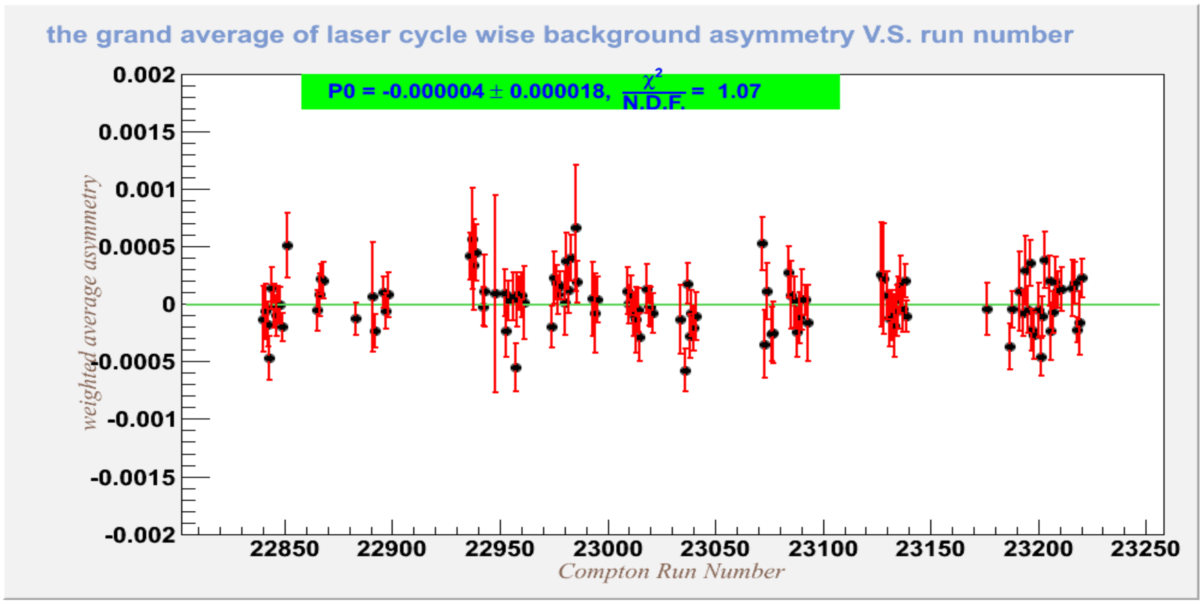

Figure 4.37: Measured background asymmetry vs. PREx Compton run. The error bar for each round point is statistical only for the laser-wise method.

Chapter 5

Helicity-Correlated Beam Asymmetry (HCBA)

The false asymmetry cuased by the helicity-correlated beam asymmetry should be subtracted from the measured asymmetry. Before we start discussing the complementary analysis strategies employed to calibrate the measured asymmetry in the next chapter, the techniques for configuring the polarized electron source in order to minimize fluctuations in the beam's intensity, trajectory and energy under the helicity reversal are required to introduce here. A well-control of the electron source configuration can help suppress the effect of HCBA. A not 100% completely perfect source configuration, however, still gives rise to the remaining corrections to the measured asymmetry. My dissertation primarily concentrates on the development of analysis strategies to study how to minimize the size of the residual asymmetry correction.

5.1 Formalism

The helicity-correlated beam asymmetry fundamentally arises from the difference in the number of electrons per second from the injector between two helicity states. Both helicity-correlated beam intensity and position difference inherit from an asymmetry in the intensity of the electron beam after the PC. While the incoming linearly polarized laser light enters the PC, the imperfect PC set-up as well as the PC angular, position and voltage misalignment would introduce the phase shift on the outgoing laser light. As a result, the output laser light from the PC is not 100% fully circularly polarized. Two helicity electrons, which are generated from the photoemission of a GaAsP photocathode by using the imperfect circular polarization of the laser light, have the difference in their intensities. Below, we will analytically explain how different types of phase shifts caused by the PC makes the significant impact on producing the helicity-correlated beam asymmetry. How can we do to suppress different sources of phase shifts based on different approaches?

The phase shift arisen from the PC can be expressed as below:

$$\delta^{\mathrm{R}} = -(\frac{\pi}{2} + \alpha) - \Delta; \quad \delta^{\mathrm{L}} = +(\frac{\pi}{2} + \alpha) - \Delta, \tag{5.1}$$

where both α and Δ result in the residual linear polarization. The former is symmetric; the later is anti-symmetric. Hence, the intensities of the transmitted laser light with the phase shifts of δ^{R} and δ^{L} for the right- and left-hand circular polarizations, respectively, are

$$I^{\mathrm{R(L)}} \quad \propto \quad \epsilon T cos(\delta^{\mathrm{R(L)}}) cos(2\psi), \tag{5.2}$$

where ϵ is the difference in the transmitted intensity of the laser light between two circular polarization states. T is the average transmitted intensities of two polarization laser light. Here, ψ represents the inclined angle with respect to the horizontal. According to Equation 5.1 and 5.2, the helicity-correlated beam asymmetry can be expressed below:

$$\mathcal{A}_{\mathrm{q}} \quad = \quad \frac{I^{\mathrm{R}} - I^{\mathrm{L}}}{I^{\mathrm{R}} + I^{\mathrm{L}}} = -\frac{\epsilon}{T}[\Delta cos(2\epsilon)]. \tag{5.3}$$

The detailed derivation of Equation 5.3 is described in [47].

In Equation 5.3, $\frac{\epsilon}{T}$ is referred to the analyzing power, and Δ is just the phase shift appearing in the helicity-correlated beam asymmetry. At the same time, Δ is linearly proportional to HCBA. After adding a rotatable half-wave plate (RHWP) downstream of the PC and an additional retardation plate downstream of the RHWP, Equation 5.3 becomes [47]:

$$\mathcal{A}_{\mathrm{q}} = -\frac{\epsilon}{T}[\beta\sin(2\rho-2\psi)+\gamma\sin(2\theta-2\psi)+(\Delta-\Delta^{\circ})cos(4\theta-2\psi)], \tag{5.4}$$

where β is the phase shift induced by the retardation plate, ρ is the angle of the retardaton plate with respect to the horizontal, γ is the angle of RHWP against IHWP, and θ is the angle of RHWP relative to the horizontal.

There are two schematics used to study the effects of the residual linear polarization: 1) the laser table source studies; 2) the electron beam source studies. Equation 5.4 characterizes various sources leading to the residual linear polarization:

- ϵ, T and ψ arise from:
    - the photocathode during the electron beam studies;
    - the analyzer during the laser table studies.
- β and ρ arise from:
    - the vacuum window during the electron beam studies (the dominant one);
    - the insertable mirror and len's effect during the laser table studies.
- γ and θ arise from the RHWP for both electron beam and laser table studies.
- Δ and Δ° arise from the PC for both electron beam and laser table studies.

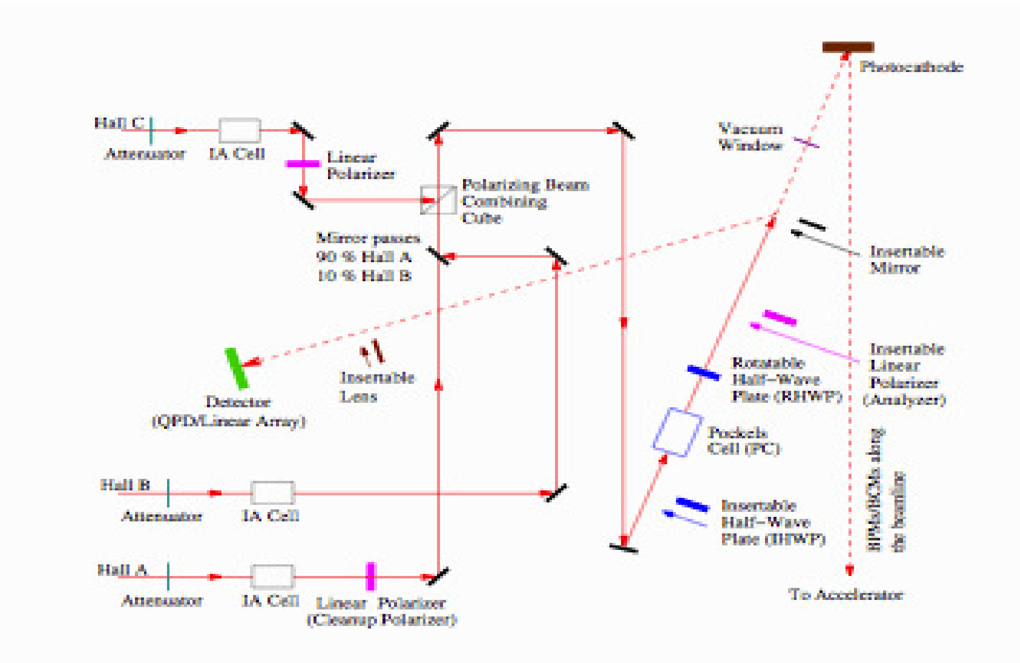
Photocathode
Hall C
Attenuator
IA Cell
Linear Polarizer
Vacuum Window
Polarizing Beam Combining Cube
Mirror passes 90 % Hall A 10 % Hall B
Insertable Mirror
Insertable Linear Polarizer (Analyzer)
Rotatable Half−Wave Plate (RHWP)
Detector (QPD/Linear Array)
Insertable Lens
Pockels Cell (PC)
Hall B
Attenuator
IA Cell
Insertable Half−Wave Plate (IHWP)
BPMs/BCMs along the beamline
Hall A
Attenuator
IA Cell
Linear Polarizer (Cleanup Polarizer)
To Accelerator

Figure 5.1: A schematic of the polarized electron source set-up in the injector part at JLab. The laser light was circularly polarized by PC. Through the photoemission from a GaAsP photocathode, the polarized electrons were released, because they were excited from the valence band to the conducting band via the absorption of the incident photon energies from the circularly polarized laser light. The polarity of the laser light determines the helicity state of the electron beam. The insertable mirror guides the beam onto either a quad-photodiode (QPD) or a linear array-photodiode (LAPD) detector during the laser table studies. On the other hand, the insertable mirror and the insertable polarizer are retraced during the electron beam studies and the production data-taking as well. In addition, the insertable half-wave plate is inserted and retraced alternatively during the laser table studies, the electron beam studies and the production data-taking period.

5.2 PITA Effects

In this section, we will focus on how to control the phase shift, Δ, induced by the PC. According to Equation 5.3, the charge asymmetry is linearly proportional to Δ, which is adjusted by changing the value of the voltage applied to the PC. Hence, Δ can be expressed below:

$$\Delta = \frac{\pi}{2V_{\lambda/4}} V_{\mathrm{PC}}^{\mathrm{R(L)}}, \tag{5.5}$$

where $V_{\lambda/4}$ is the voltage required for the quarter-wave phase retardation of the laser light, and $V_{\mathrm{PC}}^{\mathrm{R(L)}}$ is the voltage used to transform the linearly polarization laser light into the circular polarization laser light.

As a result, we have:

$$\mathcal{A}_{\mathrm{q}} = -\frac{\epsilon}{T}[\Delta cos(2\epsilon)] = -\frac{\epsilon}{T}[\frac{\pi}{2V_{\lambda/4}} V_{\mathrm{PC}}^{\mathrm{R(L)}} cos(2\epsilon)]. \tag{5.6}$$

The equation above is called the Polarization Induced Transport Asymmetry (PITA) [48] equation. The PITA equation as shown in Equation 5.6 characterizes the sensitivity of $V_{\mathrm{PC}}^{\mathrm{R(L)}}$ to the residual linear polarization which leads to $\mathcal{A}_{\mathrm{q}}$. $\mathcal{A}_{\mathrm{q}}$ can be adjusted by changing the magnitude of $V_{\mathrm{PC}}^{\mathrm{R(L)}}$. See Figure 5.2.

5.3 Phase Gradients

The helicity-correlated position difference along x (Δ_{x}) and y (Δ_{y}) can be derived from taking the derivative of the charge asymmetry as listed below, respectively:

$$\Delta_{\mathrm{x}} = \frac{\partial \mathcal{A}_{\mathrm{q}}}{\partial \mathrm{x}}, \quad \Delta_{\mathrm{y}} = \frac{\partial \mathcal{A}_{\mathrm{q}}}{\partial \mathrm{y}}. \tag{5.7}$$

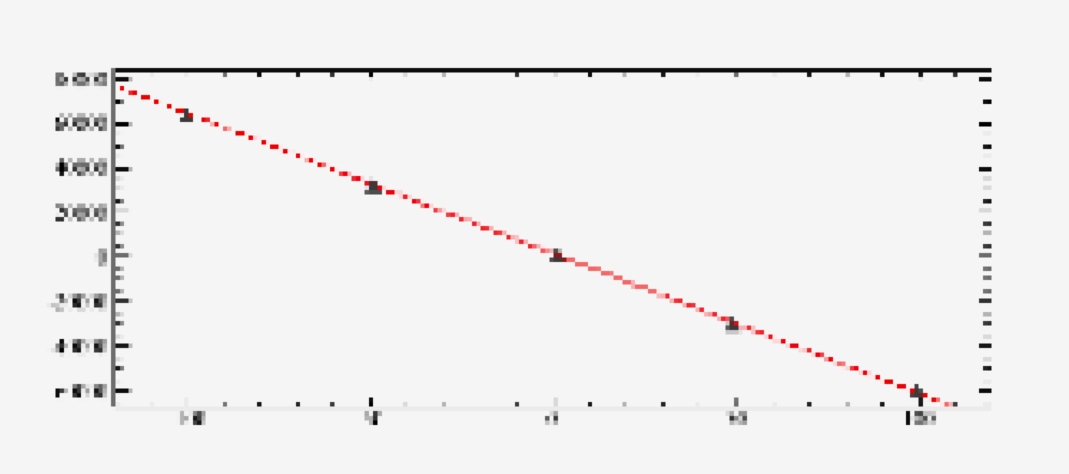

Figure 5.2: A typical PITA scan plot. HCBA ($\mathcal{A}_\mathrm{q}$) is plotted on the y-axis, and $V_\mathrm{PC}^\mathrm{R(L)}$ is on the x-axis. In a PITA scan, $V_\mathrm{PC}^\mathrm{R(L)}$ is adjusted anti-proportionally, and $\mathcal{A}_\mathrm{q}$ is measured at each of the specific $V_\mathrm{PC}^\mathrm{R(L)}$.

A spatially varying phase shifts across the lateral face of the beam gives rise to the possibility of the higher-moment HC effects. A linear variation in the magnitude of the phase shift (Δ) leads to the displacement of the beam toward two opposite directions for two separate helicity states. The helicity-correlated position difference is thus created.

5.4 Controlling Helicity-Correlated Position Differences

According to Equation 5.4, we know couple of different sources contributing to the non-zero charge asymmetry. Equation 5.4 can be re-expressed, because each term in Equation 5.4 can be labelled based on various sources:

$$\mathcal{A}_\mathrm{q} \quad = \quad \text{Photocathode} \times [\text{Vacuum Window} + \text{RHWP} + \text{PC}], \tag{5.8}$$

where:

- Photocathode (analyzing power): affects $\frac{\epsilon}{T}$;

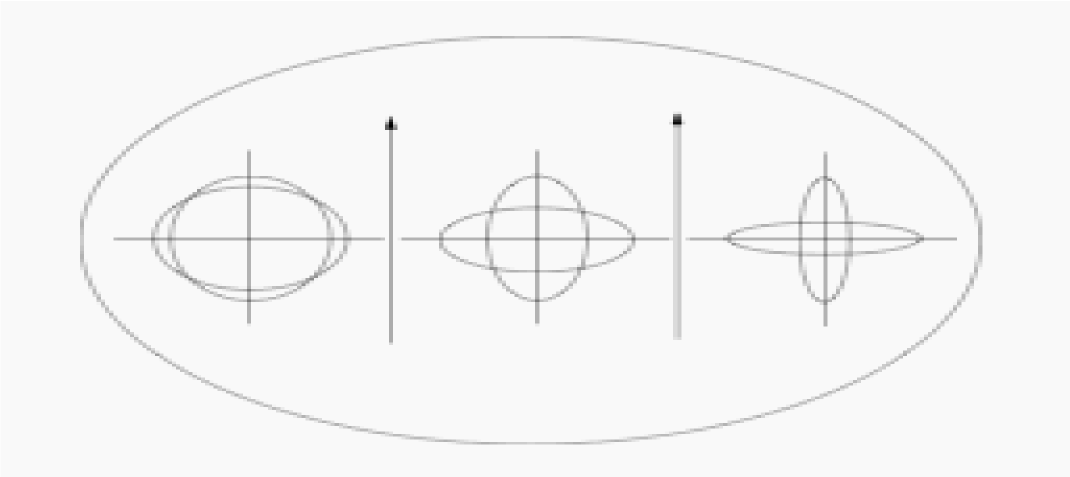

Figure 5.3: A spatially varying Δ-phase leads to the helicity-correlated phase shift across the beam spot. The amount of the residual linear polarization is larger on the left relative to the right.

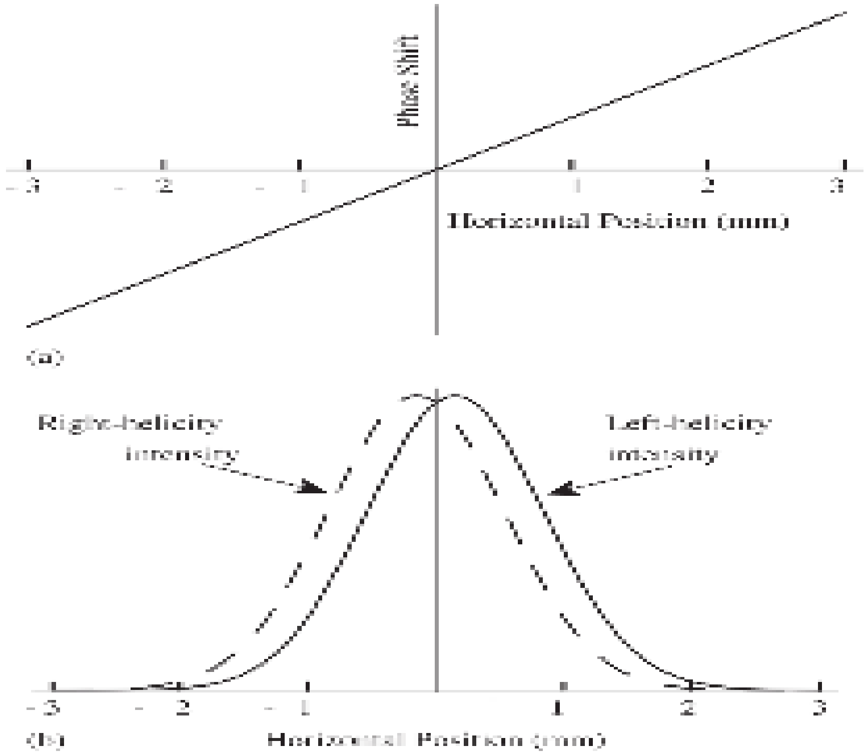

Figure 5.4: The linear relation between Δ and the beam's spatial displacement (top panel). The change in the intensity of the laser light between two helicity states as expressed in Equation 5.2 versus the beam's displacement toward two opposite directions for each helicity state respectively. The solid line represents the left-handed intensity, and the dash line corresponds to the right-handed intensity (bottom pannel).

- Vacuum Window (off-set term): is associated with the change in β, ρ and ψ;
- RHWP (2θ term): makes impact on both γ and θ;
- PC (4θ term): changes Δ.

Firstly, we want to minimize $\frac{\epsilon}{T}$. However, the electron beam's polarization becomes only around 35%, as $\frac{\epsilon}{T} = 0$. In order to highly polarize the beam (up to $\sim 90\%$), a non-zero analyzing power in the photocathode is unavoidable. Consequently, a non-zero quantity of $\frac{\epsilon}{T}$ should be judiciously controlled, so that the effect of a non-zero analyzing power could be appropriately suppressed, and at the same time, the polarization of the electron beam is still remained to be high without being reduced.

Secondly, we have learned that Δ can be nulled by adjusting the PC alignment and voltage. However, nulling both the off-set and 2θ terms is very difficult to achieve. Since the vacuum window cannot be rotated at JLab., ρ is fixed. In addition, β is hard to be zero due to an imperfect vacuum window. As a result, the only way to minimize the off-set term is to adjust ψ. Similarly, we can either adopt a perfect RHWP to make γ be equal to zero or adjust RHWP to set $\theta = \psi$, so that the 2θ term is accordingly suppressed.

In sum, the off-set term arises from the vacuum window effect, and only can be nulled by means of adjusting ψ to be equal to ρ. Since ψ is the orientation of the photocathode, the optimization of ψ can only be done with the electron beam studies. On the other hand, both the 2θ and 4θ terms depend on the laser table studies to be sufficiently optimized. The center of the laser table studies focuses on the optimization of the PC alignment and the PC voltage adjustment.

5.4.1 Sources of Helicity-Correlated Position Differences

In this section, we list the contribution of each term in Equation 5.4 and Equation 5.8 to the formation of helicity-correlated position differences.

1. Photocathode (analyzing power): affects $\frac{\epsilon}{T}$. The position differences arise from the variation in the analyzing power; in other words, either $\frac{\partial}{\partial \mathrm{x}}(\frac{\epsilon}{T})$ or $\frac{\partial}{\partial \mathrm{y}}(\frac{\epsilon}{T})$ ot both are not zero.
2. Vacuum Window (off-set term): is associated with the change in β, ρ and ψ. The dominant source is from the vacuum window.
3. RHWP (2θ term): makes impact on both γ and θ. The large Δ_X and Δ_Y indicate the significant phase gradient across RHWP.
4. PC (4θ term): changes Δ. The large Δ_X and Δ_Y indicate the significant phase gradient across $(\Delta - \Delta^\circ)$.

5.4.2 Sources of Helicity-Correlated Spot Size and Shape Difference

Likewise, the second-moment helicity-correlated effects arising from the spatial derivative of $\frac{\partial \mathcal{A}\mathrm{q}}{\partial \mathrm{x}}$ and $\frac{\partial \mathcal{A}\mathrm{q}}{\partial \mathrm{y}}$ as well can be also large.

1. Vacuum Window (off-set term): is associated with the change in β, ρ and ψ. The dominant source is from the vacuum window.
2. RHWP (2θ term): makes impact on both γ and θ. The large Δ_X and Δ_Y indicate the significant second-moment of the phase gradient across RHWP.
3. PC (4θ term): changes Δ. The large Δ_X and Δ_Y indicate the significant

second-moment of the phase gradient across $(\Delta - \Delta^{\circ})$.

5.5 Final Optimization

In this section, we summarize the final optimization result based on both the laser table and electron beam studies below:

1. Vacuum Window (off-set term): is associated with the change in β, ρ and ψ. The dominant source is primarily from the vacuum window, and the off-set term remains large after optimizing the RHWP orientation during the electron beam studies. We will discuss how to suppress the off-set via a combination of the photocathode rotation and the PC translation during the laser table studies in the next section.
2. RHWP (2θ term): makes impact on both γ and θ. The 2θ term is still large after optimizing the RHWP orientation.
3. PC (4θ term): changes Δ. All of the 4θ terms are suppressed to be small at the zero PITA off-set voltage through the PC alignment and the PC voltage adjustment during the laser table studies.

Next, we will discuss how to further minimize both the off-set and 2θ terms.

5.5.1 Offset Term

The off-set term is nulled by rotating the photocathode and translating the PC. We are about to discuss how to do via combining these two ways, respectively.

5.5.1.1 Photocathode Rotation

The off-set term in $\mathcal{A}_{\mathrm{q}}$ is suppressed to be the minimum value at the orientation angle of the photocathode $\sim 45^\circ$. However, the helicity-correlated position differences, $\frac{\partial \mathcal{A}_q}{\partial \mathrm{X}}$ and $\frac{\partial \mathcal{A}_q}{\partial \mathrm{Y}}$, in the off-set term are still large. The significant D_{X} and D_{Y} indicate the non-negligible phase gradient either across the vacuum window or in the photocathode's analyzing power, say, $\frac{\epsilon}{T}$.

5.5.1.2 PC Translation

In order to further suppress both Δ_{X} and Δ_{Y} in the off-set term, the PC is translated in order to obtain the minimum measurements of helicity-correlated position differences. A representative set of the photocathode orientation angles, along with different positions of the PC translations, correspond to separate setting of RHWP. The former is related to the helicity states of the electron beam, whereas the later does not depend on the helicity states. That is, either right- or left-hand helciity electrons respond to each individual setting of the PC translation equivalently. Through chaning the PC positions, the off-set term can be much better minimized than the 2θ and 4θ terms.

5.5.2 2θ Term

The 2θ term is suppressed by optimizing the RHWP angle as described below.

5.5.2.1 RHWP Determination

As mentioned earlier, RHWP is supplied to optimize the sensitivity of the optical elements to the residual linear polarization as seen in the imperfect circular polarization laser light during the laser table studies. The characteristic RHWP angle determination ought to be done after the optimization of the photocathode's orientation angle and the PC translation are completed. We have learned that both Δ_{X} and Δ_{Y} still remain big even after the zeroth-moment of the charge asymmetry is adjusted to be zero by means of rotating the photocathode. Consequently, the goal of determining the RHWP angle is to find the minimum values of Δ_{X} and Δ_{Y}, along with a non-zero but tiny $\mathcal{A}_{\mathrm{q}}$ PITA slope. Not surprisingly, only a few optimal RHWP angles meet the requirement, in which both Δ_{X} and Δ_{Y} are simultaneously minimize after the adjustment of the PC voltage is made to be tiny even equal to zero. In addition, the optimal angle of RHWP is supposed to be available for two separate helicity electrons and different IHWP states. The optimal RHWP angle is set to be 50°.

5.6 Wien Optimization

In PREx, the Wien filter is introduced and located between the photocathode and the first BPM. The Wien filter, combined with IHWP, is used to perform the slow helicity reversal, so that the pick-up of the preferred electronic helicity signals can be avoided by using IHWP and the Wien filter to alter the sign of the electron beam polarization. Besides, we do not expect the addition of the Wien filter to the beam line will influence the suppresion result of both the charge asymmetry and helicity-correlated position differences as discussed in the previous sections. Below, we describe how each term as shown in Equation 5.4 and Equation 5.8 is changed after adding the Wien filter.

1. Vacuum Window (off-set term): is associated with the change in β, ρ and ψ. No change was found.

2. RHWP (2θ term): makes impact on both γ and θ. The Wien filter only changed the polarity of Δ_{X} and Δ_{Y}.

3. PC (4θ term): changes Δ. Same as above.

The dedicated study of the Wien angle adjustment is still needed in order to understand the sources which cuased the helicity-correlated position differences being varied with time for the future experiment. In PREx, the variations of helicity-correlated position differences were found to be substantial and can be measured at the most upstream BPM, which is closest to the photocathode. We will show some results about this in great details in the most begining of the following chapter.

Figure 5.5: A schematic of flowchart for the suppression of $\mathcal{A}_{\mathrm{q}}$, Δ_{X} and Δ_{Y} as shown in Equation 5.4 and Equation 5.8.

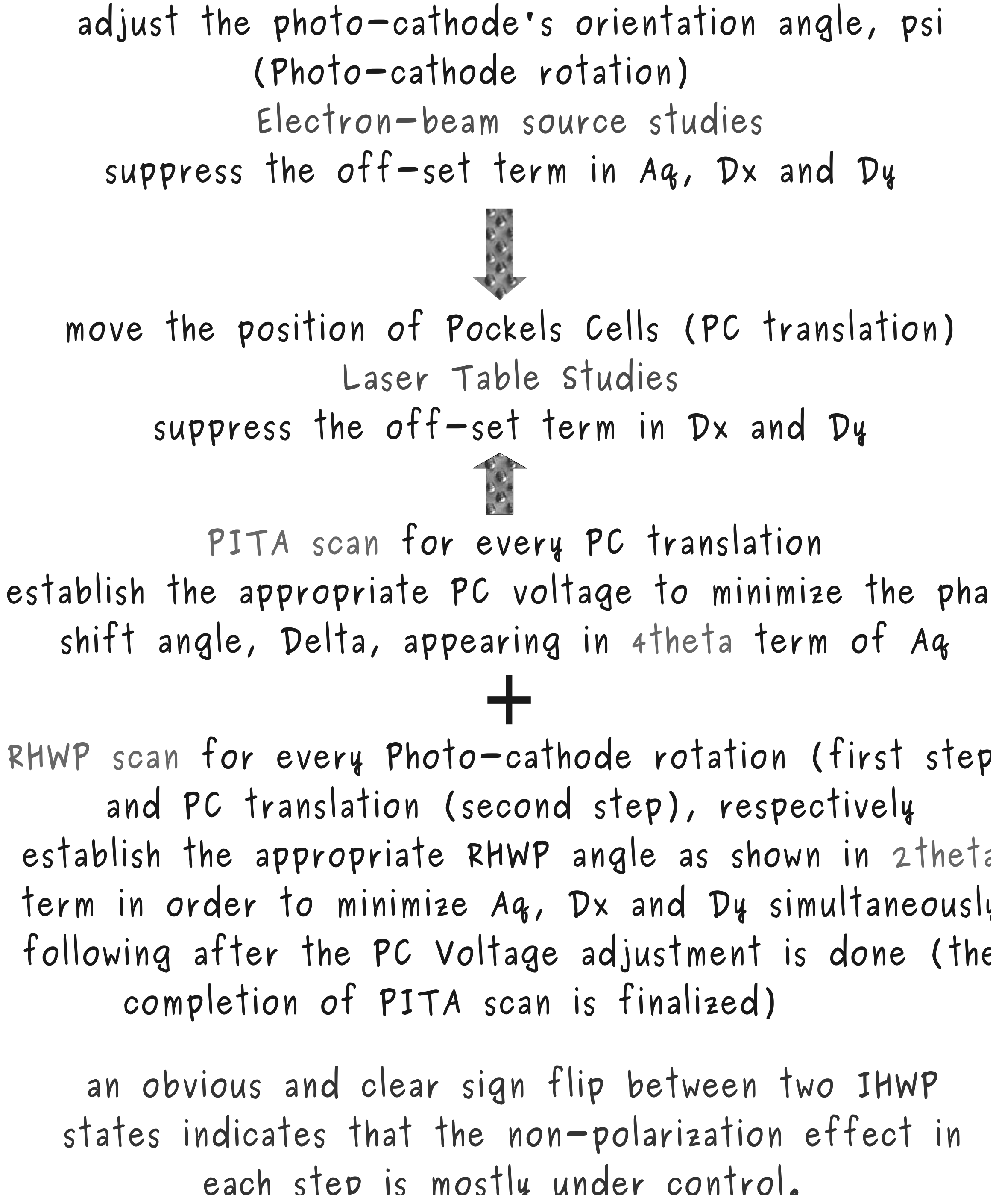

adjust the photo-cathode's orientation angle, psi
(Photo-cathode rotation)
Electron-beam source studies
suppress the off-set term in Aq, Dx and Dy

move the position of Pockels Cells (PC translation)
Laser Table Studies
suppress the off-set term in Dx and Dy

PITA scan for every PC translation
establish the appropriate PC voltage to minimize the pha
shift angle, Delta, appearing in 4theta term of Aq

+

RHWP scan for every Photo-cathode rotation (first step
and PC translation (second step), respectively
establish the appropriate RHWP angle as shown in 2theta
term in order to minimize Aq, Dx and Dy simultaneousl
following after the PC Voltage adjustment is done (the
completion of PITA scan is finalized)

an obvious and clear sign flip between two IHWP
states indicates that the non-polarization effect in
each step is mostly under control.

Chapter 6

Developed Strategies to Control Helicity-Correlated Beam Asymmetry

6.1 Motivation

The differential cross-section is a function of beam parameters such as the beam energy and scattering angle, θ. The differences in the beam energy, position and scattering angle on the target between two helicity states change the kinematics of the accepted electrons at all of the detectors and hence their scattering rates, leading to the unwanted asymmetry, named Helicity-Correlated Beam Asymmetry (HCBA), part of the false asymmetry. In order to subtract HCBA from the measured raw asymmetry, we measure the size of the fake asymmetry to make correction on the raw asymmetry by means of the Beam Modulation (BM) system.

The beam is modulated through driving VME-DAC to seven air-core coils and the energy vernier sequentially with VME-4145 sine waveform generator at a frequency of 15 Hz. The VME-DAC which is controlled by the parity DAQ system supplies the control voltage to operate the coils and vernier. The displacement of the beam is around 0.3-0.5 μm under the perturbation driven by each coil, and it is 0.75 mm by modulating the beam to the energy vernier. Since the helicity state of the electron beam flips at either 120 Hz or 240 Hz, each phase point is read-out via the VME-DAC and recorded by the parity DAQ system in the duration of each integrated helicity window. Hence, for each 15 Hz sine waveform, there are 8 and 16 phase points for 120 Hz and 240 Hz helicity flipping

Figure 6.1: The schematic geometry of the beam modulation system.

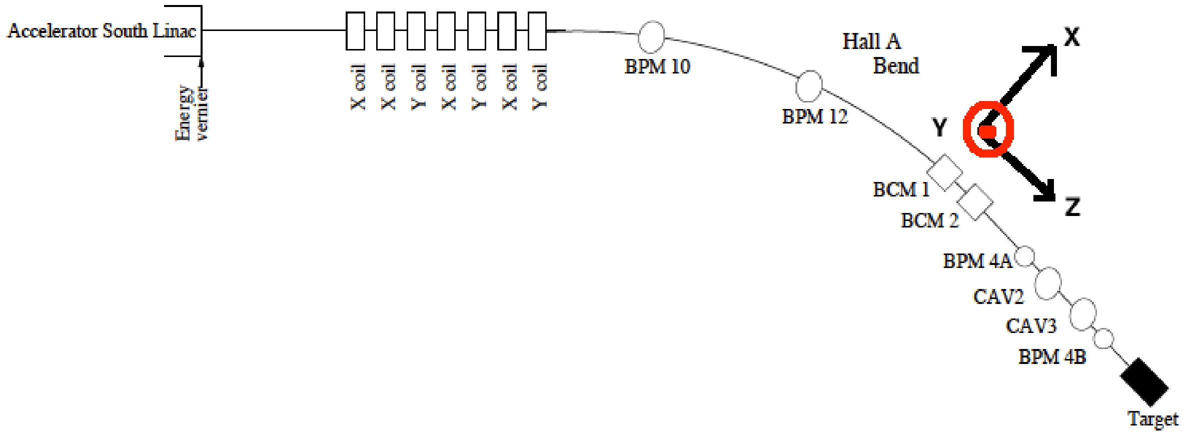

frequencies, respectively. Each dithering cycle consists of a series of beam modulations by driving DAC to seven coils and the energy vernier sequentially. In average, each full dithering cycle comprises 512 phase points or so. The whole period of each dithering cycle lasts 85.68 secs, and it takes 4.267 secs each to modulate the beam for the individual coil and the energy vernier. The duration between perturbations on two coils is 5.28 secs, and it takes 6.48 secs to be off before re-activating the beam modulation on the energy vernier. The duration between two separate dithering cycles is 9 mins and 36 secs. Each parity run takes almost one hour long to complete.

Both responses of the detector and beam monitor to the intentional beam perturbation are quantitatively described by two typical slopes, $\frac{\partial \sigma_j^m}{\partial \mathcal{C}_i}$ and $\frac{\partial \mathcal{M}_j}{\partial \mathcal{C}_i}$, and they are measured directly by the BM system. Note that m refer to different detector elements downstream of the target, i represent separate beam monitors, named BPM4A, BPM4B and BPM12, placed in different locations upstream of the target, and j are a series of coils near the entrance of the experimental hall. BPM4A and BPM4B are located 7.52 m and 2.21 m upstream of the target, respectively.

Figure 6.2: Strip line monitors near the target on the Hall-A beam line. The beam was deflected by steering coils.

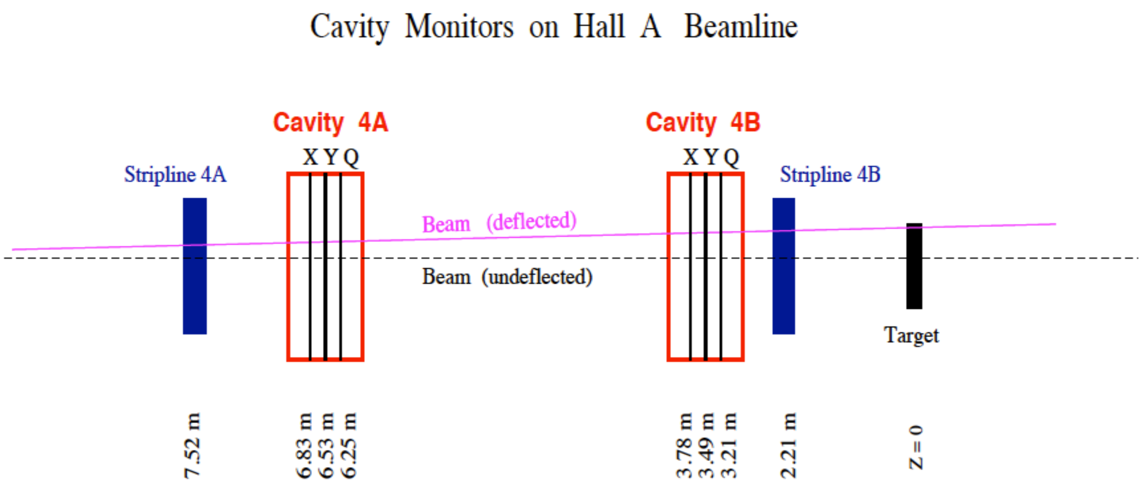
Cavity Monitors on Hall A Beamline
Cavity 4A
X Y Q
Stripline 4A
Cavity 4B
X Y Q
Stripline 4B
Beam (deflected)
Beam (undeflected)
Target
7.52 m
6.83 m
6.53 m
6.25 m
3.78 m
3.49 m
3.21 m
2.21 m
Z = 0

Figure 6.3: (top panel) The response of the beam monitor (BPM4B) to the modulation by driving the VME-DAC to one selected coil (coil-5) in the direction of x with waveforms generated by the sine waveform generator. (bottom panel) One coil, e.g. coil-5, is driven by VME-DAC to perturbe the beam movement along x. Each colorful point indicates the phase point, and different colors are used to identify individual phases. (data: dithering cycle 65, parity run 4755, slug 40)

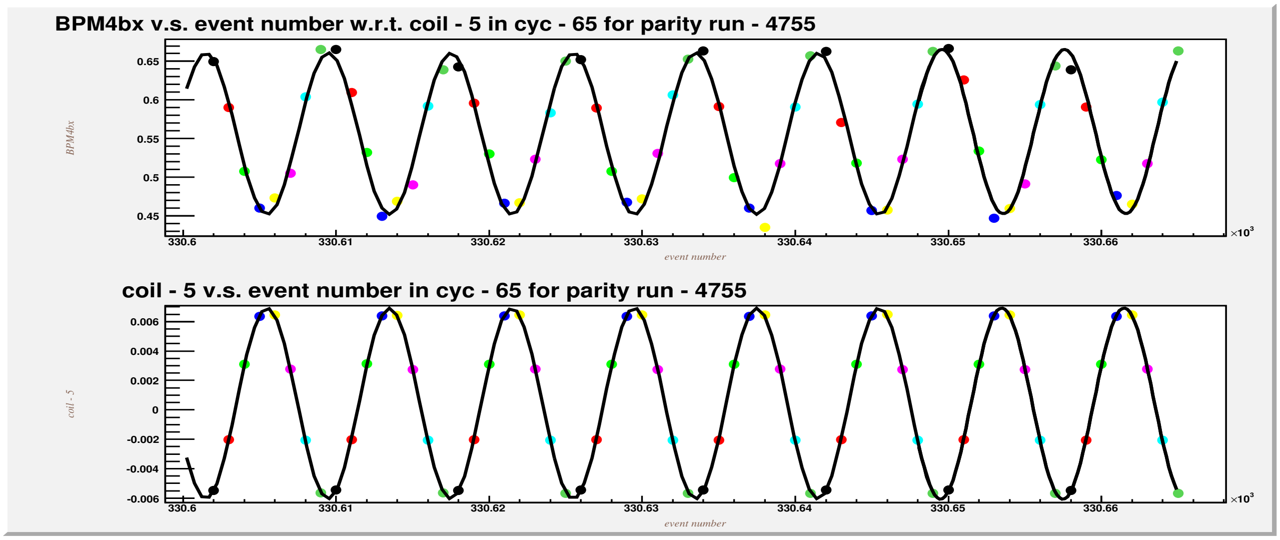

Figure 6.4: The corresponding dithering slope, $\frac{\partial \mathcal{M}_{4bx}}{\partial \mathcal{C}_5}$, to the beam modulation as depicted in Fig. 6.3 with an arbitrary unit. Each point refers to the average size of one phase point for BPM4B (y-axis) and coil such as coil-5 (x-axis), in a full dithering cycle. (data: dithering cycle 65, parity run 4755, slug 40)

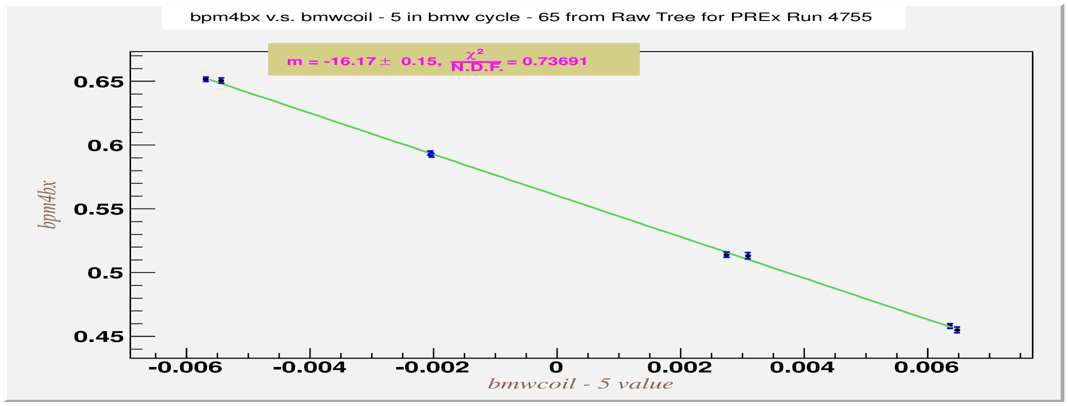

Figure 6.5: (top panel) The response of one detector, sitting on the top side behind the left-arm high resolution spectrometer, to the modulation by driving the VME-DAC to one selected coil (coil-1) in the direction of x with waveforms generated by the sine waveform generator. (bottom panel) Similar plot to the bottom of Fig. 6.3 but with respect to a different coil, e.g. coil-1. (data: dithering cycle 65, parity run 4755, slug 40)

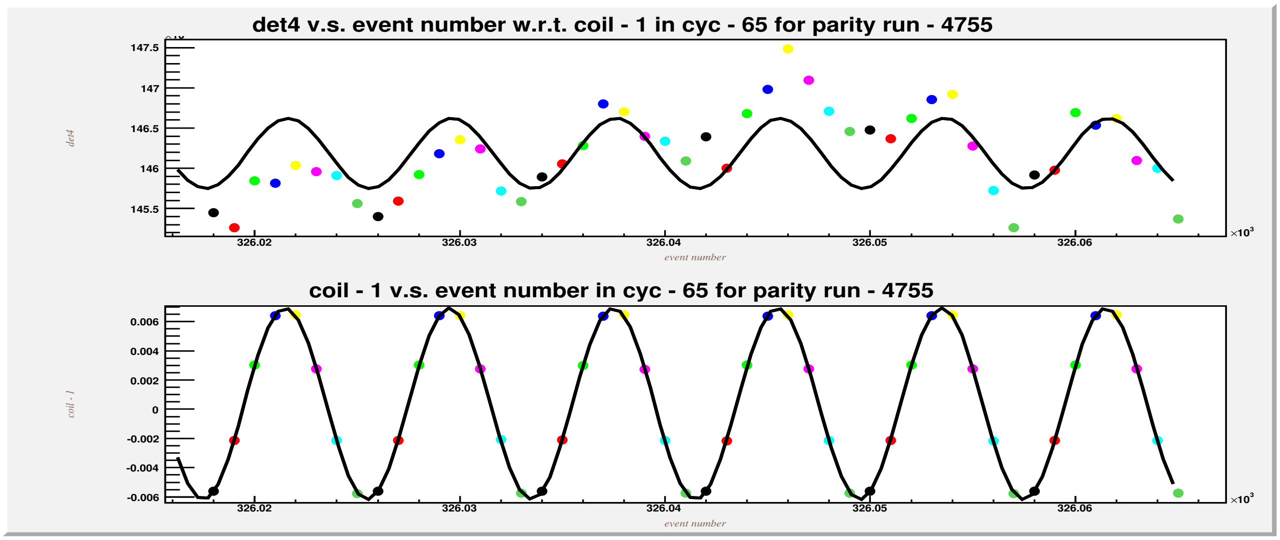

Figure 6.6: Similar to Fig. 6.4. The corresponding dithering slope, $\frac{\partial\sigma_4}{\partial\mathcal{C}_1}$, to the beam modulation as depicted in Fig. 6.5 with an arbitrary unit. Each point refers to the average size of one phase point for the detector, sitting on the top side behind the left-arm high-resolution spectrometer (y-axis), and the coil, e.g. coil-1 (x-axis), in a full dithering cycle. (data: dithering cycle 65, parity run 4755, slug 40)

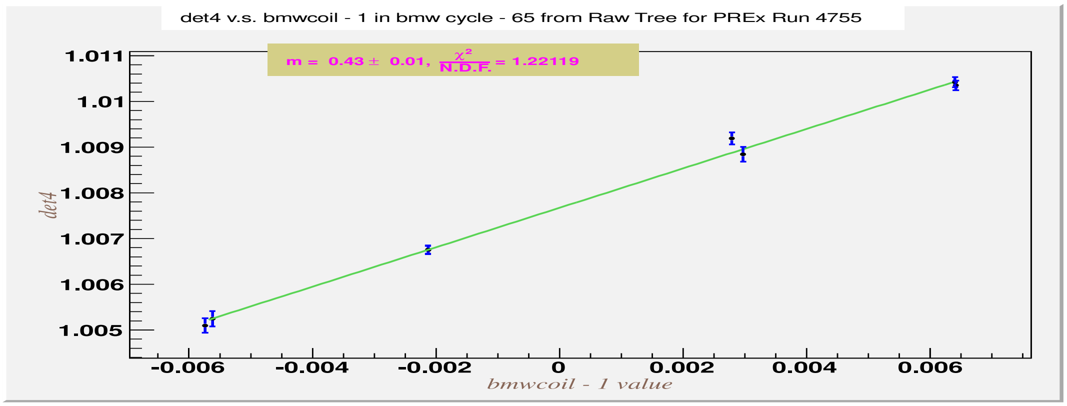

Figure 6.7: This graph reflects the slow drift of the signal flux in one detector which responds to the modulation via coil-5 during the whole period of one dithering cycle due to the variation in temperature of the instrument. (data: dithering cycle 63, run 4755, slug 40)

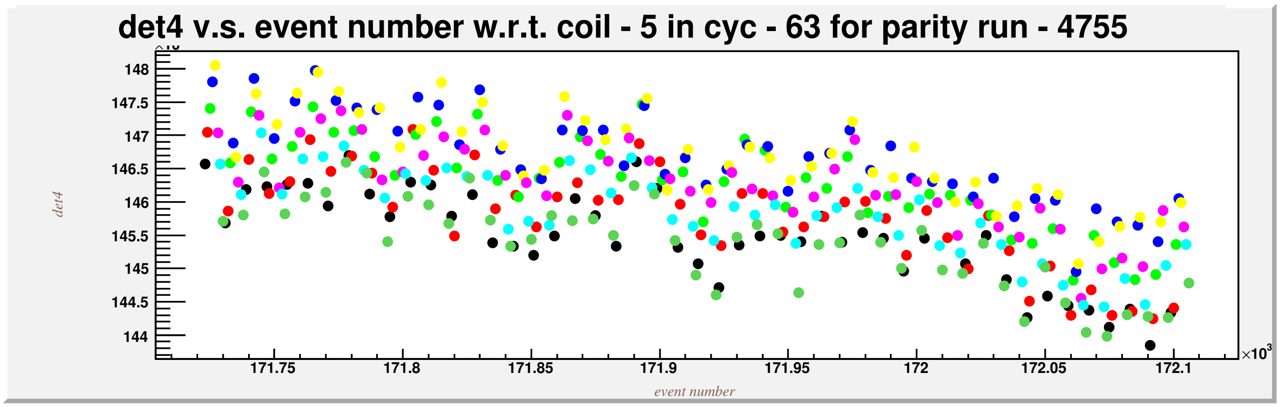

Figure 6.8: This graph reflects the wiggling of the signal flux in one detector which responds to the modulation via coil-1 during the whole period of one dithering cycle. (data: dithering cycle 65, run 4755, slug 40)

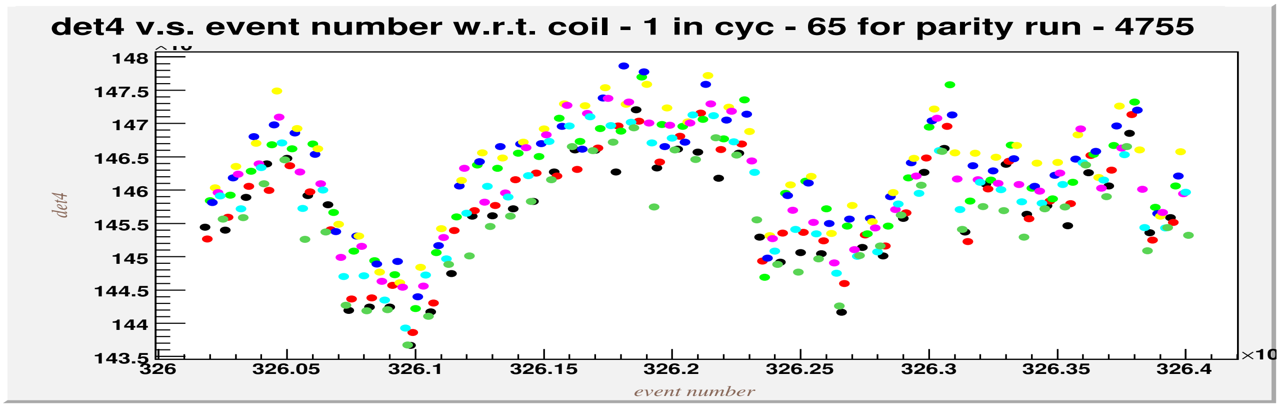

Figure 6.9: The shift in the responding phases of both detector and beam position monitor against the driving phase of coil-3 is maximum and around 35°.

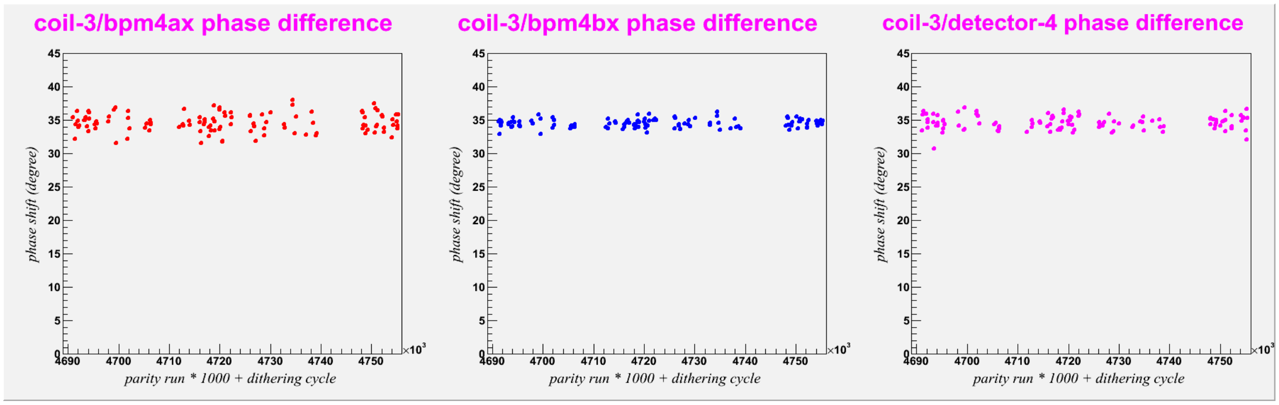

The difference in modulation phase between the responses of either beam position monitor or detector and signal to the coil is studied. The responses of all monitors and detectors to the modulation and one of the driven coils, say, coil-3, are out-of-phase in all high-current (70μA) parity runs [1]. The phase shift as drawn in Fig. 6.9 is up to 35°. On the other hand, a variety of shifts in the responding phases of all instruments against the driven phases of the rest of coils are below 10°. Fig. 6.10 demonstrated different phase shift quantities with respect to different coils.

---

[1] I didn't look at the low current (50μA) runs.)

Figure 6.10: Histograms of different shifts in phase with respect to different coils.

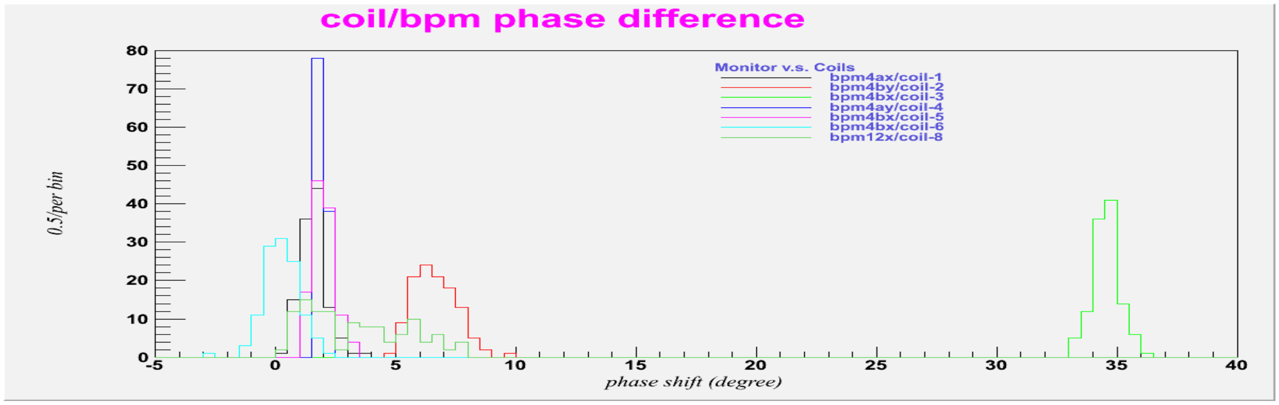

The BM system is employed to modulate the beam motion; therefore, both the beam position and angle are deviated from the center along planes parallel and perpendicular to the horizontal plane. The energy of beam is also slightly altered, accordingly. So, we have the calculated slopes as depicted in Fig. 6.4 and Fig. 6.6 to represent $\frac{\partial \mathcal{M}_j}{\partial \mathcal{C}_i}$ and $\frac{\partial \sigma_j^m}{\partial \mathcal{C}_i}$, respectively. The relation between $\frac{\partial \mathcal{M}_j}{\partial \mathcal{C}_i}$ and $\frac{\partial \sigma_j^m}{\partial \mathcal{C}_i}$ is expressed in Equation 6.1.

$$\frac{\partial \sigma_j^m}{\partial \mathcal{C}_i} = \left(\frac{\partial \sigma_j^m}{\partial \mathcal{M}_j}\right)\left(\frac{\partial \mathcal{M}_j}{\partial \mathcal{C}_i}\right), \tag{6.1}$$

where $\mathcal{M}_j$ meets the requirement for completeness in order to sufficiently span a linear vector space with a complete set of real bases such as x, y, θ_x, θ_y and E. We invert the 5x5 $\frac{\partial \mathcal{M}_j}{\partial \mathcal{C}_i}$ matrix in Equation 6.1 to extract the coefficient, $\frac{\partial \sigma_j^m}{\partial \mathcal{M}_j}$, also named dithering coefficient, for each constituent detector. So we have:

$$\frac{\partial \sigma_j^m}{\partial \mathcal{M}_j} = \left(\frac{\partial \sigma_j^m}{\partial \mathcal{C}_i}\right)\left(\frac{\partial \mathcal{M}_j}{\partial \mathcal{C}_i}\right)^{-1}, \tag{6.2}$$

which indicates a measure of the sensitivity of each detector's cross-section to the variation in the position (x and y), scattering angle (θ_x and θ_y) and energy at the target.

By expanding the raw asymmetry to the first-order approximation in terms of the beam parameters, the calibration on the raw asymmetry to account for the helicity-correlated beam asymmetry is calculated below and can be directly subtracted from the raw asymmetry measurement:

$$\begin{aligned}\mathcal{A}_{\text{false}}\,(\text{for one constituent detector}) = \Delta\mathcal{A}_{\text{PV}}^{\text{1st-order}} &= \frac{\sum_j \frac{\partial\sigma_j^m}{\partial\mathcal{M}_j}\Delta\mathcal{M}^j}{\sigma^{\text{R}}_{+,\text{sig}}+\sigma^{\text{L}}_{\text{-,sig}}} \\ &= \frac{1}{\sigma^{\text{R}}_{+,\text{sig}}+\sigma^{\text{L}}_{\text{-,sig}}}\,(\frac{\partial\sigma}{\partial\theta_x}\Delta\theta_x+\frac{\partial\sigma}{\partial\theta_y}\Delta\theta_y+\frac{\partial\sigma}{\partial x}\Delta x+\frac{\partial\sigma}{\partial y}\Delta y+\frac{\partial\sigma}{\partial E}\Delta E\,),\end{aligned} \tag{6.3}$$

where the asymmetry correction is normalized to the sum of differential cross-sections, $\sigma^{\text{R}}_{+,\text{sig}}+\sigma^{\text{L}}_{\text{-,sig}}$ $(=\sigma^{\text{sum}}_{\text{sig}})$, for both right- and left-hand helicity states. So we have the calibrated asymmetry:

$$\mathcal{A}_{\text{meas}}\,(\text{for one constituent detector}) = \mathcal{A}_{\text{raw}} - \Delta\mathcal{A}_{\text{PV}}^{\text{1st-order}} - \text{others}, \tag{6.4}$$

where others include contributions of background sources, the non-linearity effect of PMTs and ADCs in detectors and the ADC pedestal drift to the asymmetry. These contributions are way too tiny though. So, they are not as interesting as the contribution of the helicity-correlated beam asymmetry to the raw asymmetry.

This chapter primarily describes a newly established analysis methodology used to study following issues occurring in the error analysis for PRExI runs:

- The singularity of the 5x5 dithering matrix, $\mathcal{D}_{5x5}$.

$$\frac{\partial\mathcal{M}}{\partial\mathcal{C}} = \mathcal{D}_{5x5} = \begin{pmatrix} \frac{\partial\mathcal{M}_{4ax}}{\partial\mathcal{C}_1} & \frac{\partial\mathcal{M}_{4bx}}{\partial\mathcal{C}_1} & \frac{\partial\mathcal{M}_{12x}}{\partial\mathcal{C}_1} & \frac{\partial\mathcal{M}_{4ay}}{\partial\mathcal{C}_1} & \frac{\partial\mathcal{M}_{4by}}{\partial\mathcal{C}_1} \\ \frac{\partial\mathcal{M}_{4ax}}{\partial\mathcal{C}_5} & \frac{\partial\mathcal{M}_{4bx}}{\partial\mathcal{C}_5} & \frac{\partial\mathcal{M}_{12x}}{\partial\mathcal{C}_5} & \frac{\partial\mathcal{M}_{4ay}}{\partial\mathcal{C}_5} & \frac{\partial\mathcal{M}_{4by}}{\partial\mathcal{C}_5} \\ \frac{\partial\mathcal{M}_{4ax}}{\partial\mathcal{C}_8} & \frac{\partial\mathcal{M}_{4bx}}{\partial\mathcal{C}_8} & \frac{\partial\mathcal{M}_{12x}}{\partial\mathcal{C}_8} & \frac{\partial\mathcal{M}_{4ay}}{\partial\mathcal{C}_8} & \frac{\partial\mathcal{M}_{4by}}{\partial\mathcal{C}_8} \\ \frac{\partial\mathcal{M}_{4ax}}{\partial\mathcal{C}_2} & \frac{\partial\mathcal{M}_{4bx}}{\partial\mathcal{C}_2} & \frac{\partial\mathcal{M}_{12x}}{\partial\mathcal{C}_2} & \frac{\partial\mathcal{M}_{4ay}}{\partial\mathcal{C}_2} & \frac{\partial\mathcal{M}_{4by}}{\partial\mathcal{C}_2} \\ \frac{\partial\mathcal{M}_{4ax}}{\partial\mathcal{C}_4} & \frac{\partial\mathcal{M}_{4bx}}{\partial\mathcal{C}_4} & \frac{\partial\mathcal{M}_{12x}}{\partial\mathcal{C}_4} & \frac{\partial\mathcal{M}_{4ay}}{\partial\mathcal{C}_4} & \frac{\partial\mathcal{M}_{4by}}{\partial\mathcal{C}_4} \end{pmatrix}.$$

If for any two coils, the responses of all monitors are exactly the same, then the matrix, $\mathcal{D}_{5x5}$, is singular. In practice, similar responses of monitors result in an approximately singular matrix, leading to large fractional errors of dithering coefficients.

- Error analysis. The beam jitter adds noises to all monitors and detectors. However, studying the beam noise level of dithering coefficients by inverting the 5x5 matrix described above is complicated. In addition, unlike the random noise, the beam noise in all instruments is highly correlated. The strong correlation plays an important role in the error analysis for PRExI, for it leads to the lack of insight into the major noise sources. That is, it's difficult to isolate the dominate source of error. As a consequence, the correlation of errors which influence the error propagation makes the error analysis even more complicated.

Presumably the driven coil modulates the beam in the direction of x without making any influence on the beam motion along y (i.e. $\frac{\partial \mathcal{M}_y}{\partial \mathcal{C}_x} \approx 0$), the 5x5 dithering matrix ($\mathcal{D}_{5x5}$) can be approximate to one 2x2 matrix. The 2x2 matrix describes the responses of BPM4A and BPM4B to the variation in beam position and scattering angle through driving the VME-DAC to the coils in the direction of x. Furthermore, after regarding the modulation on the position and energy with coils and the vernier, the responses of BPM4A, BPM4B and BPM12 to coils and vernier are added to the 2x2 matrix, and the 3x3 matrix is formed. We introduce both the 2x2 and 3x3 matrices, because they are much easier to parameterize than the full 5x5. Hence, those issues listed above can be quantitatively described for the further improvement.

The 2x2 matrix is parametrized, and one of the parameters, α, is introduced in order to quantify the singular problem. Besides, one single parameter, β, straightforwardly refers to the dominate source of error after quoting all correlations of errors. In Sec. 6.2, their definitions will be described in great details.

Based on the assumption that all magnets situated between beam monitors and a pair of collimators right behind the target are off, the ratio of β to α remains roughly constant with time. Nevertheless, the sizes of both α and β are influenced by these factors: slow drifting [2], major beam re-tune [3] and minor beam re-tune [4]. As a result, these factors give rise to way smaller magnitudes of α and β, which lead to increasing the fractional errors of dithering coefficients.

One parameter, δ, is defined in the parameterization of the 3x3 matrix. δ indicates the possibility of the energy (position) fluctuation in BPM12 [5] turning into the angular fluctuation in BPM4A and BPM4B. More details about δ will be discussed in Sec. 6.5.

A higher magnitude of δ manifests the occurrence of energy fluctuation turning into the angular variation, resulting in the unwanted longitudinal parity-violating asymmetry which cannot be measured due to that both BPM4A and BPM4B are insensitive to the angular fluctuation. Only an appropriate tune can further suppress the quantity of δ, so that both the sizes and fractional errors of dithering coefficients will not be enhanced too much due to the additional term with a significantly large δ.

Dithering coefficients $(\frac{\partial \sigma_j^m}{\partial \mathcal{M}_j})$ [53], based on the 5x5 conventional dithering analysis, behaved unstably in several PRExI data sets. By means of the 2x2 and 3x3 dithering analysis, we can investigate the reason to account for the causes of unstable dithering coefficients. In the future runs, the second generation of PREx, both the 2x2 and 3x3 dithering analysis can help identify problems immediately via monitoring α, β and δ.

---

[2] Due to the change in the instrument temperature, the drifting of signals occurs. It is grouped into the slow noise, for it makes impact on a series of runs.

[3] The major beam tune results from avoiding the imperfect function of the adiabatic damping in the beam transportation from the accelerator. Also, an intentional increase on the beam spot size to prevent the target from being melt is also achieved by the major beam tune.

[4] The minor beam tune is as a result of reducing the beam halo effect occurring in Compton polarimeter.

[5] The variation in position transforms into the energy fluctuation at the most dispersive location of the beam line, where BPM12 is placed.

6.2 Introduction to 2x2 dithering analysis

In 2x2,

$$\begin{pmatrix} \frac{\partial \sigma_j^m}{\partial \mathcal{C}_1} \\ \frac{\partial \sigma_j^m}{\partial \mathcal{C}_5} \end{pmatrix} = \mathcal{D}M_{2x2} \begin{pmatrix} \frac{\partial \sigma_j^m}{\partial \mathcal{M}_{4ax}} \\ \frac{\partial \sigma_j^m}{\partial \mathcal{M}_{4bx}} \end{pmatrix},$$

where $\mathcal{D}M_{2x2}$ refers to the 2x2 dithering matrix. $\mathcal{M}_j$ indicate BPM4A and BPM4B, and C_i are chosen to be coil-1 and coil-5.

$$\mathcal{D}M_{2x2} = \begin{pmatrix} \frac{\partial \mathcal{M}_{4ax}}{\partial \mathcal{C}_1} & \frac{\partial \mathcal{M}_{4bx}}{\partial \mathcal{C}_1} \\ \frac{\partial \mathcal{M}_{4ax}}{\partial \mathcal{C}_5} & \frac{\partial \mathcal{M}_{4bx}}{\partial \mathcal{C}_5} \end{pmatrix}.$$

This matrix as mentioned above can be re-expressed in terms of four variables, α, β, Λ and $\mathcal{K}$:

$$\mathcal{K} \begin{pmatrix} 1-\beta \\ 1 \end{pmatrix} = \begin{pmatrix} 1 & 1-\alpha \\ 1 & 1 \end{pmatrix} \begin{pmatrix} \frac{\partial \sigma_j^m}{\partial \mathcal{M}_{4ax}} \\ \Lambda \frac{\partial \sigma_j^m}{\partial \mathcal{M}_{4bx}} \end{pmatrix}$$

Here, α, β, Λ and $\mathcal{K}$ are defined:

$$1-\alpha = \frac{\frac{\partial \mathcal{M}_{4bx}}{\partial \mathcal{C}_1} \frac{\partial \mathcal{M}_{4ax}}{\partial \mathcal{C}_5}}{\frac{\partial \mathcal{M}_{4ax}}{\partial \mathcal{C}_1} \frac{\partial \mathcal{M}_{4bx}}{\partial \mathcal{C}_5}}, \tag{6.5}$$

$$1-\beta = \frac{\frac{\partial \sigma_j^m}{\partial \mathcal{C}_1} \frac{\partial \mathcal{M}_{4ax}}{\partial \mathcal{C}_5}}{\frac{\partial \mathcal{M}_{4ax}}{\partial \mathcal{C}_1} \frac{\partial \sigma_j^m}{\partial \mathcal{C}_5}}, \tag{6.6}$$

$$\mathcal{K} = \frac{\frac{\partial \sigma_j^m}{\partial \mathcal{C}_5}}{\frac{\partial \mathcal{M}_{4ax}}{\partial \mathcal{C}_5}} \tag{6.7}$$

$$\Lambda = \frac{\frac{\partial \mathcal{M}_{4bx}}{\partial \mathcal{C}_5}}{\frac{\partial \mathcal{M}_{4ax}}{\partial \mathcal{C}_5}} \tag{6.8}$$

The two dithering coefficients are:

$$\begin{aligned}(\frac{\partial\sigma_j^m}{\partial\mathcal{M}_{4ax}})\Delta\theta \text{ in BPM4bx are fixed} &= \mathcal{K}(1-\frac{\beta}{\alpha}), \\ (\frac{\partial\sigma_j^m}{\partial\mathcal{M}_{4bx}})\Delta\theta \text{ in BPM4ax are fixed} &= \frac{\mathcal{K}}{\Lambda}\frac{\beta}{\alpha}\end{aligned} \tag{6.9}$$

A detailed derivation of a pair of dithering coefficients in Equation 6.9 can be found in Appendix A.

According to the PRExI geometry, approximate calculations of dithering coefficients for all detectors can be numerically estimated by using the distance between each BPM and the target and the distance from the target to the Q_1 bore collimator sitting on each arm. The calculation in Appendix B shows that the magnitude of $\frac{\partial\sigma_j^m}{\partial\mathcal{M}_{4bx}}$ is greater than that of $\frac{\partial\sigma_j^m}{\partial\mathcal{M}_{4ax}}$ by approximately a factor of two. Also, the sign of $\frac{\partial\sigma_j^m}{\partial\mathcal{M}_{4bx}}$ is opposite to that of $\frac{\partial\sigma_j^m}{\partial\mathcal{M}_{4ax}}$.

$$|\frac{\partial\sigma_j^m}{\partial\mathcal{M}_{4bx}}| \sim 2.15\times|\frac{\partial\sigma_j^m}{\partial\mathcal{M}_{4ax}}|$$

6.3 Fractional error of dithering slope

Unlike HAPPEX (Hall A Proton Parity Experiment), where the flipping helicity frequency is 30 Hz, the polarized electron beam's helicity state in PREx is modulated to flip at the frequency of either 120 Hz or 240 Hz. In HAPPEX, the instability level of beam jitters is determined during the course of several data sets (runs) taken in every single day, while it is measured in every ten dithering cycles, lasting in 2−3 runs, for PREx.

The beam jitter (fast noise), besides the random noise (counting statistics), contributes to the uncertainty of each dithering slope, resulting in noisier dithering slopes between adjacent dithering cycles and groups of dithering cycles [6]. In Fig. 6.11, the root-mean-square (RMS for short) of each dithering slope reflects the absolute error of beam jitters in each dithering group. On the contrary of the random noise, also called the uncorrelated error, beam jitters cause the uncertainties of different dithering slopes with respect to one specific coil to be correlated to each other between cycles. We can calculate the correlation coefficient by defining the residual of one typical dithering slope for each dithering cycle in Equation 6.10:

$$\begin{aligned} \Delta\frac{\partial\mathcal{M}_{4bx}}{\partial\mathcal{C}_5} &= \frac{\partial\mathcal{M}_{4bx}}{\partial\mathcal{C}_5} - < \frac{\partial\mathcal{M}_{4bx}}{\partial\mathcal{C}_5} >, \\ \Delta\frac{\partial\sigma_4}{\partial\mathcal{C}_5} &= \frac{\partial\sigma_4}{\partial\mathcal{C}_5} - < \frac{\partial\sigma_4}{\partial\mathcal{C}_5} >, \end{aligned} \tag{6.10}$$

where $< \frac{\partial\mathcal{M}_{4bx}}{\partial\mathcal{C}_5} >$ and $< \frac{\partial\sigma_4}{\partial\mathcal{C}_5} >$ are the average dithering slopes over ten dithering cycles for each dithering group, the correlation coefficient of residuals between a pair of dithering slopes, i and j, can be named ρ_{ij} as below used to identify the correlation level of beam jitters in between two individual dithering slopes with respect to the same coil:

$$\rho_{ij} = \frac{\sum_{i=1}^{m_1}\sum_{j(j>i)}^{m-m_1}\Delta_i\Delta_j}{\sqrt{\sum_{i=1}^{m}\Delta_i^2}}. \tag{6.11}$$

In Fig. 6.12, the strong correlation of beam jitters between each pair of dithering slopes of beam monitors is very obvious. However, since the counting statistics (uncorrelated errors) dominates over beam jitters (correlated errors) in the overall uncertainty sources of each typical $\frac{\partial\sigma_j^m}{\partial\mathcal{C}_i}$, Fig. 6.13 depicts a much weaker but non-zero correlation of residuals in between $\frac{\partial\sigma_j^m}{\partial\mathcal{C}_{1,5}}$ and $\frac{\partial\mathcal{M}_{4ax,4bx}}{\partial\mathcal{C}_{1,5}}$ than in between $\frac{\partial\mathcal{M}_{4ax}}{\partial\mathcal{C}_{1,5}}$ and $\frac{\partial\mathcal{M}_{4bx}}{\partial\mathcal{C}_{1,5}}$.

In Fig. 6.14, the width of residuals is around 200 times smaller than the average dithering slope value. Likewise, while looking at the correlation of residuals in either

---

[6] each dithering group consists of ten dithering cycles.

Figure 6.11: History plots of root-mean-square errors for $\frac{\partial \mathcal{M}_{4bx}}{\partial \mathcal{C}_1}$ (top-left pannel), $\frac{\partial \mathcal{M}_{4bx}}{\partial \mathcal{C}_5}$ (top-right pannel), $\frac{\partial \sigma_4}{\partial \mathcal{C}_1}$ (bottom-left pannel) and $\frac{\partial \sigma_4}{\partial \mathcal{C}_5}$ (bottom-right pannel) vs. good dithering cycle.

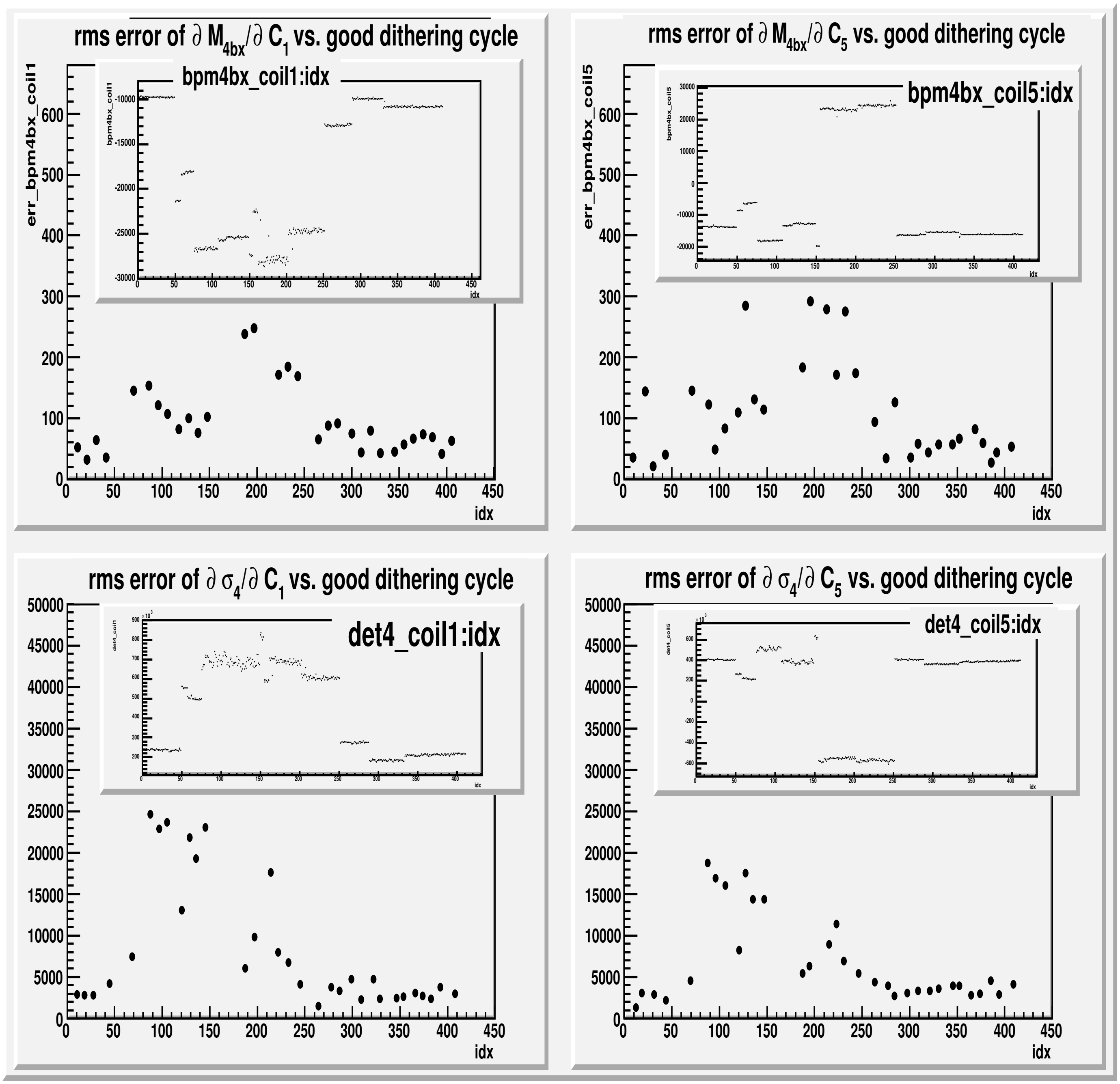

Figure 6.12: Correlations of residuals between $\frac{\partial\mathcal{M}_{4bx}}{\partial\mathcal{C}_5}$ and $\frac{\partial\mathcal{M}_{4ax}}{\partial\mathcal{C}_5}$ (left pannel) and $\frac{\partial\mathcal{M}_{4bx}}{\partial\mathcal{C}_1}$ and $\frac{\partial\mathcal{M}_{4ax}}{\partial\mathcal{C}_1}$ (right pannel).

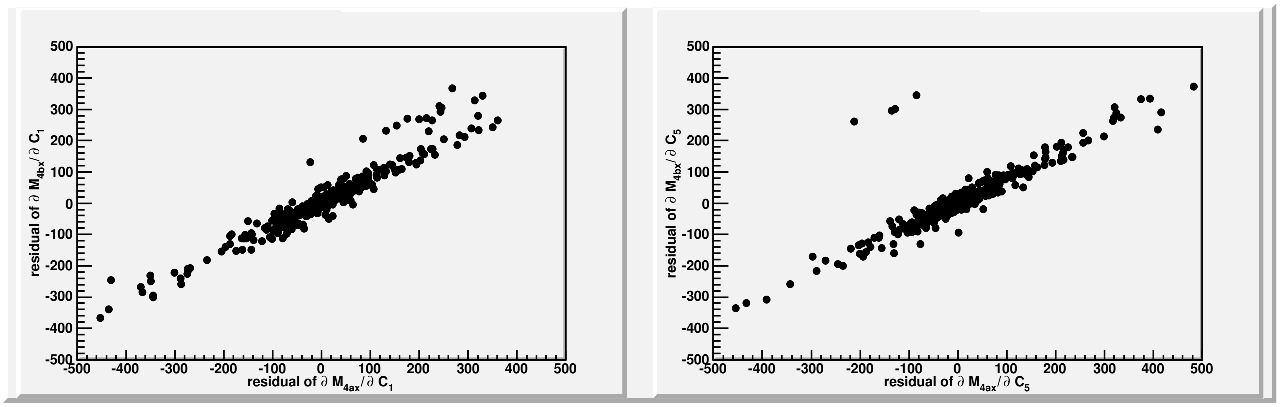

Figure 6.13: Correlations of residuals between $\frac{\partial\mathcal{M}_{4bx}}{\partial\mathcal{C}_5}$ and $\frac{\partial\sigma_4}{\partial\mathcal{C}_5}$ (top-left pannel) and $\frac{\partial\mathcal{M}_{4bx}}{\partial\mathcal{C}_1}$ and $\frac{\partial\sigma_4}{\partial\mathcal{C}_1}$ (bottom-left pannel). Histograms of residuals for $\frac{\partial\sigma_4}{\partial\mathcal{C}_5}$ (top-right pannel) and $\frac{\partial\sigma_4}{\partial\mathcal{C}_1}$ (top-left pannel).

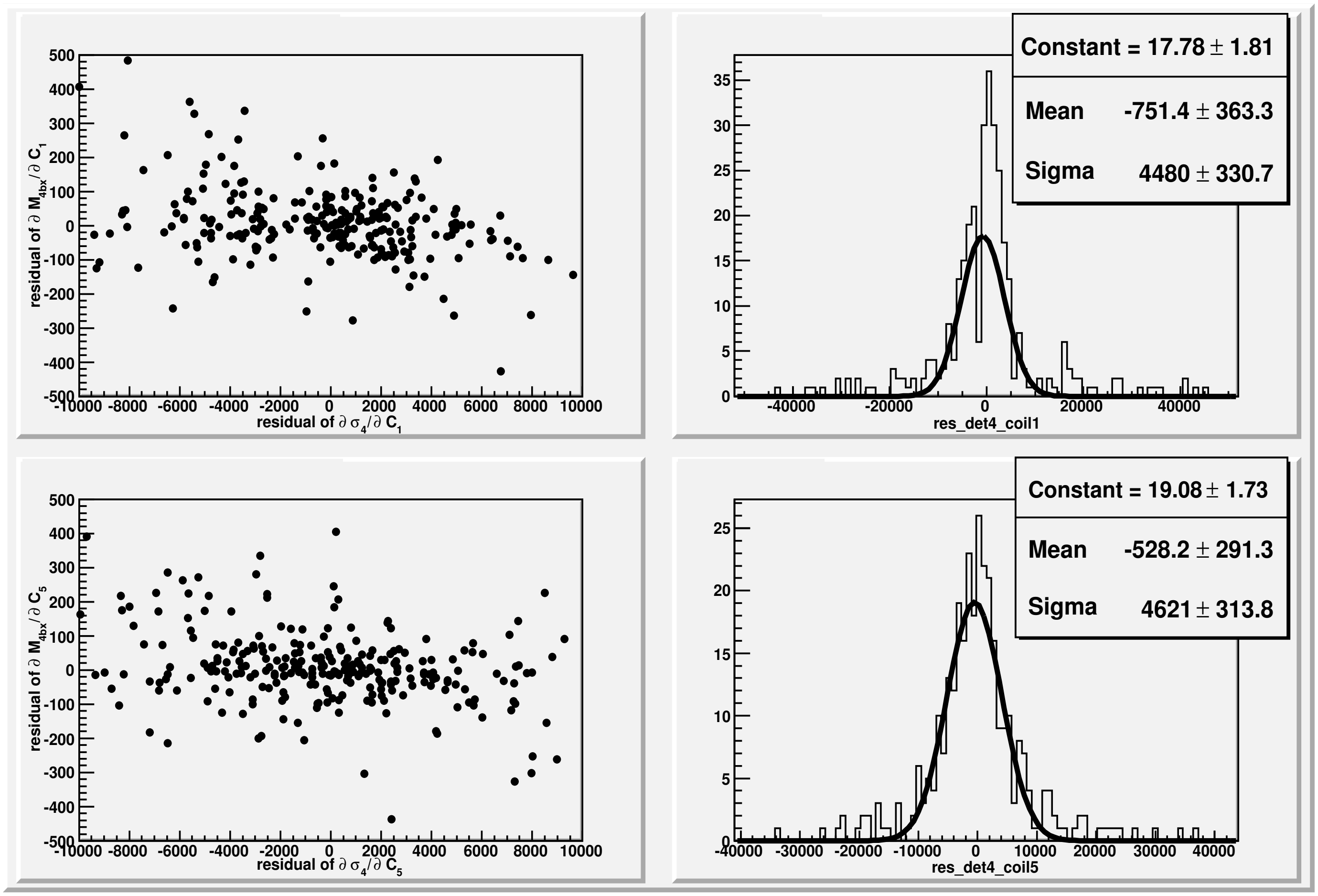

between $\frac{\partial \mathcal{M}_{4bx}}{\partial \mathcal{C}_1}$ and $\frac{\partial \sigma_4}{\partial \mathcal{C}_1}$ (first raw) or between $\frac{\partial \mathcal{M}_{4bx}}{\partial \mathcal{C}_5}$ and $\frac{\partial \sigma_4}{\partial \mathcal{C}_5}$ (second raw) as plotted in Fig. 6.13, the width of residuals is 50 times smaller in $\frac{\partial \mathcal{M}_{4bx}}{\partial \mathcal{C}_5}$ ($\frac{\partial \mathcal{M}_{4bx}}{\partial \mathcal{C}_1}$) than in $\frac{\partial \sigma_4}{\partial \mathcal{C}_5}$ ($\frac{\partial \sigma_4}{\partial \mathcal{C}_1}$), which is 100 times smaller than the average $\frac{\partial \sigma_4}{\partial \mathcal{C}_5}$ ($\frac{\partial \sigma_4}{\partial \mathcal{C}_1}$). In average, the fractional error of $\frac{\partial \sigma_j^m}{\partial \mathcal{C}_i}$ is twice of the fractional error of $\frac{\partial \mathcal{M}_j}{\partial \mathcal{C}_i}$, which is 0.5%. The sum of correlated fractional errors of dithering slopes, σ_i, in quadrature is obtained in Equation 6.12 after quoting all correlations of residuals in pairs of dithering slopes:

$$\text{the total error of}\,\Pi_{i=1}^{m_1}\Pi_{j(j>p)}^{m-m_1}\sigma_i \times \sigma_j^{\pm 1} = \sqrt{\sum_{i=1}^{m}\sigma_{i,i=j}^2 \pm \sum_{i=1}^{m_1}\sum_{j(j>p)}^{m-m_1}\rho_{pq}\sigma_i\sigma_j}, \tag{6.12}$$

where σ_i and σ_j refer to fractional errors of two separate dithering slopes. In Equation 6.12, the positive sign in the correlation coefficient implies the inner product of two dithering slopes; the negative sign instead indicates the division of them. In the next section, we will see how much the correlation of residuals in between a pair of dithering slopes with respect to the same coil can suppress the percentage errors of α, β, $\mathcal{K}$ and Λ. These parameters consist of either single or double divisions of dithering slopes in their definitions.

The (major and minor) beam tune and slow drifting, compared to beam jitters, also lead to the relatively slow change in quantities of dithering slopes, $\frac{\partial \mathcal{M}_j}{\partial \mathcal{C}_i}$ and $\frac{\partial \sigma_j^m}{\partial \mathcal{C}_i}$, as plotted in Fig. 6.15 and Fig. 6.16. A series of coils are perturbed by driving the VME-DAC with a stopped interval of half of minute between them, and the impact of both beam tune and slow drift on varying dithering slopes, corresponding to separate coils driven in series, cannot be easily seen until it lasts to the extend of several dithering groups. It suggests the uncertainty of each type of dithering slope be primarily as a result of the instability of beam jitters.

Figure 6.14: Histograms of residuals for dithering slopes such as $\frac{\partial \mathcal{M}_{4bx}}{\partial \mathcal{C}_1}$ (top-left pannel), $\frac{\partial \mathcal{M}_{4ax}}{\partial \mathcal{C}_1}$ (top-right pannel), $\frac{\partial \mathcal{M}_{4bx}}{\partial \mathcal{C}_5}$ (bottom-left pannel) and $\frac{\partial \mathcal{M}_{4ax}}{\partial \mathcal{C}_5}$ (bottom-right pannel).

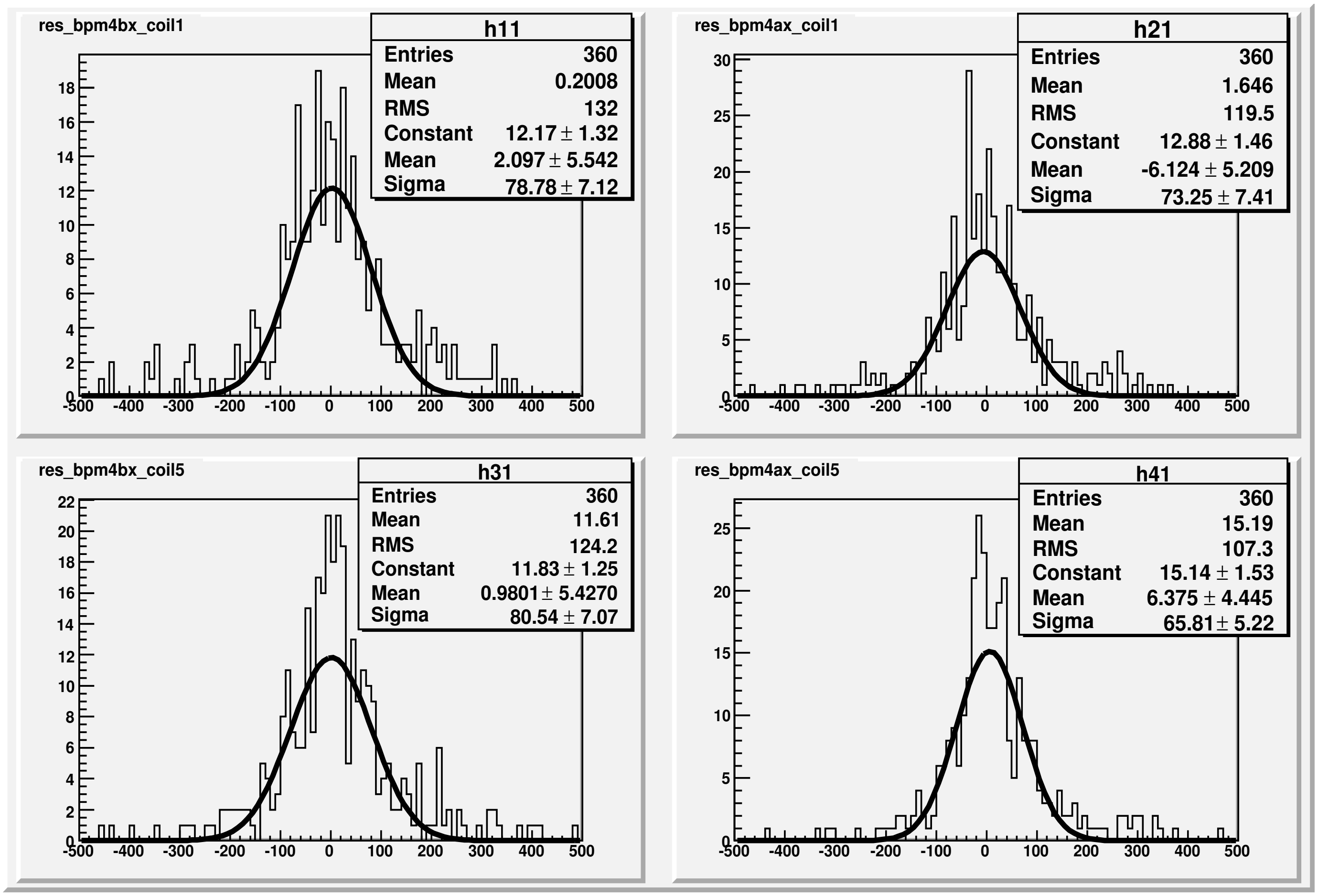

Figure 6.15: History plots of $\frac{\partial \mathcal{M}_{4bx}}{\partial \mathcal{C}_1}$ (black) and $\frac{\partial \mathcal{M}_{4bx}}{\partial \mathcal{C}_5}$ (blue) vs. good dithering cycle.

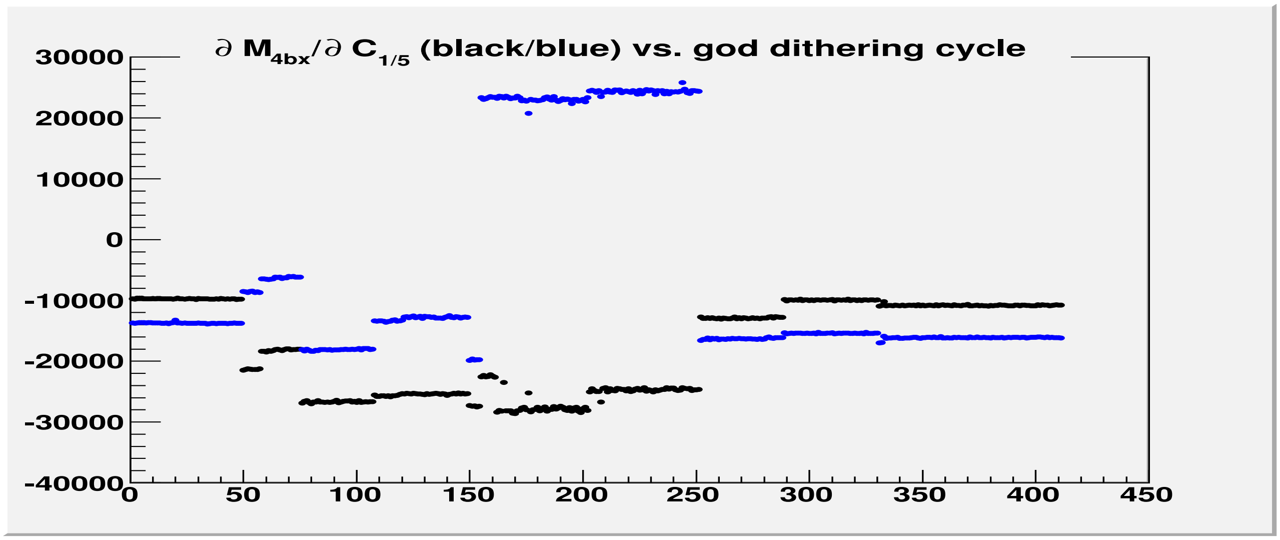

Figure 6.16: History plots of $\frac{\partial \sigma_4}{\partial \mathcal{C}_1}$ (black) and $\frac{\partial \sigma_4}{\partial \mathcal{C}_5}$ (blue) vs. good dithering cycle.

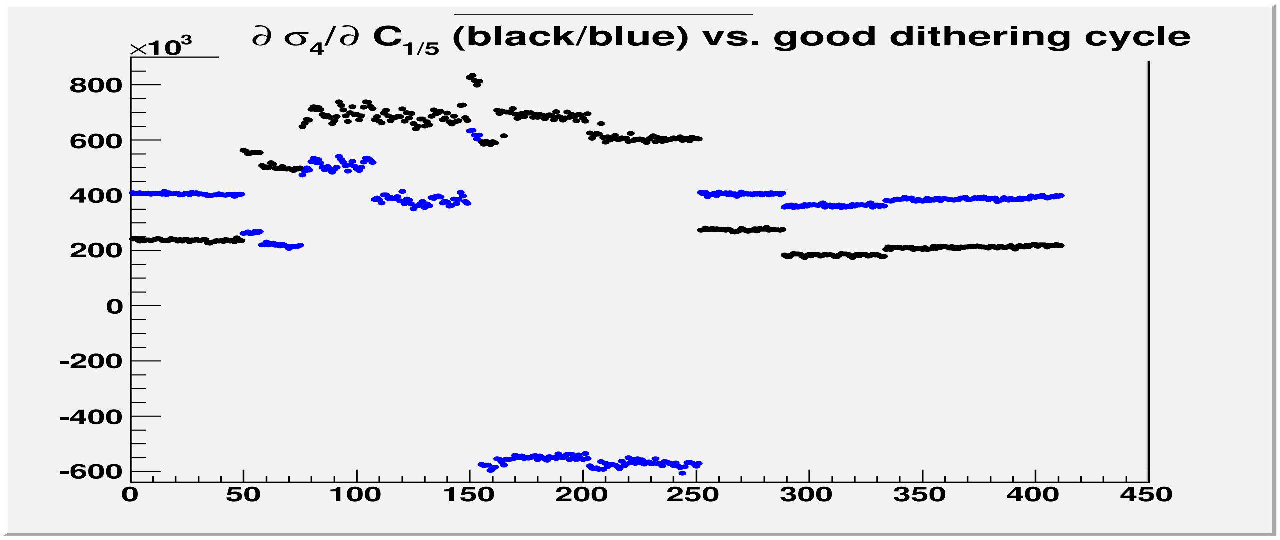

6.4 Fractional errors of α, β, Λ, $\mathcal{K}$ and 2x2 dithering coefficients

The relative error of $1-\alpha$ in Equation 6.13 can be expressed in terms of the fractional error of each individual dithering slope and the residual correlation coefficient in between each pair of slopes.

$$\begin{aligned}\frac{\delta_{1-\alpha}}{1-\alpha} &= \sqrt{\sum_{i=1}^{m}\sigma_i^2+\sum_{i=1}^{m_1}\sum_{j(j>i)}^{m-m_1}\rho_{ij}\sigma_i\sigma_j}, \\ \rho_{ij} &= \frac{\sum_{i=1}^{m_1}\sum_{j(j>i)}^{m-m_1}\Delta_i\Delta_j}{\sqrt{\sum_{i=1}^{m}\Delta_i^2}}.\end{aligned} \tag{6.13}$$

Assuming $\rho_{ij}=0$ (no correlation of residuals in between each pair of dithering slopes with respect to the same coil), both of the fractional errors of $1-\alpha$ and α can be simply expressed as follows:

$$\frac{\delta_{1-\alpha}}{1-\alpha} = \sqrt{(0.5\%)^2\times 4} = 1\% \tag{6.14}$$

$$\frac{\delta\alpha}{\alpha} = (\frac{1-\alpha}{\alpha})\frac{\delta_{1-\alpha}}{1-\alpha} = \begin{cases} 9\times\frac{\delta_{1-\alpha}}{1-\alpha} = 9\times 1\% \quad (\alpha<0.25\,\mathrm{or}\,\alpha>0.4); \\ 1.86\times\frac{\delta_{1-\alpha}}{1-\alpha} = 1.86\times 1\% \quad (\alpha = 0.25-0.4); \end{cases},$$

where $\frac{\delta(\frac{\partial\mathcal{M}_j}{\partial\mathcal{C}_i})}{\frac{\partial\mathcal{M}_j}{\partial\mathcal{C}_i}} \sim 0.5\%$. However, Fig. 6.19 shows us that the fractional error of α in data, where $0.25<\alpha<0.4$, is 0.8% other than 1.86%. Apparently, the fractional error of α drops by 50% after regarding the correlation of beam noises within dithering slopes. It's because the total amount of errors of all of the dithering slopes in Equation 6.13 is significantly suppressed due to the cancellation of a great deal of correlated noises in two pairs of dithering slopes.

Likewise, Λ is defined as one single ratio of $\frac{\partial M_{4bx}}{\partial\mathcal{C}_5}$ to $\frac{\partial M_{4ax}}{\partial\mathcal{C}_5}$, where residuals in both $\frac{\partial M_{4bx}}{\partial\mathcal{C}_5}$

and $\frac{\partial M_{4ax}}{\partial \mathcal{C}_5}$ are highly correlated to each other as drawn in Fig. 6.12. Likewise, as a consequence of the cancellation of correlated noises, the fractional error of Λ is extremely tiny ($\sim 0.1\%$). Despite the negligible fractional errors of α and Λ (both are below 1%), a close to zero magnitude of either α or λ can lead to the corresponding fractional error blowing up. Take α as shown in Equation 6.5, an inappropriate beam tune may give rise to $\frac{\frac{\partial \mathcal{M}_{4bx}}{\partial \mathcal{C}_1} \frac{\partial \mathcal{M}_{4ax}}{\partial \mathcal{C}_5}}{\frac{\partial \mathcal{M}_{4ax}}{\partial \mathcal{C}_1} \frac{\partial \mathcal{M}_{4bx}}{\partial \mathcal{C}_5}} \approx 1$, leading to an almost nullified α and thus an approximately infinite fractional error of α in Equation 6.15.

$$\frac{\delta\alpha}{\alpha} = (\frac{1-\alpha}{\alpha})\frac{\delta_{1-\alpha}}{1-\alpha} \to \infty \tag{6.15}$$

In short,

- a smaller fractional error of α (λ) arises from the cancellation of correlated noises in each pair of dithering slopes;
- a smaller size of α (λ) leads to the fractional error of α (λ) expanding unlimitedly.

Another parameter, β, is formed by replacing the dithering slope, $\frac{\partial M_{4bx}}{\partial \mathcal{C}_i}$, in α with $\frac{\partial \sigma_j^m}{\partial \mathcal{C}_i}$; therefore, it is a double ratio of $\frac{\partial \sigma_j^m}{\partial \mathcal{C}_i}$ to $\frac{\partial M_j}{\partial \mathcal{C}_i}$. According to Fig. 6.17, a roughly constant ratio of β to α indicates that β varies with α. Like α (or λ), the magnitude of β is also influenced by the effect of tune changes. A maladjustment of the tune also results in an approximately infinite fractional error of β in Equation 6.16.

$$\frac{\delta\beta}{\beta} = (\frac{1-\beta}{\beta})\frac{\delta_{1-\beta}}{1-\beta} \to \infty \tag{6.16}$$

Presumably both of the sizes of α and β are controlled to remain reasonable under the proper choice of the beam tune, a non-zero but much weaker correlations of residuals in between $\frac{\partial \sigma_j^m}{\partial \mathcal{C}_i}$ and $\frac{\partial M_j}{\partial \mathcal{C}_i}$ for β than in between $\frac{\partial M_{4ax}}{\partial \mathcal{C}_i}$ and $\frac{\partial M_{4bx}}{\partial \mathcal{C}_i}$ for α results in a much larger fractional error of β than that of α. An only 10% ($\rho_{ij} \sim 0.33$) contributions of correlated noises to the cancellation of the quadratic sum of all error sources as shown in Equation 6.12 makes β noisier than α, where the amount of correlated noise contributions ($\rho_{ij} \sim 0.99$) almost fully cancels out the quadratic sum of dithering slope uncertainties, regarded as independent (uncorrelated) noises.

In real data, Fig. 6.19 and Fig. 6.20 show that the fractional error of β are around 2% and 12% for $0.25 < \alpha < 0.4$ and $\alpha < 0.25$ or $\alpha > 0.4$, respectively. Among parameters defined in Sec. 6.2, the fractional error of β is the most significant one after taking the residual correlation of dithering slopes into consideration. Consequently, as mentioned in Sec. 6.2, the fractional error of β is directly used to indicate the noise level of dithering coefficients.

Like Λ, $\mathcal{K}$ is also composed of a single ratio of two dithering slopes. The numerator of Λ is $\frac{\partial M_j}{\partial \mathcal{C}_i}$. In contrast, the numerator of $\mathcal{K}$ is $\frac{\partial \sigma_j^m}{\partial \mathcal{C}_i}$, whose residuals are merely weakly correlated with residuals of $\frac{\partial M_j}{\partial \mathcal{C}_i}$. Hence, the residual correlation coefficient of $\mathcal{K}$ is about three times smaller than that of Λ. The fractional error of $\mathcal{K}$ is around $(1-2)\%$; the fractional error of Λ is below 1% instead. Overall, both of the magnitudes of Λ and $\mathcal{K}$ are relatively steady with time.

Without regarding the energy fluctuation (we assumed the energy is rigidly fixed to some value.), a pair of 2x2 dithering coefficients as shown in Fig. 6.21 remain fairly constant with time. As mentioned in Sec. 6.2, the fractional error [7] of β can be approximately regarded as the unit size of fractional error of each dithering coefficient. In addition, Equation 6.17 and Fig. 6.22 show that the fractional error of $\frac{\partial \sigma_j^m}{\partial \mathcal{M}_{4ax}}$ is three times larger than that of $\frac{\partial \sigma_j^m}{\partial \mathcal{M}_{4bx}}$. Both Fig. 6.23 and Fig. 6.24 prove that:

- the fractional error of β is the unit size of the fractional error of each dithering

---

[7] The fractional error is determined by taking the RMS of either β or $\frac{\partial \sigma_j^m}{\partial \mathcal{M}_{4ax}}$ (or $\frac{\partial \sigma_j^m}{\partial \mathcal{M}_{4bx}}$) histogram which was re-booked in every ten entries to divide by the mean (weighted-average) of the histogram. Due to the slight non-uniformity of $\frac{\partial \sigma_j^m}{\partial \mathcal{M}_{4ax}}$ (or $\frac{\partial \sigma_j^m}{\partial \mathcal{M}_{4bx}}$), the whole data were chopped into three groups: 3445-3492, 3626-4412 and 4522-4755 in the cycle-average.

Figure 6.17: constant ratio, β over α, history plot.

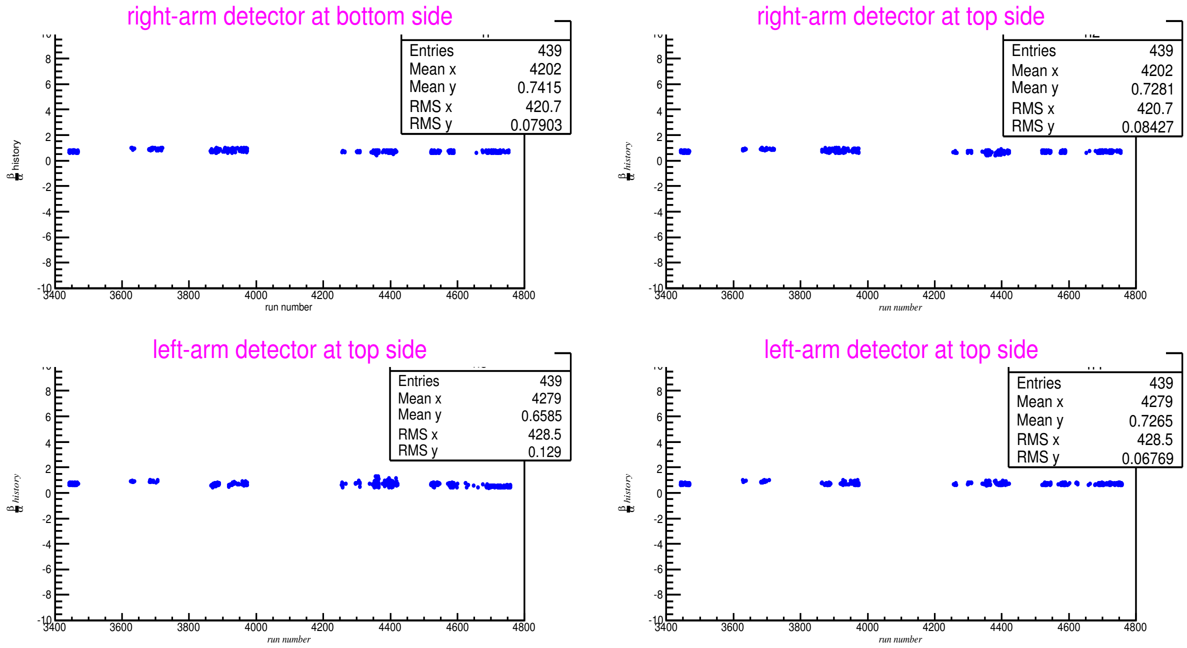

coefficient;

- the fractional error of $\frac{\partial\sigma_j^m}{\partial\mathcal{M}_{4ax}}$ = 3× the fractional error of $\frac{\partial\sigma_j^m}{\partial\mathcal{M}_{4bx}}$ (see Equation 6.17):
  - $\frac{\delta(\frac{\partial\sigma_j^m}{\partial\mathcal{M}_{4ax}})}{|\frac{\partial\sigma_j^m}{\partial\mathcal{M}_{4ax}}|} \approx 3\frac{\delta\beta}{\beta}$
  - $\frac{\delta(\frac{\partial\sigma_j^m}{\partial\mathcal{M}_{4bx}})}{|\frac{\partial\sigma_j^m}{\partial\mathcal{M}_{4bx}}|} \approx \frac{\delta\beta}{\beta}$

$$\begin{aligned}
\sigma(\frac{\partial\sigma_j^m}{\partial\mathcal{M}_{4ax}}) &= \frac{\delta(\frac{\partial\sigma_j^m}{\partial\mathcal{M}_{4ax}})}{|\frac{\partial\sigma_j^m}{\partial\mathcal{M}_{4ax}}|} = \frac{\frac{\beta}{\alpha}}{|1-\frac{\beta}{\alpha}|}\frac{\delta(\frac{\beta}{\alpha})}{\frac{\beta}{\alpha}} \sim 3\frac{\delta\beta}{\beta} \qquad (6.17)\\
\sigma(\frac{\partial\sigma_j^m}{\partial\mathcal{M}_{4bx}}) &= \frac{\delta(\frac{\partial\sigma_j^m}{\partial\mathcal{M}_{4bx}})}{|\frac{\partial\sigma_j^m}{\partial\mathcal{M}_{4bx}}|} \sim \frac{\delta\beta}{\beta}
\end{aligned}$$

Figure 6.18: α (red solid dot), β (blue solid dot), Λ (magenta solid dot) and $\mathcal{K}$ (green solid dot) history plots.

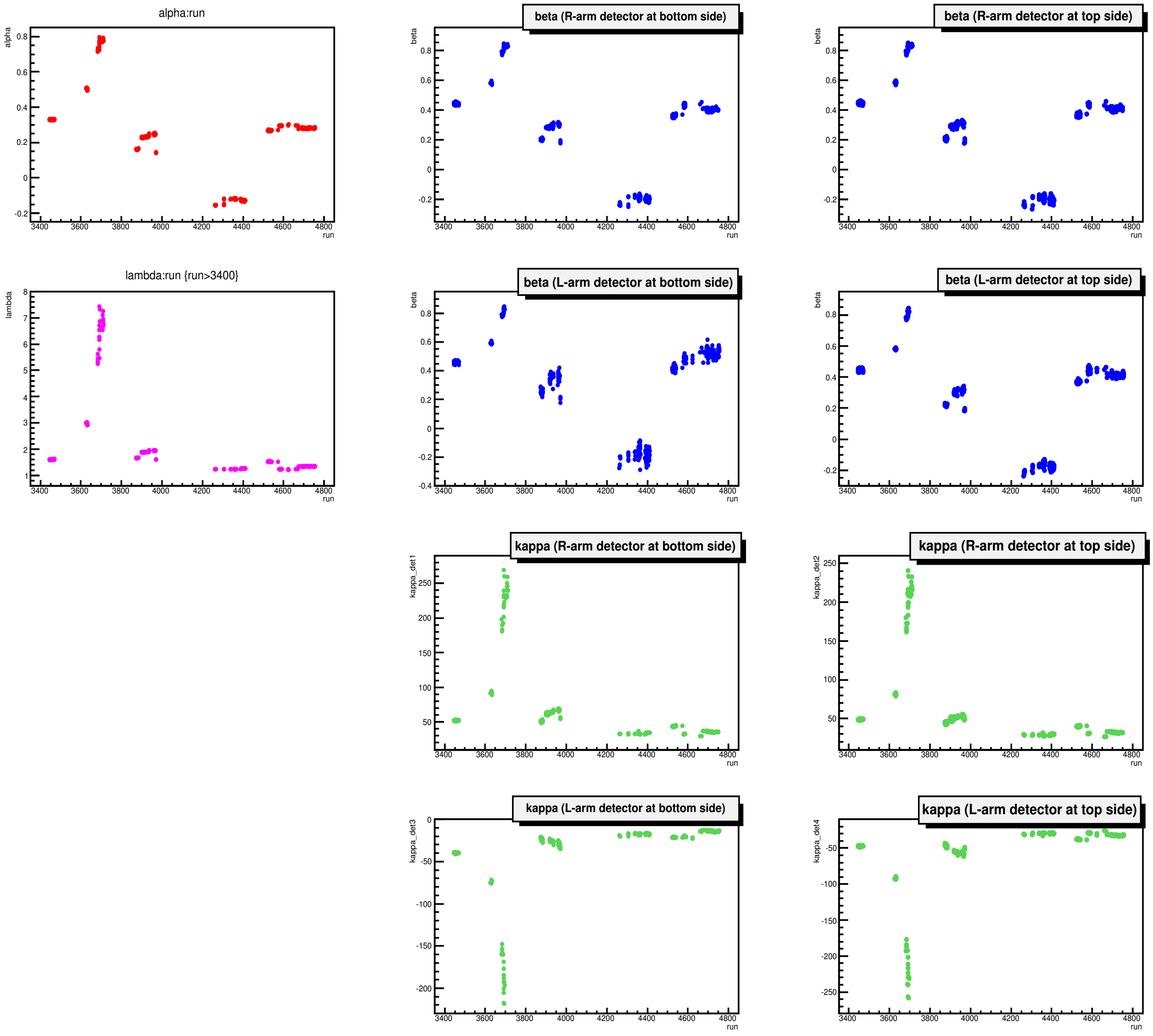

Figure 6.19: fractional errors of α (red), β (blue), Λ (magenta) and $\mathcal{K}$ (green) (in the cycle-average level), where $0.25 < \alpha < 0.4$.

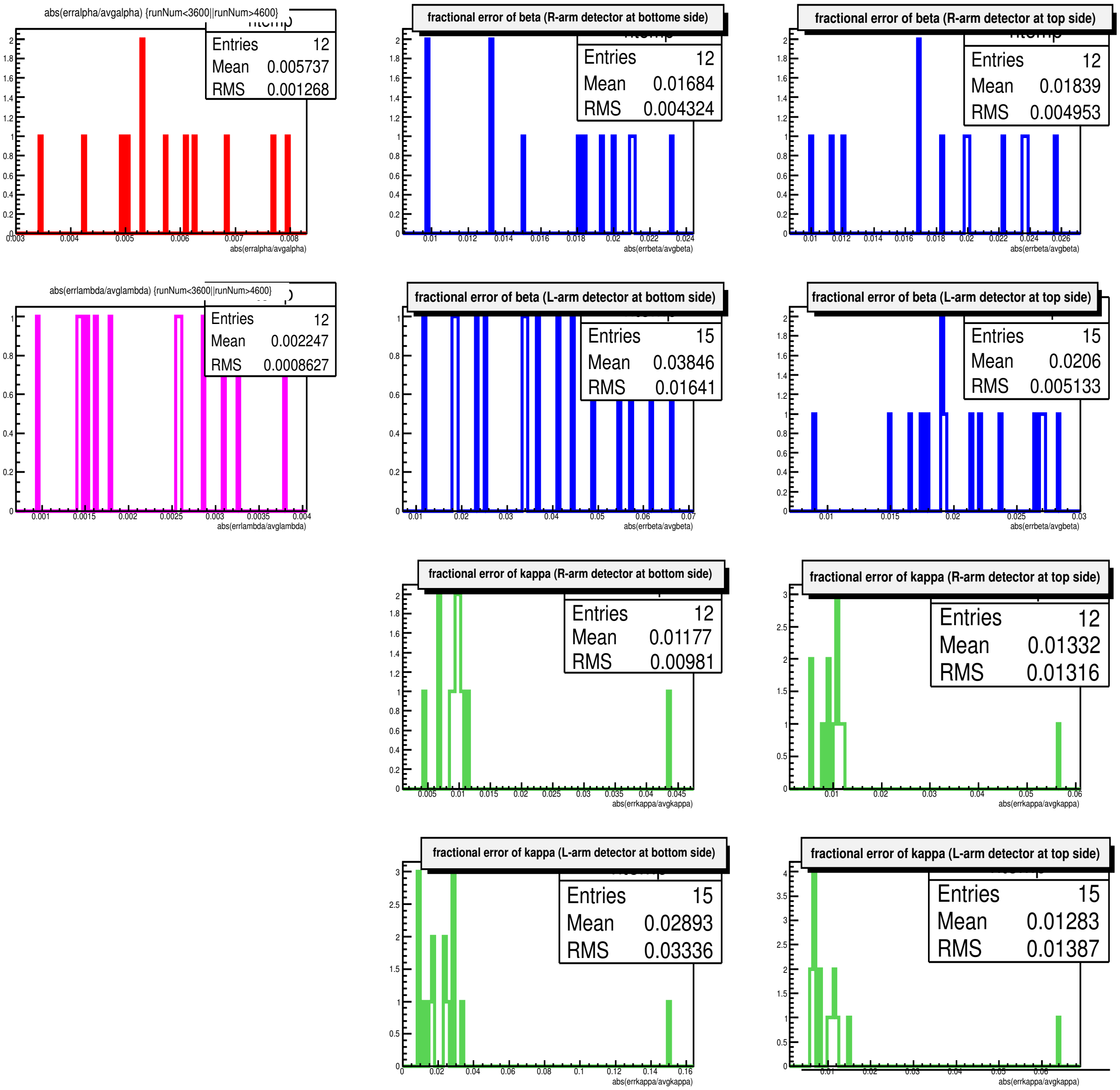

Figure 6.20: fractional errors of α (red), β (blue), Λ (magenta) and $\mathcal{K}$ (green) (in the cycle-average level), where $\alpha > 0.4$ or $\alpha < 0.25$.

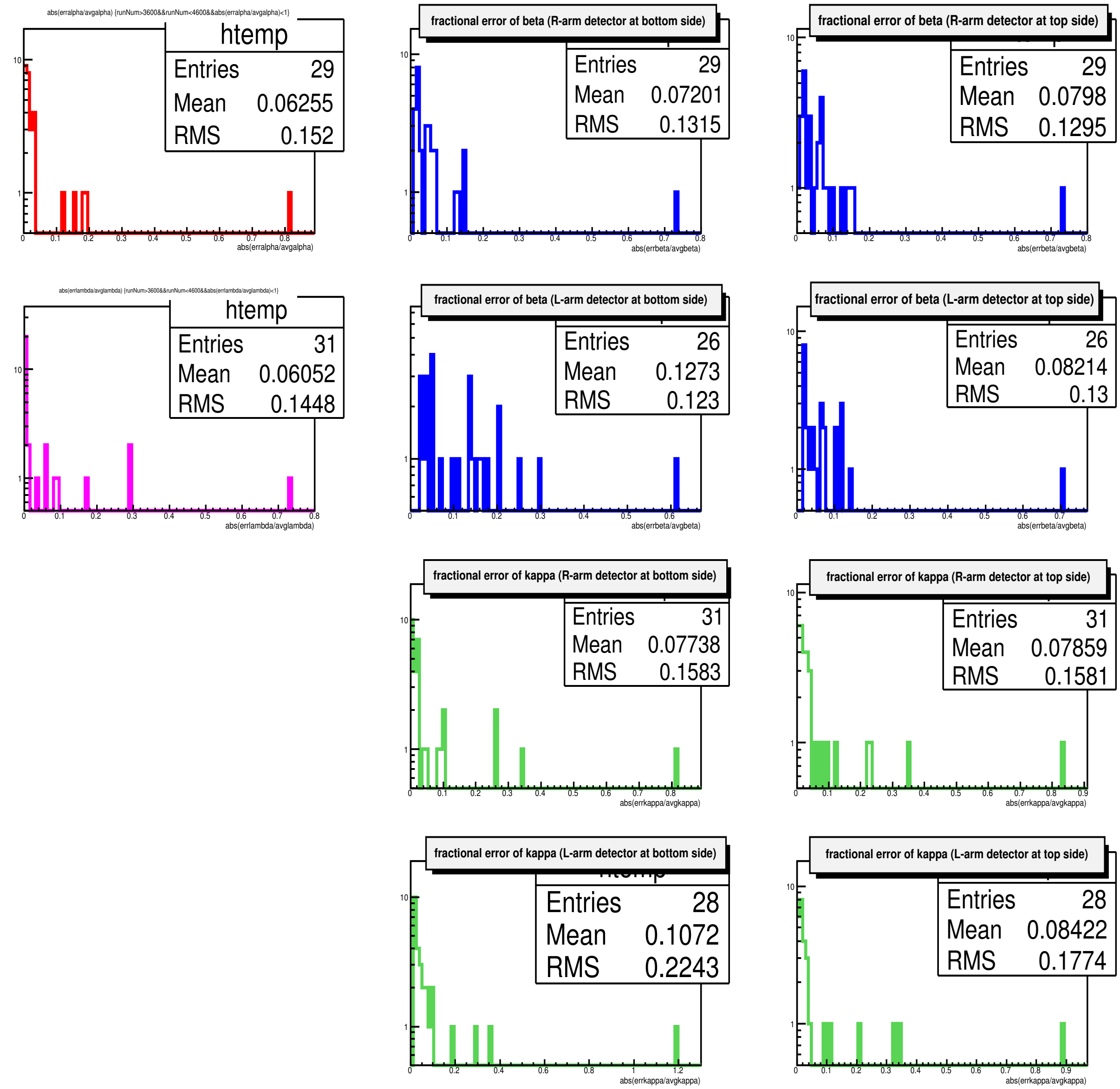

Figure 6.21: 2x2 (top panel) $\frac{\partial\sigma_j^m}{\partial\mathcal{M}_{4ax}}$ and (bottom panel) $\frac{\partial\sigma_j^m}{\partial\mathcal{M}_{4bx}}$ dithering coefficient history plots (unit: $\frac{ppm}{\mu m}$). From left to right: right-arm detector at the bottom side; right-arm detector at the top side; left-arm detector at the bottom side; left-arm detector at the top side.

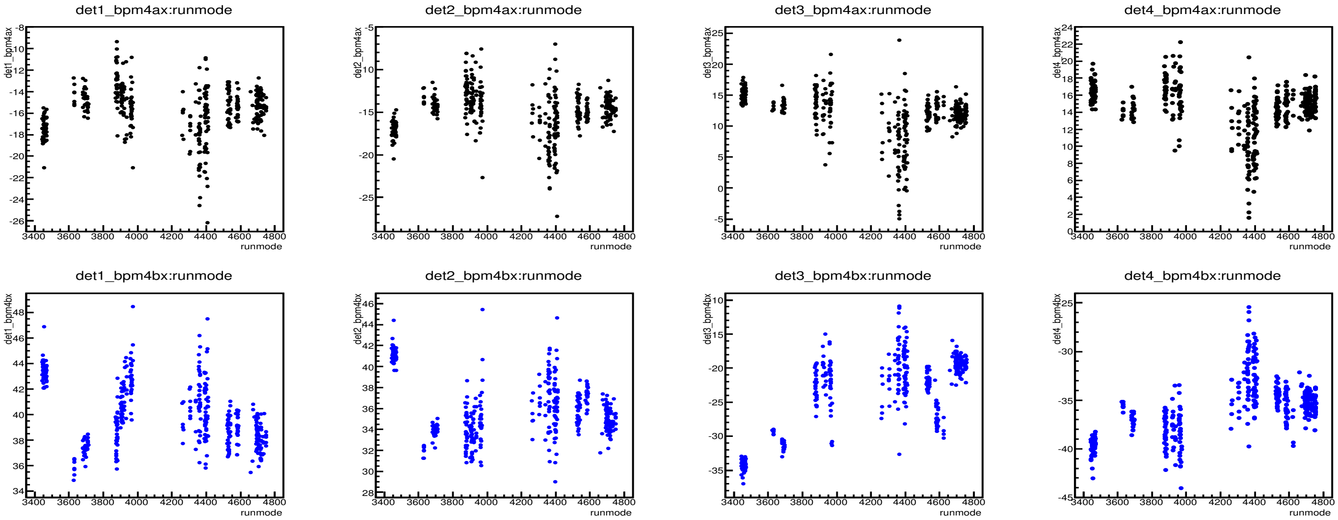

6.5 Introduction to 3x3 dithering analysis

In addition to considering the effect of possible energy fluctuations, we try finding the reason to account for the unusually significant sensitivity of the cross-section to energy fluctuations. Hence, the energy is put back and added into 2x2 to form a 3x3 matrix. So, we have:

$$\begin{pmatrix} \frac{\partial\sigma_j^m}{\partial\mathcal{C}_1} \\ \frac{\partial\sigma_j^m}{\partial\mathcal{C}_5} \\ \frac{\partial\sigma_j^m}{\partial\mathcal{C}_8} \end{pmatrix} = \mathcal{D}M_{3x3} \begin{pmatrix} \frac{\partial\sigma_j^m}{\partial\mathcal{M}_{12x}} \\ \frac{\partial\sigma_j^m}{\partial\mathcal{M}_{4ax}} \\ \frac{\partial\sigma_j^m}{\partial\mathcal{M}_{4bx}} \end{pmatrix},$$

where $\mathcal{D}M_{3x3}$ below is called 3x3 dithering matrix.

$$\mathcal{D}M_{3x3} = \begin{pmatrix} \frac{\partial\mathcal{M}_{12x}}{\partial\mathcal{C}_1} & \frac{\partial\mathcal{M}_{4ax}}{\partial\mathcal{C}_1} & \frac{\partial\mathcal{M}_{4bx}}{\partial\mathcal{C}_1} \\ \frac{\partial\mathcal{M}_{12x}}{\partial\mathcal{C}_5} & \frac{\partial\mathcal{M}_{4ax}}{\partial\mathcal{C}_5} & \frac{\partial\mathcal{M}_{4bx}}{\partial\mathcal{C}_5} \\ \frac{\partial\mathcal{M}_{12x}}{\partial\mathcal{C}_8} & \frac{\partial\mathcal{M}_{4ax}}{\partial\mathcal{C}_8} & \frac{\partial\mathcal{M}_{4bx}}{\partial\mathcal{C}_8} \end{pmatrix}$$

Figure 6.22: the fractional error comparison/correlation between $\sigma(\frac{\partial \sigma_j^m}{\partial \mathcal{M}_{4ax}})$ (x-axis) and $\sigma(\frac{\partial \sigma_j^m}{\partial \mathcal{M}_{4bx}})$ (y-axis) for the individual detectors. Upper left: the right-arm detector on the bottom side; upper right: the right-arm detector on the top side; lower left: the left-arm detector on the bottom side; lower right: the left-arm detector on the top side.

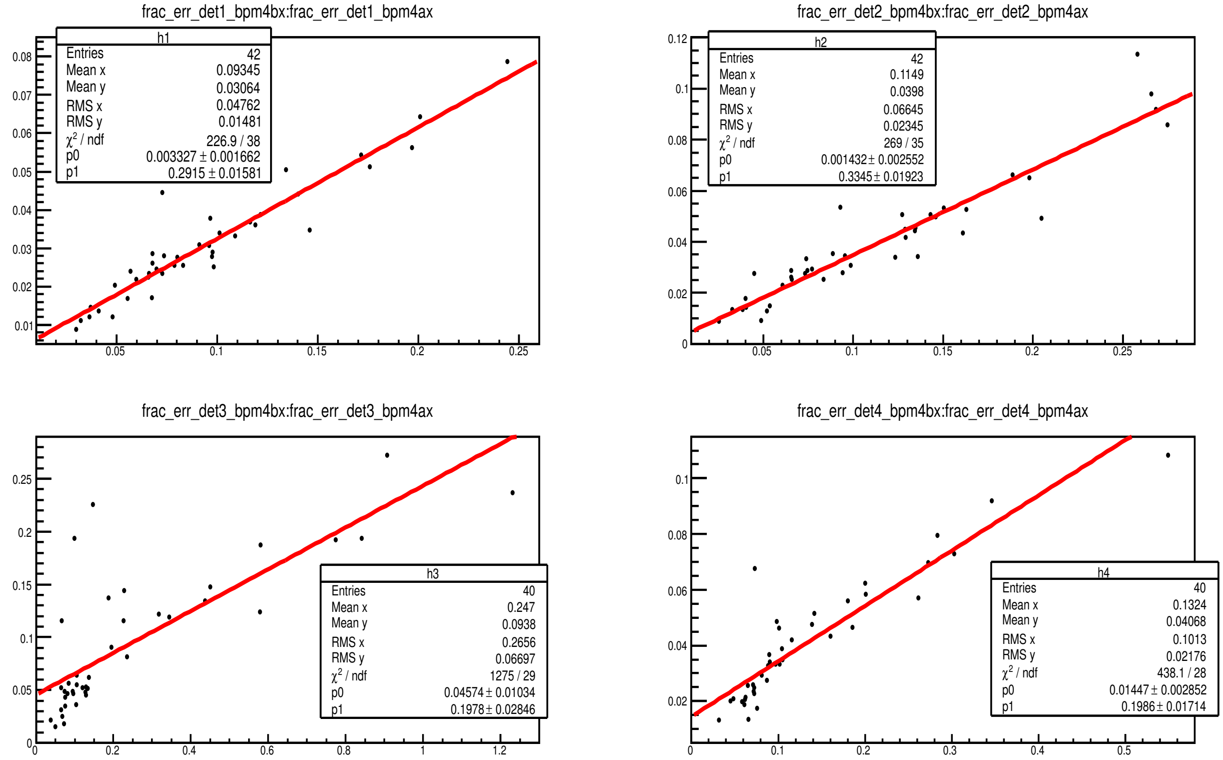

Figure 6.23: the fractional error comparison between $\sigma\beta$ (blue solid dot) and $\sigma(\frac{\partial\sigma_j^m}{\partial\mathcal{M}_{4ax}})$ (open square) for the individual detectors. Upper left: the right-arm detector on the bottom side; upper right: the right-arm detector on the top side; lower left: the left-arm detector on the bottom side; lower right: the left-arm detector on the top side.

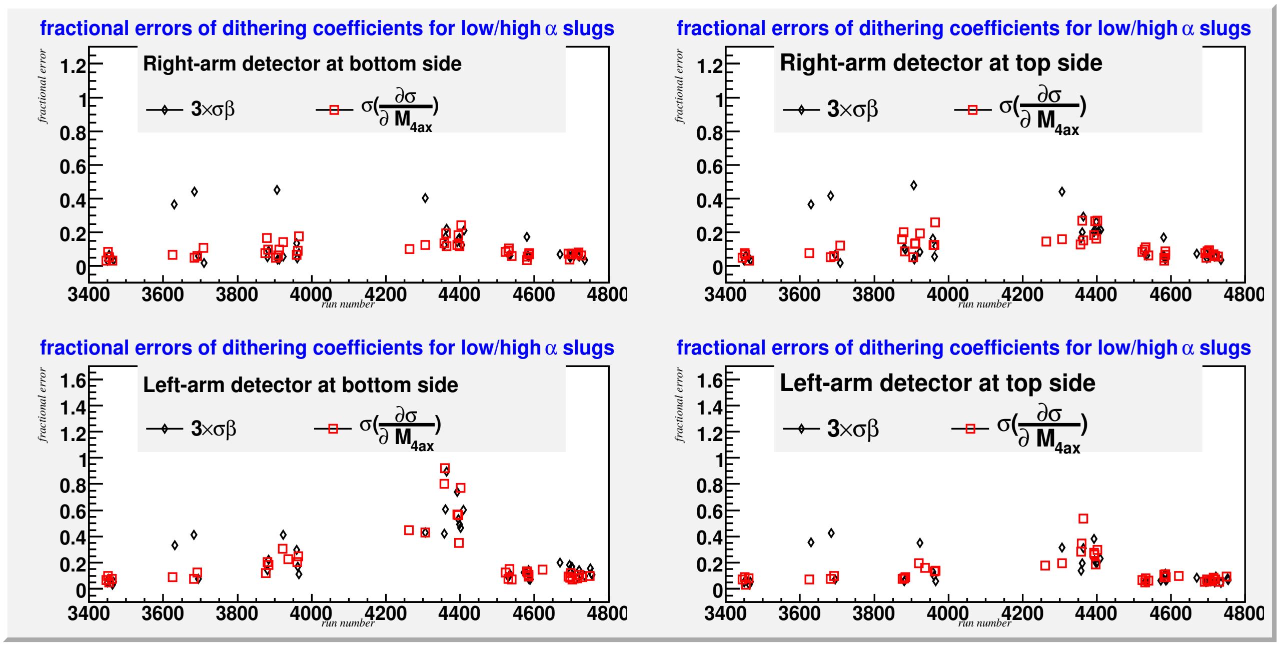

We re-parameterized $\mathcal{D}M_{3x3}$ in terms of one 2x2 parameterized matrix, composed of α, β, Λ and $\mathcal{K}$, plus three additionally introduced parameters, say, δ, Γ and $\mathcal{B}'$ as defined below:

$$\mathcal{K}\begin{pmatrix} 1-\beta \\ 1 \\ \mathcal{B}' \end{pmatrix} = \begin{pmatrix} \Gamma & 1 & 1-\alpha \\ \delta & 0 & \alpha \\ 1 & 0 & 0 \end{pmatrix} \begin{pmatrix} \frac{\partial\sigma_j^m}{\partial\mathcal{M}_{12x}} \\ \frac{\partial\sigma_j^m}{\partial\mathcal{M}_{4ax}} \\ \Lambda\frac{\partial\sigma_j^m}{\partial\mathcal{M}_{4bx}} \end{pmatrix},$$

where:

$$\delta = \frac{\frac{\partial\mathcal{M}_{12x}}{\partial\mathcal{C}_5}}{\frac{\partial\mathcal{M}_{4ax}}{\partial\mathcal{C}_5}} - \frac{\frac{\partial\mathcal{M}_{12x}}{\partial\mathcal{C}_1}}{\frac{\partial\mathcal{M}_{4ax}}{\partial\mathcal{C}_1}}, \tag{6.18}$$

$$\Gamma = \frac{\frac{\partial\mathcal{M}_{12x}}{\partial\mathcal{C}_1}}{\frac{\partial\mathcal{M}_{4ax}}{\partial\mathcal{C}_1}}, \tag{6.19}$$

Figure 6.24: the fractional error comparison between $\sigma\beta$ (blue solid dot) and $\sigma(\frac{\partial\sigma_j^m}{\partial\mathcal{M}_{4bx}})$ (open triangle) for the individual detectors. Upper left: the right-arm detector on the bottom side; upper right: the right-arm detector on the top side; lower left: the left-arm detector on the bottom side; lower right: the left-arm detector on the top side.

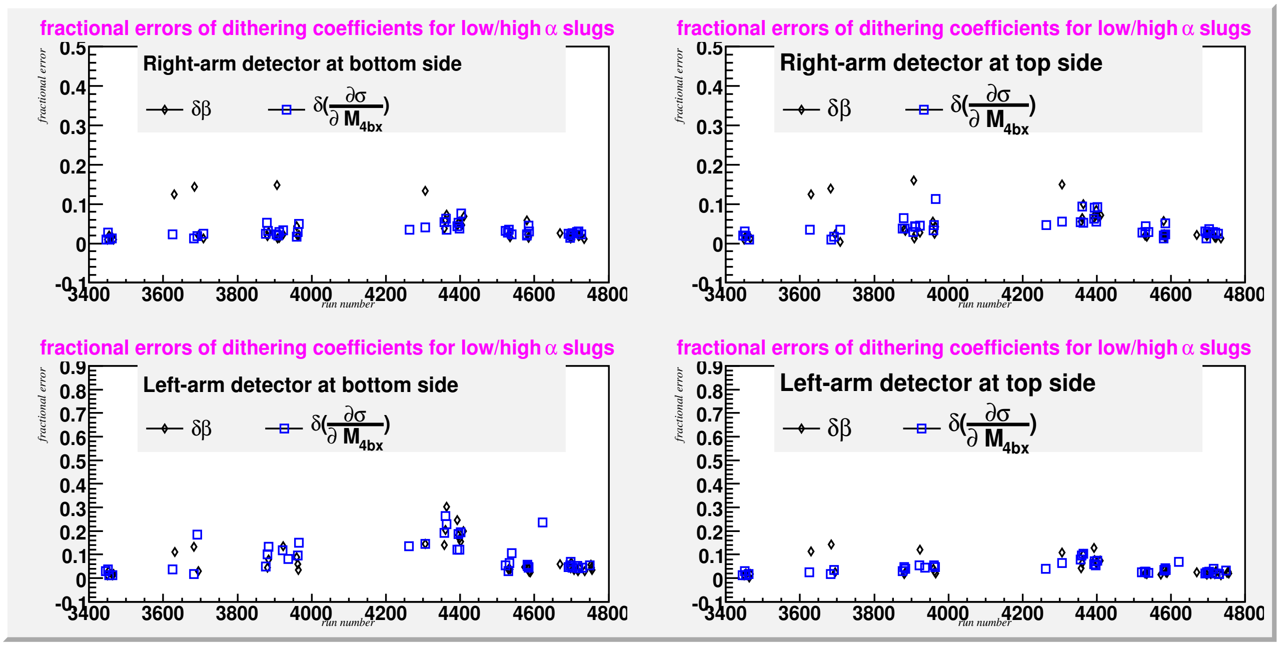

$$\mathcal{B}' = \frac{\frac{\partial\sigma_j^m}{\partial\mathcal{C}_8}\frac{\partial\mathcal{M}_{4ax}}{\partial\mathcal{C}_5}}{\frac{\partial\sigma_j^m}{\partial\mathcal{C}_5}\frac{\partial\mathcal{M}_{12x}}{\partial\mathcal{C}_5}}. \tag{6.20}$$

Similar to definitions of α and β in Equation 6.5 and Equation 6.6, one subtraction is involved in the definition of δ. The maladjustment is also likely to cause the magnitude of δ close to be zero, so that the fractional error of δ in Equation 6.21 approximates to the infinity which is disallowed.

$$\begin{aligned}
\frac{\delta\alpha}{\alpha} &= (\frac{1-\alpha}{\alpha})\frac{\delta_{1-\alpha}}{1-\alpha} \rightarrow \infty, \quad \text{as } \alpha \rightarrow 0 \\
\frac{\delta\beta}{\beta} &= (\frac{1-\beta}{\beta})\frac{\delta_{1-\beta}}{1-\beta} \rightarrow \infty, \quad \text{as } \beta \rightarrow 0 \\
\frac{\delta\delta}{\delta} &\rightarrow \infty, \quad \text{as } \delta \rightarrow 0.
\end{aligned} \tag{6.21}$$

All parameters listed in Table 6.1 are now categorized into two groups: one is called the singularity group; the other is called the scale group.

Table 6.1: parameter categories.

category	singularity	scale
	α, β, δ	$\mathcal{K}$, Λ, Γ, $\mathcal{B}'$

The 3x3 dithering coefficients can be thus expressed in terms of a pair of 2x2 dithering coefficients and one energy-related dithering coefficient:

$$\begin{aligned}
\frac{\partial\sigma_j^m}{\partial\mathcal{M}_{12x}} &= \mathcal{K}\mathcal{B}', \\
(\frac{\partial\sigma_j^m}{\partial\mathcal{M}_{4ax}})_{3x3} &= \frac{\partial\mathcal{M}_{12x}}{\partial\mathcal{M}_{4ax}}\frac{\partial\sigma_j^m}{\partial\mathcal{M}_{12x}} + (\frac{\partial\sigma_j^m}{\partial\mathcal{M}_{4ax}})_{2x2} \\
&= -[\,(\,\frac{1}{\alpha} - 1\,)\,\delta - \Gamma\,]\,\frac{\partial\sigma_j^m}{\partial\mathcal{M}_{12x}} + (\frac{\partial\sigma_j^m}{\partial\mathcal{M}_{4ax}})_{2x2}, \\
(\frac{\partial\sigma_j^m}{\partial\mathcal{M}_{4bx}})_{3x3} &= \frac{\partial\mathcal{M}_{12x}}{\partial\mathcal{M}_{4bx}}\frac{\partial\sigma_j^m}{\partial\mathcal{M}_{12x}} + (\frac{\partial\sigma_j^m}{\partial\mathcal{M}_{4bx}})_{2x2} \\
&= \frac{\delta}{\alpha\Lambda}\frac{\partial\sigma_j^m}{\partial\mathcal{M}_{12x}} + (\frac{\partial\sigma_j^m}{\partial\mathcal{M}_{4bx}})_{2x2}.
\end{aligned} \tag{6.22}$$

Ideally, the quantity of $(\frac{\partial\sigma_j^m}{\partial\mathcal{M}_{4ax,4bx}})_{3x3}$ is supposed to be similar to that of $(\frac{\partial\sigma_j^m}{\partial\mathcal{M}_{4ax,4bx}})_{2x2}$, if and only if $\frac{\partial\mathcal{M}_{12x}}{\partial\mathcal{M}_{4ax}}$ $(-[\,(\,\frac{1}{\alpha} - 1\,)\,\delta - \Gamma\,])$ and $\frac{\partial\mathcal{M}_{12x}}{\partial\mathcal{M}_{4bx}}$ $(\frac{\delta}{\alpha\Lambda})$ in Equation 6.22 are close to zero. We, however, found both $\frac{\partial\mathcal{M}_{12x}}{\partial\mathcal{M}_{4ax}}$ and $\frac{\partial\mathcal{M}_{12x}}{\partial\mathcal{M}_{4bx}}$ are unusually large in some data sets due to the inappropriate beam tune. See Fig. 6.29.

Non-zero $\frac{\partial\mathcal{M}_{12x}}{\partial\mathcal{M}_{4ax}}$ and $\frac{\partial\mathcal{M}_{12x}}{\partial\mathcal{M}_{4bx}}$ imply that the position fluctuation [8] around the region, where BPM12x is situated, turns into the angular fluctuation [9] as seen from the collimator, downstream of the target. Fig. 6.25 demonstrates how the position fluctuation near BPM12x turns into the angular fluctuation after the scattering from the target.

A pair of beam position monitors, located upstream of the target, are insensitive to the

---

[8] the direction of the displacement is the same for both beam position monitors. $\mathcal{N}_1 = \mathcal{M}_{4ax} + \mathcal{M}_{4bx}$

[9] the sign of the displacement in one beam position is opposite to that in the other. $\mathcal{N}_2 = \mathcal{M}_{4ax} - \mathcal{M}_{4bx}$

Figure 6.25: a simple depiction of position and angular fluctuations as measured in the collimator.

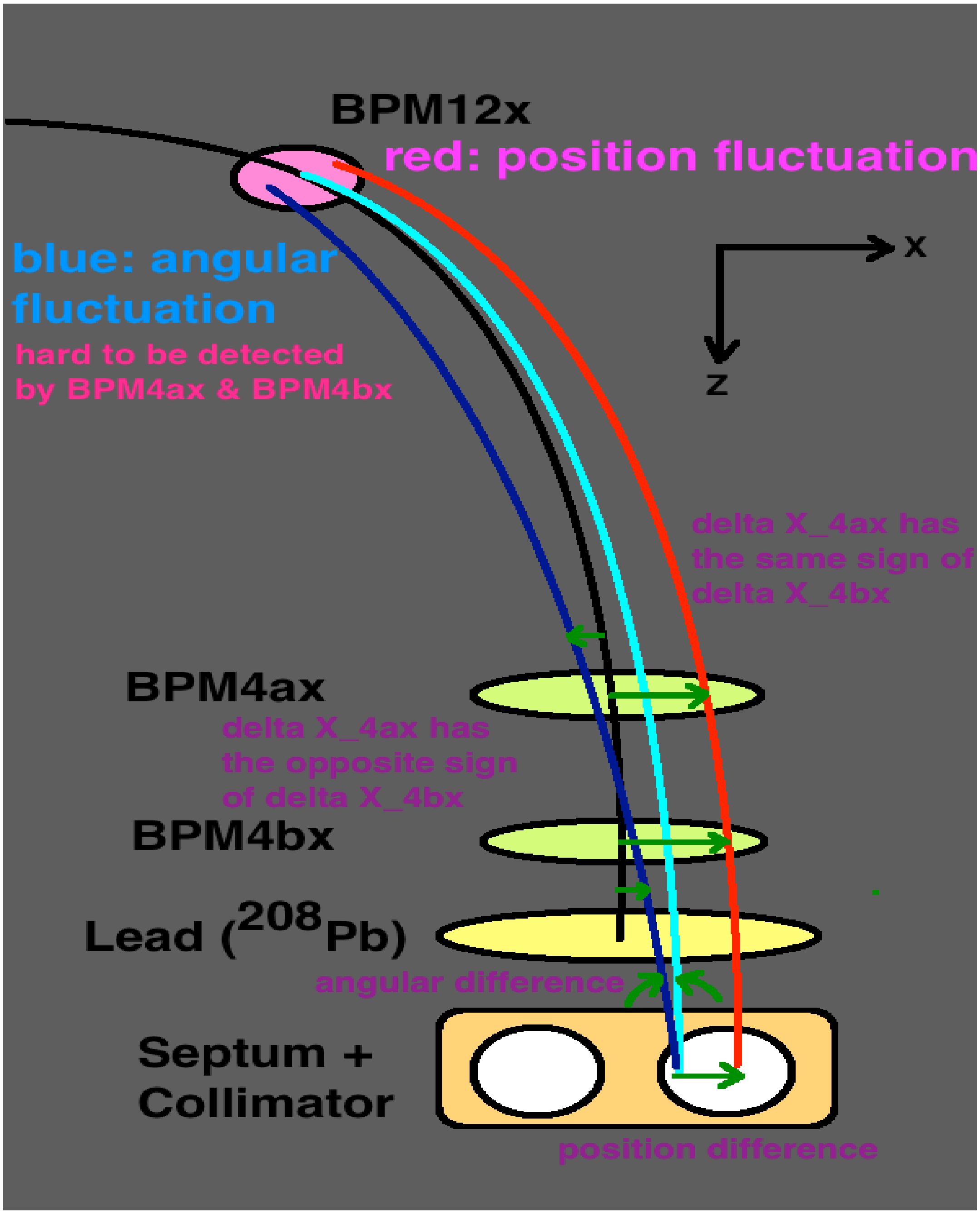
BPM12x
red: position fluctuation
blue: angular fluctuation
hard to be detected by BPM4ax & BPM4bx
x
z
delta X_4ax has the same sign of delta X_4bx
BPM4ax
delta X_4ax has the opposite sign of delta X_4bx
BPM4bx
Lead (208Pb)
angular difference
Septum + Collimator
position difference

Figure 6.26: (red open square) $\frac{\partial \mathcal{M}_{12x}}{\partial \mathcal{N}_1}$ (correlation to the position fluctuations) and (blue open triangle) $\frac{\partial \mathcal{M}_{12x}}{\partial \mathcal{N}_2}$ (correlation to the angular fluctuations) history plot.

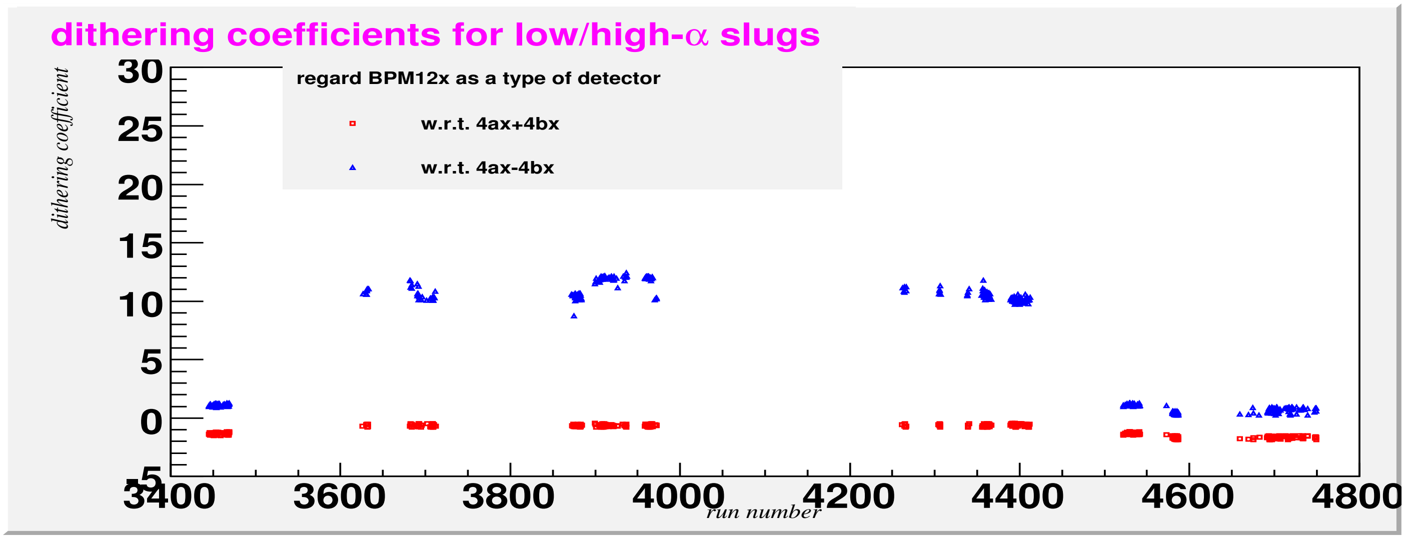

angular fluctuation, for they are close to each other, and limited to be only sensitive to the position variation. However, by means of monitoring $\frac{\partial \mathcal{M}_{12x}}{\partial \mathcal{N}_2}$ as drawn in Fig. 6.26, the impact of the angular fluctuation on the cross-section can be detected and measured. The helicity-correlated beam asymmetry as a result of the angular fluctuation is thus able to be calculated. In order to further suppress the angular fluctuation, we can adjust the beam optics by tuning quadrupoles sitting between BPM12x (beam energy monitor) and a pair of beam position monitors (BPM4ax and BPM4bx) along the beam line. Consequently, we need one additional parameter used to indicate the operation of beam tune changes, leading to well-controlled angular fluctuations. Two questions listed below are then arisen:

- which parameter does matter to reflect the beam tune option?
- what is the criterion on the primary parameter to help select the best beam tune option which leads to the minimal angular fluctuation?

Both $\mathcal{D}M_{2x2}$ and $\mathcal{D}M_{3x3}$ are re-parameterized to have the same determinant, called α. A larger quantity of α guarantees that both $\mathcal{D}M_{2x2}$ and $\mathcal{D}M_{3x3}$ won't be singular matrices. A close-to-zero α also results in blowing up the magnitudes of dithering coefficients defined in

Figure 6.27: (left panel) 2x2 vs. (right panel) 3x3 $\frac{\partial \sigma_j^m}{\partial \mathcal{M}_{4ax}}$ (red open square) and $\frac{\partial \sigma_j^m}{\partial \mathcal{M}_{4bx}}$ (open blue triangle) dithering coefficient history plots (unit: $\frac{ppm}{\mu m}$). From top to bottom: right-arm detector at the bottom side; right-arm detector at the top side; left-arm detector at the bottom side; left-arm detector at the top side.

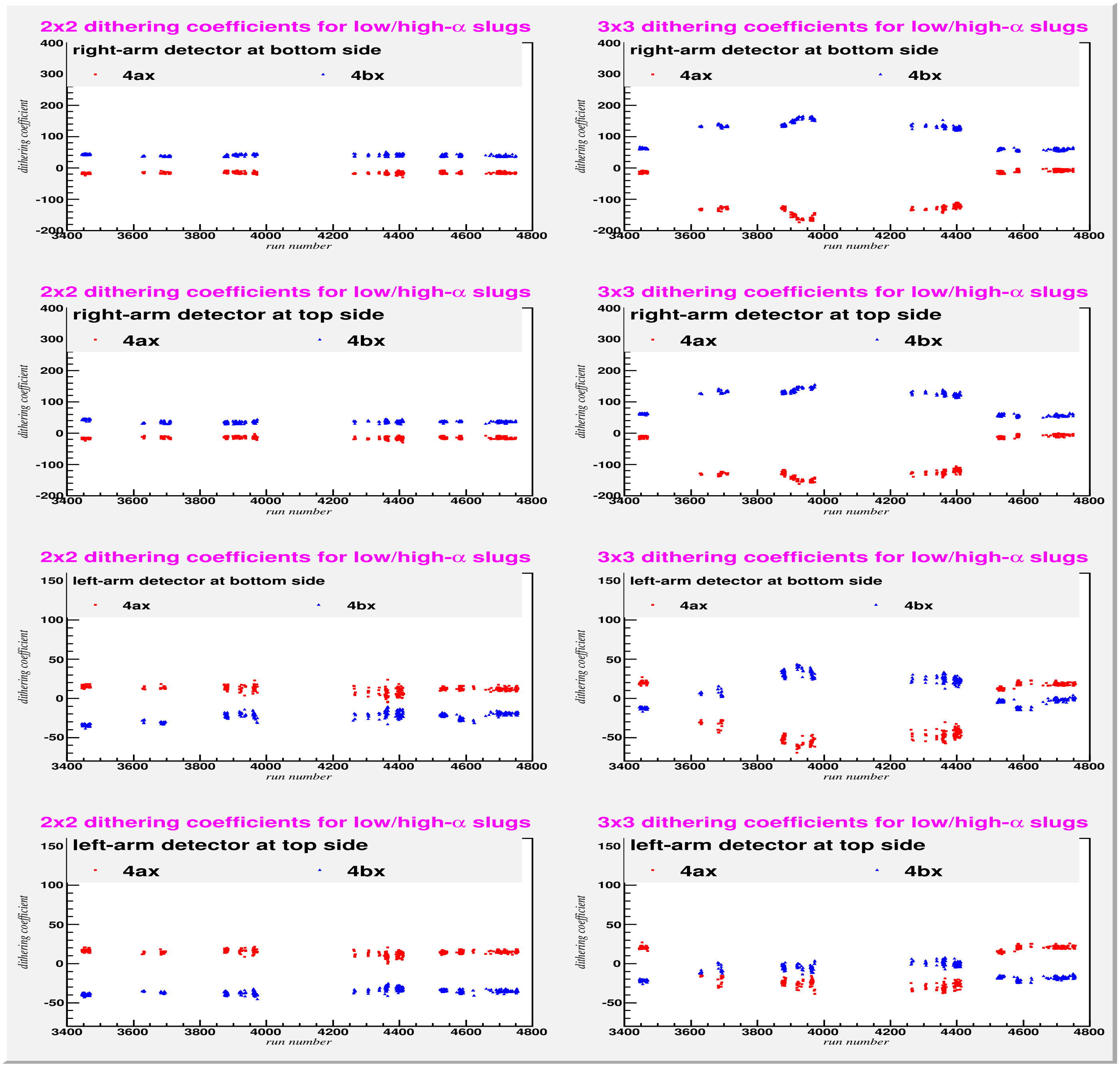

Figure 6.28: 3x3 $\frac{\partial \sigma_j^m}{\partial \mathcal{M}_{12x}}$ dithering coefficient history plot (unit: $\frac{ppm}{\mu m}$). Upper left: the right-arm detector on the bottom side; upper right: the right-arm detector on the top side; lower left: the left-arm detector on the bottom side; lower right: the left-arm detector on the top side.

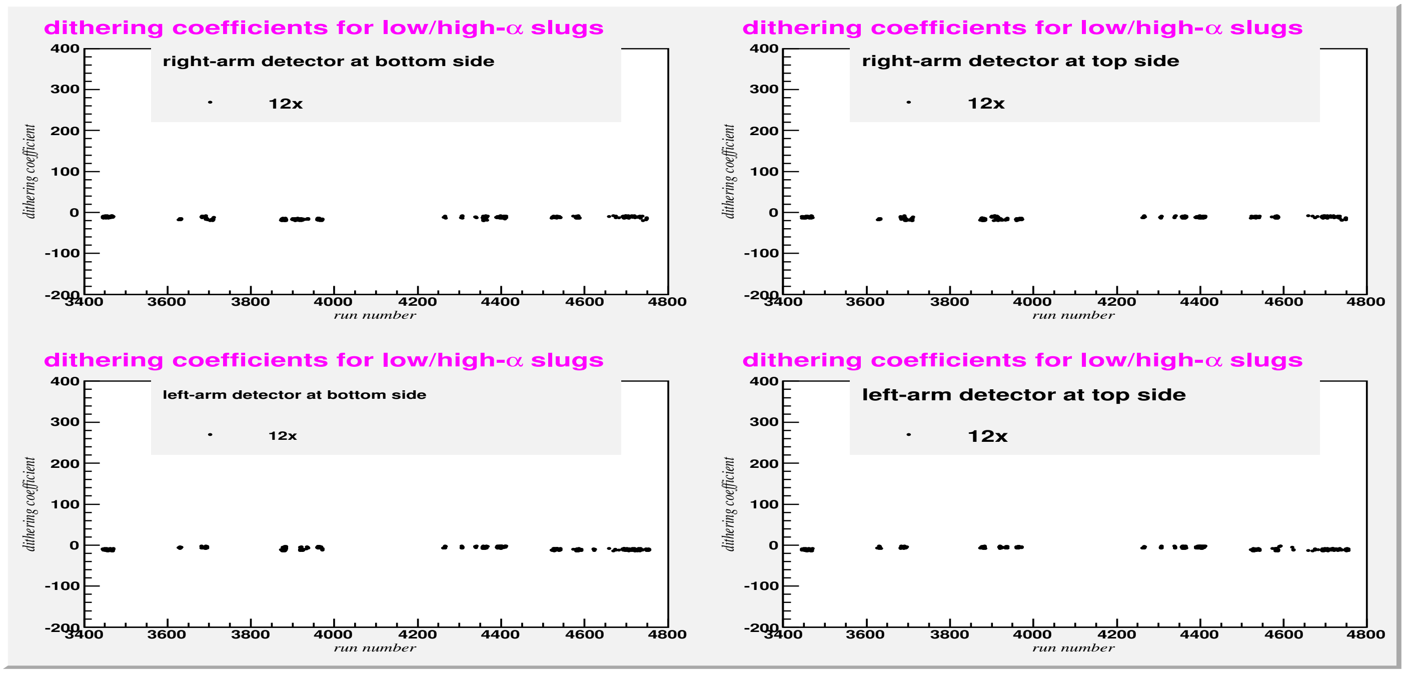

Figure 6.29: (red open square) $\frac{\partial \mathcal{M}_{12x}}{\partial \mathcal{M}_{4ax}}$ and (blue open triangle) $\frac{\partial \mathcal{M}_{12x}}{\partial \mathcal{M}_{4bx}}$ history plot.

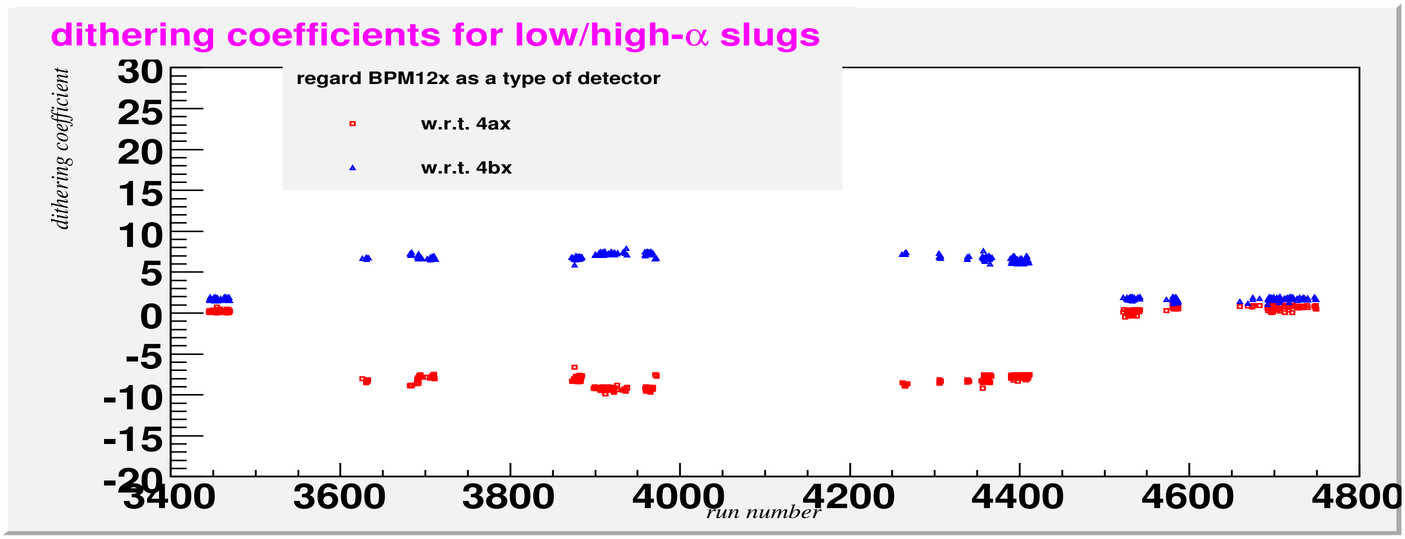

Figure 6.30: $\frac{\delta}{\alpha}$ history plot.

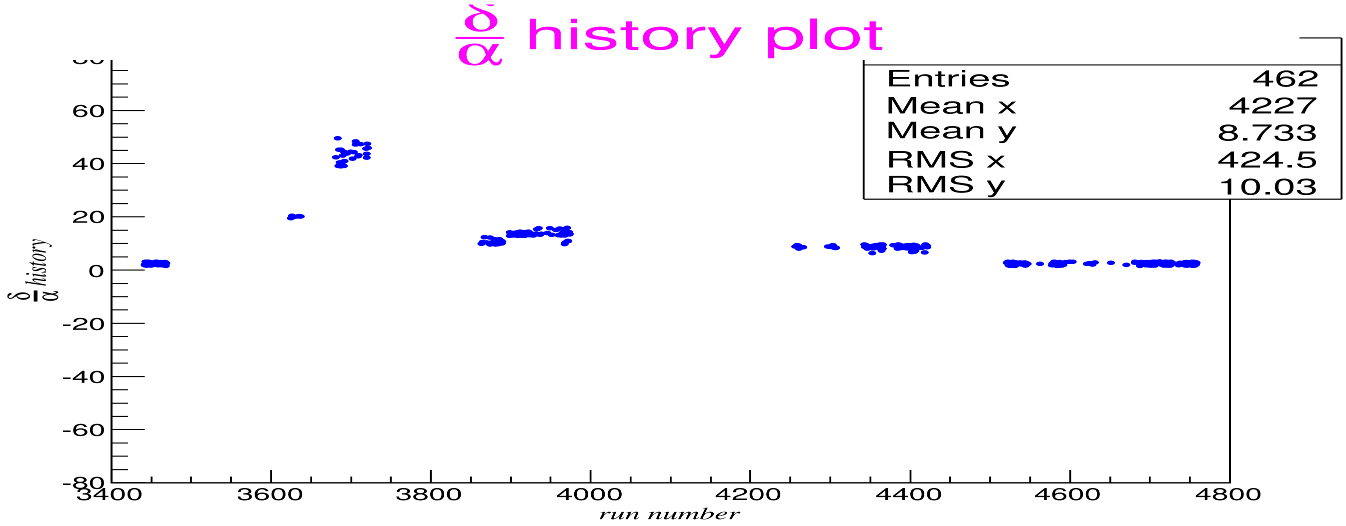

Equation 6.9 and Equation 6.22.

Another parameter, called δ, indicates the likelihood of position fluctuations turning into angular variations. The ratio of δ to α in Fig. 6.30 is formed to manifest issues as described above. Fig. 6.30 depicts not only the singularity property of the dithering matrix ($\mathcal{D}M_{2x2,3x3}$) but the level of angular fluctuations. Now, we can answer those two questions raised in the previous section:

- Q: which parameter does matter to reflect the beam tune option?

  A: α and δ.

- Q: what is the criterion on the primary parameter to help select the best beam tune option which leads to the minimal angular fluctuation?

  A: the ratio of $\frac{\delta}{\alpha}$ with respect to α is supposed to be kept constant and remains as small as possible.

6.6 Correlation removal

In Sec. 6.4, we discussed the fractional error of each dithering slope and the correlation coefficient of residuals in between two respective dithering slopes with respect to the same coil. In order to simplify the error calculation, we can find another set of parameters to re-express dithering slopes and dithering coefficients after removing the residual correlation between beam monitors. The correlation between $\Delta\mathcal{M}_{4ax}$ and $\Delta\mathcal{M}_{4bx}$ as shown in the left pannel of Fig. 6.31 is very obvious, and so is the correlation of residuals in between them as depicted in the left pannel of Fig. 6.32. The residual correlation coefficients, named ρ_{pq}, in different data sets are given in Table 6.2.

Table 6.2: ρ_{pq}, $\mathbf{S}_{pp}$, $\mathbf{S}_{qq}$ and $\mathbf{S}_{pq}$ in low and high α, respectively.

run number	high α	low α	ρ_{pq}	$\mathbf{S}_{pp}$	$\mathbf{S}_{qq}$	$\mathbf{S}_{pq}$
3445 - 3469	X		0.75849	0.03606	0.03341	0.02633
3470 - 3633	X		0.99738	0.00643	0.01598	0.01011
3634 - 3695	X		0.95431	0.00164	0.00487	0.00270
3696 - 3712	X		0.93866	0.00385	0.00816	0.00526
3713 - 3884		X	0.99624	0.03355	0.05703	0.04358
3885 - 3916		X	0.99975	0.00570	0.01527	0.00933
3917 - 3968		X	0.99677	0.17538	0.35810	0.24980
3969 - 3972		X	-0.40089	0.00004	0.00002	-0.00001
3973 - 4413		X	0.99813	0.72780	1.26303	0.95698
4413 - 4572	X	X	0.98256	0.09586	0.13743	0.11278
4573 - 4588	X		0.98239	0.01138	0.01123	0.01110
4589 - 4626	X		0.90898	0.06733	0.05466	0.05514
4627 - 4669	X		0.99061	0.03449	0.05340	0.04251
4670 - 4749	X		0.98679	0.20327	0.25834	0.22613
4750 - 4755	X		0.99593	0.01116	0.01509	0.01292

The correlation of residuals in between two different beam monitors can be removed by constructing a covariance matrix (or called dispersion matrix), $\mathbf{S}$, in Equation 6.23 in which each matrix element is the covariance of residuals for two arbitrarily chosen states.

Then, we have:

$$\begin{aligned}
\rho_{pq} &= \frac{\mathbf{S}_{pq}}{\sqrt{\mathbf{S}_{pp}\,\mathbf{S}_{qq}}}, \\
\mathbf{S}_{pq} &= \Sigma_{4ax,4bx} = cov(\delta(\Delta\mathcal{M}_{4ax}), \delta(\Delta\mathcal{M}_{4bx})) = \\
\mathbf{S}_{qp} &= \Sigma_{4bx,4ax} = cov(\delta(\Delta\mathcal{M}_{4bx}), \delta(\Delta\mathcal{M}_{4ax})) \neq 0, \\
\mathbf{S}_{pp} &= \sigma^2_{\delta(\Delta\mathcal{M}_{4ax})} \neq 0, \\
\mathbf{S}_{qq} &= \sigma^2_{\delta(\Delta\mathcal{M}_{4bx})} \neq 0,
\end{aligned} \tag{6.23}$$

where ρ_{pq} is the expectation value of the residual correlation coefficient; S_{pq} is the cross-covariance of residuals; S_{pp} and S_{qq} are the variance of residuals. $\mathbf{S}$ in Equation 6.23 approximates to a symmetric matrix. Through applying the rotation transformation to $\mathbf{S}$, a set of uncorrelated monitors, named as $\Delta\mathcal{N}_1$ and $\Delta\mathcal{N}_2$, is introduced. Hence, the matrix elements of the covariance matrix, $\mathbf{S}$ in Equation 6.24, now become:

$$\begin{aligned}
\rho_{12} &= \frac{\mathbf{S}_{12}}{\sqrt{\mathbf{S}_{11}\,\mathbf{S}_{22}}} = 0, \\
\mathbf{S}_{12} &= \Sigma_{1,2} = cov(\delta(\Delta\mathcal{N}_1), \delta(\Delta\mathcal{N}_2)) = \\
\mathbf{S}_{21} &= \Sigma_{2,1} = cov(\delta(\Delta\mathcal{N}_2), \delta(\Delta\mathcal{N}_1)) = 0, \\
\mathbf{S}_{11} &= \sigma^2_{\delta(\Delta\mathcal{N}_1)} \neq 0, \\
\mathbf{S}_{22} &= \sigma^2_{\delta(\Delta\mathcal{N}_2)} \neq 0.
\end{aligned} \tag{6.24}$$

The variances of $\Delta\mathcal{N}_1$ and $\Delta\mathcal{N}_2$ are the eigen-values of $\mathbf{S}'$ matrix in Equation 6.25 deduced as follows:

$$\mathbf{S}' = \mathbf{X}^{-1}\mathbf{S}\mathbf{X} = \begin{pmatrix} \sigma^2_{\delta(\Delta\mathcal{N}_1)} & \emptyset \\ \emptyset & \sigma^2_{\delta(\Delta\mathcal{N}_2)} \end{pmatrix}, \tag{6.25}$$

$$\sigma_{\delta(\Delta\mathcal{N}_1)} = \sqrt{\sigma^2_{\delta(\Delta\mathcal{N}_1)}} = \sqrt{\frac{1}{2}\left[\,(\,\mathbf{S}_{pp} + \mathbf{S}_{qq}\,) \,+\, \sqrt{(\,\mathbf{S}_{pp} - \mathbf{S}_{qq}\,)^2 \,+\, 4\,\mathbf{S}^2_{pq}}\,\right]}$$

$$\sigma_{\delta(\Delta\mathcal{N}_2)} = \sqrt{\sigma^2_{\delta(\Delta\mathcal{N}_2)}} = \sqrt{\frac{1}{2}\left[\,(\,\mathbf{S}_{pp} + \mathbf{S}_{qq}\,) \,-\, \sqrt{(\,\mathbf{S}_{pp} - \mathbf{S}_{qq}\,)^2 \,+\, 4\,\mathbf{S}^2_{pq}}\,\right]}$$

Figure 6.31: take run 4749: the correlation between $\Delta\mathcal{M}_{4ax}$ and $\Delta\mathcal{M}_{4bx}$ (left : $\rho_{pq} \neq 0$) within quartet windows; the correlation between $\Delta\mathcal{N}_1$ and $\Delta\mathcal{N}_2$ (right : $\rho_{12} = 0$) within quartet windows.

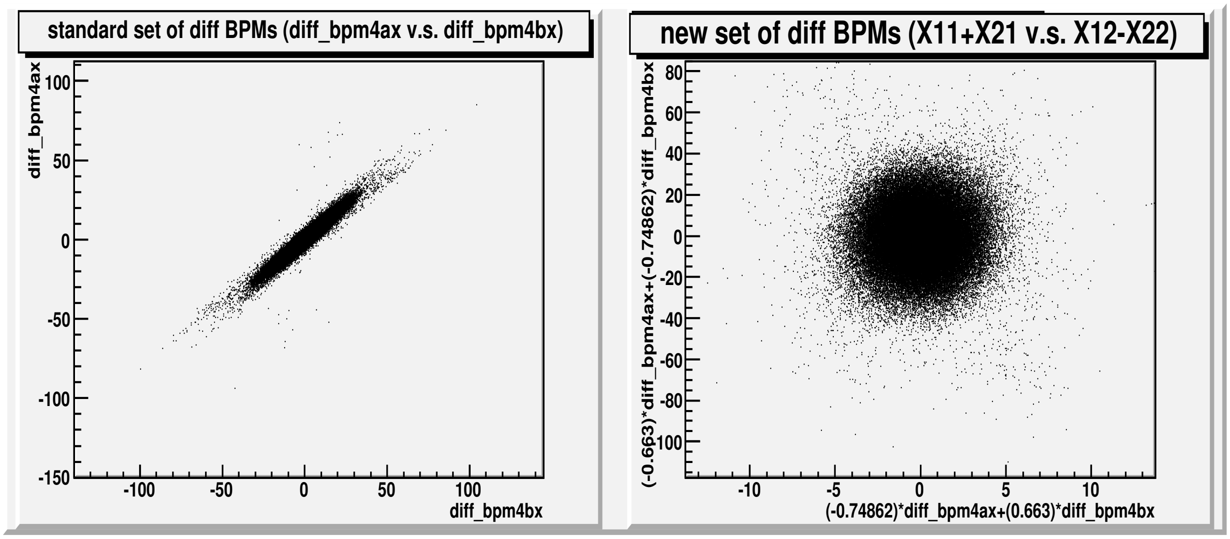

$$< \Delta\mathcal{N}_1 > = \mathbf{X}_{11} < \Delta\mathcal{M}_{4ax} > + \mathbf{X}_{21} < \Delta\mathcal{M}_{4bx} >$$

$$< \Delta\mathcal{N}_2 > = \mathbf{X}_{12} < \Delta\mathcal{M}_{4ax} > + \mathbf{X}_{22} < \Delta\mathcal{M}_{4bx} > .$$

Here, $\mathbf{X}$ is an orthogonal and real 2x2 matrix, composed of a pair of eigen-states:

$$\mathbf{X} = \begin{pmatrix} \mathbf{X}_{11} & \mathbf{X}_{12} \\ \mathbf{X}_{21} & \mathbf{X}_{22} \end{pmatrix} \cong \begin{pmatrix} 1 & -1 \\ 1 & 1 \end{pmatrix} = \begin{pmatrix} \cos\psi & -\sin\psi \\ \sin\psi & \cos\psi \end{pmatrix}$$

, where $\psi \cong 45°$. The right pannel of Fig. 6.31 shows the correlation between $\Delta\mathcal{N}_1$ and $\Delta\mathcal{N}_2$ is hard to be seen after removing the residual correlation in between $\Delta\mathcal{M}_{4ax}$ and $\Delta\mathcal{M}_{4bx}$. The right pannel of Fig. 6.32 ensures the residual correlation in between $\Delta\mathcal{N}_1$ and $\Delta\mathcal{N}_2$ approximates to zero.

Figure 6.32: take runs 4674-4749: the correlation of residuals between $\Delta\mathcal{M}_{4ax}$ and $\Delta\mathcal{M}_{4bx}$ (left : $\rho_{pq} \neq 0$) within different runs; the correlation of residuals between $\Delta\mathcal{N}_1$ and $\Delta\mathcal{N}_2$ (right : $\rho_{12} = 0$) within different runs.

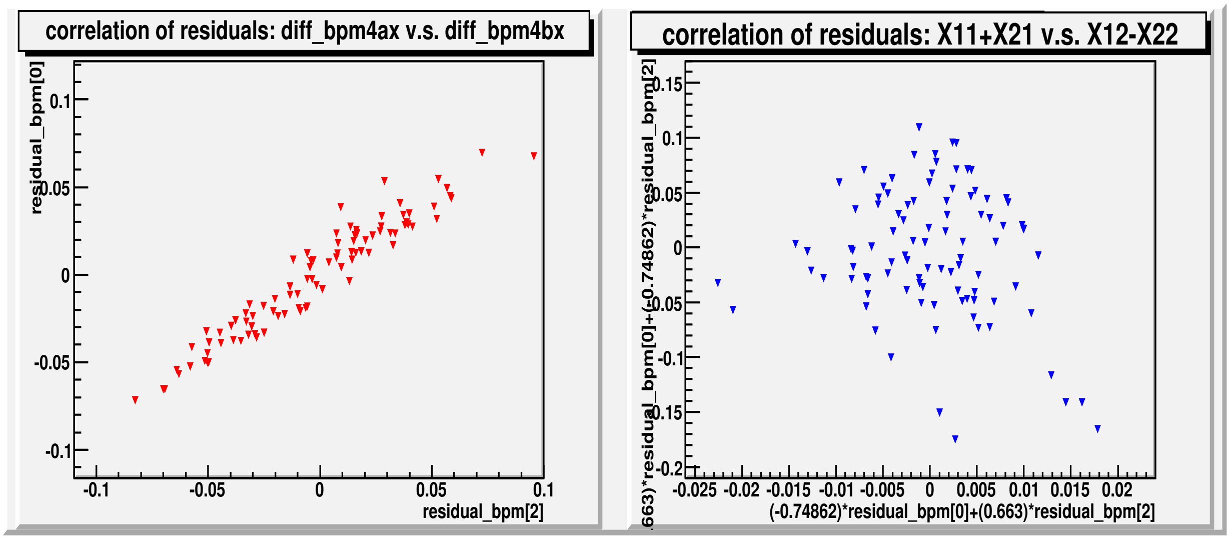

Chapter 7

Review of $\mathcal{A}_T$ (or $\mathcal{A}_n$) Analysis for PREx

The portion of the electron beam polarization pointing to the y-axis, perpendicular to the electron's scattering plane, induced the horizontal polarization, measured by different beam polarimeters, i.e. Compton, Moller and Mott, along the injector part and separate experiment Halls (A,B,C). By means of the rotation of the Wien filter, the direction of the electron spin can be varied along the plane parallel to the electric field without any disturbance applied to the motion of the beam. Above is the spin dance. The spin dance is a way used to measure the portion of the electron beam polarization along the Z-axis, the longitudinal direction. Despite the identical magnitude of the beam polarization, multiple beam polarimeters in individual experiment Halls can measure different longitudinal beam polarizations. This disagreement among different beam polarimeters reflects the systematic effects and the uncertainty of the analyzing power.

The horizontal polarization gives rise to the y (or up-down)-dependent transverse asymmetry, resulted from the non-parity violation, and can be determined by the spin dance. Therefore, an optimized Wein angle is required to minimize the horizontal polarization less than 1%. Otherwise, the transverse asymmetry would be an-order-magnitude larger than the longitudinal asymmetry, which is in an order of magnitude of 10^{-6}-10^{-4}. In PREx, under the experimentally running condition of the low-Q^2, the size of the longitudinal asymmetry is around 10^{-6} (or 1 ppm). The other main purpose to find an optimize Wein angle is to control the spot size at the target. One reason to account for the instability of the spot size is induced by the associated error of the analyzing power. The existence of the retardation phase shift angle (Δ) due to the residual linear polarization in a imperfectly circular polarization of laser light also causes the difference in the spot size between two helicity states, corresponding to the second-order (area=length^2) helicity-correlated systematics for the differential cross-section of each detector's.

Beside the horizontal polarization, there exists the vertical polarization measured by the Mott polarimeter in the 5 MeV region of the injector part. Likewise, the vertical polarization is required to be less than 1% in order to reduce the size of the left-right dependent transverse asymmetry. The left-right dependent transverse asymmetry, along with the up-down dependent transverse asymmetry with a non-zero factor, sinϕ (as $\phi < 5°$, sin$\phi \approx \phi$, the portion of the transverse asymmetry along the beam axis), are regarded as one of the systematic sources for the longitudinal asymmetry measurement, for they can lead to a false asymmetry. The alignment for the symmetry of apparatus from both up-down and left-right directions is strongly compulsory without applying any external filed, so that the septum was required to be turned off during the alignment procedure. In addition, the effect of the beam jitter along the scattering plane should be pondered, and the noise level of beam which makes the impact on the accuracy of the transverse asymmetry measurement is needed to be examined.

Two methods used to determine the quantity of the transverse asymmetry were implemented and performed during the course of 2010 PREx. One way is to put 4 gram Beryllium up on one arm collimator and down on the other, respectively, for the background asymmetry coming from the inelastic scattering electrons should be subtracted automatically in the combination of both $\mathcal{A}_{T,L}$ and $\mathcal{A}_{T,R}$. The other way is to establish the auxiliary detectors 1.2 m downstream of the focal plane on each arm. These detectors as shown in the data stream are called flumi$_{1/2}$ for the right- and left-arm, respectively. This document describes the reviewing procedure of $\mathcal{A}_T$ analysis for 2010 PREx experiment.

The integrated electron signals accumulated in detectors, sitting in each arm, comes from the elastic scattering and other background processes:

$$S = S_E + \sum_i S_B^i \tag{7.1}$$

The measured (corrected) asymmetry, after subtracting the beam false asymmetry from the raw asymmetry to account for the helicity-correlated beam parameters caused by the beam jitter (real noises), can be expressed in Eqn. 7.2 below:

$$\begin{aligned}
\mathcal{A}_{cor.} &= \frac{S^R - S^L}{S^R + S^L} \\
&= \frac{(S_E^R - S_E^L) + \sum_i (S_B^{Ri} - S_B^{Li})}{(S_E^R + S_E^L) + \sum_i (S_B^{Ri} + S_B^{Li})} \\
&= \frac{(S_E^R - S_E^L)}{(S_E^R + S_E^L) + \sum_i (S_B^{Ri} + S_B^{Li})} + \frac{\sum_i (S_B^{iR} - S_B^{iL})}{(S_E^R + S_E^L) + \sum_i (S_B^{Ri} + S_B^{Li})} \\
&= \frac{(S_E^R - S_E^L)}{(S_E^R + S_E^L)} \frac{1}{1 + \frac{\sum_i (S_B^{iR} + S_B^{iL})}{(S_E^R + S_E^L)}} + \sum_i \frac{(S_B^{iR} - S_B^{iL})}{(S_B^{iR} + S_B^{iL})} \frac{1}{1 + \frac{(S_E^R + S_E^L)}{(S_B^{iR} + S_B^{iL})}} \\
&= \frac{(S_E^R - S_E^L)}{(S_E^R + S_E^L)}\left(1 - \frac{(S_E^R + S_E^L)}{(S_E^R + S_E^L) + \sum_i (S_B^{Ri} + S_B^{Li})}\right) + \sum_i \frac{(S_B^{iR} - S_B^{iL})}{(S_B^{iR} + S_B^{iL})} \frac{(S_E^R + S_E^L)}{(S_E^R + S_E^L) + \sum_i (S_B^{Ri} + S_B^{Li})} \\
&= \mathcal{A}_E \left(1 - \sum_i f_i\right) + \sum_i f_i \mathcal{A}_{Bi},
\end{aligned} \tag{7.2}$$

where f_i, a so-called dilution factor, is the fraction of each kind of the background asymmetry. $\mathcal{A}_E$ is the fractional difference in the differential cross-section of the elastic electron scattering between two helicity states. On the other hand, $\mathcal{A}_B$ is the asymmetry for the scattering electrons through the background processes. Equation 7.2 can be approximated to Equation 7.3, as f_i is much lesser than 1, and the second-order of the f_i

term is dropped out.

$$\begin{aligned} \mathcal{A}_E &= \frac{(\mathcal{A}_{cor.} - \sum_i f_i \mathcal{A}_{Bi})}{(1-\sum_i f_i)} \approx (\mathcal{A}_{cor.} - \sum_i f_i \mathcal{A}_{Bi})(1+\sum_i f_i) \\ &\sim (1+\sum_i f_i)\mathcal{A}_{cor.} - \sum_i f_i \mathcal{A}_{Bi} \end{aligned} \tag{7.3}$$

As mentioned earlier, $\mathcal{A}_E$ is the corrected asymmetry. $\mathcal{A}_{phys}$ is obtained by scaling $\mathcal{A}_E$ with the electron beam polarization and the finite acceptance as follows:

$$\begin{aligned} \mathcal{A}_{phys} &= \frac{K}{P_b}\mathcal{A}_E = \frac{K}{P_b}\frac{\mathcal{A}_{cor.} - \sum_i f_i \mathcal{A}_{Bi}}{(1-\sum_i f_i)} \\ &\sim \frac{K}{P_b}[(1+\sum_i f_i)\mathcal{A}_{cor.} - \sum_i f_i \mathcal{A}_{Bi}] \end{aligned} \tag{7.4}$$

We can express the fluctuation of $\mathcal{A}_{phys}$ for Lead by Equation 7.5:

$$\begin{aligned} \sigma\mathcal{A}^{Pb}_{phys} &\sim \frac{1}{P_b}[\sum_i(\sigma f_i)\mathcal{A}_{cor.} + (1+\sum_i f_i)(\sigma\mathcal{A}_{cor.}) - \sum_i(\sigma f_i)\mathcal{A}_{Bi} - \sum_i f_i(\sigma\mathcal{A}_{Bi})] \\ &+ \frac{(-1)(\sigma P_b)}{P_b^2}[(1+\sum_i f_i)\mathcal{A}_{cor.} - \sum_i f_i \mathcal{A}_{Bi}] \end{aligned} \tag{7.5}$$

Table 7.2 shows us where statistical uncertainties are primarily originated from. The

Table 7.1: dithered transverse asymmetries, $\mathcal{A}^{Pb}_{cor.}$ and $\mathcal{A}^{C}_{cor.}$, for Lead ($^{208}_{82}$Pb) and Carbon (^{12}C), physics transverse asymmetries, $\mathcal{A}^{Pb}_{phys}$ and $\mathcal{A}^{C}_{phys}$ ($\mathcal{A}_{Bi}$), the dilution factor and the electron beam polarization.

physics measurement	central value	statistics
$\mathcal{A}^{Pb}_{cor.}$ ($\mathcal{A}_{cor.}$)	$0.2207 \times 10^{-6} \sim 10^{-7}$	$0.1761 \times 10^{-6} \sim 10^{-7}$
$\mathcal{A}^{C}_{cor.}$	$5.788 \times 10^{-6} \sim 10^{-5}$	$0.3221 \times 10^{-6} \sim 10^{-7}$
$\mathcal{A}^{Pb}_{phys}$ ($\mathcal{A}_E$)	$-0.2796 \times 10^{-6} \sim 10^{-7}$	$0.214 \times 10^{-6} \sim 10^{-7}$
$\mathcal{A}^{C}_{phys}$ ($\mathcal{A}_{Bi}$)	$6.489 \times 10^{-6} \sim 10^{-5}$	$0.3611 \times 10^{-6} \sim 10^{-7}$
f_i	$0.0854 \sim 10^{-1}$	$0.00427 \sim 10^{-3}$
P_b	$0.892 \sim 10^{0}$	$0.0104 \sim 10^{-2}$

dominant term is $\frac{(\sigma\mathcal{A}_{cor.})}{P_b}$.

Table 7.2: The order of magnitude for statistical errors of $\mathcal{A}^{Pb}_{phys}$ ($\sigma\mathcal{A}^{Pb}_{phys}$).

$\frac{\sigma f_i \mathcal{A}_{cor.}}{P_b}$	$\frac{(\sigma\mathcal{A}_{cor.})}{P_b}$	$\frac{f_i(\sigma\mathcal{A}_{cor.})}{P_b}$	$\frac{\sigma f_i \mathcal{A}_{Bi}}{P_b}$	$\frac{f_i(\sigma\mathcal{A}_{Bi})}{P_b}$	$\frac{(-1)(\sigma P_b)\mathcal{A}_{cor.}}{P_b^2}$	$\frac{(-1)(\sigma P_b)\sum_i f_i \mathcal{A}_{cor.}}{P_b^2}$	$\frac{(-1)(\sigma P_b)(-1)f_i\mathcal{A}_{Bi}}{P_b^2}$
10^{-10}	10^{-7}	10^{-8}	10^{-8}	10^{-8}	10^{-9}	10^{-10}	10^{-8}

Since $\mathcal{A}^C_{cor.}$ itself belongs to the background asymmetry, there is no need to subtract any additional background asymmetry from $\mathcal{A}^C_{cor.}$. Similarly, $\mathcal{A}^C_{phys}$ is also needed to be scaled by the electron beam polarization and the acceptance:

$$\begin{aligned} \mathcal{A}^C_{phys} &= \frac{K}{P_b}\mathcal{A}^C_{cor.} \\ \sigma\mathcal{A}^C_{phys} &\sim \frac{\sigma\mathcal{A}_{cor.}}{P_b} + \frac{(-1)(\sigma P_b)\mathcal{A}_{cor.}}{P_b^2} \end{aligned} \tag{7.6}$$

$\frac{\sigma\mathcal{A}^C_{cor.}}{P_b}$ is the main statistical error to determine $\sigma\mathcal{A}^C_{phys}$.

Table 7.3: $\sigma\mathcal{A}^C_{phys}$.

	$\frac{\sigma\mathcal{A}^C_{cor.}}{P_b}$	$\frac{(-1)(\sigma P_b)\mathcal{A}^C_{cor.}}{P_b^2}$
	10^{-7}	10^{-9}

We start discussing different sources of systematic uncertainties. The first is the systematic for the electron beam's polarization, determined by Equation 7.7 below:

$$\begin{aligned} \sigma\mathcal{A}^{Pb}_{phys} &\sim \frac{(-1)(\sigma P_b)}{P_b^2}[(1+\sum_i f_i)\mathcal{A}_{cor.} - \sum_i f_i\mathcal{A}_{Bi}] \\ &= \frac{-1\times 0.01}{(0.892)^2}[(1+0.08445)\times 0.2207 - 0.08445\times 5.788] = 0.00314(ppm) \\ \sigma\mathcal{A}^C_{phys} &\sim \frac{(-1)(\sigma P_b)\mathcal{A}_{cor.}}{P_b^2} \\ &= \frac{-1\times 0.01\times 5.788}{(0.892)^2} = -0.0727(ppm). \end{aligned} \tag{7.7}$$

Figure 7.1: the physics asymmetry for Lead

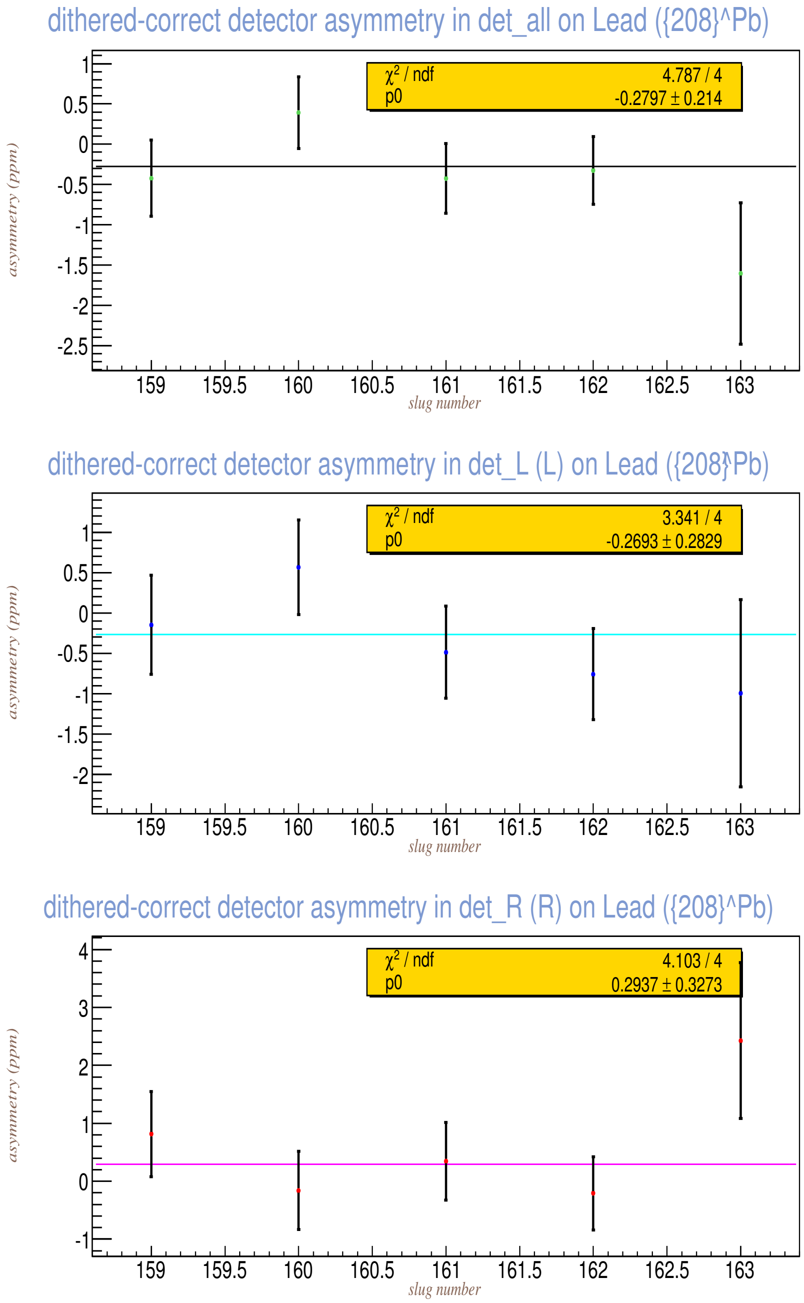

Figure 7.2: the physics asymmetry for Carbon

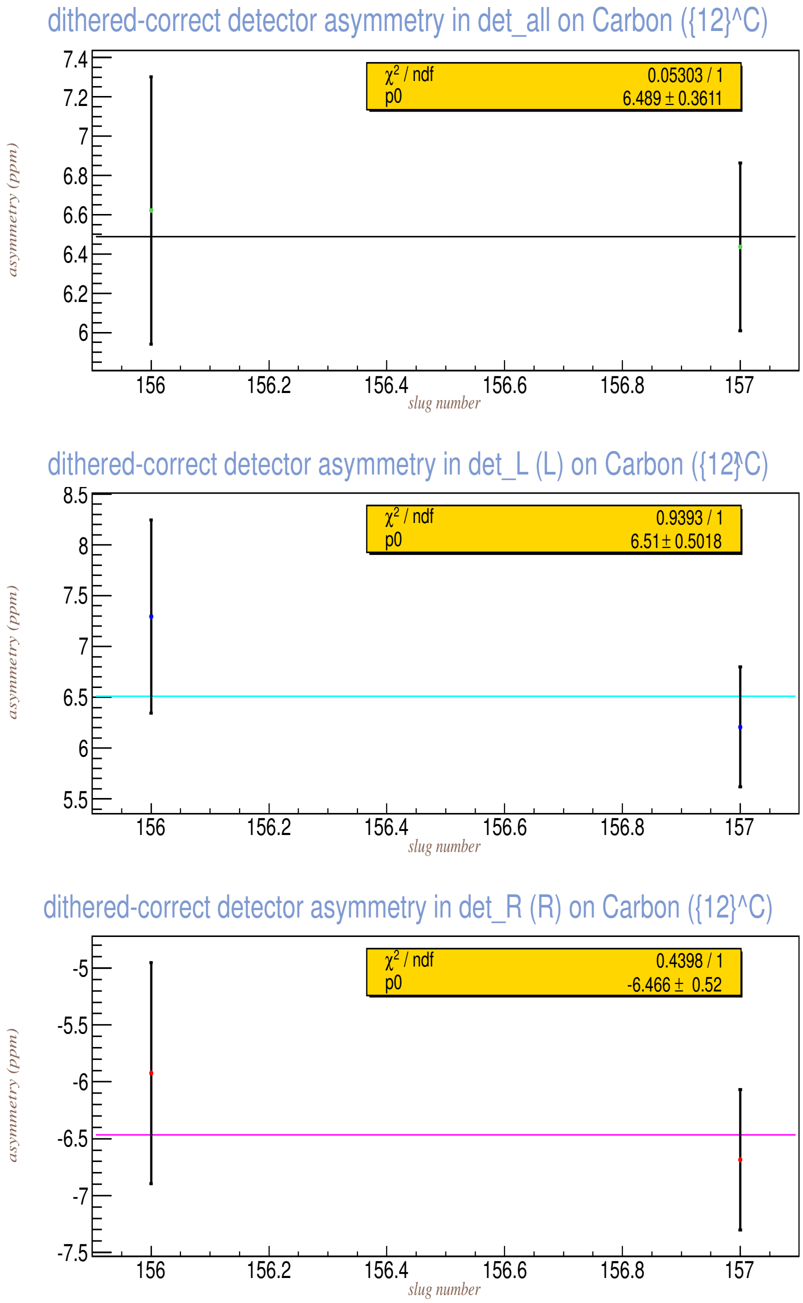

Figure 7.3: the corrected asymmetry for Lead

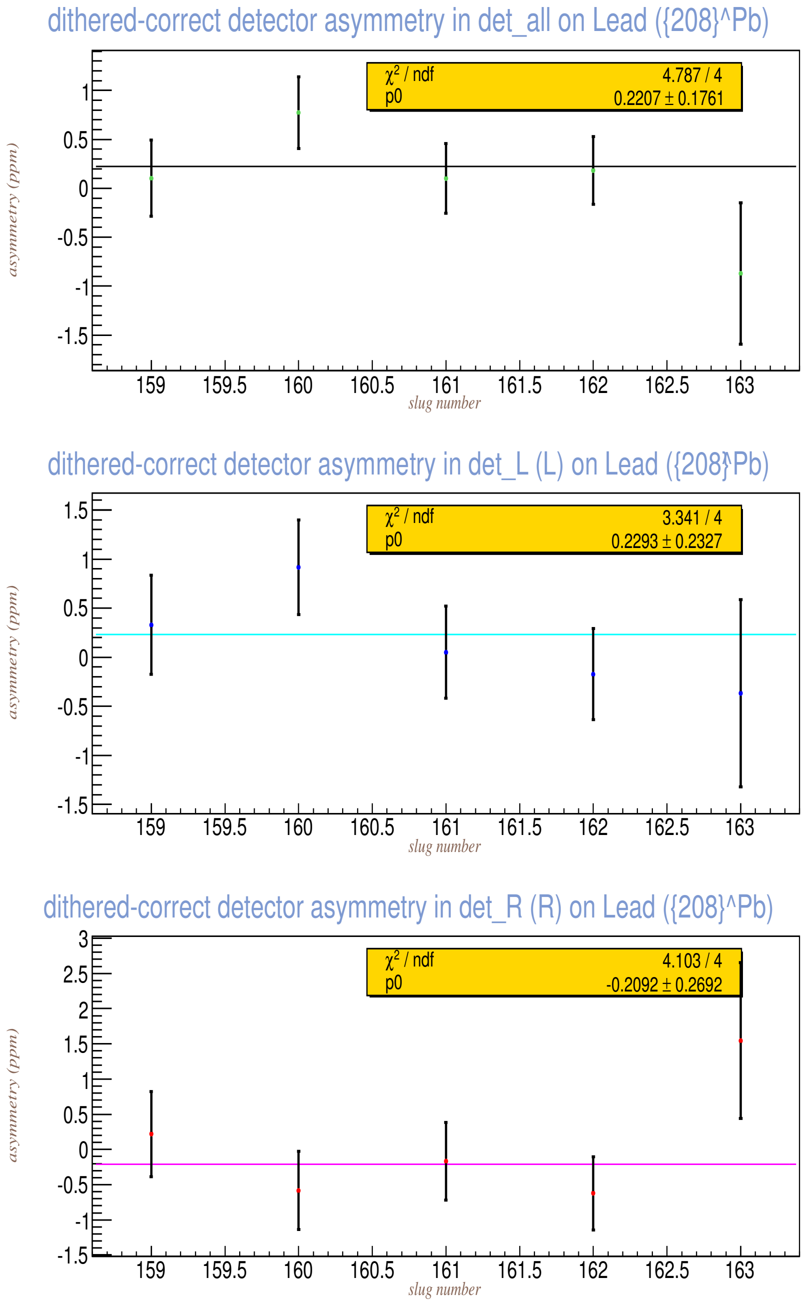

Figure 7.4: the corrected asymmetry for Carbon

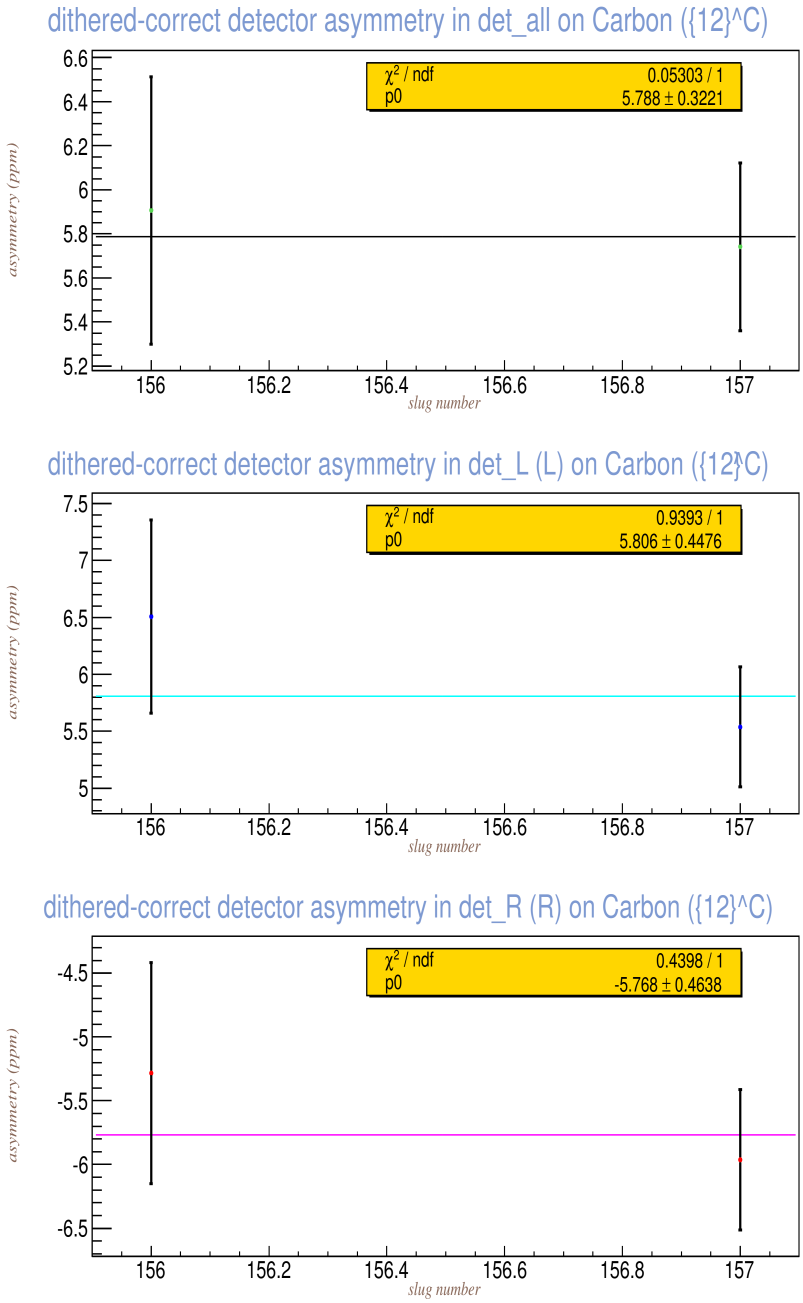

Secondly, the systematic for the background's asymmetry is:

$$\begin{aligned}\sigma\mathcal{A}^{Pb}_{phys} &\sim \frac{1}{P_b}\sum_i f_i(\sigma\mathcal{A}_{Bi}) \\ &= \frac{1}{0.892}\times 0.08445\times 0.3221 = 0.0305(ppm).\end{aligned} \tag{7.8}$$

Thirdly, the systematic for the corresponding dilution factor to the background asymmetry is:

$$\begin{aligned}\sigma\mathcal{A}^{Pb}_{phys} &\sim \frac{1}{P_b}[\sum_i(\sigma f_i)\mathcal{A}_{cor.} - \sum_i(\sigma f_i)\mathcal{A}_{Bi}] \\ &= \frac{1}{0.892}[0.08445\times 0.05\times 0.2207 - 0.08445\times 0.05\times 5.788] = -0.0264(ppm)\end{aligned} \tag{7.9}$$

Table 7.4: The systematic of $\mathcal{A}^{phys.}_T$. (unit: ppm)

	systematics (ppm)
P_b for Lead	0.00314
P_b for Carbon	0.0727
$\mathcal{A}_{Bi}$ for Lead	0.0305
f_i for Lead	0.0264
combined	0.04034
detector linearity for Lead (raw $\mathcal{A}_Q$)	$0.015\times 0.2013 = 0.00302$
detector linearity for Carbon (raw $\mathcal{A}_Q$)	$0.015\times 0.06289 = 0.000943$
detector linearity for Lead (physics $\mathcal{A}_Q$)	$0.015\times 0.25 = 0.00375$
detector linearity for Carbon (physics $\mathcal{A}_Q$)	$0.015\times 0.0705 = 0.00106$
detector linearity for Lead (physics $\mathcal{A}_{phys}$)	$0.01\times 0.2797 = 0.002797$
detector linearity for Carbon (physics $\mathcal{A}_{phys}$)	$0.01\times 6.489 = 0.06489$
detector linearity for Lead (combined)	0.004678
detector linearity for Carbon (combined)	0.064899

The raw charge asymmetries for Lead and Carbon, respectively, are depicted in Fig. 7.5

and Fig. 7.6. Regarding the Carbon contamination and the electron beam's polarization, the physics charge asymmetry for Lead and Carbon, respectively, can be obtained as shown in Fig. 7.7 and Fig. 7.8. The systematic to account for the detector's non-linearity is 1.5% of the physics charge asymmetry and 1.0% of the physics transverse asymmetry for both Lead and Carbon.

Speaking of the systematic for the beam false asymmetry, we multiply each dithering coefficient with respect to one specific beam position (or energy) monitor by the difference in the position (or energy) between helicity states. Officially, both of the magnitude of each dithering coefficient and the position (or energy) difference are averaged over all of Lead and Carbon runs. In other words, the asymmetry correction is calculated by taking the product of the slug-average of each dithering coefficient and the corresponding position (or energy) difference as expressed below:

$$\Delta\mathcal{A}_i^{false} = \frac{\partial\sigma_i}{\partial\mathcal{M}_j} \times \Delta\mathcal{M}_j, \tag{7.10}$$

where σ_i represents the left- (L) and right-arm (R) detector, respectively.

The weighted average of both single-arm's false asymmetries for Lead and Carbon, respectively, can be computed below:

$$\Delta\mathcal{A}_{carbon/Lead}^{false} = 30\% \times \frac{\frac{\Delta\mathcal{A}_L^{false}}{\sigma_L^2} - \frac{\Delta\mathcal{A}_R^{false}}{\sigma_R^2}}{\frac{1}{\sigma_L^2} + \frac{1}{\sigma_R^2}}, \tag{7.11}$$

where σ_L is the slug-average noise level of the single-left arm detector, and so is σ_R for the single-right arm's. In other words, the conventional (traditional) way to obtain the asymmetry correction for each beam position (or energy) monitor is based on:

$$\Delta\mathcal{A}_{carbon/Lead}^{false} = 30\% \times \frac{\frac{<\frac{\partial\mathcal{D}_L}{\partial\mathcal{M}_j}>\times<\Delta\mathcal{M}_j>}{\sigma_L^2} - \frac{<\frac{\partial\mathcal{D}_R}{\partial\mathcal{M}_j}>\times<\Delta\mathcal{M}_j>}{\sigma_R^2}}{\frac{1}{\sigma_L^2} + \frac{1}{\sigma_R^2}} \tag{7.12}$$

Figure 7.5: the charge asymmetry ($\mathcal{A}_Q^{raw}$) for Lead

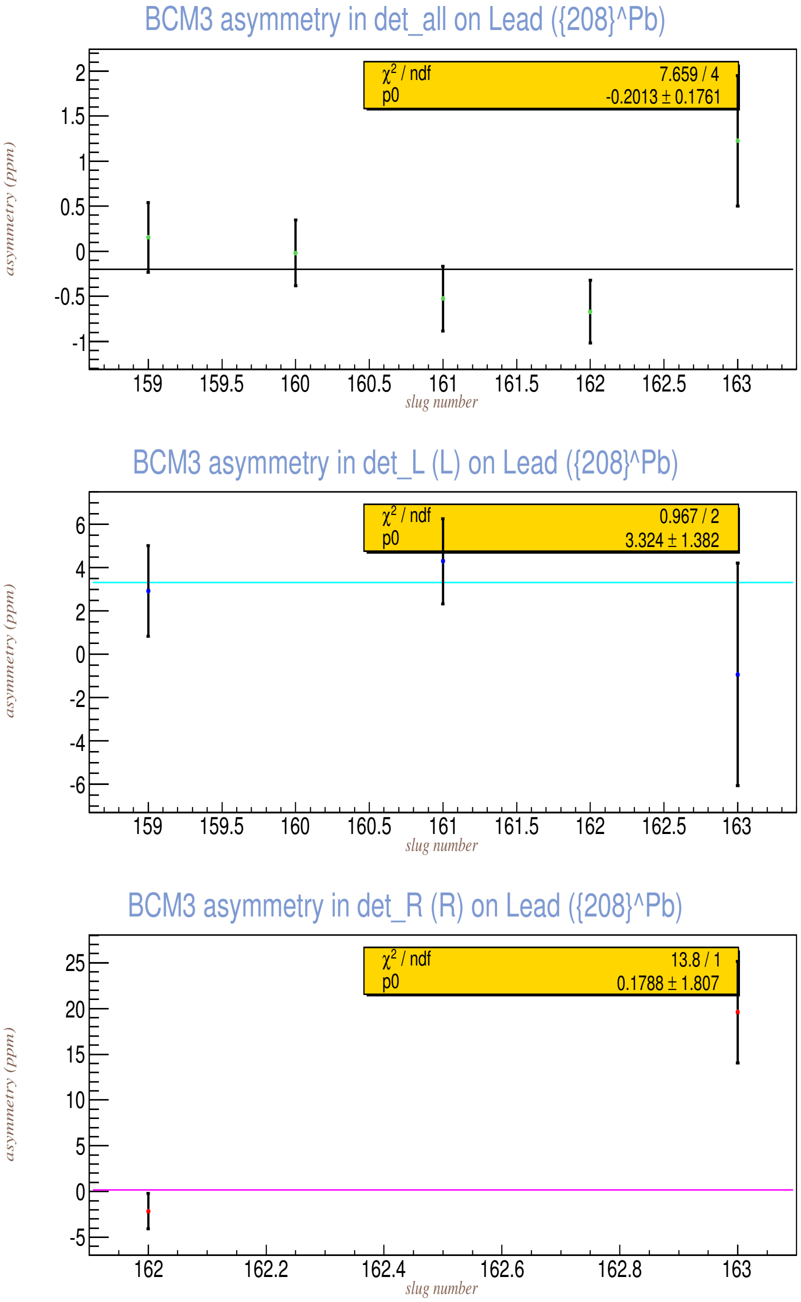

Figure 7.6: the charge asymmetry ($\mathcal{A}_Q^{raw}$) for Carbon

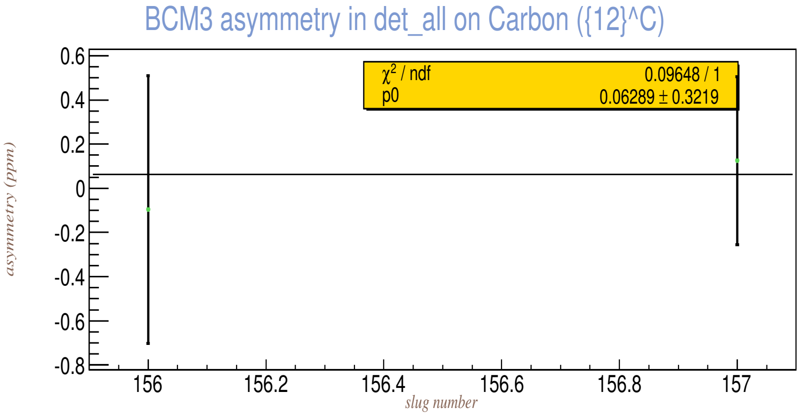

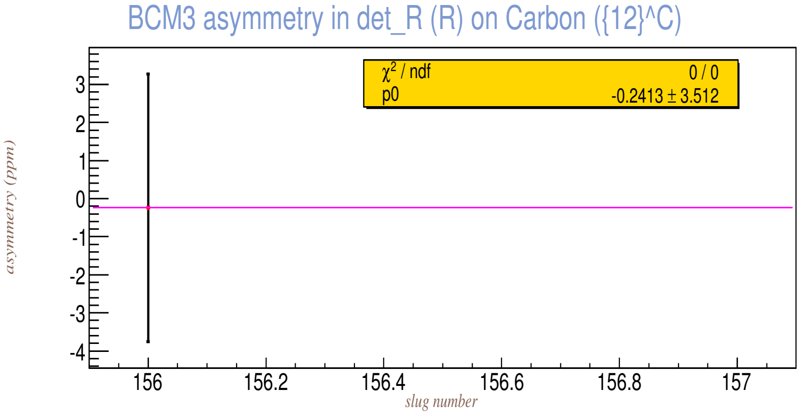

Figure 7.7: the physics charge asymmetry ($\mathcal{A}_Q^{phys}$) for Lead with the correction of the Carbon contamination and the electron beam's polarization.

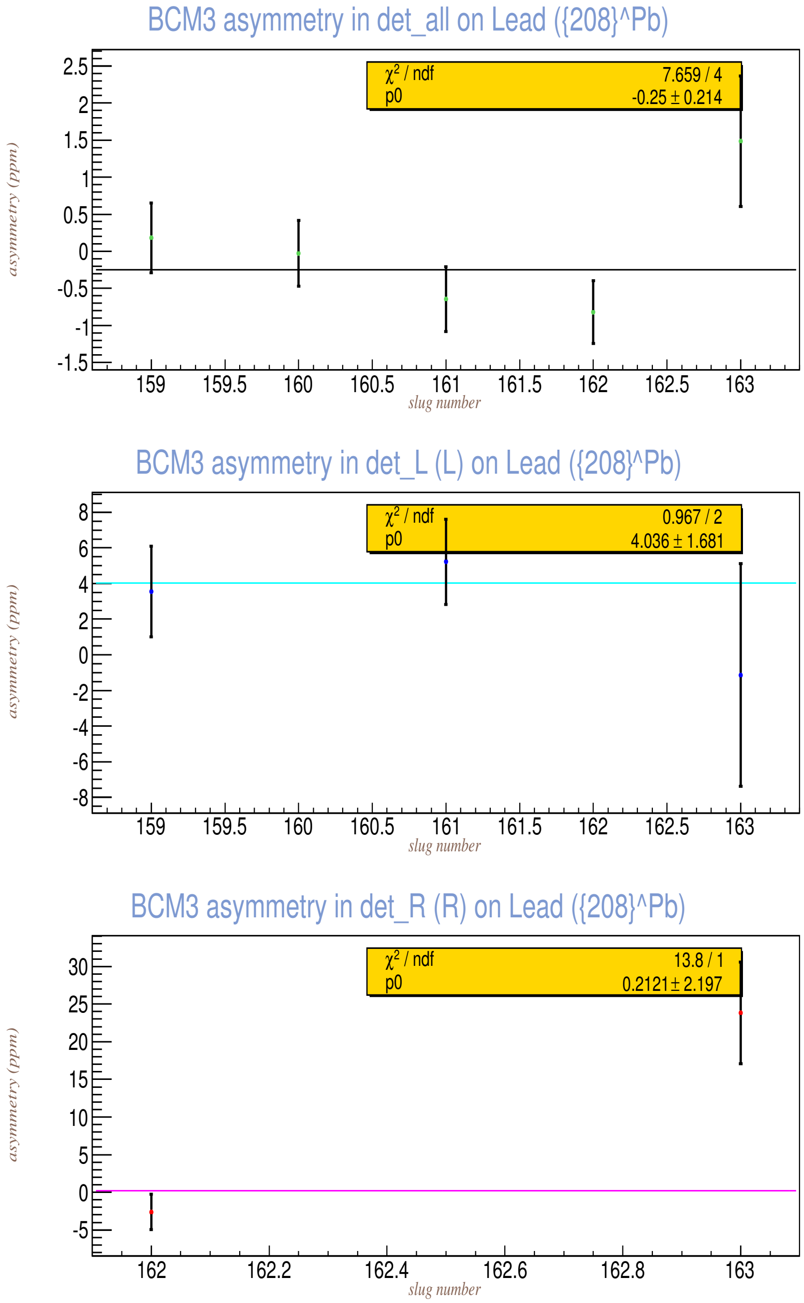

Figure 7.8: the physics charge asymmetry ($\mathcal{A}_Q^{phys}$) for Carbon with the correction of the Carbon contamination and the electron beam's polarization.

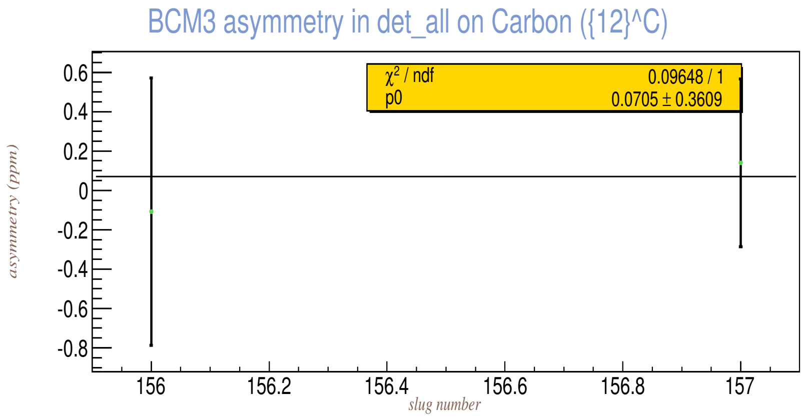

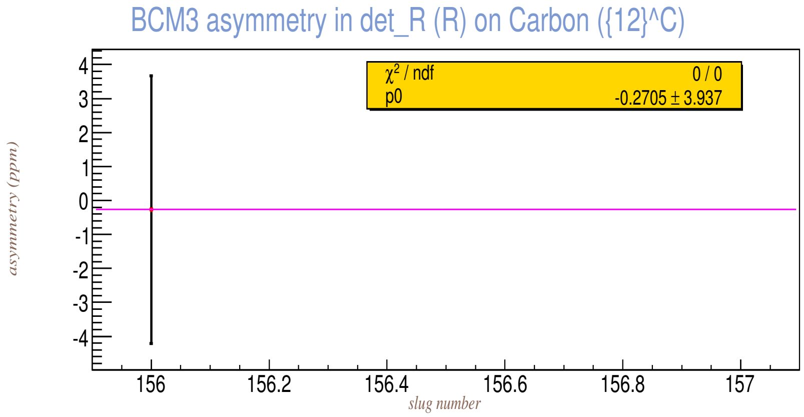

On the other hand, we can try an alternative way to get the systematic for the beam false asymmetry as below:

$$\Delta\mathcal{A}^{false}_{carbon/Lead} = < 30\% \times \frac{\frac{\frac{\partial\mathcal{D}_L}{\partial\mathcal{M}_j}\times\Delta\mathcal{M}_j}{\sigma_L^2} - \frac{\frac{\partial\mathcal{D}_R}{\partial\mathcal{M}_j}\times\Delta\mathcal{M}_j}{\sigma_R^2}}{\frac{1}{\sigma_L^2}+\frac{1}{\sigma_R^2}} > \tag{7.13}$$

Instead of taking the product of the slug-average of both dithering coefficient and position/energy difference at the target, we can multiply each dithering coefficient by the position (or energy) difference for each run firstly and take the overall average weighted by each-arm detector's noise level afterward. Fig. 7.9 and Fig. 7.10 demonstrate the fitted asymmetry correction results for Lead and Carbon, respectively. The associated error bar to each data point, i.e. the unit of each data point is slug (data-set), is determined by:

$$\sigma\Delta\mathcal{A}^{false}_{carbon/Lead} = \sqrt{\frac{1}{\sum_i \frac{1}{\sigma_i^2}}}, \tag{7.14}$$

where i indicates different detector's types.

Table 7.5: The systematic for both Lead and Carbon asymmetry corrections, $\Delta\mathcal{A}^{flase}_{Lead}$ and $\Delta\mathcal{A}^{flase}_{Carbon}$. The dilution factor is 0.0854, and the electron beam's polarization is 0.892. (unit: ppb)

	$\Delta\mathcal{A}^{flase}_{Lead}$ (ppb)	$\Delta\mathcal{A}^{flase}_{Carbon}$ (ppb)
BPM12x	-7.688	-2.291
BPM4ax	37.944	-8.690
BPM4ay	-1.026	0.935
BPM4bx	-109.994	-10.946
BPM4by	2.818	-6.021
quadratic sum (raw)	116.647	15.418
quadratic sum (physics)	$\frac{116.647\times(1+0.0854)}{0.892} = 141.820$	$\frac{15.418}{0.892} = 17.285$

Apparently, these two methods yield us similar asymmetry correction quantities. Please refer to Jon Wexler's $\mathcal{A}_T$ analysis draft on hap-log 2808. Despite the correlation of one-arm detector's beam noises to the other arm's, the uncertainty of the detector signal is still primarily overpassed by the counting statistics, belonging to uncorrelated uncertainties. Hence, the correlation of the beam noise between the cross-sections from two separate arms' detectors is weaker, and the beam noises in the cross-sections of two arms' detectors are cancelled out to each other. Here, the so-called beam noise is induced by the fluctuation of the beam modulation system.

The systematic arising from the beam jitter and the electronics noise, which is around 10% of the beam jitter, is overestimated to be 30% of the size of the asymmetry correction, and 30% is conservative enough. In sum, the systematic in the Lead transverse asymmetry measurement is tremendously dominated by the beam false asymmetry. On the other hand, both beam polarization and detector's non-linearity are the primary sources of the systematic uncertainty for the Carbon transverse asymmetry measurement.

Table 7.6: The summary systematic of $\mathcal{A}_T^{phys.}$ for Lead and Carbon. (unit: ppm)

	systematics (ppm)
P_b for Lead	0.00314
P_b for Carbon	0.0727
$\mathcal{A}_{Bi}$ and f_i combined for Lead	0.04034
detector linearity for Lead (combined)	0.004678
detector linearity for Carbon (combined)	0.064899
beam false asymmetry for Lead	0.14182
beam false asymmetry for Carbon	0.017825
quadratic sum for Lead	0.14755
quadratic sum for Carbon	0.09907

Figure 7.9: the weighted average of the asymmetry correction in the run-average level for Lead with separate insertable half-wave plat and wein angle (spin flipper) states.

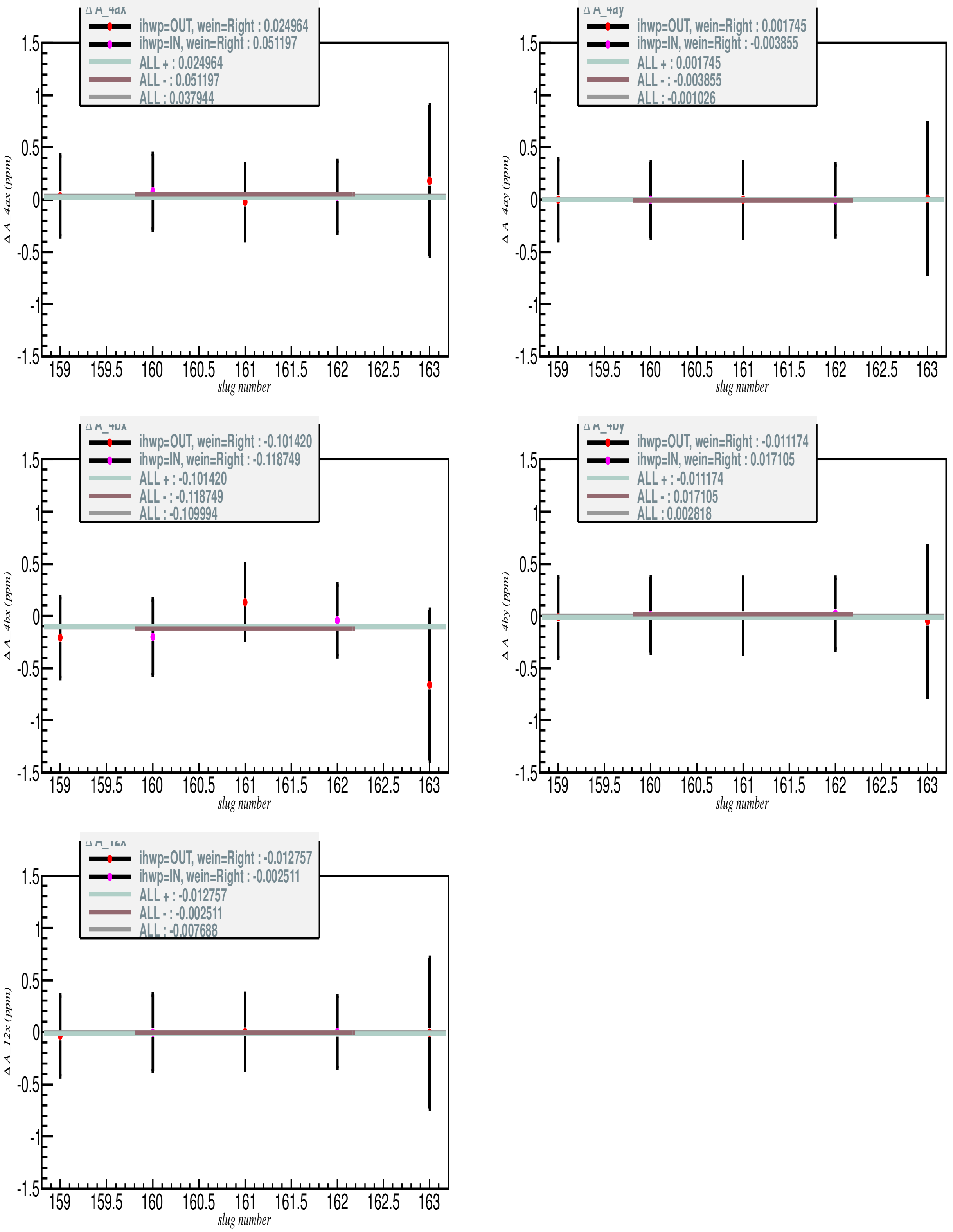

Figure 7.10: the weighted average of the asymmetry correction in the run-average level for Carbon with separate insertable half-wave plat and wein angle (spin flipper) states.

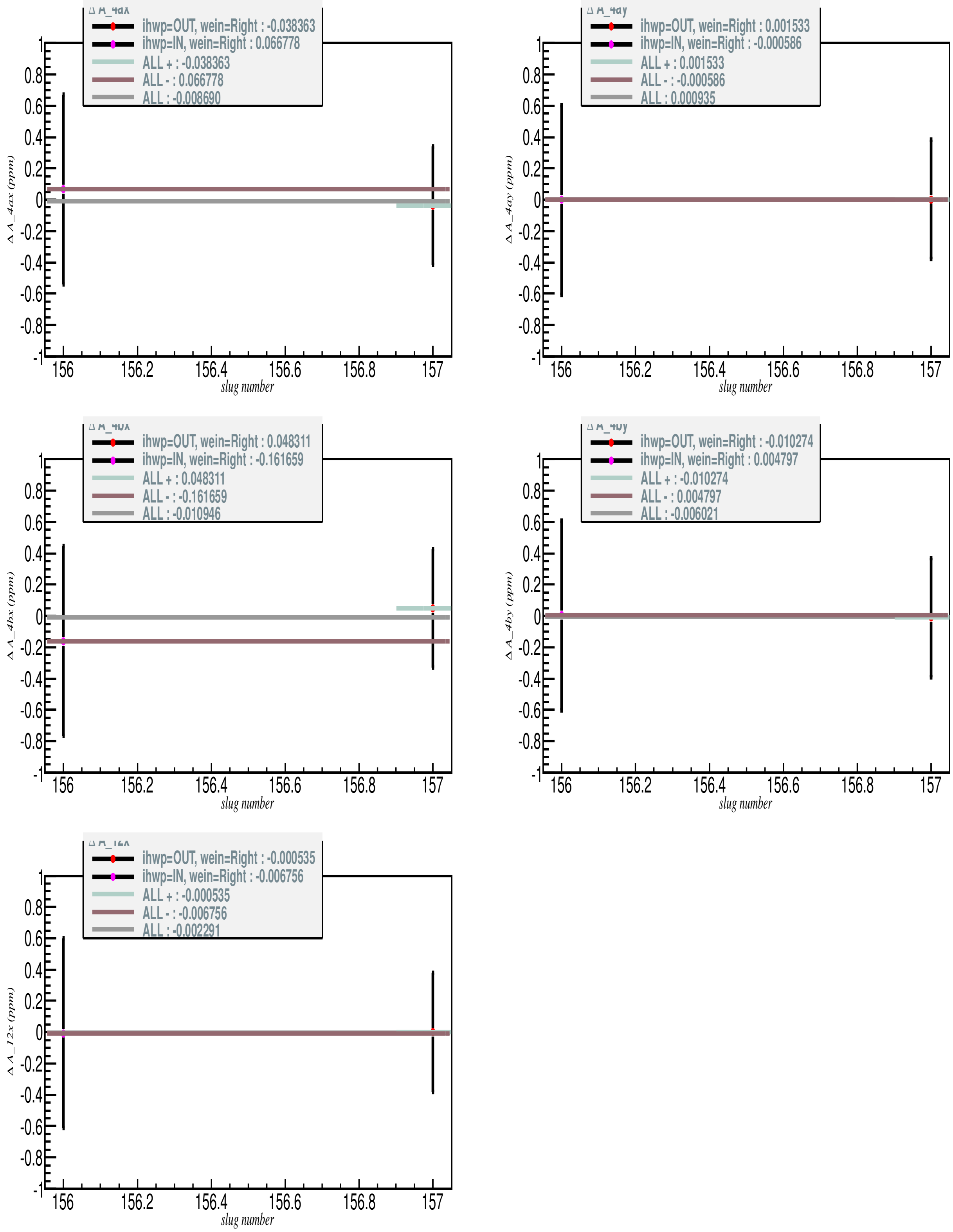

Figure 7.11: the standard set of beam position monitor difference structures ($\Delta\mathcal{M}_j^{j=4ax}$, $\Delta\mathcal{M}_j^{j=4bx}$, $\Delta\mathcal{M}_j^{j=4ay}$, $\Delta\mathcal{M}_j^{j=4by}$, $\Delta\mathcal{M}_j^{j=12x}$) for Lead in separate half-wave plat states and wein angle states.

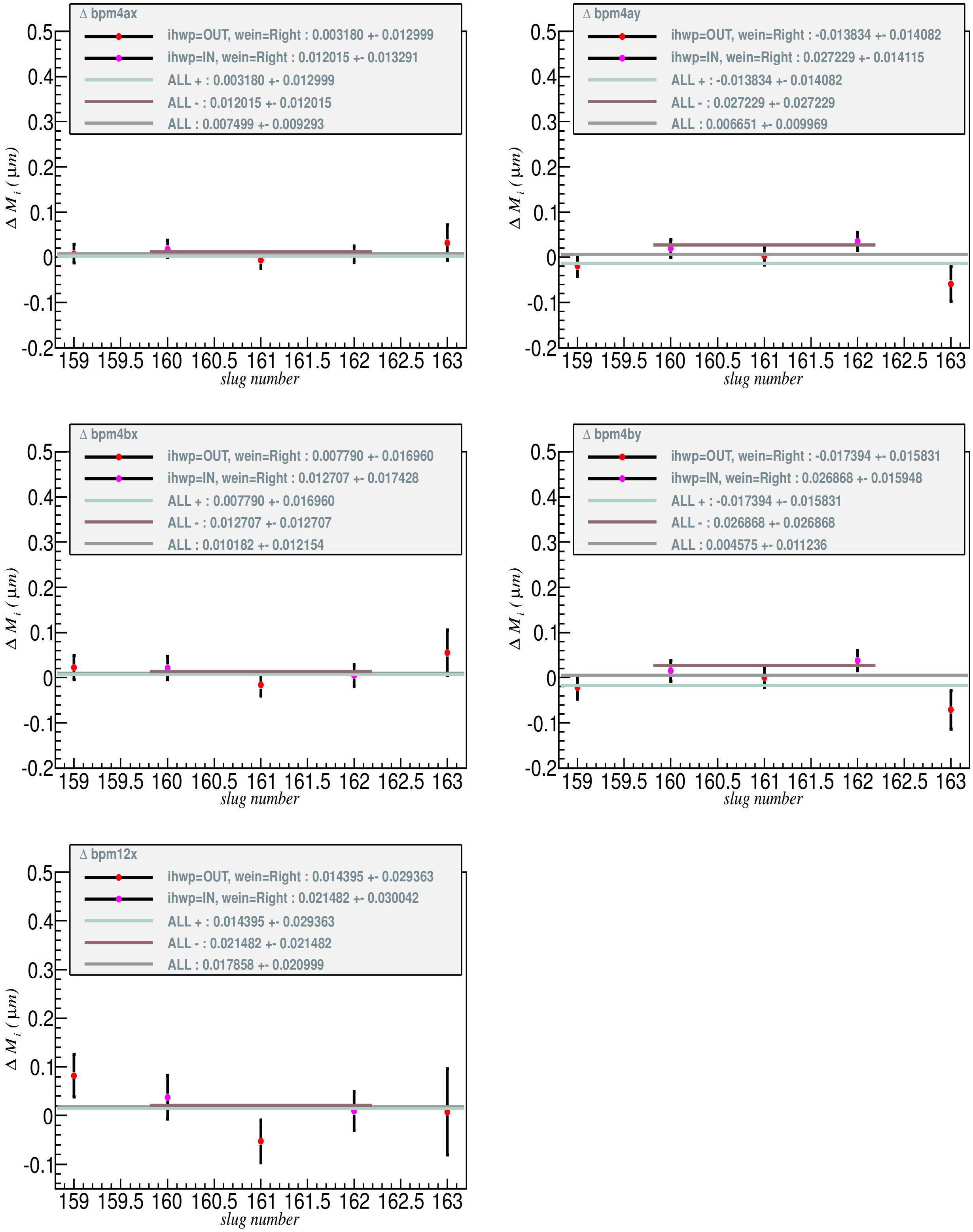

Figure 7.12: the standard set of beam position monitor difference structures ($\Delta\mathcal{M}_j^{j=4ax}$, $\Delta\mathcal{M}_j^{j=4bx}$, $\Delta\mathcal{M}_j^{j=4ay}$, $\Delta\mathcal{M}_j^{j=4by}$, $\Delta\mathcal{M}_j^{j=12x}$) for Carbon in separate half-wave plat states and wein angle states.

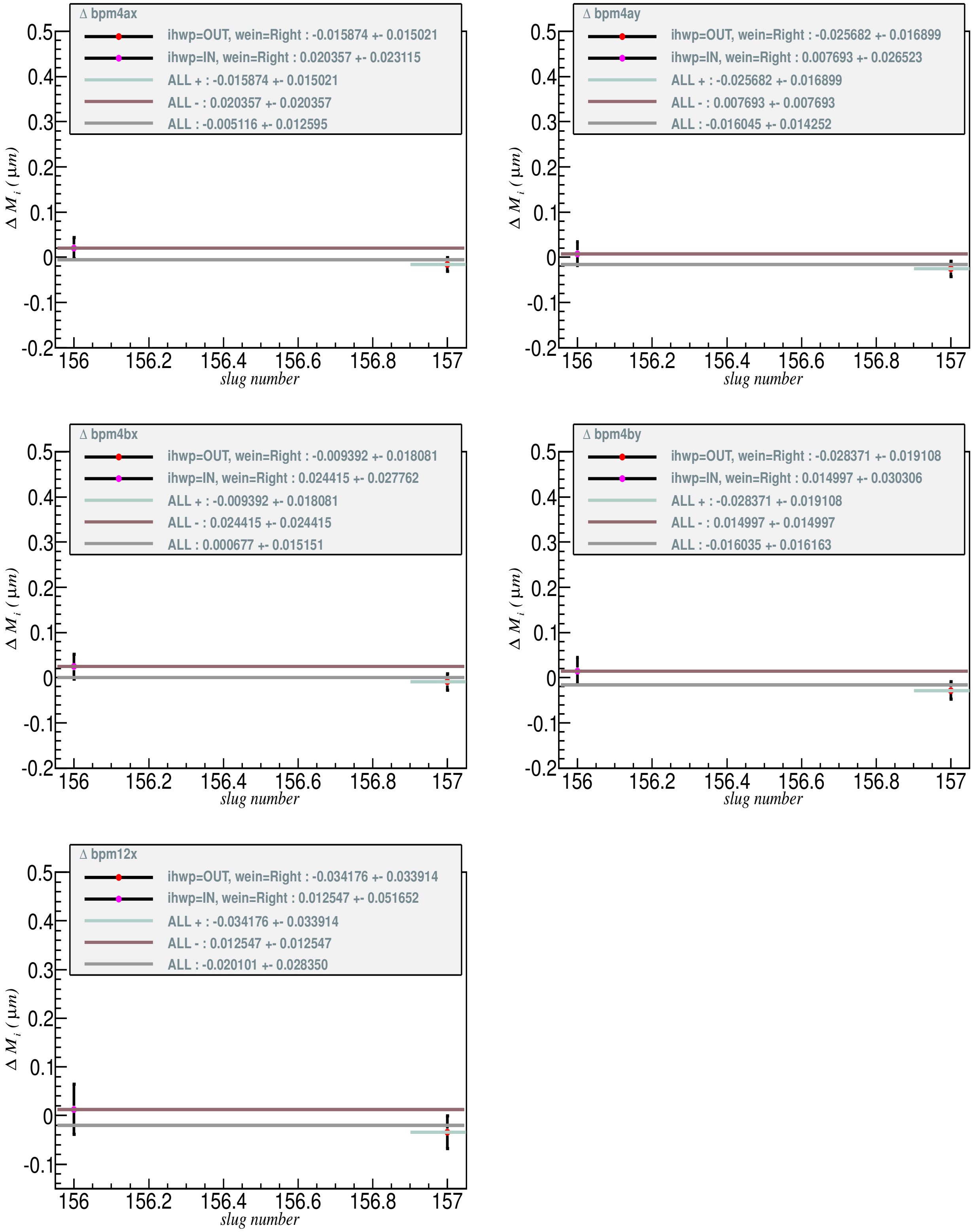

Figure 7.13: the dithering coefficients (unit: ppm/μm) for the left-arm detector versus beam position (or energy) monitors ($\frac{\partial \mathcal{D}_k^{k=L}}{\partial \mathcal{M}_j}$) in Lead.

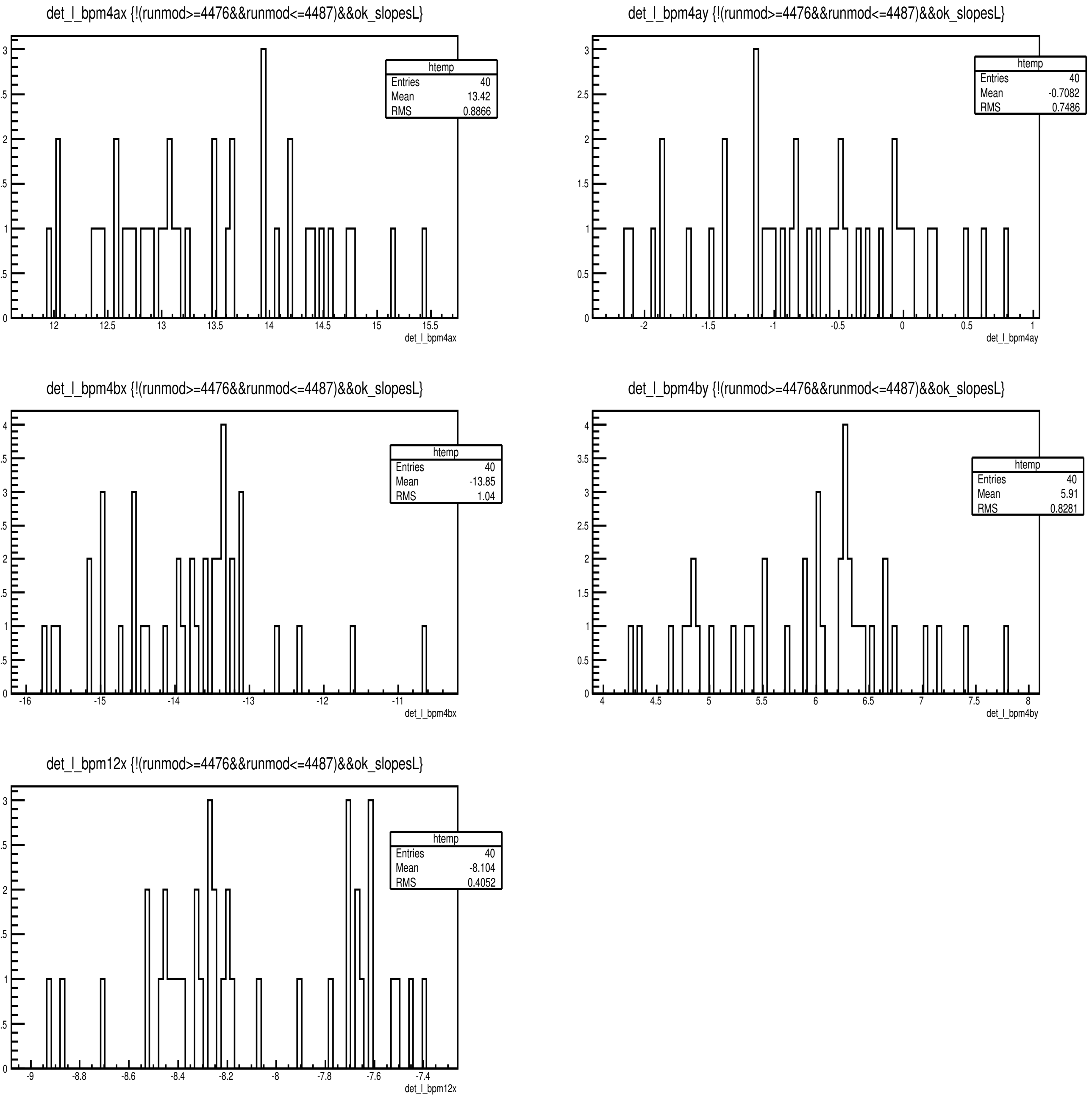

Figure 7.14: the dithering coefficients (unit: ppm/μm) for the right-arm detector versus beam position (or energy) monitors ($\frac{\partial\mathcal{D}_k^{k=R}}{\partial\mathcal{M}_j}$) in Lead.

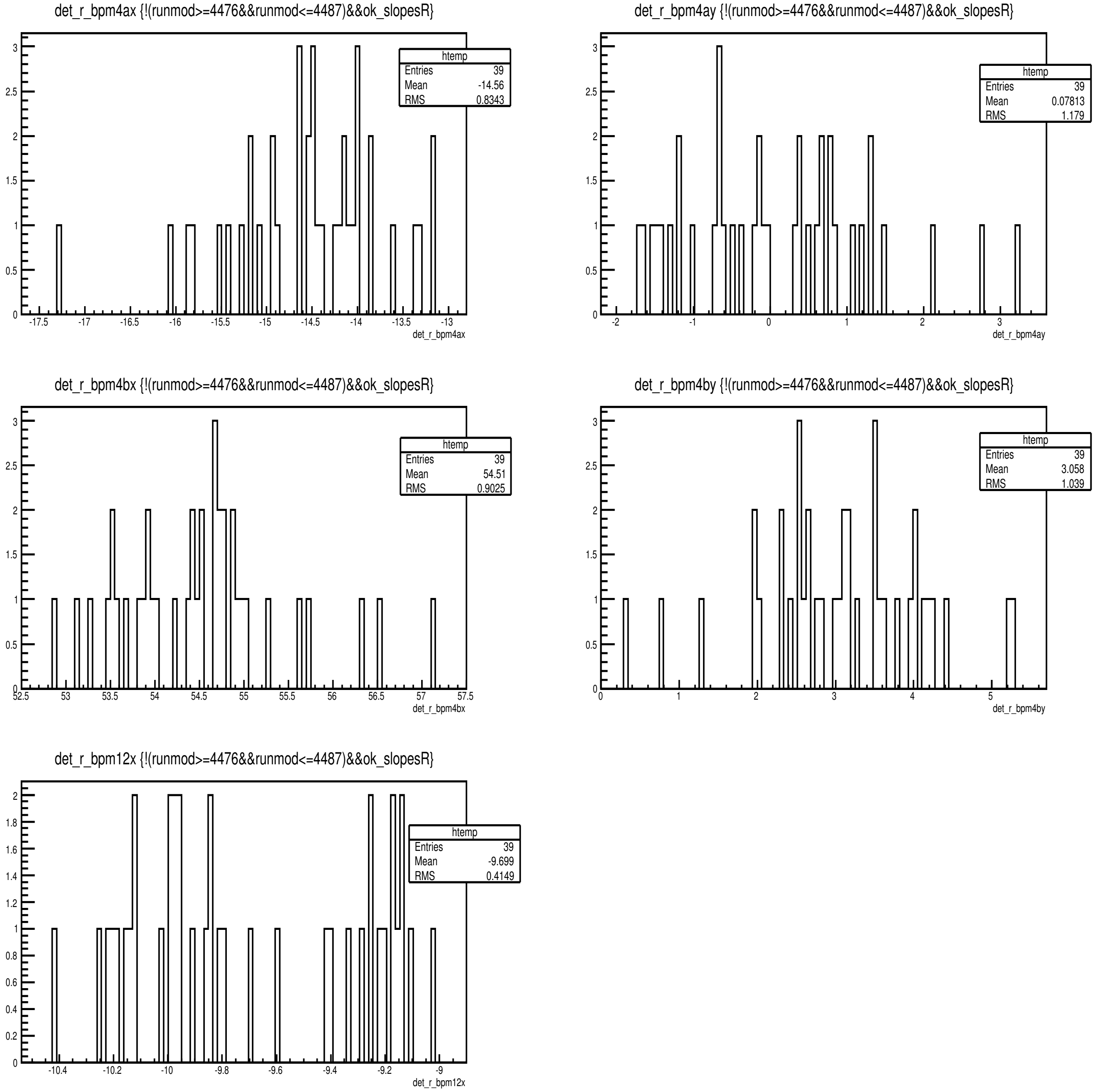

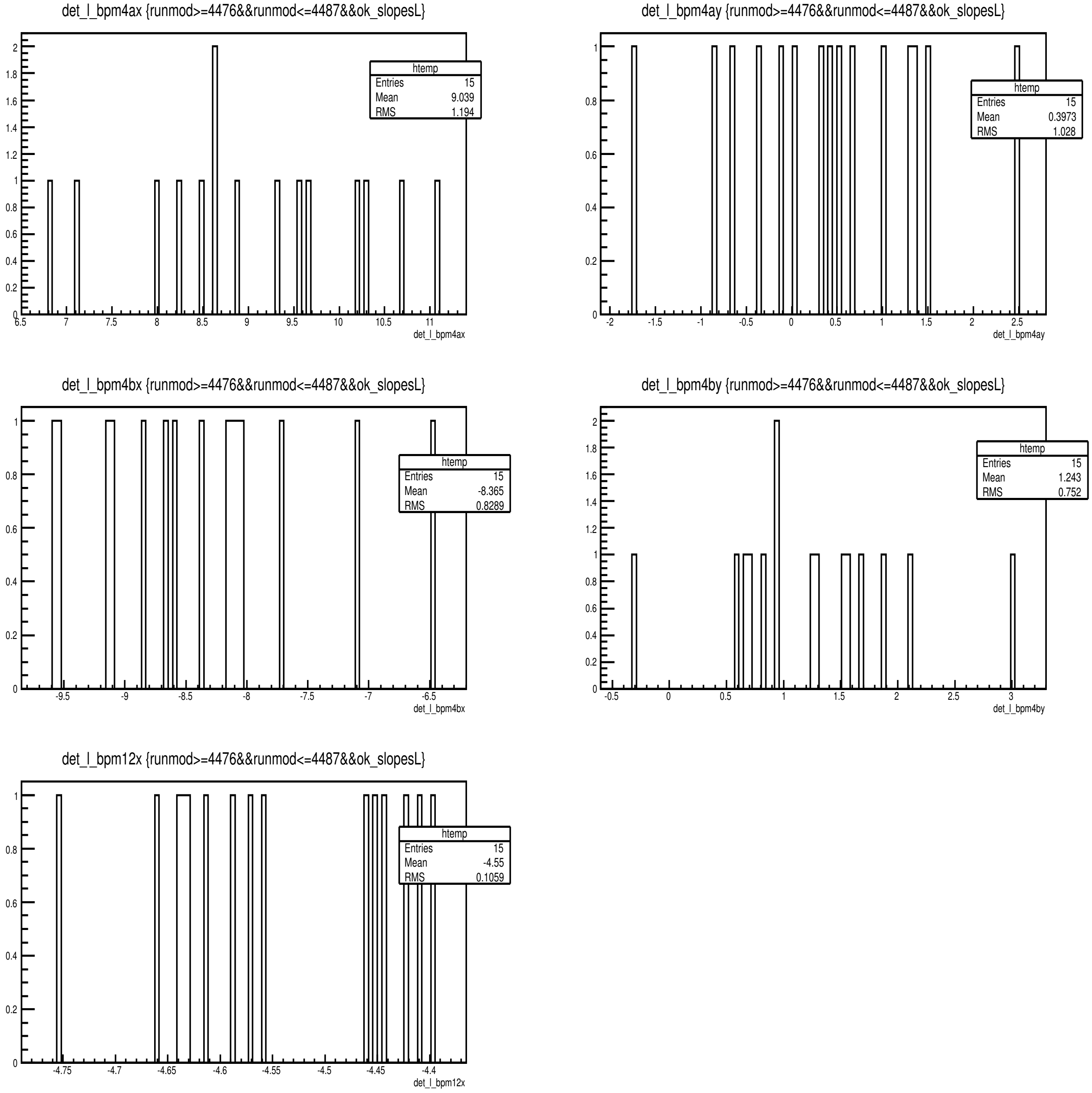

Figure 7.15: the dithering coefficients (unit: ppm/μm) for the left-arm detector versus beam position/energy monitors ($\frac{\partial \mathcal{D}_k^{k=L}}{\partial \mathcal{M}_j}$) in Carbon.

Figure 7.16: the dithering coefficients (unit: ppm/μm) for the right-arm detector versus beam position/energy monitors ($\frac{\partial \mathcal{D}_k^{k=R}}{\partial \mathcal{M}_j}$) in Carbon.

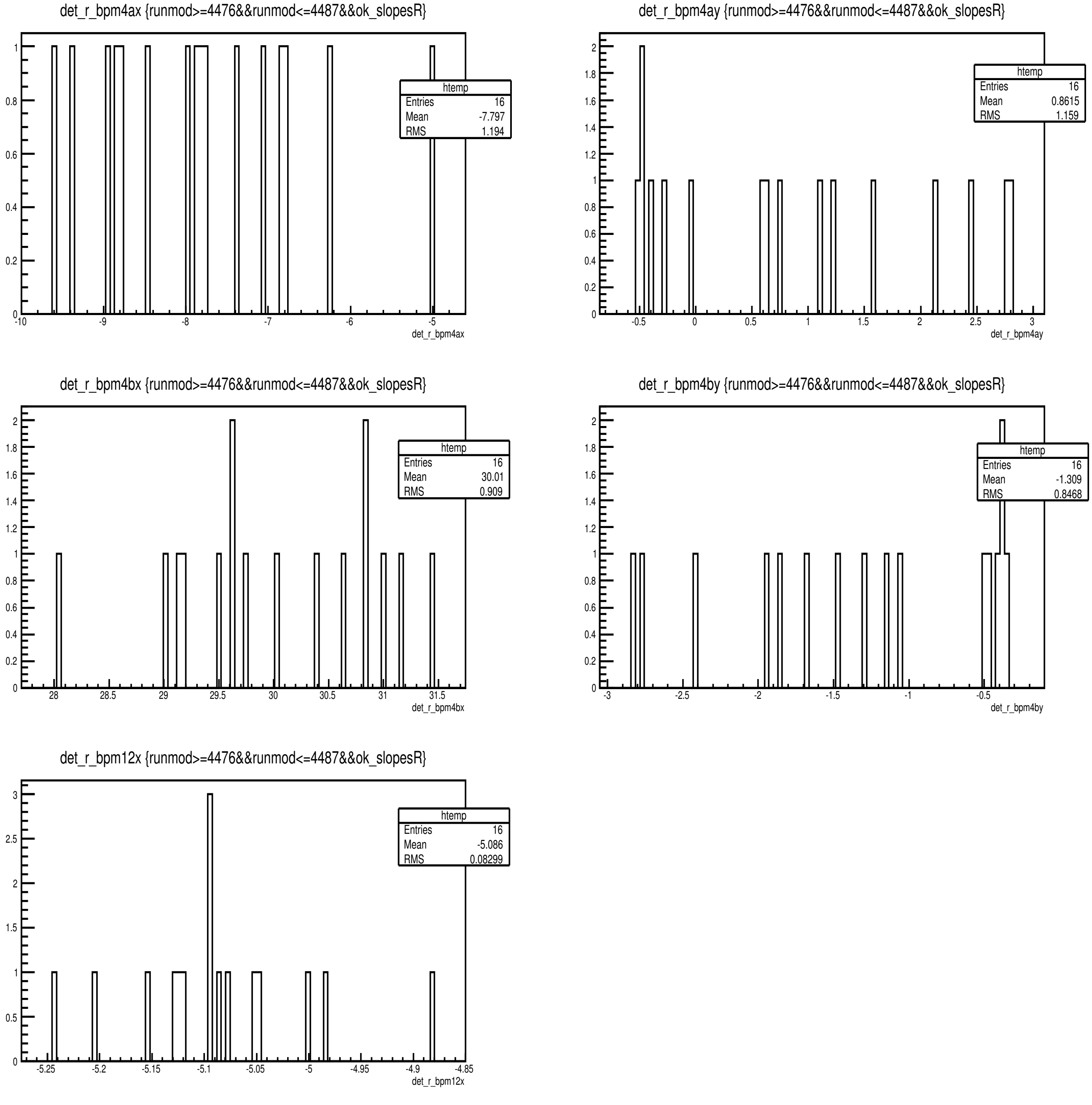

Appendix A

Derivation of Dithering Coefficients

In 2x2,

$$\begin{pmatrix} \gamma_1 \\ \gamma_2 \end{pmatrix} = \begin{pmatrix} \alpha_1 & \beta_1 \\ \alpha_2 & \beta_2 \end{pmatrix} \begin{pmatrix} x_1 \\ x_2 \end{pmatrix},$$

Re-write the matrix above,

$$\begin{pmatrix} \frac{\gamma_1}{\alpha_1} \\ \frac{\gamma_2}{\alpha_2} \end{pmatrix} = \begin{pmatrix} 1 & \frac{\beta_1}{\alpha_1} \\ 1 & \frac{\beta_2}{\alpha_2} \end{pmatrix} \begin{pmatrix} x_1 \\ x_2 \end{pmatrix},$$

Replace $\frac{\beta_2}{\alpha_2} x_2$ with x_2' and pull out $\frac{\gamma_2}{\alpha_2}$, we get:

$$\frac{\gamma_2}{\alpha_2} \begin{pmatrix} \frac{\gamma_1}{\alpha_1}\frac{\alpha_2}{\gamma_2} \\ 1 \end{pmatrix} = \begin{pmatrix} 1 & \frac{\beta_1}{\alpha_1}\frac{\alpha_2}{\beta_2} \\ 1 & 1 \end{pmatrix} \begin{pmatrix} x_1 \\ x_2' \end{pmatrix},$$

Now, we change variables: $1 - \alpha \equiv \frac{\beta_1}{\alpha_1}\frac{\alpha_2}{\beta_2}$ and $1 - \beta \equiv \frac{\gamma_1}{\alpha_1}\frac{\alpha_2}{\gamma_2}$. Then, we have:

$$\frac{\gamma_2}{\alpha_2} \begin{pmatrix} 1 - \beta \\ 1 \end{pmatrix} = \begin{pmatrix} 1 & 1 - \alpha \\ 1 & 1 \end{pmatrix} \begin{pmatrix} x_1 \\ x_2' \end{pmatrix},$$

and

$$x_1 = \kappa(1 - \frac{\beta}{\alpha}), \quad x_2 = \frac{\kappa\beta}{\alpha\lambda}$$

Appendix B

Derivation of Dithering Coefficients w/ PREx geometry

$$\Delta\theta_{1,4ax} + \Delta\theta_{2,4ax} = \frac{\Delta x_1}{L} + \frac{(S - \frac{L}{2})\Delta x_1}{DL}$$

$$\Delta\theta_{1,4bx} + \Delta\theta_{2,4bx} = -(\frac{\Delta x_2}{L} + \frac{(S + \frac{L}{2})\Delta x_2}{DL})$$

$$\frac{\partial \mathcal{D}_k}{\partial 4ax} = \frac{\partial(\Delta\theta_{1,4ax} + \Delta\theta_{2,4ax})}{\partial \Delta x_1} = \frac{1}{L} + \frac{(S - \frac{L}{2})}{DL} = 0.362$$

$$\frac{\partial \mathcal{D}_k}{\partial 4bx} = -(\frac{\partial(\Delta\theta_{1,4bx} + \Delta\theta_{2,4bx})}{\partial \Delta x_2}) = -(\frac{1}{L} + \frac{(S + \frac{L}{2})}{DL}) = -0.779$$

Figure B.1: the geometry of the beam modulation system.

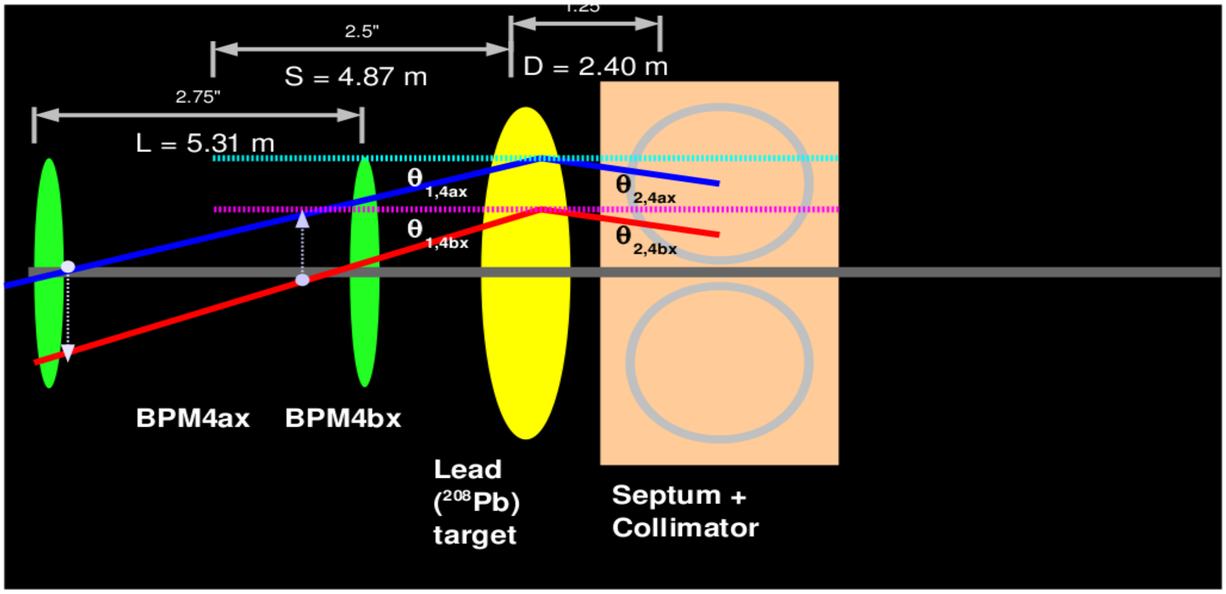
1.25
2.5"
S = 4.87 m
D = 2.40 m
2.75"
L = 5.31 m
$\theta_{1,4ax}$
$\theta_{1,4bx}$
$\theta_{2,4ax}$
$\theta_{2,4bx}$
BPM4ax
BPM4bx
Lead (^{208}Pb) target
Septum + Collimator

Bibliography

[1] B. Frois et al., Phys. Rev. Lett. **38**, 152, (1977).

[2] G. Fricke, C. Bernhardt, K. Heilig, L. A. Schaller, L. Schellenberg, E. B. Shera, and C. W. de Jager, At. Data Nucl. Data Tables **60**, 177 (1995).

[3] C. Garcia-Recio, J. Nieves and E. Oset, Nucl. Phys. **A 547**, 473 (1992).

[4] B. Friedman and V.R. Pandharipande, Nucl. Phys. **A361**, 502 (1981).

[5] B. A. Brown, Phys, Rev. C **58**, 220 (1998).

[6] L. Ray, W. R. Coker, G. W. Hoffmann, Phys. Rev. **C 18**, 2641 (1978).

[7] V. E. Starodubsky, N. M. Hintz, Phys. Rev. **C 49**, 2118 (1994).

[8] B. C. Clark, S. Hama, L. J. Kerr, Phys. Rev. **C 67**, 054605 (2003).

[9] A. Trzcinska et al., Phys. Rev. Lett. **87**, 082501 (2001).

[10] H. Lenske, Hyperfine Interact. **194**, 277 (2009).

[11] T. W. Donnelly, J. Dubach, Ingo Sick, Nucl. Phys. **A 503**, 589 (1989).

[12] C. J. Horowitz, Phys. Rev. **C 57**, 3430 (1998).

[13] C. J. Horowitz, S. J. Pollock, P. A. Souder, and R. Michaels, Phys. Rev. **C 63**, 025501 (2001).

[14] B. Alex Brown, Phys. Rev. Lett. **85**, 5296 (2000).

[15] J. D. Walecka, Nucl. Phys. **A285** (1977) 349.

[16] J. Friedrich and Th. Walcher Eur. Phys. J. A **17**, 607 (2003).

[17] R. D. McKeown, Phys. Lett. B **219** (1989) 140.; D. T. Spayde, *et al.* Phys. Lett.

B583 (2004) 79; T. Ito, *et al.* Phys. Rev. Lett. **92** (2004) 102003.

[18] K. A. Aniol *et al.*, Phys. Lett. B **509** (2001) 211; K. A. Aniol *et al.*, Phys. Rev. C **69** (2004) 065501; K. A. Aniol *et al.*, Phys. Rev. Lett. **96** (2006) 022003; K. A. Aniol *et al.*, Phys. Lett. B **635** (2006) 275; A. Acha *et al.*, Phys. Rev. Lett. **98** (2007) 032301. Z. Ahmed *et al.*, arXiv:1107.0913 [nucl-ex].

[19] D. H. Beck, Phys. Rev. **D 39** (1989) 3248; D. S. Armstrong *et al.*, Phys. Rev. Lett. **95** (2005) 092001; D. Androic *et al.*, Phys. Rev. Lett. **104** (2010) 012001.

[20] F. E. Maas *et al.*, Phys. Rev. Lett. **93** (2004) 022002; F. E. Maas *et al.*, Phys. Rev. Lett. **94** (2005) 152001; S. Baunack *et al.*, Phys. Rev. Lett. **102** (2009) 151803.

[21] R. D. Young, J. Roche, R. D. Carlini, A. W. Thomas, Phys. Rev. Lett **97** (2006) 10200.

[22] J. Liu, R. D. McKeown, M. J. Ramsey-Musolf, Phys. Rev. **C 76** (2007) 025202.

[23] B. G. Todd-Rutel, J. Piekarewicz, Phys. Rev. Lett. **95**, 122501 (2005).

[24] D. Vautherin, D. M. Brink, Phys. Rev. **C 5**, 626 (1972).

[25] M. Beiner, H. Flocard, N. Van Giai, P. Quentin, Nucl. Phys. **A 238**, 29 (1975).

[26] E. Chabanat, P. Bonche, P. Haensel, J. Meyer, R. Schaeffer, Nucl. Phys. **A 635**, 231 (1998).

[27] G. A. Lalazissis, J. Konig, and P. Ring, Phys. Rev. **C 55**, 540 (1997).

[28] S. Ban, C. J. Horowitz, R. Michaels, J. Phys. G **39**, 015104 (2012).

[29] S. Abrahamyan *et al.* (the PREx collaboration), Phys. Rev. Lett. 108, 112502 (2012).

[30] P. A. Souder *et al.*, Proposal to Jefferson Lab PAC 38: PREX-II: precision parity-violating measurement of the neutron skin of Lead"

(http://hallaweb.jlab.org/parity/prex/prexII.pdf).

[31] R. H. Helm, Phys. Rev. **104**, 1466 (1956).

[32] M. Rosen, R. Raphael, H. Uberall, Phys. Rev. **163**, 927 (1967).

[33] R. Raphael, M. Rosen, Phys. Rev. **C 1**, 547 (1970).

[34] S. Mizutori *et al.*, Phys. Rev. **C 61**, 044326 (2000).

[35] R. W. Hasse and W. D. Myers, *Geometrical relationships of macroscopic nuclear physics* (Springer-Verlag, Heidelberg, 1988)

[36] J. Piekarewicz and M. Centelles, Phys. Rev. **C 79**, 054311 (2009). (arXiv:0812.4499)

[37] R. J. Furnstahl, Nucl. Phys. **A706**, 85 (2002).

[38] C. J. Horowitz and J. Piekarewicz, Phys. Rev. **C 64**, 062802 (2001).

[39] C. J. Horowitz and J. Piekarewicz, Phys. Rev. Lett. **86**, 5647 (2001).

[40] A. W. Steiner, M. Prakash, J. M. Lattimer, and P. J. Ellis, Phys. Rept. **411**, 325 (2005).

[41] J. Carriere, C. J. Horowitz and J. Piekarewicz, Astrophys. J. **593**, 463 (2003).

[42] C. J. Horowitz and J. Piekarewicz, Phys. Rev. **C 66**, 055803 (2002).

[43] F. J. Fattoyev and J. Piekarewicz, Phys. Rev. **C 82**, 025810 (2010).

[44] C. Y. Prescott, SLAC preprint TN-73-1 (1973).

[45] S. Agostinelli *et al.*, Nucl. Instr. and Meth. A 506 (2003) 250.

[46] G. Bardin, C. Cavata, and J-P Jorda, "Compton Polarimeter Studies for TESLA", CEA, Saclay, France (1997).

[47] T. B. Humensky *et al.*, SLAC's polarized electron source laser system and

minimization of electron beam helicity correlations for the E-158 parity-violation experiment, Nucl. Instr. Methods Phys. Res. A **521** (2004). 108, 123, 124, 135, 136, 144, 311.

[48] G. D. Cates *et al.*, Nucl. Instr. Methods Phys. Res. **A 278**, 293 (1989). 129, 130.

[49] difference between laser-wise and laser cycle wise methods, http://ace.phys.virginia.edu/HAPPEX/2315.

[50] Appendix-I: Derivation of Dithering Coefficients.

[51] Appendix-II: Derivation of Relative Dithering Coefficients w/ PREx geometry.

[52] T.D. Lee; C.N. Yang (1956). "Question of Parity Conservation in weak interaction". Phys. Rev. **104** (1): 254-258.

[53] dithering coefficients history plots and orthogonality problem w/ the standard BPM set, http://ace.phys.virginia.edu/HAPPEX/2564.

Curriculum Vitae

EDUCATION

Doctor of Philosophy, Physics

Syracuse University, Syracuse, NY GPA 3.8/4.0 Aug., 2007 - May, 2013

Research focusing on parity (P) violating asymmetry measurements for HAPPEX, PVDIS, PREx and Moller experiments conducted at Hall-A in Thomas Jefferson National Accelerator Facility (TJNAF), Newport News, VA, USA THESIS - First Leptonic Probe of the Neutron Density Profile in ^{208}Pb at Low-Q^2

Adviser: Prof. Paul A. Souder

Master of Science, Physics

National Taiwan University, Taipei, Taiwan Aug., 2002 - May, 2005

Research focusing on direct charge-parity (CP) violating asymmetry measurements in rare-B decay channels with one ω meson in the final state for Belle experiments performed at KEK, Tsukuba, Ibaraki, Japan THESIS - Improved Measurements of Branching Fractions and CP Asymmetry for $B \to \omega h$" "Search for $B \to \omega\eta$"

Adviser: Prof. Paoti Chang

RESEARCH EXPERIENCE

Graduate Research Assistant Dec., 2012 - May, 2013

stationed at Department of Physics, Syracuse University, Syracuse, NY

Simulation Projects for 12GeV Moller Experiment

- physics simulation - target length optimization study
- physics simulation - comprehensive comparison of Moller simulation software packages
- ROOT/GEANT4/Moller software installation on the personal laptop

Graduate Research Assistant Jun., 2012 - Nov., 2012

stationed at Department of Physics, Syracuse University, Syracuse, NY

Thesis Writing, Oral Presentation Practice and Interview Training

- learn how to communicate my completed and on-going jobs with the scientific profession
- learn how to organize my professional presentations for the general audience from diverse research groups
- learn how to wrap up my well-done projects in written documents (technique notes) for my colleagues

Graduate Research Assistant May., 2011 - May., 2012

stationed at Department of Physics, Syracuse University, Syracuse, NY

PRExII: Proposing an On-line (and Off-line) Data Analysis Methodology to Study the Systematic Uncertainty for Helicity-Correlated Beam Asymmetries

- cross-check the validity of the conventional (standard) beam modulation analysis methodology

- help suppress the helicity-correlated beam asymmetry size and its associated systematic uncertainty

Graduate Research Assistant Apr., 2011

stationed at Department of Physics, Syracuse University, Syracuse, NY

PRExI: Systematic Uncertainty Sources for Helicity-Correlated Beam Asymmetry Corrections, the Re-scattering Background and the Analyzing Power on the Photon Detector for Compton Polarimeter

- Helicity-Correlated Beam Asymmetries:
  - compare feedback properties for different combinations of beam position monitors
  - evaluate beam correction quantities on the measured raw asymmetry for different combinations of beam position monitors
- Re-scattering Background:
  - measure and fit the re-scattering probability function
  - quote the total amount of discrepancy under the integration of the product of both probability function and asymmetry over momenta between data and MC
- Systematic Uncertainties for the Analyzing Power in Compton Polarimetry result from:
  - the change in collimator displacement
  - the non-linearity of PMTs in the photon detector
  - the radiation correction

Graduate Research Assistant Oct., 2010 - Mar., 2011

stationed at Department of Physics, Syracuse University, Syracuse, NY

PRExI: Helicity-Correlated Beam Asymmetry Analysis w/ New Beam Modulation System

- diagnose flaws of the beam modulation system
- investigate the (in-)stability of the beam properties and the damping in the accelerator
- understand the phase advance/retardation between monitors and coils driven by DAC
- study selection criteria
- find the most credential approach to take the weighted asymmetry average toward final resultes for publications
- update the fast-dithering differential analysis algorithm

Graduate Research Assistant Jul., 2010 - Sep., 2010

stationed at Department of Physics, Syracuse University, Syracuse, NY

PRExI: Compton Polarimetry in Studying Analyzing Power of Photon Detector with GEANT4 Simulation

- obtain the analyzing power (the theoretical photon asymmetry) with the photon detector (calorimeter)
- fit the photon detectors response function generated by the counting mode Monte Carlo and the photon data accumulated by the integration mode of the DAQ system to obtain the electron beams polarization

Graduate Research Assistant Mar., 2010 - Jun., 2010

stationed at Jefferson Lab., Newport News, VA

PRExI: Serving As New Beam Modulation System On-line Data Analysis Coordinator

work on both the regression and dithering data quality check

Graduate Research Assistant Sep., 2009 - Apr., 2010

stationed at Jefferson Lab., Newport News, VA

PVDIS-6GeV and PRExI: Upgrading the Counting DAQ System to the Integrating Flash-ADC (FADC) System for Moller Polarimetry

- understand both decoders written in FORTRAN and C++ for the counting mode DAQ and the integrating mode FADC
- help implement the old DAQ analyzer written in PAW into the data-analysis algorithm for the FADC decoder written in ROOT
- diagnose the FADC decoder and finalize all corrections

Graduate Research Assistant Apr., 2009 - Aug., 2010

stationed at Department of Physics, Syracuse University, Syracuse, NY

PVDIS-12GeV SoLID: Tracking Reconstruction Algorithm with GEANT4 Simulation

work on a simple simulation of the PVDIS spectrometer with GEANT4 Monte Carlo and develop a preliminary version of tracking reconstruction algorithm

COMPUTING SKILLS

Experienced in C++, ROOT, ROOFIT, GEANT4, Python, PAW, REVTEX4, MINUITFIT

PUBLICATIONS

- New Measurements of the Transverse Beam Asymmetry for Elastic Electron Scattering from Selected Nuclei.
  HAPPEX and PREX Collaborations (S. Abrahamyan (Yerevan Phys. Inst.) et al.). Aug 2012. 6 pp.
  Published in Phys.Rev. Lett. 109, (2012) 192501
  DOI: 10.1103/PhysRevLett.109.192501 e-Print: arXiv:1208.6164v3 [nucl-ex] — PDF

- Weak charge form factor and radius of 208Pb through parity violation in electron scattering.
  C.J. Horowitz (Tennessee U. and Indiana U.), Z. Ahmed, C.M. Jen, A. Rakhman, P.A. Souder (Syracuse U.), M.M. Dalton, N. Liyanage, K.D. Paschke, K. Saenboonruang, R. Silwal (Virginia U.) et al.. Feb 2012. 5 pp.
  Published in Phys.Rev. C85 (2012) 032501
  JLAB-PHY-12-1409
  DOI: 10.1103/PhysRevC.85.032501
  e-Print: arXiv:1202.1468v1 [nucl-ex] — PDF

- Measurement of the Neutron Radius of 208Pb Through Parity-Violation in Electron Scattering.
  S. Abrahamyan (Yerevan Phys. Inst.), Z. Ahmed (Syracuse U.), H. Albataineh (Clermont-Ferrand U.), K. Aniol (Cal State, L.A.), D.S. Armstrong (William-Mary Coll.), W. Armstrong (Temple U.), T. Averett (William-Mary Coll.), B. Babineau (Longwood U.), A. Barbieri (Virginia U.), V. Bellini (INFN, Catania) et al.. Jan 2012. 6 pp.
  Published in Phys.Rev.Lett. 108 (2012) 112502
  JLAB-PHY-12-1480

DOI: 10.1103/PhysRevLett.108.112502

e-Print: arXiv:1201.2568 [nucl-ex] — PDF

- New Precision Limit on the Strange Vector Form Factors of the Proton.

  HAPPEX Collaboration (Z. Ahmed (Syracuse U.) et al.). Jul 2011. 5 pp.

  Published in Phys.Rev.Lett. 108 (2012) 102001

  JLAB-PHY-11-1479

  DOI: 10.1103/PhysRevLett.108.102001

  e-Print: arXiv:1107.0913 [nucl-ex] — PDF

- PREX II proposal for PAC38. Exp E12-11-101. (Status: approved with A rating in August 2011.)

- Improved measurements of branching fractions and CP partial rate asymmetries for B $\to \omega$K and B $\to \omega\pi$.

  Belle Collaboration (C.-M. Jen (Taiwan, Natl. Taiwan U.) et al.). Sep 2006. 6 pp.

  Published in Phys.Rev. D74 (2006) 111101

  DOI: 10.1103/PhysRevD.74.111101

  e-Print: hep-ex/0609022 — PDF